Helsinki University of Technology
Department of Electrical and Communications Engineering
Optoelectronics Laboratory
Espoo, Finland 2004

OPTICAL MICROSYSTEMS BASED ON INTEGRATED OPTICS AND MICROMECHANICS

Pekka Katila

Dissertation for the degree of Doctor of Science in Technology to be presented with due permission of the Department of Electrical and Communications Engineering for public examination and debate in Auditorium S1 at Helsinki University of Technology, Espoo, Finland, on the 20th August, 2004, at 12 o'clock noon.

Helsinki University of Technology
Department of Electrical and Communications Engineering
Optoelectronics Laboratory

Teknillinen Korkeakoulu
Sähkö- ja tietoliikennetekniikan osasto
Optoelektroniikan laboratorio

Distribution:
Helsinki University of Technology
Department of Electrical and Communications Engineering
Optoelectronics Laboratory
P.O.Box 3500
FIN-02150 HUT
Finland

ISBN 951-22-7207-5

Abstract

Optical microsystems based on silicon technology have been studied in this work. Components applying integrated optical structures and microelectromechanical systems (MEMS) have been developed. New functionality, lower component costs, and improved reliability have been aimed at by the integration and miniaturization of the novel concepts. The four components studied in this work represent new ideas based on well established material technologies and manufacturing schemes. The first three components are based silicon integrated optics and the fourth component is based on silicon micromechanics.

A novel architecture for a surface plasmon resonance (SPR) sensor based on a silicon nitride slab waveguide structure was proposed and studied. Industrial aspects and feasibility for the practical sensor design of the introduced concept were considered. As a main result a proof-of-concept was shown by demonstrating the device sensitivity to humidity. A surface plasmon sensor fabricated with a silicon nitride waveguide technology has applications as a chemical and biochemical sensor.

A thermally tunable integrated optical ring resonator device was developed to study the optical characteristics of a ring resonator, waveguide quality, and electrical characteristics of thermo-optical control with in situ temperature sensing. The device was based on Si_3N_4 waveguides. The ring perimeter of the resonator was 6.76 mm and the free spectral range was 26 GHz. The thermal control was implemented by using poly-silicon resistive heaters integrated on top of the waveguide layer. The thermal tuning was demonstrated to be a feasible tool for an accurate optical phase control. The measured temperature coefficient of Si_3N_4 rib waveguide can be applied in the design of future devices based on similar structures. This type of ring resonator structures are suitable for sensing applications, as high refractive index difference enables flexible designs with small radius waveguide bends.

New type of integrated optical beam combiner circuits were proposed, designed and fabricated based on a silicon oxynitride waveguide technology, to provide a replacement for optical fiber coupler components in a phased array antenna demonstrator. The insertion loss of the pigtailed devices turned out to be moderately high but the coupling ratio of the 3 dB couplers were better than 47:53, and polarization extinction ratio was above 10 dB. Based on the results of the fabricated test devices the specified optical requirements for a practical application were considered achievable with the proposed SiON technology by further reducing the propagation loss of the waveguide and the excess loss of the 3 dB couplers.

Lastly, microelectromechanical variable optical attenuators (VOA) based on the silicon-on-insulator (SOI) technology were developed for optical fiber networks. Two novel VOA architectures were proposed and developed. As a result both configurations were shown to have optical performance satisfying the general requirements set by modern fiber optical networks for VOAs. The major achievement was a reflective type VOA device with low insertion loss below 0.8 dB, ultra-low polarization sensitivity below 0.1 dB, 30 dB dynamic attenuation range, and with optical repeatability better than 0.03 dB.

Keywords: *optical microsystem, integrated optic, waveguide, MEMS, MST, micromechanics, surface plasmon resonance, ring resonator, variable optical attenuator*

Preface

Major part of this work was done at the Photonics Group at VTT Microelectronics 1994-2000. I wish to express my gratitude to Prof. Matti Leppihalme, for creating inspiring and motivating atmosphere in our team. I would also like to thank Prof. Jouni Heleskivi, the former leader of the laboratory, for his encouragement.

During two and half years between 2000-2003, I had a privilege to participate in the development of optical network products at Memscap S.A. in Grenoble. I wish to thank Dr. Jean-Michel Karam, the CEO of Memscap S.A., for enabling this thesis project.

The results gained in this mostly experimental work were based on team collaboration and effort of several persons. I want to express my gratitude to my ex-colleagues at VTT Microelectronics. Especially I want to thank former and current members of the Photonics Group who were participating in the work described in my thesis: Dr. Jaakko Aarnio who was the driving force on the project related to surface plasmon and the ring resonator devices. He also designed the optical ring resonator device, and with whom I had many valuable discussions concerning the optical measurements. Mrs. Päivi Heimala for the collaboration as her knowledge and experience with the process issues was essential in the fabrication of the studied integrated optical devices. Mr. Timo Aalto for creating the design of the beam combiner circuits and making thorough analysis of measurement data. Mrs. Arja Heinämäki for helping to understand the thermal issues of the ring resonator chip. I wish to thank Mr. Jukka Pihlainen, Mr. Ingmar Stuns, and Mr. Ari Hokkanen for helping out with experimental set-ups and measurement arrangements. I wish to thank Dr. Janusz Sadowski and Dr. Jukka Lekkala at VTT Information Technology and Mr. Leif Grönberg at VTT Microelectronics for their collaboration concerning the work done with the SPR device. I thank Prof. Walter Leeb and his group at Technical University of Vienna for the collaboration in the development of the integrated beam combiner devices.

Several persons contributed to the development of the variable optical attenuators at Memscap S.A. I wish to thank all my former colleagues in the Optical Communications Business Unit at Grenoble, Cairo and San Jose offices, especially Dr. Nan Zhang, Mr. Arnaud Delpoux, Prof. Diaa Khalil, Mr. Bassam Saadany, Mr. Aymen Bashir, and Dr. Jerome Goy. I want to thank Mr. Nicolas Ogier who was responsible for the test software development and carried out a large number of optical measurements and device testing. I want to express my gratitude to all personnel who contributed to the VOA fabrication in the Front-end and Back-end Manufacturing Units in Crolles. Dr. Philippe Hélin and Dr. Eric Lebrasseur I wish to thank for many valuable discussions concerning the component development, and the warm atmosphere in our office.

Dr. Ari Tervonen of Nokia Research Center I wish to thank for his valuable comments concerning the manuscript, and Ms. Sam Newson for proofreading the manuscript and her efforts to improve my English.

Finally, I thank all my friends, my family, and especially Tiina for encouragement and support to finalize this thesis.

Pekka Katila
Bassano del Grappa 20.05.2004

CONTENTS

Abstract

Preface ..... **v**

Contents ..... **vii**

Abbreviations and Acronyms ..... **ix**

1 Introduction **1**
1.1 Author's contribution 2

2 Background **4**
2.1 Integrated optics 5
2.2 Optical MEMS 7
2.3 Concepts for VOAs 8
2.3.1 PLC VOAs 8
2.3.2 MEMS VOAs 9

3 Integrated Optical Surface Plasmon Resonance Sensor **12**
3.1 Design of SPR sensor 13
3.2 Manufacturing technology 17
3.3 Results 17
3.4 Conclusions 19

4 Thermally Tunable Integrated Optical Ring Resonator **21**
4.1 Design considerations 23
4.2 Design of ring resonator 25
4.3 Manufacturing technology 26
4.4 Device characterization 27
4.4.1 Calibration of poly-Si thermistor 27
4.4.2 Optical evaluation 29
4.4.3 Accuracy of temperature measurement 32
4.4.4 Temperature coefficient of the optical path length 33
4.4.5 Consideration of thermistor characteristics 33
4.4.6 Response speed and power consumption 35
4.5 Conclusions 38

5 Integrated Optical Beam Combiner **41**
5.1 Design considerations 42
5.1.1 Layouts of test devices 42
5.1.2 Specifications of test devices 44
5.2 Design of test devices 47
5.2.1 Comparison of couplers 55
5.2.2 Design conclusions and summary 61
5.3 Manufacturing technology 64
5.4 Results from chip measurements 69
5.5 Fiber attachment 78
5.6 Results from fiber attachment 82
5.7 Optical performance 82
5.8 Conclusions 87

6 MEMS Variable Optical Attenuator....89
6.1 Specifications for VOA....90
6.2 VOA concepts....92
6.3 Manufacturing technology....94
6.3.1 Design rules....96
6.4 Design of VOAs....96
6.4.1 Optical fiber for TVOA and RVOA....97
6.4.2 Fiber-to-fiber alignment tolerance....99
6.4.3 Fiber-to-MEMS alignment tolerance and attenuation response....100
6.4.4 Actuator design....103
6.4.5 Numerical modeling....106
6.5 TVOA shutter....110
6.6 WDL and PDL sensitivity to fiber alignment....112
6.7 Process non-idealities....114
6.8 Design conclusions and summary....121
6.9 Pictures of fabricated structures....122
6.10 Optical performance....124
6.10.1 TVOA....125
6.10.2 RVOA....128
6.10.3 Optical repeatability....131
6.11 Conclusions....131

7 Discussion....134

References....138

Abbreviations and Acronyms

2D-BPM	Two dimensional beam propagation method
AO	Acousto-optic
AR	Anti-reflection
AWG	Arrayed waveguide grating
BE	Back-end
BHF	Buffered hydrogen fluoride
CAD	Computer assisted design
CCD	Charge coupled device
CD	Critical dimension
CMOS	Complementary metal-oxide semiconductor
DC	Directional coupler
DFB	Distributed feed-back
DGE	Dynamic gain equalizer
DMD	Digital micromirror device
DMM	Digital multi meter
DOS	Digital optical switch
DR	Dynamic range
DUT	Device under test
DWDM	Dense wavelength division multiplexing
EDFA	Erbium doped fiber amplifier
EIM	Effective index method
EO	Electro-optic
ESA	European Space Agency
FE	Front-end
FEA	Finite element analysis
FEM	Finite element method
FP	Fabry-Perot
FSR	Free spectral range
FWHM	Full width half maximum
GaAs	Gallium arsenide
HeNe	Helium-neon
HF	Hydrogen fluoride
IC	Integrated circuit
IL	Insertion loss
InP	Indium phosphide
IO	Integrated optics
IORR	Integrated optical ring resonator
IP	Intellectual property
IR	Infrared
ITU	International Telecommunications Union
KGD	Known good dies
LC	Liquid crystal
LED	Light emitting diode
$LiNbO_3$	Litium niobate
LPCVD	Low pressure chemical vapour deposition
LTO	Low temperature oxide
MEMS	Microelectromechanical system
MFD	Mode field diameter
MM	Multi mode
MMI	Multi mode interference
MOEMS	Micro-optoelectromechanical system

MST	Microsystem technology
MZI	Mach-Zehnder interferometer
NC	Normally closed
Nd:YAG	Neodynium:yttrium aluminium garnet
NO	Normally open
PC	Personal computer
PDL	Polarization dependent loss
PECVD	Plasma enhanced chemical vapour deposition
PER	Polarization extinction ratio
PL	Polarizer
PLC	Planar lightwave circuit
PM	Polarization maintaining
PMD	Polarization mode dispersion
PMF	Polarization maintaining fiber
PSG	Phosphosilicate glass
R	Optical attenuation repeatability
R&D	Research and design
RIE	Reactive ion etching
RL	Return loss
RR	Ring resonator
RVOA	Reflective variable optical attenuator
Rx	Receiver
SEM	Scanning electron microscope
Si_3N_4	Silicon nitride
SiO_2	Silicon dioxide
SiON	Silicon oxynitride
SM	Single mode
SMF	Single mode fiber
SOI	Silicon-on-insulator
SPR	Surface plasmon resonance
SPW	Surface plasmon wave
TDL	Temperature dependent loss
TE	Transverse electric
TM	Transverse magnetic
TMI	Two-mode interference
TO	Thermo-optic
TUV	Technical University of Vienna
TVOA	Transmission variable optical attenuator
Tx	Transmitter
UV	Ultraviolet
VOA	Variable optical attenuator
VTT	Technical Research Centre of Finland
WD	Working distance
WDL	Wavelength dependent loss
WDM	Wavelength division multiplexing

1 INTRODUCTION

The microelectronics industry started to apply moving mechanical structures such as membranes and cantilevers in integrated components in the late 1960's to enable new functions in electronic devices. After the late 1960's, components having not only electromechanical structures but also optical, chemical, and fluidic functions implemented on integrated chip, were introduced. These technologies are now commonly known as microsystem technologies (MST) or microelectromechanical systems (MEMS). This thesis is particularly focused on components with optical functions.

Planar optical circuits or integrated optical structures offer the possibility to miniaturize bulk optical functions and also they provide means to create completely new functions not possible with free space or bulk optical components. Attractive possibilities relate to transducers and sensors, as for example interferometric structures can be made small size and low cost by exploiting the batch fabrication and manufacturing processes originally developed for the integrated circuits (IC).

There are applications and consumer products which have been enabled by the MEMS techniques. These include accelerometers for the air-bag control modules used in cars, and digital mirror devices enabling commonly used video projectors for office and home use. Communications areas such as fiber optical telecommunications offer multiple target applications for integrated optics and MEMS, and they are considered as key enabling technologies for high bandwidth optical networks.

Optical microsystems based on silicon technology have been studied in this work [1-7]. Three components applying integrated optical structures and one component applying micro-electromechanics have been developed and studied. The different components represent new ideas based on well established material technologies and manufacturing schemes. Particularly with the integrated optical devices the work focused on exploiting novel concepts to achieve new functionality by integration and miniaturization.

A surface plasmon device fabricated with a silicon nitride waveguide technology has potential applications in chemical and biochemical sensing [1]. The idea of miniaturizing surface plasmon resonance device with the aid of integrated optics was novel [8]. A surface plasmon resonance (SPR) device was based on a proposed silicon nitride (Si_3N_4) slab waveguide structure. In this study a new type of sensor structure was designed, fabricated, and tested. As a main result, a proof-of-concept was shown by demonstrating the device sensitivity to humidity. The industrial aspects and feasibility for the practical sensor design of the introduced concept were considered.

A thermally tunable integrated optical ring resonator device was developed to study the optical characteristics of a ring resonator, waveguide quality, and electrical characteristics of thermo-optical (TO) control with in situ temperature sensing [2,3]. The characteristics of small size (perimeter 6.7 mm) Si_3N_4 based ring resonator structure with an integrated thermo-optical control were studied. In this work the thermal tuning was demonstrated to be a feasible tool for an accurate optical phase control [3]. The measured temperature coefficient of Si_3N_4 rib waveguide can be applied in the design of future devices based on similar structures. Si_3N_4-waveguide based ring resonator structures are suitable for sensing applications as high refractive index difference enables flexible designs with small radius waveguide bends. With small design modifications, the structure is suitable for chemical or biochemical

sensing based on evanescent wave coupling [1]. Additional applications of ring resonators and thermo-optical control lie in optical communications. The thermally controlled optical ring resonator structure is considered to have possible applications in both sensing and optical communications.

An integrated optical beam combiner device was developed for a phased array antenna demonstrator, intended for free space optical communications [4,5]. Integrated optical beam combiner circuits were meant to replace the optical fiber coupler components in the phased array demonstrator. The development of the integrated beam combiner for the optical phased array antenna system was justified by the need to improve the system performance, reduce system complexity, weight, and cost. The development included the design, manufacturing, packaging and optical evaluation of the test devices based on silicon oxynitride (SiO_xN_y) waveguides. With the fabricated basic building blocks the manufacturing capabilities and limitations of the waveguide technology were studied. Furthermore the fiber interfacing of integrated optical chip with polarization maintaining fibers (PMF) was studied.

A microelectromechanical variable optical attenuator (VOA) based on the silicon-on-insulator (SOI) technology was developed for optical telecommunication networks which apply wavelength division multiplexing (WDM) technology [6,7]. Two types of MEMS VOA architectures are introduced with details of design, fabrication, and optical results included. In the work related to optical MEMS, improvements were introduced to earlier reported structures in variable optical attenuators to achieve performance requirements of fiber optical communication networks. The application, including the definition of the optical specifications for a commercial product, is shortly discussed. The design part is summarized including main principles of mechanical and optical design. The results of process characterization and test structures are presented. The optical results of the two components are discussed and compared with each other. As a result both architectures were shown to have optical performance fulfilling the general requirements set by modern fiber optical network for such components.

This thesis has been motivated by the research of novel component ideas and the miniaturization needs required in order to develop new types of optical sensor structures, integrated optical circuits, and micromechanical devices. The studies of new integrated optical structures on silicon suitable for transducers and optical communications were supported by the funding from Finnish industry, the National Technology Agency of Finland (TEKES), and the European Space Agency (ESA).

The development of the MEMS VOAs was motivated by industrial ambitions related to fiber optical communications and a particularly strong economical boom in this field in the late 1990's. The fabrication process had been originally planned for manufacturing 1×2 and 2×2 optical switches. Thus there was additional motivation when challenging the MEMS industry's dilemma: *one-process-one-product*. The technical research and development was motivated by high expectations set for the optical performance of the introduced VOA device concepts.

1.1 Author's contribution

The author worked with the layout design of the surface plasmon resonance device introduced in chapter three [1]. He contributed to chip manufacturing and conducted the preliminary functional optical tests, whereas the final tests were performed elsewhere (VTT Chemical laboratory, Tampere, Fi).

The author was responsible of the optical evaluation of the optical ring resonator component presented in chapter four [2,3]. The author realized the measurement bed and measured the optical and electrical characteristics, and analyzed the measurement data.

In chapter five associated with the integrated optical beam combiner [4,5], the author contributed to the design of test structures and carried out the optical evaluation of the test structures. He theoretically compared sensitivity of different coupler structures. He contributed to the design and selection of the waveguide materials and structure. The author was responsible of the chip characterization work prior to the packaging, and contributed to fabrication of the packaged devices. He did the fiber interfacing at VTT Electronics, and was involved in the definition of the U-groove block for the fiber interfacing, and was involved with the packaging of device #4.

In the work described in chapter six, the author created the mechanical design of the electrostatic actuator used in VOA, and contributed to optical design of the structures [6,7]. The author was responsible for measuring the process parameters and analyses of the test structures prior to finalizing the layouts. The author was responsible for preparing the final component layouts. Additionally the author defined the optical evaluation steps needed to carry out the final characterization, and analyzed the measurement data.

2 BACKGROUND

The research of the microsystems can be categorized into study of materials, concepts, and manufacturing technologies [9]. As an 'old material', silicon characteristics are well known and the fabrication processes are highly advanced. The research related to silicon optical microsystem is largely focused on the implementation of new concepts [10]. Despite the maturity of the silicon technology, interesting optical innovations based on conventional fabrication technology still emerge [11,12,13]. The objective of the development of optical microsystems is to exploit and benefit from the advantageous scaling properties of miniaturized optical structures, batch fabrication and monolithic integration of electronic circuits on the same chip [14].

The optical microsystems, particularly planar lightwave circuits (PLC) and micro-opto-electromechanical systems (MOEMS), are considered attractive for numerous tasks in optical communications. The communications industry clearly drives the development of the optical microsystems [15,16,17,18]. Since the advent of room-temperature semiconductor laser and low-loss optical fiber in 1970, there has been a demand for miniature components for processing lightwaves [19,20]. The demand for larger network capacity together with novel optical communication schemes has accelerated the research of optical devices. The silicon based integrated optical components appeared early in communications, while optical MEMS devices have very recently surfaced in this field [17,21]. Another major field consists of different transducers used for sensing applications.

There is a large variety of different applications of optical microsystems and device designs. Diverse selection of materials and highly specific fabrication processes have been introduced for optical sensors and various components in optical communications. Figure 2.1 represents a cursory classification of applications of optical microsystems. In this classification only applications concerning sensing and communications have been presented. Other application fields falling outside these are too numerous to be listed.

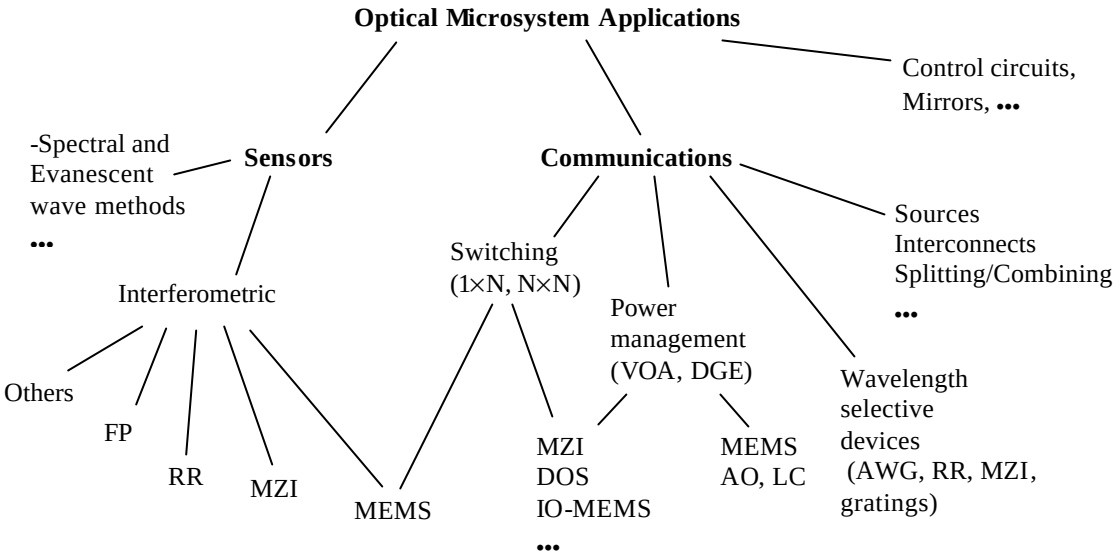

Figure 2.1. Classification of optical microsystem applications. The communication applications have been developed for switching, power management, wavelength selective routing, and control purposes. In sensing applications, spectral transmission and evanescent wave methods, are the most often applied methods. Various interferometric measurement devices have been demonstrated based on integrated optics such as MZI and RR structures [22,23,24], and MEMS [25].

2.1 Integrated optics

Integrated optics can be categorized into silicon based and other technologies (see figure 2.2). Silicon based structures can be further divided into silica-on-silicon and silicon-on-insulator technologies. Devices based on doped silicon dioxide (silica) penetrated the communications sector in the early 1990's [15,16,21], and are currently commercially exploited by many manufacturers. Silicon waveguides were first commercialized by Bookham Inc. (UK) [26]. Examples of such structures for instance are thermo-optical and plasma-dispersion switches [27,28,29]. Other materials based on silicon and on its oxides (SiO_x) are also exploited. Silicon oxynitride material was first considered for sensor applications at visible wavelengths. Silicon oxynitride offers flexibility as the nitrogen content and thus the molecular composition can be adjusted continuously in the plasma enhanced chemical vapour deposition (PECVD) fabrication process [30,31]. The possibility of tailoring the refractive index over wide range and low loss are advantages that make this material interesting in sensing application. Recently silicon oxynitride (SiON) has gained popularity with the introduction of devices with large refractive index difference, applied in components for optical communications [32,33]. The flexibility of SiON structures and compatibility with CMOS technology has been shown in the work of Bezzaoui et al. [34]. Another interesting material structure for passive integrated optics is $SiO_2/Si_3N_4/SiO_2$ on silicon substrate [35,36]. The silicon nitride layers deposited with the PECVD or low pressure chemical vapour deposition (LPCVD) method were first introduced for integrated optics by Stutius et al. [37]. Silicon nitride waveguides have been particularly targeted at sensing applications [24,38,39]. The advantages of Si_3N_4 waveguide devices are the ease of manufacturing, high packaging density, and relatively low transmission loss.

The difficulty of achieving efficient coupling with standard single mode fiber is the barrier that hinders their application in optical communications. Furthermore the deposited Si_3N_4 films have a large birefringence i.e. polarization sensitivity [24,37].

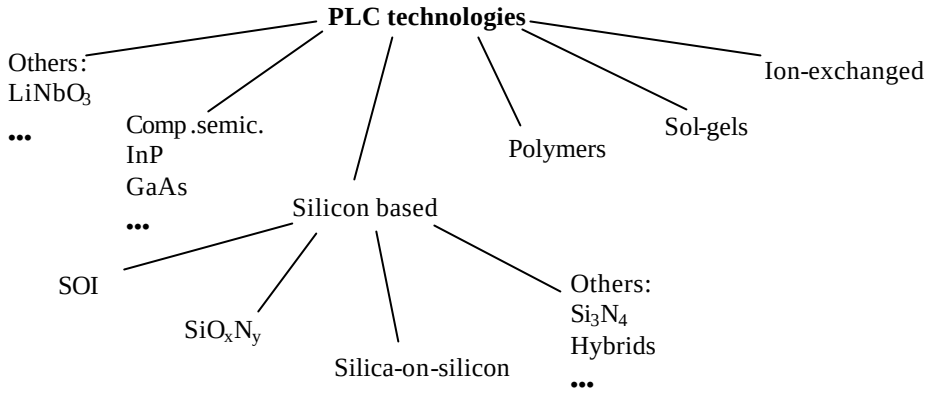

Figure 2.2. Classification of PLC technologies.

Integrated optics is an attractive technology for various sensing applications. Integration offers advantages to optical gyros and biochemical sensors. Miniaturization with batch fabrication yields higher reliability and lower-cost components. Integrated optical ring resonator (IORR) provides a convenient way to implement different types of sensing devices. The resonance characteristics can be made sensitive e.g. to external refractive index changes [39], strain [10], or pressure [22]. Refractive index measurements were conducted by Sohlström with a Si_3N_4 based IORR [39]. A pressure sensor based on SiON waveguides on a micromachined membrane was introduced by Brabander et al. [22]. In this work the ring resonator was reported to be highly sensitive to temperature variations. A ring resonator based chemical sensor has been shown to reach ppm-level sensitivity for isopropanol by Ksendzov et al. [40]. A micro ring resonator on a micromachined cantilever as a sensitive displacement sensor for scanning probe microscopy, has been proposed in [41], representing a hybridization of integrated optics and MEMS.

Various configurations and concepts for applying evanescent wave method in sensing have been reported. Typically evanescent wave methods have been applied with interferometric devices to enhance sensitivity [23,38,40]. Other measurement schemes have been proposed such as a heterodyne method presented by Cohen et al. [42]. To enhance evanescent wave coupling with an external medium, surface plasmons can be applied [43]. Surface plasmon resonance is commonly applied as an ultra-sensitive tool in biochemical analysis [44,45]. Although the existing measurement systems are large and expensive, only a few studies have been made targeting miniaturization and planar integration of the SPR equipment. The first application of the SPR phenomena on an IO-chip was carried out by Harris at al. [46]. This device was based on ion-exchanged waveguides. A device for pesticide analysis was demonstrated based on a Y-branch, with one arm being sensitive and one arm acting as a reference. The same configuration was later applied in another application as a biochemical sensor [47], and to study electro-chemical surface reaction [48]. A humidity SPR sensor has also been demonstrated with integrated optics by Weiss et al. [49].

In optical communications silica based passive planar lightwave circuits are used in splitters, combiners, switches, and wavelength selective splitters. In optical switching, demonstrated devices typically rest on thermo-optical. Advanced switches based on thermal control have been reported with at least silica-on-silicon [50,51], polymer [52], and SOI-waveguides [53]. A TO controlled silica-based 8×8 optical switch in a MZI-configuration, used control power of 90 mW to achieve switching speed of 5 ms [51]. A 2×2 switch based on SOI waveguides applying a MZI configuration was reported to have control power of 50 mW, and switching time below 3.5 µs [53]. These figures correspond to a π phase change as applied configurations were based on MZI interferometer structures.

The ring resonators have numerous possible applications in optical communication networks. Thermo-optic effect has crucial important role in most of the introduced device concepts. The ring resonator structures with thermal control have been proposed for the construction of chromatic dispersion compensators [54,55], frequency selective filters [56], optical cross-connects [57], and wavelength selective amplifiers [58].

Integrated optical beam combining has its niche applications in areas such as coherent optical communications [59,60], microwave communications [61,62], and astronomy [63,64], as demonstrated earlier. Planar beam combiners based on the InP technology for phased array antennas have been recently studied [59]. A beam combiner with active phase control on a chip was recently developed based on the InP technology [60]. The compound semiconductor technology enables integration of active functions such as phase control and detectors on the same substrate. The drawbacks of the presented solutions based on the InP technology have been high chip losses and low coupling efficiency with the optical fibers [59,60].

2.2 Optical MEMS

Micro-optoelectromechanical systems have advanced rapidly since the first optical silicon components, reviewed by Petersen in his seminal paper [65]. The applications of MOEMS cover such fields as optical switching, optical power management and display technology. MOEMS chips are already commonly exploited on an everyday basis. One of the most advanced applications is Texas Instrument's digital micromirror device (DMD), introduced commercially in 1996 [66].

Micromechanics is considered a feasible technology to realize components for optical networking. The silicon-on-insulator technology is one viable solution for manufacturing MOEMS devices for fiber optical communications. The SOI-technology enables the processing of high aspect ratio moving silicon mirrors [67,68]. In these demonstrations a 75 µm device layer height was used to integrate a mirror with a standard single mode fiber. The optical MEMS devices we have studied were based on similar SOI-technology. The first devices based on this technology were optical 2×2 switches [67,68]. Sensing devices based on the same technology have also been demonstrated [25]. The optical properties of these types of device depend on the quality of the mirror and the characteristics of the optical fiber. Surface roughness (rms) of 36 nm and mirror vertical angle below 0.7° resulted in insertion loss (IL) of 0.6-1.6 dB and 1.4-3.5 dB in bar and cross states, respectively [67]. In this case the gap between the applied standard single mode fibers (SMF) was 50 µm.

Hybrids of integrated optics and MEMS take advantage of the guided wave optics and control mechanisms based on moving structures. Optical switching and

power management tasks are examples of this trend. There are hybrid components emerging in the field of optical cross-connects [69]. In this work optical waveguide chip is combined with electrostatic MEMS piston mirrors to achieve switching functionality with a similar principle of IO-MEMS hybridization for VOA presented in [70]. A 1×N optical switch has been manufactured based on moving waveguides [71]. Optical power control schemes have been introduced based on moving structures and hollow waveguides [72], and on expanded silica waveguides [73]. It is evident that optical communications is to offer many fruitful application areas for optical MEMS. Such components as MEMS controlled tunable external cavity lasers [74], and optical switch fabrics [75] represent some of the most advanced hybrid components demonstrated.

2.3 Concepts for VOAs

One of the key components for fiber optical communications is the variable optical attenuator. A large number of different concepts have been introduced to accomplish power management functions for optical networks. The power control of fiber amplifiers and channel equalization are typical tasks which are implemented by VOAs. Both integrated optics and MEMS provide various means for this task. Although integrated optics is an attractive technique for implementing VOA, the problems with insertion loss, dynamic range, polarization sensitivity and power consumption have hindered PLCs cornering VOA markets. With integrated optics or PLCs at least silica-on-silicon, polymer waveguides, and material hybrids of silica and polymers have been demonstrated. A typical concept applied is Mach-Zehnder interferometer configuration with thermo-optical control to establish the adjustable transmission. Application of bent-waveguide structure with thermo-optical control has been demonstrated to implement a VOA [76]. Components based on SOI waveguides and plasma-dispersion based control have been demonstrated [77]. MEMS-VOAs with a laterally or vertically moving blocking vane, or a tilting mirror have been demonstrated. Reflective and transmission optical concepts have been applied in VOAs. Diffractive gratings based on moving ribs have been applied to implement a VOA and dynamic gain equalizer (DGE) [78].

Additionally, liquid crystals integrated with optical fibers and bulk acousto-optics have been applied for VOAs [79,80,81,82]. Furthermore hybrid structures applying optical waveguides combined with moving micromechanical structures have been applied in VOAs [83]. Evanescent wave coupling, blocking vane with hollow waveguides, or with expanded core waveguide structures are examples of these IO-MEMS hybrids [72,73].

2.3.1 PLC VOAs

The following reviews the state-of-the-art, and results gained with industrially mature concepts based on integrated optics.

Silica-on-silicon waveguides in Mach-Zehnder (MZI)-configuration and with TO-control were applied in a VOA [84]. Insertion loss below 1 dB and dynamic range of 20 dB were achieved with this device, while the time response was as low as 0.4 ms. A similar structure was applied by fabricating the silica-on-silicon waveguides with UV patterning [85]. Insertion loss of 0.7 dB and dynamic range of 30 dB were

achieved. The polarization dependent loss (PDL) increased from 0.2 dB to 1.2 dB, while attenuation levels changed from 0 dB to 30 dB, respectively. The wavelength dependent loss (WDL) was 0.8 dB over the spectral range of 45 nm (C-band). The control power was over 600 mW and chip length was ~21 mm.

A VOA concept based on combined polymer-silica structures has been demonstrated [86]. The attenuation was based on a bent-waveguide channel, whose transmission was thermo-optically controlled, in a similar fashion as presented by Veldhuis et al. [76]. Insertion loss of 1.5 dB, and dynamic range of >40 dB was achieved with control power of 250 mW. In both cases [76,86] the control power was quite high compared to other control schemes.

A polymer based VOA with thermo-optical control has been demonstrated [87]. Low control power of 1.5 mW and large dynamic range of 30 dB were achieved. The maximum PDL was reported to be 0.25 dB. The device length was ~10 mm.

Advanced device based on SOI waveguides was demonstrated by Day et al. [88]. Insertion loss was 1.1 dB and dynamic range of 40 dB was reported achievable with 200 mW power consumption. The PDL level was reported to be 0.1 dB at 0 dB attenuation level, while for a similar structure 0.8 dB PDL at 20 dB attenuation level was reported earlier [77]. High speed and integratability with arrayed waveguide grating devices (AWG) were advantages of this device [88].

The possibility of integrating VOA with an AWG and/or a switching matrix is a major benefit with most of the concepts demonstrated with integrated optics. This type of integration has been demonstrated both with silica-on-silicon and SOI -technologies.

2.3.2 MEMS VOAs

One of the first MEMS-VOAs was introduced by Barber et al., based on a vertically moving vane between two standard single mode fibers [89,90]. The air gap between the SMFs was 20 µm. The device insertion loss was determined by the alignment accuracy, and the gap size. The minimum insertion loss was 0.8 dB, and maximum dynamic range was over 30 dB. The PDL varied from device to device between 0.3 and 1.3 dB (at maximum attenuation). The WDL was ~1 dB over 100 nm spectral range (1500-1600 nm) at attenuation level of 13 dB. A similar device was later presented by Zhang et al. with comparable optical performance [91].

A more advanced device based on a SOI structure and laterally moving blocking vane between two fibers was later presented by Marxer et al. [92]. This transmission type device applied SMFs with a gap of 25 µm. Insertion loss below 1.5 dB was determined by the gap between the two SMFs. Dynamic range of 50 dB, response time of 5 ms, and return loss higher than 37 dB were achieved. Improved performance was later reported with tapered fibers, resulting IL of 1.0 dB, and PDL 0.5 dB at attenuation level of 10 dB. Based on the same technology a reflection type device was later presented by Marxer et al. [93]. The comparison between the two concepts showed that the reflection type device had lower PDL (mean value below 0.1 dB at 10 dB attenuation level) versus the PDL of 0.3 dB of the earlier device. The reflection type device suffered from large wavelength dependency (C-band), over 1 dB at 10 dB attenuation level [93].

Based on a similar concept as in [92], a VOA was developed by Morimoto et al. at Furukawa Inc. (JP) [94]. The device applied graded index fibers with outer diameter of 125 µm with angled polished facets and an anti-reflection (AR) coating. IL

of 0.6 dB, dynamic range of 30 dB, and polarization dependency below 0.35 dB were achieved. The return loss varied between 60 and 45 dB depending on the wavelength (1530 to 1610 nm), and the attenuation setting (0 to 30 dB).

Several other designs based on blocking vane principle have been recently presented. Some of them were based on electromagnetic actuation [95,96,97,98]. The advantage of magnetic actuation is low power consumption, but the disadvantage is that more complex fabrications schemes are needed to deposit magnetically actuated permalloy structures. The optical performance of these components has been on the level of earlier demonstrated devices.

A MEMS VOA based on thermal-actuation mechanism was demonstrated by Wood et al. [99]. The device was based on a reflection from a moving mirror. IL close to 1.0 dB, dynamic range of 40 dB, PDL below 0.3 dB, and WDL of 0.5 dB were achieved with this device. Other configurations based on a reflection from a MEMS mirror have been demonstrated [100,101]. A tilting mirror configuration based on electrostatic actuation was shown to have IL below 1.0 dB and dynamic range of 18 dB. PDL of this device was reported to be relatively low 0.06 dB up to 15 dB attenuation levels. WDL was reported to be below 0.2 dB (C-band) [100]. In another device based on a laterally moving electrostatically actuated mirror and lensed fibers; the IL was reported to be 0.9 dB and dynamic range 25 dB. Measured PDL was below 0.25 dB and WDL below 0.7 dB over a spectral range of 50 nm (1530-1580 nm) [101]. Devices based on tunable optical filter and refractive designs have also been demonstrated [102,103]. Although the optical performance of these devices was reported to be worse than other devices reviewed.

A latching feature is one considerable benefit that can be implemented with MEMS designs. A novel latching VOA scheme was recently introduced by Syms et al. [104]. A moving shutter between two optical fibers was mechanically clamped in this device by a tooth bar. Though the attenuation resolution was only 0.2 to 1.0 dB, the concept was shown to be feasible to achieve zero power consumption between two adjustment phases.

Liquid crystal (LC) based devices have been shown to be very promising for accomplishing VOA [79,80,81]. These presented concepts do not fall within MEMS or PLC categories, but as small sized devices they could be considered as optical microsystems. Furthermore not only due to successful miniaturization but also because of promising optical performance it is worth reviewing some of the results gained with these LC-VOAs. One such concept based on reflection and transmission control by LC block was presented by Pan et al. [79]. IL of 0.6 dB, dynamic range of 20 dB and WDL of 0.5 dB (C-band) were reported for this device. Another LC-VOA configuration gave results of rather high PDL of ~3 dB at attenuation levels of 12 to 18 dB [81]. Acousto-optic (AO) technology has been used to implement a VOA function. As far as is known, integrated or miniaturized AO-VOAs have not been reported. Still it is again worth noticing the level of technology as reported by Mughal et al. [82]. A bulk optical VOA with IL of 2.5 dB, but with 2.8 µs response time, ultra low polarization sensitivity PDL below 0.03 dB and dynamic range of 65 dB was reported. The high power consumption of several hundred milliwatts was one of the drawbacks of this device.

Table 2.1 compares commercially available state-of-the-art VOAs based on silica-on-silicon-, polymer-, or SOI –waveguides. The MEMS VOAs are based on thermo-mechanic, and electro-static control. Return loss typically exceeds 40 dB for these component types. The typical value for polarization mode dispersion is 0.1 to 0.2 ps for both MEMS and integrated optical devices. Optical repeatability is typically

specified to be better than 0.1 dB. The optical performance of MEMS devices is comparable or better when compared with typical values of PLC VOAs. The PLC VOAs' advantage is integratability with other optical functions (AWG and switches) and faster response speed. Also PLC VOAs can easily be applied in multi channel configuration.

Commonly with reviewed optical MEMS devices the optical fibers, fiber lenses or applied micro-optics, and the alignment accuracy of the packaging of the optical subcomponents largely determine the optical performance. Insertion loss, polarization dependent loss, and wavelength dependent loss are often more dependent on for instance the alignment accuracy of optical fibers than on the quality of the MEMS. Also in our work the accuracy of the fiber alignment process to achieve the optimum performance was critical, as shown in the case of transmission type MEMS-VOA.

Table 2.1. Performance summary of three PLC VOAs based on different waveguide technologies and two state-of-the art MEMS VOAs.

	PLC			**MEMS**	
	SiO_2-on-Si (TO)	Polymer (TO) [87]	SOI [77,88]	Therm.mech.[1] [99]	Electr.static[2]
Insertion loss (dB)	1.3	0.8	1.1	1.1	0.8
Power need (mW)	20 (at 20 dB)	2	200	150	0.01
Dynamic range (dB)	40	20	40	20	20
PDL (dB)	0.3 (at 20 dB)	0.4	0.8 (at 20 dB)	0.2	0.2 (at 10 dB)
WDL (dB)	1	1	-	0.3	0.7
Wavelength range	C+L band	C - band	C - band	C or L band	C or L band
Response time (ms)	0.4	3	< 0.0002	20	5

[1]) JDS Uniphase Inc., http://www.jdsu.com, (online datasheet)
[2]) Dicon FO Inc., http://www.diconfiberoptics.com, (online datasheet)

3 INTEGRATED OPTICAL SURFACE PLASMON RESONANCE SENSOR

An integrated optical surface plasmon resonance sensor has been developed. The research was motivated by the novel idea of applying planar waveguides to miniaturize a SPR sensor on an integrated chip [8]. Possible application fields of such a sensor are in chemical and biochemical sensing such as in immuno-assays and in pollution detection [46,105,106,107]. Our research was focused on the concept study. The immediate objective was to demonstrate the surface plasmon resonance device with integrated optics and establish proof of concept with the proposed configuration [1]. Firstly, we aimed at humidity sensing to demonstrate the device functionality, and secondly to apply it in more challenging applications. As the long-term target was recognized to be a disposable low-cost chip, the manufacturability of the integrated optical device was studied and the feasibility of the planarized concept was considered for industrial purposes. Although earlier much effort has been put on studying the possibilities of SPR, miniaturization for example with integrated optics has not gained much attention. The application of surface plasmon resonance is known to enhance the sensitivity to refractive index changes by a factor of 30 to 200 [43,108]. The SPR provides a label free method with sensitivity comparable to radioactive and fluorescence labeling methods [105].

The surface plasmon based sensing falls into the category of evanescent wave methods such as attenuated total internal reflection and guided wave evanescent sensing (see figure 2.1, chapter 2). An evanescent wave penetrating out of the actual waveguide can be applied for constructing sensors [1,23,38,39,43]. The evanescent field couples refractive index changes in the external medium to the effective index of the waveguide, modulating the phase of the optical field in the waveguide. The phase changes can be detected by various interferometric methods. Typical planar configurations apply Mach-Zehnder [23], or for instance ring resonator structures [39]. In SPR sensor a surface plasmon wave extrudes in to the medium to be sensed instead of the optical evanescent wave. With SPR sensor it is possible to exploit angular or wavelength scanning instead of using interferometric configuration [43]. A phase sensitive method based on polarization interferometry and free space MZI configuration has been demonstrated [109]. The angular interrogation is considered to be more sensitive than intensity measurement or wavelength scanning methods [43]. It is possible to apply direct intensity measurements as carried out by Harris et al. [46]. In fact their device applied multimoded waveguide (in principle angular scanning) and also a reference wavelength [47].

The limitation in the integration of the SPR phenomenon is the special geometry needed to excite the surface plasmons. The SPR method is commercially available for various analysis purposes but only relatively large size and costly equipment is available [44]. Miniaturized sensing based on integrated optics is an attractive possibility that could provide compact and low cost analysis equipment. Although the method is highly sensitive the difficulties related with the needed geometry have prohibited successful application of for example integrated optics to reach chip type integration. Based on multimode ion-exchanged waveguides an approach was adapted to develop a miniaturized SPR sensor for environmental sensing [46]. A reference and sensing channel were adjacently fabricated on a glass substrate and the outputs were compared to find the intensity change due to the surface plasmon coupling in the sensing channel. A similar scheme was later applied to monitor electrochemical

oxidation of gold surface [48]. An integrated optical humidity sensor has been demonstrated based on ion-exchanged waveguide device [49]. Another approach based on hybridization of LED source, active sensing prism and detector array has been presented commercially [45]. The footprint of this device was 2.2×3.0 cm^2, and it included thermal stabilization of the active sensing area.

3.1 Design of SPR sensor

Figure 3.1 shows the Kretschmann-Raether attenuated total reflection (ATR) prism arrangement for exciting surface plasmon wave (SPW) at the metal-dielectric interface [110]. In the arrangement p-polarized light is directed through a prism and is reflected from the metal film on one side of the prism. A SPR occurs when the projected wavevector k_x matches with the wavevector of the plasmon wave k_{SP} [112]

$$k_{SP} = k_0 n_0 \sin(q), \tag{3.1}$$

where $k_0 = 2p/l$, l is wavelength in vacuum, and n_0 is the prism's refractive index. The condition (3.1) can be fulfilled by scanning the coupling angle q, or the wavelength as the surface plasmons follow the dispersion relation [112]

$$k_{SP} = \frac{2p}{l}\left[\frac{e_1(l)e_2(l)}{e_1(l)+e_2(l)}\right]^{1/2} \tag{3.2}$$

Where e_1 and e_2 are wavelength dependent dielectric constants of the metal and the bulk medium ($n_1=\sqrt{e_1}$ and $n_2=\sqrt{e_2}$).

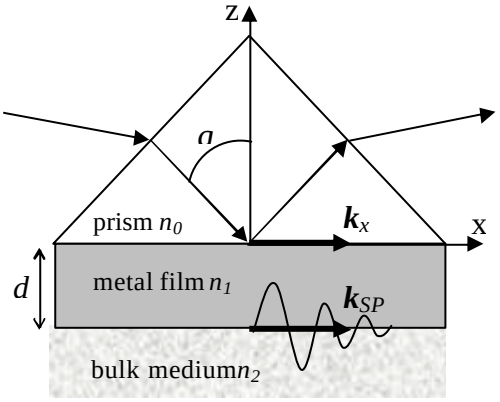

Figure 3.1. SPR principle with Kretschmann-Raether prism arrangement [110]. The n_1 and n_2 are the complex refractive indices of the metal and the bulk medium, respectively.

The reflected intensity can be calculated by applying Fresnel reflection coefficients of the three layer system (n_0, n_1, n_2). Following the formulation of Yamamoto, the total reflection coefficient is of the form [113]

$$R = \left|r_{012}\right|^2 = \left|\frac{r_{01} + r_{12}e^{2ik_{z1}d}}{1 + r_{01}r_{12}e^{2ik_{z1}d}}\right|^2 \tag{3.3}$$

where $k_{z1}d$ represents the optical path length in the metal layer, r_{01} and r_{12} are the complex reflection coefficients between the prism-metal and metal-bulk medium layers, and d is the metal layer thickness. The shape of the intensity-angle curve, i.e. the resonance width and contrast, depends strongly on the exact dielectric properties of the materials and on the absorption losses due to the surface roughness. When the reflection coefficient R reaches its minimum value the electromagnetic field is maximum on the surface. At resonance, energy is transferred from the optical wave to the induced electric field, and this can be seen as a dip in the transmission curve recorded against incidence angle.

The device was based on silicon nitride slab waveguide structure. The silicon nitride structure was selected for the application for two reasons. Firstly the measurements had been planned for visible wavelengths at 633 nm. Secondly silicon nitride offered high refractive index difference enabling the proposed configuration with focusing groove mirrors. The critical angle q_C of total internal reflection in Si_3N_4-air interface is ~30°, while for example with silica-air mirror structure the q_C is already 43° and the design would have been more constrained.

Figure 3.2 shows a schematic layout of the proposed configuration for applying a slab waveguide structure. A fixed angle configuration was used. A SPR thus causes a dip in the angular intensity distribution. The source and detector were planned to be external. The input light was to be coupled by aid of a lens providing the necessary divergent beam. A CCD camera was used to record the intensity distribution from the chip edge. Transmission through the chip was determined by the propagation losses at the slab waveguide, and mainly by the reflectance of the mirrors. The acceptable incidence angle in the air-groove mirror limited the design. The incidence angle to slab-air mirror interface was tailored by considering the reflection coefficient obtained experimentally by Valette et al. with a similar structure (see figure 3.3) [24]. For the SPR device an incidence angle limit of 55° was chosen so that the reflectance from the mirrors was above 0.6.

The angular range defined the exact geometry of the elliptic mirror and angles of the straight mirrors used to reflect the beam out of the chip. An elliptic mirror was chosen to provide two focal points, one in the input plane and one in the SPR plane. In a typical configuration two straight mirrors were used so as to have perpendicular output from the chip. The elliptic mirror parameters i.e. focal lengths and size, and size of the straight mirrors depended on $\Delta\beta$.

The chip size was determined by considering practical issues related to the chip handling during fabrication and the optical evaluation. The smallest chip size was designed to be 10×10 mm^2, the adjacent facet was preferred for the output, so as to have room for the detector array or a CCD camera. Different geometrical configurations, such as a single output mirror configuration, were also designed and tested [1].

The slab waveguide was designed to support only the fundamental mode (TE_0). Single mode operation must be guaranteed as multimoded propagation would lead to interference, resonance peak widening and additional losses at mirror interfaces. The normalized frequency V is [111]

$$V = \frac{2p}{l} h \sqrt{n_c^{\,2} - n_s^{\,2}}\,, \tag{3.4}$$

where l is the wavelength in vacuum, and h is the height of the slab waveguide, n_c and n_s are the refractive indices of the core and buffer layer, respectively. The single mode propagation necessitates the condition $V \leq \pi$. The refractive indices for the silicon dioxide and silicon nitride at a wavelength of 633 nm are of 1.46 and 2.0, respectively. The first order mode has a cut-off when slab height h < 230 nm, thus the thickness was chosen to be 200 nm. The effective refractive index n_e of the slab waveguide was 1.89. Silver and gold are the most commonly used materials for the metal layer. Silver is known to have slightly superior resonance characteristics when compared to gold. In practice gold is preferred as it is not suffering degradation due to oxydation processes. For our purposes a gold layer was chosen, with an optimised thickness of 50 nm for the wavelength of 633 nm.

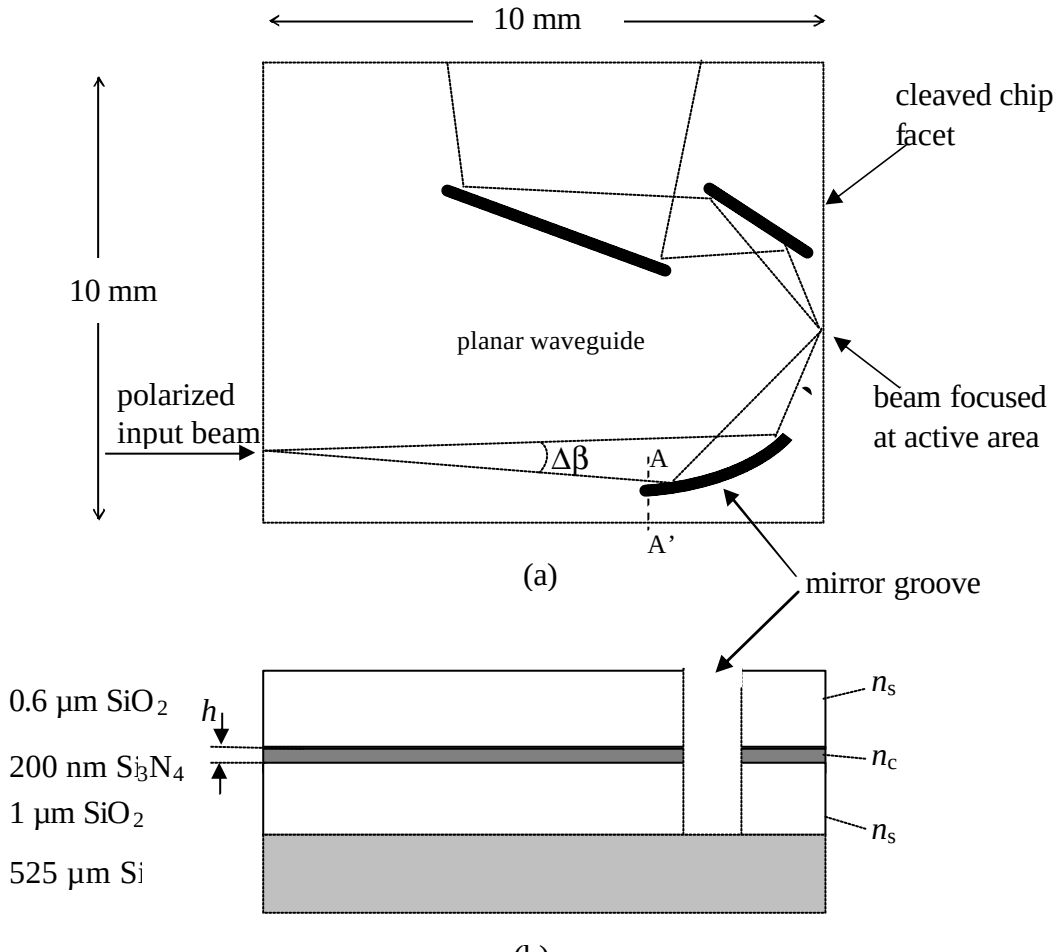

Figure 3.2. a) Schematic layout of the SPR sensor device with one elliptic mirror and two straight mirrors, and (b) the cross section (A-A) of the fabricated 3-layer structure. A divergent beam was focused with an elliptic mirror into the active SPR point. For design purposes the SPR excitation angles (q) had to be known to fix the correct angular range on chip. The divergence angle $\Delta\beta$ depended on the target application.

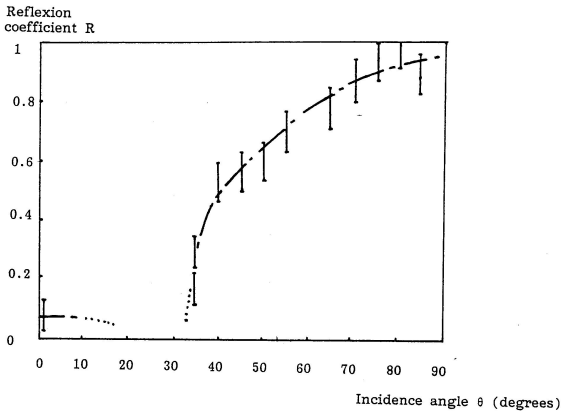

Figure 3.3. Reflection coefficient of silicon nitride slab waveguide structure with a deep etched air groove functioning as a mirror [24]. *© 1998 Taylor and Francis Group*

In the proof of concept, the configuration (angles) were selected suitably for a humidity test (air to water), and n_2 was assumed to vary between 1.0 and 1.33. In the calculation of SPR angle the effective index of the slab waveguide was used as a prism refractive index (n_e =1.89). Complex refractive index values for gold and water at wavelength of 633 nm were n_1=0.13+j3.16 and n_2=1.33+j0.002, respectively. Calculated with (3.1) and (3.2) the SPR angle is 33.7° and 50.5°, in air and water, respectively. Thus the needed angular range ($\Delta\beta$) was calculated to be 17 degrees. The angular range ($\Delta\beta$) was to be fixed by the external coupling lens. The figure 3.4 shows the resonance curves in air and water, calculated with above mentioned parameters and by applying equation (3.3) (see also [113]).

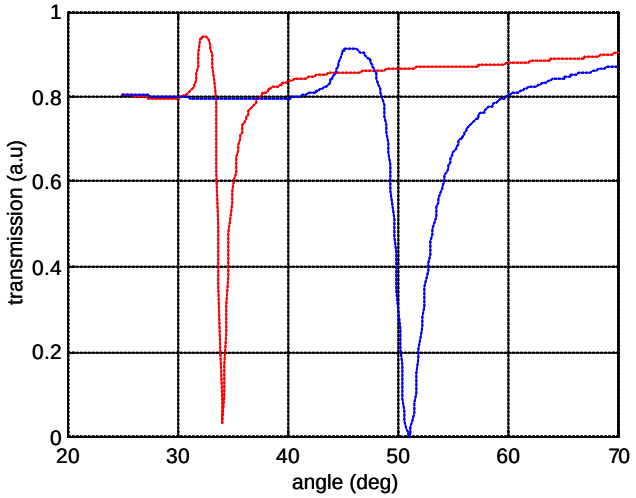

Figure 3.4. Transmission as a function of coupling angle. The first curve (solid) in air and second (dashed) in water. The refractive indices in the calculation were for air n_2=1.0, water n_2=1.33+j0.002, and for gold n_1=0.13+j3.16.

3.2 Manufacturing technology

The SPR components were fabricated using silicon nitride slab waveguides on silicon substrate. A three layer waveguide structure was formed on a 525 µm silicon substrate. The 1 µm thick under cladding was formed with wet thermal oxidation of the silicon wafer. The 200 nm thick silicon nitride layer was formed on top of the thermal oxide using low pressure chemical vapor deposition. Subsequently a 600 nm thick low temperature oxide (LTO) as top cladding layer was grown with LPCVD. A three layer resist process was used in the formation of the mirror grooves. The mirror grooves were etched through the top-oxide, nitride layer and the under cladding oxide with a reactive ion etching (RIE) process.

Finally the wafer was diced manually with scribing along the guiding grooves formed at the same time as the mirror grooves. The dies were visually controlled prior to the metal layer deposition step. The dies were mounted vertically on a special holder to accurately achieve the absolute thickness of 50 nm and to allow deposition of the metal layer only on the SPR facet. A 50 nm Au-layer was deposited on the chip edge. A thin layer of 2–3 nm of Cr was used to enhance the adsorption of the gold layer. The Cr layer was assumed to have a negligible effect on the SPR angles.

3.3 Results

The optical transmission and functioning of the fabricated devices were checked before they were delivered for further measurements at the collaborating laboratory (VTT Chemical Laboratory, FI). The photographs based on light scattering from the waveguide were obtained with long exposure times. In figure 3.5 (a) the input light beam is slightly tilted with respect to the chip active edge, and thus the output beam is not perpendicular to the output edge. Interference in the beam is clearly visible from the beam reflected from the first and second straight mirrors. Figure 3.5 (b) shows a close-up of the elliptic mirror.

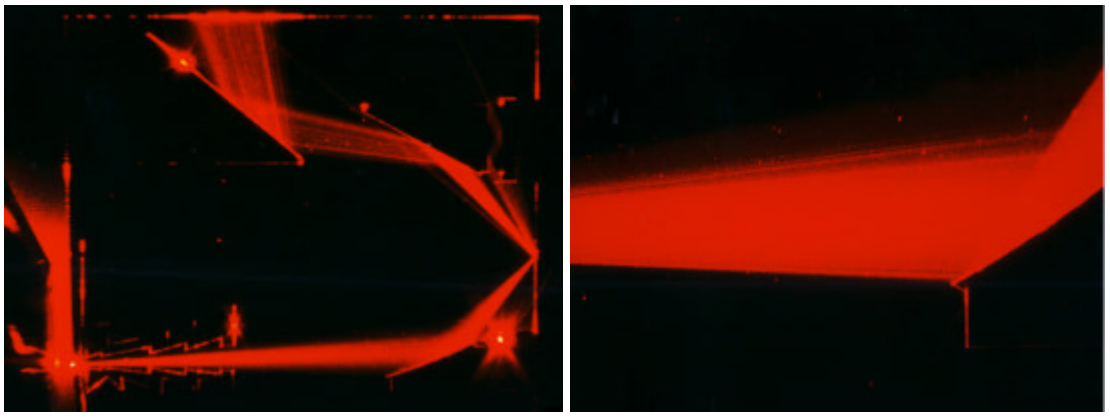

(a) (b)

Figure 3.5. SPR device photographed when red light was coupled to the chip (visual control step before metallization process). (a) Complete chip visible. The input light is not exactly perpendicular with the opposite chip edge (SPR facet), thus the exiting beam forms a small angle with the chip edge (top edge in the figure). The chip size is 10×10 mm^2. (b) Close-up of the elliptic mirror focusing the diverging beam into the active SPR-plane.

Figure 3.6 (a) shows another designed geometry with two chips before the die separation step. Figure 3.6 (b) shows a close-up of the focus point. The coupled red light shows the focusing capability of the elliptic mirror. The chip size was in this case 18×19 mm^2. The length of the focusing mirror was 8.5 mm (straight line from tip-to-tip). The focus spot size was estimated to be ~200 µm. Thus the tolerance in the die cleaving must be less than ±100 µm so as to have the active SPR plane intersect the focus plane.

Figure 3.7 shows the measurement arrangement used in the characterization of the devices. To achieve the necessary divergence angle a microscope objective (×40) was used in the input coupling. A CCD camera was used to image the chip output and to record the intensity. A gas or humidity feed was brought close to the active area to change the resonance conditions of the SPR. Figure 3.8 shows a measurement result when humidity introduced on the chip edge changed the SPR angle. The resonance was seen to shift 3.5° to 4° instantly as the humidity was introduced. Running average was used to smooth out the interference in the measurements.

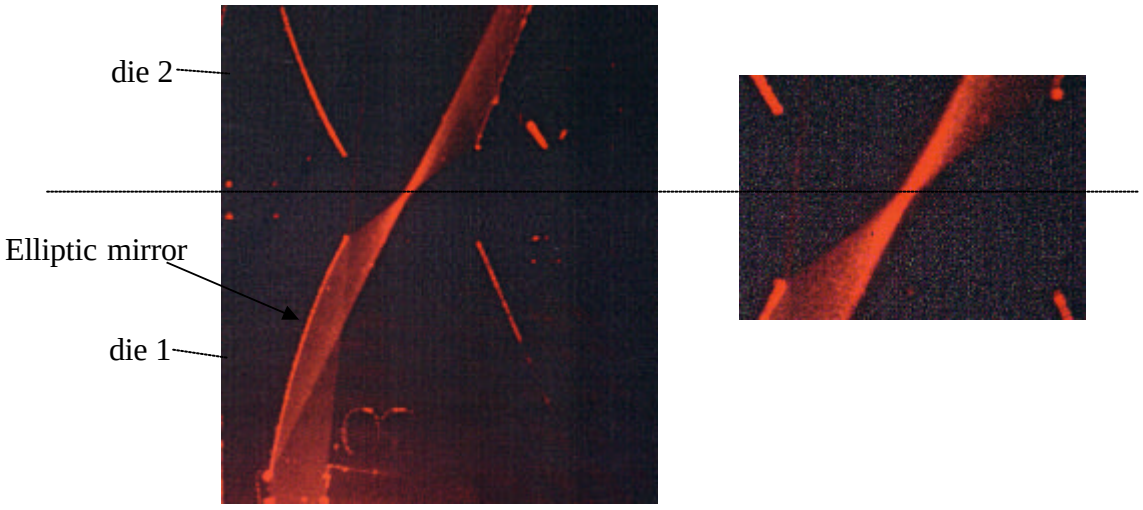

Figure 3.6. Two adjacent SPR chips (vertically) before the die separation step. a) The input light is focused by the elliptic mirror on the SPR plane (dashed line). The photograph of the two dies reveals the focusing capability of the elliptic mirror. The chip size was 18 × 19 mm^2 and mirror length was 8.5 mm. b) A close-up of the focusing plane.

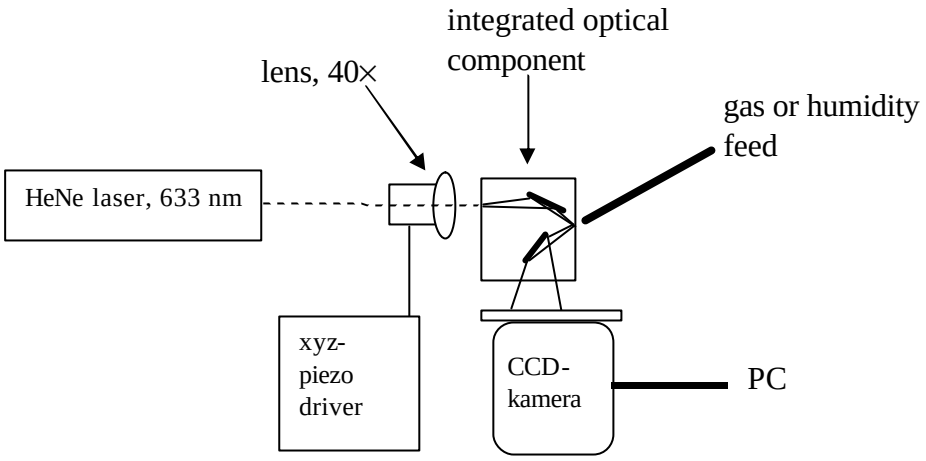

Figure 3.7. Measurement arrangement to test the SPR chip. A gas or humidity feed was brought next to the active facet of the chip.

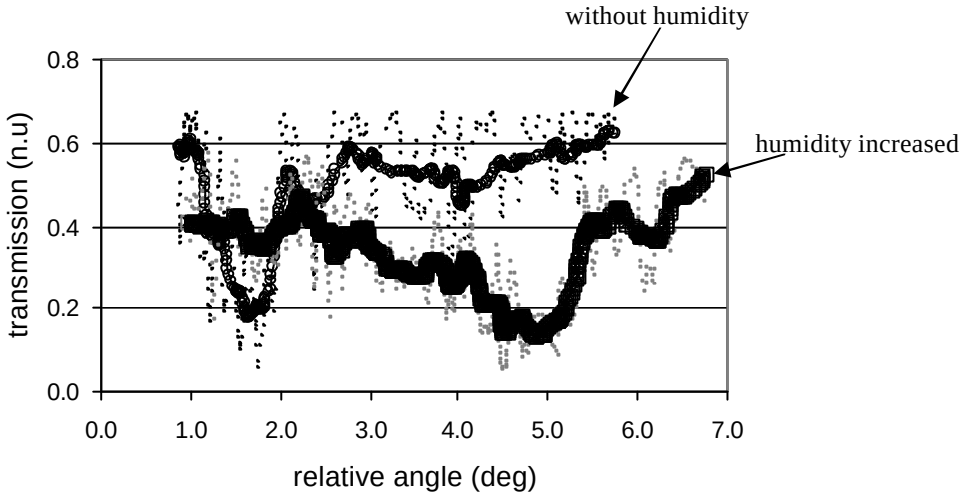

Figure 3.8. The SPR curve measured with the fabricated device with dry metal surface and shifted SPR when humidity was introduced into the metal layer. The SPR resonance shifted back to original when humidity dried out.

3.4 Conclusions

The integrated optical surface plasmon resonance sensor has been demonstrated based on silicon nitride slab waveguide. The device operation has been verified by measuring the surface plasmon resonance spectrum versus the fixed angle. The device design, fabrication, and proof of concept have been presented. The device sensitivity to humidity was verified by measuring the shift of resonance shift between air – humidity cycles. The concept based on silicon nitride technology worked well despite large interference effects recorded in the output beam. Possible reasons for this were considered to be diffraction from the edges of the chips in the input, or a core layer of wrong thickness.

The integration was not complete as the chip still required external coupling lens and a detector array. Interfacing the launch optics was problematic as correctly divergent beam had to be coupled into the slab waveguide. The alignment of the

launching optics was critical as the core layer is very thin. A stable mechanical coupling of the light source and detector array was challenging with the disposable chip. Also in our case the mechanical stabilization of the chip during measurements proved to be difficult [1]. In the proof of concept measurement the SPR shift was only a few degrees while predicted value was 17°. The reason for this large difference could have been different optical parameters than designed. Error in effective index and metal layer refractive index could change the angular range. Contamination of the active layer before the measurement could have also changed the SPR characteristics. Furthermore calculation of resonance angle assumed a completely wet environment or a thick water layer on the metal surface. It is possible that the layer of water molecules present on the active surface was thinner in the experiment than the penetration depth of the evanescent wave, and thus the shift of resonance angle was not complete as assumed theoretically.

SPR has been demonstrated to be useful in various applications, such as immuno-assays [105] and environmental monitoring [47]. A recently proposed application is an optical temperature sensor based on SPR [114]. The properties and sensing characteristics of SPR in the infra-red range and characteristics of silicon as a prism material has been recently studied [110]. New design architectures become possible if wavelengths above 1.1 μm could be used as proposed [110]. Thus silicon based slab waveguides or silicon MEMS structures could be exploited to construct a SPR device.

The silicon nitride waveguide technology offered high quality and relatively straightforward manufacturing of the proposed structure. The deposition process and associated die handling, and preparation were not suitable for volume production. More appropriate preparation of the active metal film must be developed to consider the proposed configuration for industrial application. The yield of the die preparation step was low. Accurate and acceptable cleaving of dies along the correct plane proved to be a difficult. A repeatable and higher through-put fabrication should be adapted to replace this manual step.

There are several design and fabrication issues that need additional consideration. One concern is the stability and lifetime of the deposited gold film. The contamination of the active film layer can be a substantial problem. The contamination of the mirror grooves is possible which could inhibit or destroy the operation of the mirror interface. This could be avoided by using metallized mirrors instead of air-slab interfaces. This would allow more flexibility in the design and allow larger incidence angles, increase transmission, and improve sensitivity.

4 THERMALLY TUNABLE INTEGRATED OPTICAL RING RESONATOR

A thermally tunable integrated optical ring resonator structure has been developed and its characteristics have been studied. The device was based on silicon nitride rib waveguides on silicon and the thermal control was realized with poly-Si thin film elements. The research was motivated by the possibility of identifying new component applications of the IORR in sensing and optical communications. The IORR provided an accurate tool to study the propagation losses of the fabricated waveguides. This information is essential to understand the feasibility and limitations of the technology in various applications. The introduced integrated heating system combined with the in-situ thermal monitoring offered a novel and convenient way to study the device's optical properties. The study of thermal characteristics, response speed and power consumption issues gave information considering the feasibility of the thermal phase control. The IORR's inherent thermal sensitivity must be taken into account when considering sensing applications [22,39].

The temperature dependency of the refractive-index, i.e. thermo-optical effect, can be made use of in integrated optics. With planar optical components the TO-effect can be readily applied by integrating resistive thin film heaters on a chip. The monolithic integration and small dimensions give accurate results, and a compact way of controlling the optical phase. The TO-effect has been shown to be a feasible way to add active functionality in passive devices, e.g. integrated optical switches [115,116], VOAs [86,87,117,118], and frequency selective devices [56,118,119,120] have been demonstrated. TO-effect can also be used to compensate small phase errors that are due to the deviations in fabrication process. In this way, for example, the crosstalk values of a thermo-optic matrix switch have been reduced [121]. In optical switch fabrics, VOAs, and sensor applications the TO-effect can be used to accurately adjust the phase shift to reach a correct operation point, e.g. see [122,123,124,125].

The thermo-optical coefficient of the refractive index (dn/dT) of silica is 1×10^{-5} /°C. This value is less than one tenth of the dn/dT of crystalline silicon (1.84×10^{-4} /°C) and polymers ($-1..-4\times10^{-4}$ /°C) [117]. Response speed of below 180 µs have been reported with silica 2×2 switches applying a Mach-Zehnder configuration, with a heating power being 110 mW [115]. In silicon-on-insulator 2×2 switching devices applying similar MZI-configuration 3.5 µs rise time with heating power of 50 mW have been reached [53]. In polymer based switching devices, speeds between 5 to 10 ms with typical control powers of 50 to 150 mW have been reported, based on digital optical switch (DOS) [123,125,126]. In silicon based devices the control power has been typically reduced by isolating the phase shifter from the bulk silicon by using heat isolating grooves, or micromachined bridge structures [51,115,116].

Additionally, to the potential applications of the ring resonator in telecommunication, and sensing, the device has importance at its own as a process control monitor [127,128,129]. This is because small propagation losses (<0.01 dB/cm) in relatively short integrated optical waveguides can be measured with a ring resonator [130]. In the measurement of the ring resonators the TO-effect has been widely used to tune the ring resonator output to scan through the resonance spectrum [131]. The tuning range is large and thus the thermal tuning is particularly suitable for ring resonators with large free spectral range (FSR). The waveguide is usually heated externally and the resonance spectrum is recorded as a function of time. The nonlinear

time-temperature relationship leads to the variation in finesse values over a large temperature range. Maintaining the input coupling with the sample during the heating can also be problematic, especially in the case of very small size waveguide core such as with Si_3N_4 waveguides [132]. Another method to measure the resonance spectrum is to use a wavelength tunable narrow spectral width distributed feed-back (DFB) laser diode [22,128] at constant temperature, or a thermally tuned erbium doped fiber laser [129]. The variation in finesse can be avoided by using an injection current modulated DFB laser. This method is based on the thermal modulation of the laser cavity under varying current at low modulation frequencies i.e. the lasing wavelength changes due to a change in refractive index as a function of temperature. Even if a large frequency travel can be achieved (>80 GHz/mA) [133], the problem is wider spectral linewidth of the laser diode, that causes degradation of finesse [134]. Large tuning range is achievable for example, with an external cavity laser, but in many cases with a relatively high cost.

The scope of this research was to study a tunable ring resonator with TO-control and in situ temperature measurement. In this work the limitations related to phase control speed, accuracy and power consumption have been studied. The ring resonator was based on silicon nitride waveguides to obtain a small ring radius and thus a short cavity with a large FSR. Thin film poly-Si resistors were used as a heater and thermistor. The introduced TO-control applied with a simultaneous temperature measurement is expected to have use in applications such as interferometric sensors based on ring resonator structures.

4.1 Design considerations

The device applies silicon nitride rib waveguides on silicon. The device had an integrated thin film heater and a thermistor as shown in figure 4.1. The ring resonator was coupled with the access waveguide by a directional coupler. The access waveguide had an s-shape to achieve more compact layout with a matrix of ring devices and thus more samples on the same mask layout. Furthermore the lateral shift in access waveguides prevented the coupling of possible planar waves and scattered light to the output of the resonator and to the fiber coupled to the output end. To provide the best conditions for temperature tuning of the phase shift, and for measuring the actual temperature, the heating element as well as the thermistor were integrated in the vicinity of the ring resonator.

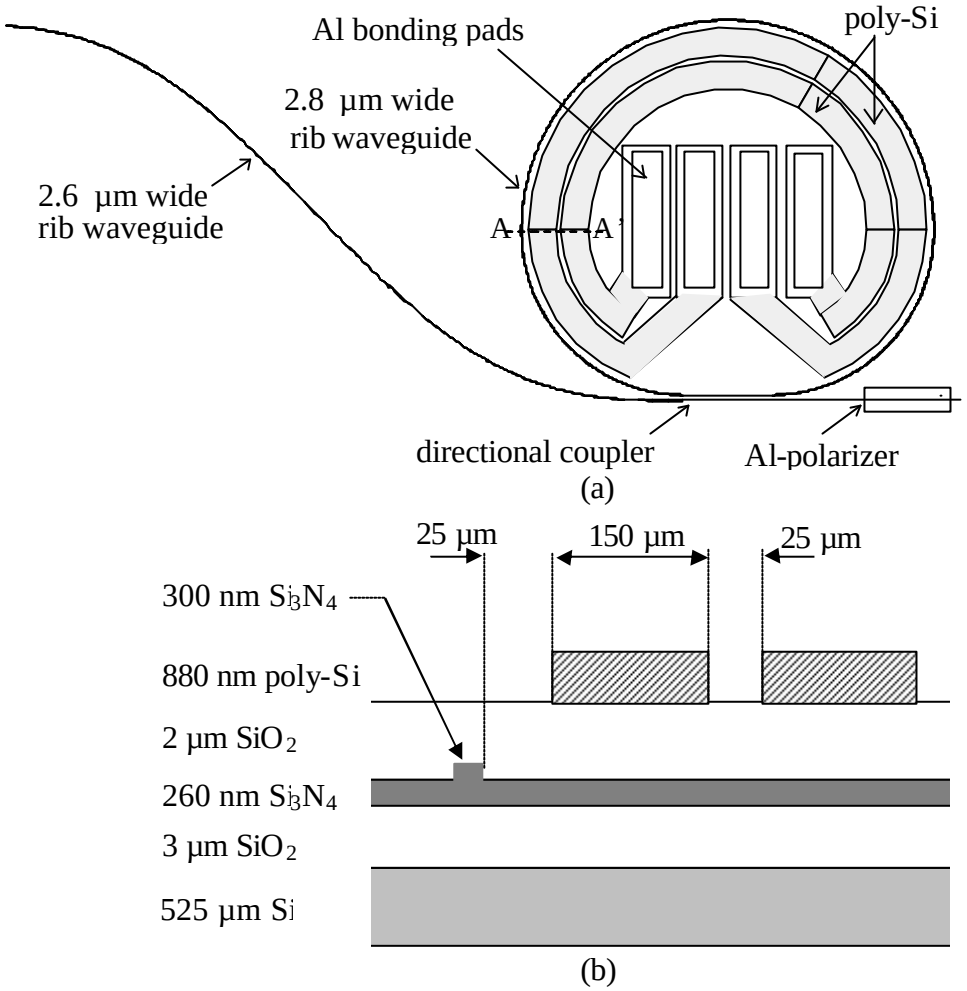

Figure 4.1. (a) Schematic layout of the IORR device and (b) the cross section (A-A') of the fabricated structure. The width of the poly-Si elements was 150 µm and the distance between the two was 25 µm and the distance of the outer resistor to the waveguide was 25 µm. The inner and outer resistor functioned as a thermistor and heater element with the nominal room temperature resistance values of 270 Ω and 425 Ω, respectively.

The optical transmission (t_r) of the ring resonator as a function of temperature (T) is calculated as a geometric sum of all waves present [2]

$$t_r = r - t^2 \sum_{n=0}^{\infty} r^n e^{-i(n+1)q} \tag{4.1}$$

where t is the coupling efficiency for fields from straight waveguide to the ring waveguide and

$$r = \sqrt{1 - t^2}, \tag{4.2}$$

$$q = gL(1 + h(T - T_0)). \tag{4.3}$$

In equation (4.3) L is the perimeter of the ring, $h(T-T_0)$ is the correction to the phase term caused by temperature difference, $h = 7\times10^{-6}$ /°C is the linear temperature coefficient of the optical path length that had been measured for a ridge loaded silicon nitride waveguide type Fabry-Perot resonator [135], T_0 is the reference temperature, and

$$g = b + ia, \tag{4.4}$$

The waveguide attenuation expressed in dB/cm is related to loss factor a used for field amplitudes in equation (4.3) by

$$a\ [1/\mathrm{m}] = -11.51 \times a_{LOSS}\ [\mathrm{dB/cm}], \tag{4.5}$$

$$b = \frac{2p}{l_0} n_e. \tag{4.6}$$

a_{LOSS} in equation (4.5) and n_e in equation (4.6) are the waveguide attenuation and the fundamental mode index in the ring waveguide, respectively, and λ_0 is the operating wavelength in vacuum. Using equation (4.1), the transmission for power (T_r) can be written as follows [2]

$$T_r(T) = \left| r - \frac{t^2 e^{-iq}}{1 - re^{-iq}} \right|^2, \tag{4.7}$$

The distance between the resonance peaks in temperature units is defined as

$$\Delta T = \frac{l_0}{n_e L h}, \tag{4.8}$$

usually expressed in frequency units as FSR. The finesse (F) and contrast (C) is calculated from the resonance curve as (e.g. see [126])

$$F = \frac{FWHM}{\Delta T} \tag{4.9}$$

and

$$C = \frac{I_{\max} - I_{\min}}{I_{\max}}, \tag{4.10}$$

where *FWHM* is the full width half maximum of the resonance, and I_{max} and I_{min} are the maximum and minimum intensities, respectively. The studied ring resonator structures were optimized to have large contrast. In the design the total propagation loss had been estimated to be in the range of 0.1...1.5 dB/cm including scattering, curvature loss, and loss of joints between straight and curved sections. Thereafter the optimum condition (in this case large contrast) is estimated for the coupling efficiency in the directional coupler in the expected propagation loss range. As seen from equation (4.7) the maximum contrast is proportional to the coupling efficiency for a given propagation loss range.

4.2 Design of ring resonator

A single mode rib waveguide forms the basic structure for the device. Single mode condition of the rib waveguide was confirmed by applying the effective index method (EIM). The effective index n_e was determined to be 1.71, when the rib width was chosen to be 2.6 µm and rib height was 40 nm. Asymmetric directional coupler (DC) was applied to guarantee a weak coupling between the access waveguide and the ring waveguide. Weak coupling was necessary to have high finesse and contrast characteristics for the estimated loss range of 0.1 to 1.5 dB/cm. A nonsymmetric directional coupler was chosen as the coupling efficiency is less sensitive to the variation in coupling length (L_C) as in a symmetric directional coupler. Even with large fabrication tolerances the designed coupler was estimated to have the necessary weak coupling. The effective index method was applied to calculate the mode indices and field distributions in the directional coupler region. The launching wave in the directional coupler was expressed as a linear combination of the fundamental mode of the access waveguide and the wave propagating the ring. The resulting wave after propagating the length (L_C) was overlapped with the field propagating in the ring guide, yielding the coupling efficiency of the directional coupler.

The width of the input waveguide was 2.6 µm and the width of the ring waveguide was 2.8 µm. The wider rib waveguide was chosen for the ring guide as the propagation loss is inversely proportional to the width of the waveguide due to the edge roughness of the rib, e.g. see [136]. The higher order modes were expected to resonate only slightly because the directional coupler was designed for the fundamental mode coupling. The minimum ring radius was 886 µm. The flattened part of the ring was designed for a directional coupler. The total length of the ring was 6.76 mm. As the effective refractive index (n_e) of the waveguide at 1.312 µm was 1.71, the FSR of the ring resonator was 26 GHz.

The resonance characteristics of different ring resonators were varied by varying the coupling efficiency from the input waveguide to the ring waveguide. The variation in coupling efficiency was done by changing the separation between the access waveguide and the flattened part of the ring waveguide. This separation (d_{DC}) was varied from 2.1 µm to 3.0 µm, corresponding to the variation in the coupling

efficiency from 24.2 % to 1.2 %, respectively, when the rib height of 40 nm was assumed. Figure 4.2 shows the calculated transmission characteristics of the ring resonator in two different cases. The coupling efficiency of the directional coupler was estimated to be nearly temperature independent changing only 4×10^{-3} % when the temperature change is 1 °C. The process parameter changes affect the coupling efficiency. Three process parameters could be identified to influence the coupling efficiency: slab thickness, rib height, and linewidth. The slab thickness was considered to be very accurate. Relative accuracy of the deposition method used was considered to be better than 10 %, thus the slab thickness variation to coupling efficiency was negligible. In silicon nitride rib waveguides the change of -5 nm in rib height can change the coupling efficiency by about 10 %. In the lateral direction the undercut of the rib width of 50 nm changes the coupling efficiency by -5 %.

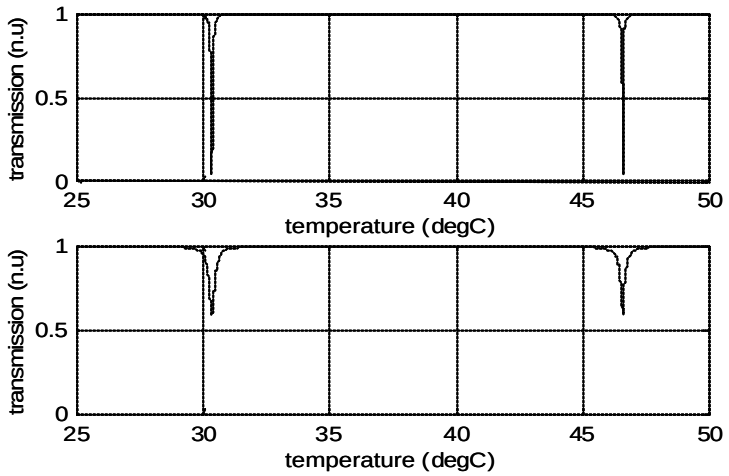

Figure 4.2. Calculated resonance spectrum as a function of temperature. The following parameters were used in the calculation of the transmission properties: The temperature coefficient of the optical path length $h = 7\times10^{-6}$ /°C and wavelength $l = 1.312$ µm, (a) $a_{LOSS} = 0.1$ dB/cm and coupling efficiency of $t = 10$ % and in (b) $a_{LOSS} = 0.5$ dB/cm and coupling efficiency of $t = 10$ %.

4.3 Manufacturing technology

The ring resonator components were fabricated using silicon nitride waveguides on silicon substrate. The 3 µm thick under cladding was formed with wet thermal oxidation of the silicon wafer at 1200 °C. The 300 nm thick silicon nitride layer was formed on top of the thermal oxide using LPCVD. Next, a 100 nm thick low temperature oxide was grown with LPCVD. This oxide was used as a mask for the wet etching of the silicon nitride layer to form the channel waveguides. After photolithography the mask oxide was etched in buffered hydrofluoric (BHF) acid and subsequently the silicon nitride core was etched in boiling phosphoric acid. Rib waveguides with nominal rib heights of 24 nm (type I) and 39 nm (type II) were formed. The rib height was measured using a surface profilometer. After the rib formation, a 2 µm thick silica cladding layer was grown using plasma enhanced chemical vapor deposition. The whole structure was annealed at 1000 °C in a nitrogen atmosphere. The annealing was done to reduce propagation losses at 1.52 µm wavelength due to O-H bonds [35].

The thermo-optic heating elements together with the temperature measurement resistors were fabricated on top of the waveguide structure (see figure 4.1 b). A poly-Si layer with a thickness of 880 nm was deposited and subsequently doped with phosphorus using a solid source. The sheet resistance of the poly-Si was measured to be 9.6 Ω/sq at room temperature. The poly-Si resistor elements were formed after photolithography with reactive ion etching.

Finally, an aluminum metallization of a thickness of 900 nm was sputter deposited. Aluminum was used for the electrical contacts of the poly-Si resistor elements. An aluminum stripe left on the straight waveguide (see figure 4.1 a) was used to wipe out possible TM polarized light propagating in the waveguide [137]. The aluminum structures were patterned using a phosphoric acid etchant. A heat treatment procedure (440 °C in nitrogen) was carried out to anneal the contact metallization to give a minimum contact resistance.

4.4 Device characterization

The device characterization included the measurement of the thermal characteristics of the poly-Si elements. The measurement of the optical transmission of the device was based on the calibration of the resistor elements. The temperature coefficient of the poly-Si elements was measured over the intended temperature range. Subsequently the optical and electrical characterization of the device was carried out. The optical transmission spectrum was recorded by thermally controlling the device i.e. sweeping the device temperature. The electrical characteristics included the measurement of the response speed and power consumption of the device.

4.4.1 Calibration of poly-Si thermistor

The temperature coefficient of the poly-Si resistor was determined by calibrating three elements in a small oven. The absolute temperature change was measured with a commercial platinum resistor (Pt100) as a reference. The platinum resistor was bonded with thermally conductive glue on the reverse side of the silicon chip thus ensuring similar thermal conduction effects compared to the poly-Si elements. Other effects from the bonding and short wiring inside the oven were omitted. The oven was heated up and subsequently slowly allowed to cool down to room temperature while the resistance values of both the poly-Si and platinum resistors were measured with two digital multi meters (DMM, HP 3478A). The accuracy of the resistance measurement was limited by the resolution of the DMM to 1 mΩ. As the mean temperature coefficient of the Pt100 is 3.85×10^{-3} /°C and the nominal resistance 100Ω, the accuracy of the resistance measurement corresponds to a temperature measurement accuracy of 0.003 °C.

A fourth order polynomial was fitted to the measured temperature-resistance curve and the result was used as a temperature calibration in the measurement of the ring resonators. The measured temperature coefficient for a poly-Si resistor with a nominal resistance of 268Ω at room temperature is shown in figure 4.3. The temperature coefficient was about 9.5×10^{-4} /°C, i.e. 25 % of the temperature coefficient of commercially available thermistors. The accuracy of the temperature measurement for the poly-Si resistor was deduced to be 0.004 °C when the measurement accuracy of the DMM was taken into account. The current fed through the thermistor to take a

resistance measurement was 1 mA. The heating effect of the current pulse during the measurement was negligible and did not affect the measured resistance.

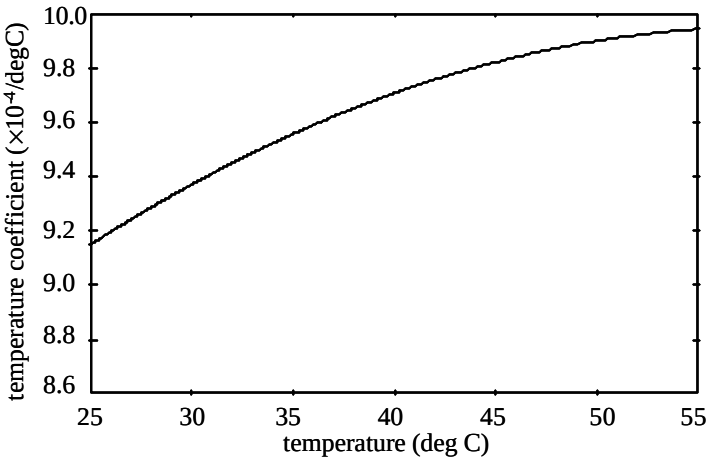

Figure 4.3. Temperature coefficient of the poly-Si resistor. The measured temperature coefficient for the fabricated thermistor is between 0.92-1.0×10^{-3} /°C, in the intended temperature range of 25 to 55 °C.

4.4.2 Optical evaluation

The schematic of the optical bench for measuring the ring resonator transmission characteristics is shown in figure 4.4. The light source was a fiber pigtailed optically isolated single longitudinal moded DFB-laser (Mitsubishi ML 974A2F), with current feedback control and thermo-electric stabilization. The operating wavelength of the laser was 1.312 µm. Light was butt coupled to the waveguide via a single mode fiber. The polarization crosstalk was observed to be negligible. Therefore, the aluminum polarizer over the curved channel waveguide was sufficient to ensure that only the TE mode propagated in the structure. The transmitted light was collected using a 20× microscope objective, and focused on a non-biased InGaAs detector. The mechanical chopper was positioned at the front of the detector, and a lock-in amplifier was used to amplify the detected signal. A PC controlled electronic circuit fed the heating current through the poly-Si element. The poly-Si resistance change was recorded with a DMM or digitizing memory oscilloscope (HP 54501A) using a bridge circuit. As the temperature was slowly swept the transmission curve of the ring resonator was obtained. Transmitted intensity was also recorded with the oscilloscope. The measured data was collected via IEEE-488 bus to the PC.

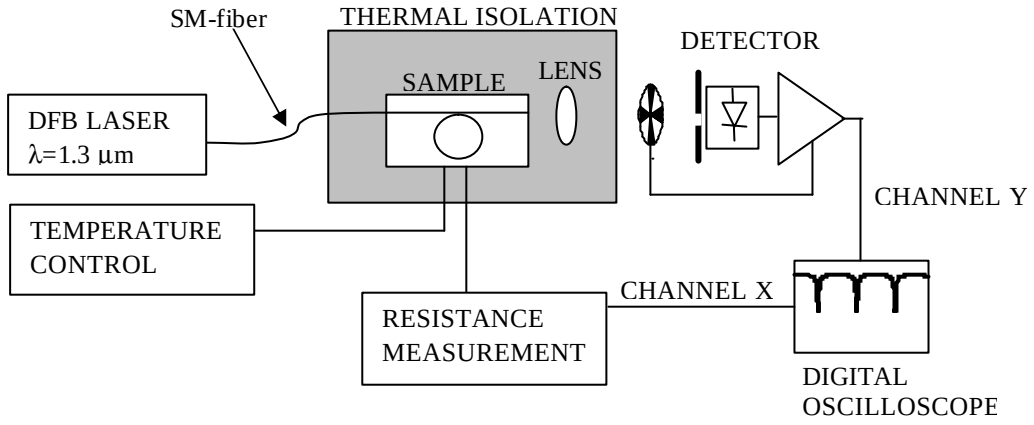

Figure 4.4. The schematic of the optical evaluation bench for measuring the ring resonator transmission characteristics.

Because the device was found to be sensitive to temperature variations of ambient air, the chip was isolated from the temperature fluctuations by enclosing it under a closed box with small windows to allow the coupling of light into the sample, and to the detector. Measurements were taken by slowly heating the device up while measuring the temperature and transmitted intensity or, alternatively, measuring the temperature and transmitted intensity while the chip was slowly cooling down.

The characteristics of the ring resonator such as the finesse and the contrast of the resonator could directly be evaluated from the measured transmission curve. Measured transmission curve for a component of type I is shown in figure 4.5. Single moded operation of the device was observed as can be seen in figure 4.5 (a) where the measured resonance spectrum is shown as a function of the resistance. The distance of the resonance peaks in power units was 240 mW. This value was temperature independent. The change in the background intensity was due to the changing butt coupling efficiency as the sample was heated. In figure 4.5 (b) the same resonance

spectra is shown after smoothing of the background intensity and the application of the temperature calibration. The finesse of the resonator was 78 and the contrast 0.34. The effect of the frequency stability of the laser on the measured finesse and contrast was small as the linewidth of the laser was less than 20 MHz.

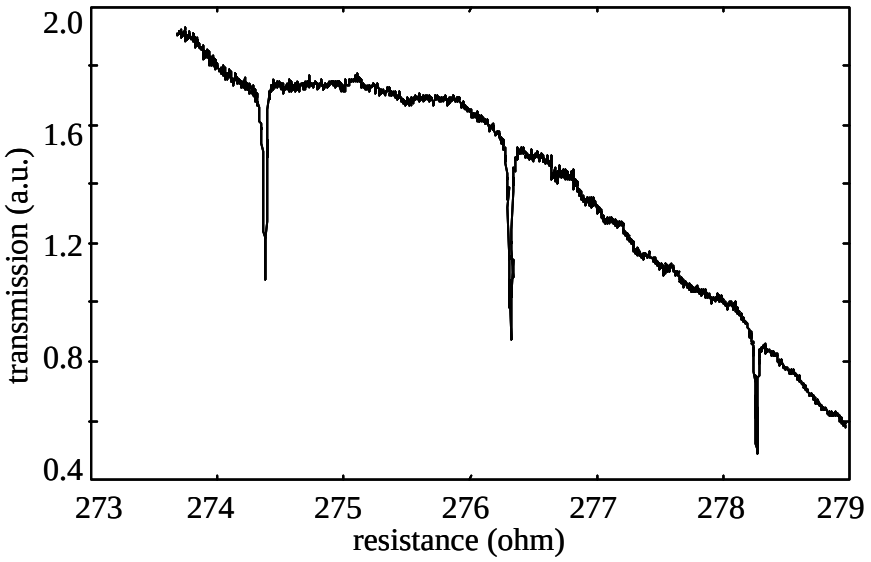

(a)

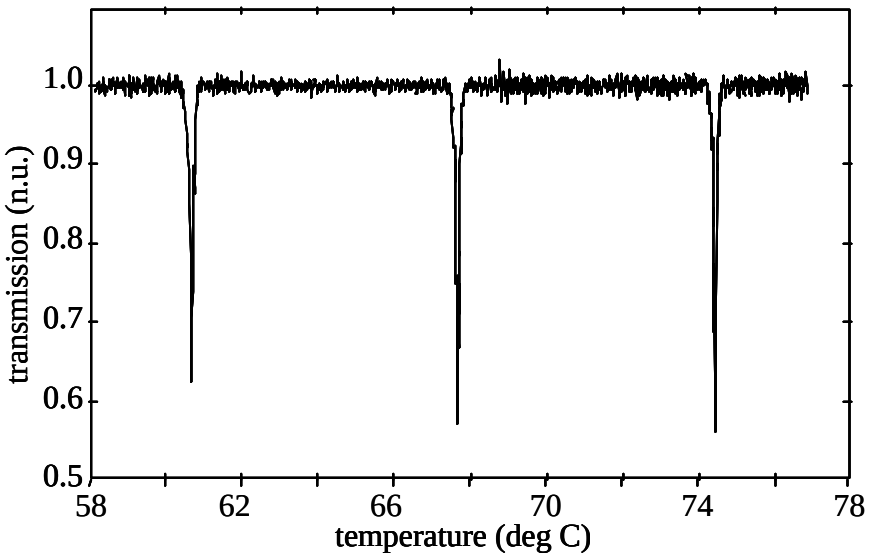

(b)

Figure 4.5. The measured ring resonator (type I) response (a) as measured and (b) after the applied temperature calibration and the normalization of the background intensity.

The propagation loss and the coupling coefficient for the fundamental mode in the ring waveguide could be calculated from the measured finesse and contrast [126]. The calculation gives two solutions, one for weak coupling and another for strong coupling. For the measured spectra shown in figure 4.5, the calculation gave the propagation loss and coupling efficiency for weak coupling to be 0.47 dB/cm and 0.8 % and in the case of strong coupling 0.05 dB/cm and 6.6 %, respectively. For this device the theoretical œupling efficiency of the fundamental mode was 4.9...7.8 %.

The variation in the theoretical value is due to the inhomogenousness of the process that has been taken into account. In the ring resonator of type II the resonator spectrum showed multimodal behavior as shown in figure 4.6. The input waveguide was verified to be single moded by monitoring the output of the waveguide with an infrared camera. According to the theory, the waveguide ring was multimodal as well as the coupling area of the directional coupler [2]. The higher order periodic fast resonances seen in figure 4.6 were due to the weak coupling of power to the second order mode in the ring guide and due to the different coupling conditions of this mode. The calculation of the finesse and contrast from the measured spectrum was done by using the maximum intensity near the resonance peak to determine the resonance depth and width. This can be done according to (4.7) because both resonances seen in the measured spectrum can be handled independently. The finesse and contrast values for the fundamental mode were 77 and 0.39 corresponding to the propagation loss of 0.47 dB/cm and the coupling efficiency of 0.9 % (the other solution is 0.06 dB/cm and 6.6 %). The theoretical coupling efficiency in this case was 2.8 %. The difference between the measured and calculated coupling efficiency is due to the process parameter deviations in the sample. The solution with a smaller coupling coefficient was selected.

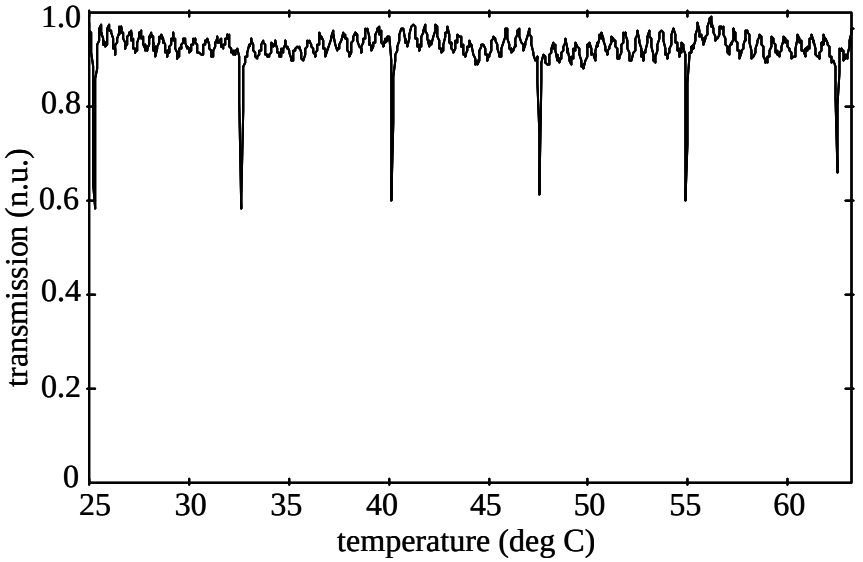

Figure 4.6. Typical resonance spectrum of a ring resonator of type II. Sharp dips represent the resonance of the fundamental mode.

Table 4.1 summarizes the results from two wafers (1 and 2) and 7 different resonators. The designed difference between resonators was the directional couplers coupling efficiency. This had been varied by changing the axial distance (d_{DC}) between the waveguides. Most of the devices had a multi moded type spectrum as shown in figure 4.6.

Table 4.1. Summary of measured finesse and contrast of samples from two wafers. Most of the measured resonance spectrums were multi moded (MM) only samples 6.10 and 6.12 on wafer 1 had a single moded (SM) resonance spectrum. d_{DC} is the axial distance between the waveguides in the directional coupler, N is the number of resonances in the spectra. The given finesse and contrast is the average value based on N resonances. A solution for both weak (1) and strong coupling (2) is shown with corresponding propagation loss values.

wafer 1 (type I)**:**

Chip	d_{DC} (μm)	type	N	F	C	Coupling$_1$ (%)	Loss$_1$ (dB/cm)	Coupling$_2$ (%)	Loss$_2$ (dB/cm)
6.4	2.3	MM	6	111	0.52	0.88	0.30	4.23	0.06
6.8	2.7	MM	4	73	0.49	1.23	0.48	6.75	0.09
6.10	2.9	SM	4	73	0.24	0.54	0.52	7.30	0.04
6.12	3.1	SM	6	78	0.34	0.76	0.47	6.59	0.05

wafer 2 (type II)**:**

chip	d_{DC} (μm)	type	N	F	C	Coupling$_1$ (%)	Loss$_1$ (dB/cm)	Coupling$_2$ (%)	Loss$_2$ (dB/cm)
6.2	2.1	MM	6	37	0.65	3.45	0.89	12.10	0.24
6.4	2.3	MM	6	61	0.67	2.20	0.53	7.30	0.15
6.6	2.5	MM	7	77	0.39	0.95	0.47	6.60	0.06

4.4.3 Accuracy of temperature measurement

Repeatability of the temperature measurement was studied by making five consecutive temperature scans (see table 4.2). In this case the inner resistor element heated, and the outer measured. In table 4.2, the mean ΔT is given together with the standard deviation (σ) for each measured ΔT. Five consecutive resonances were measured. The measured average ΔT decreased from 8.1 °C (ΔT_{12}) to 7.3 °C (ΔT_{45}) over temperature sweep of 22 °C.

A slight hysteresis was noticed between the two measurements, temperature rising or falling. This caused some variation in the measured ΔT. The linearity of the measurement, i.e. the variation in the measured ΔT, is shown in table 4.3 for four different measurements for a sample of type II. The measurements were taken for both inner and outer resistor as a thermistor, and measuring the resonance spectrum during a heating and cooling cycle. In table 4.3 the mean ΔT is given together with the standard deviation (σ) of the measured ΔT values in a single measurement. The maximum and minimum values of ΔT in each measurement are also given. In table 4.3 the temperature values corresponding to the first and 5th resonances are shown. It is assumed that the shift in absolute temperature values as seen in tables 4.2 and 4.3, was caused by the complex nature of the heat transfer to the surrounding media and by the changing contact resistances. The standard deviation in ΔT and thus in finesse was found to be about 3.5 % of the mean value. This corresponds to a variation of 0.03 dB/cm in the calculated propagation loss and of 8 % in the calculated coupling efficiency.

Table 4.2. The measured variation in measured ΔT of five consecutive temperature scans done for the ring resonator of type II, with five resonance peaks in the spectrum.

	ΔT (°C)						
	scan 1	**scan 2**	**scan 3**	**scan 4**	**scan 5**	**mean**	s
ΔT_{12}	7.83	8.31	8.50	8.04	7.95	8.13	0.28
ΔT_{23}	7.56	7.70	7.85	7.60	7.59	7.66	0.12
ΔT_{34}	7.40	7.39	7.56	7.37	7.44	7.43	0.08
ΔT_{45}	7.21	7.30	7.37	7.56	7.25	7.34	0.14
Mean	7.50	7.68	7.82	7.64	7.56		

Table 4.3. The measured variation in ΔT of four measurements taken for the ring resonator of type II. The measured temperature values corresponding to the first (T_1) and the fifth (T_5) resonance in the resonance spectrum are given.

poly-Si thermistor	ΔT (°C)					Temperature (°C)	
	mean	s	**max-min**	**max**	**min**	**T_1**	**T_5**
Inner							
- heating	8.1	0.21	0.4	8.3	7.9	34.4*	58.7
- cooling	7.5	0.09	0.2	7.6	7.4	28.9	58.9
Outer							
- heating	7.8	0.27	0.6	8.0	7.4	28.4	59.6
- cooling	7.4	0.32	0.7	7.8	7.1	29.9	59.7

* The value given for 2nd resonance.

4.4.4 Temperature coefficient of the optical path length

The temperature coefficient of the optical path length of the silicon nitride rib waveguide was calculated from the measured ΔT by using (4.8). The calculated effective refractive index n_{eff} of the ring guide was 1.71. This gives $h=1.5\times10^{-5}$ /°C. The value is about twice as large as the value used in the modeling of the device. This is due to the different device structure and process conditions compared to design value [135].

4.4.5 Consideration of thermistor characteristics

In order to find out the effect of heating on the bulk temperature of the sample, the die temperature was measured using thermistors of the adjacent rings on the die while one of the TO heating elements was heated up to 82 °C. The result is shown in figure 4.7 where the discrete data points stand for the measured temperature values and the curve shows the result of the complementary error function fitted to the measured data. The complementary error function was used rather than exponential fit because of the diffusion nature of the thermal conduction [140]. The center-to-center distance of the ring resonators was 4 mm and the device diameter was 2 mm. The poly-Si thermistor measured the average temperature over the thermistor length, and that was used to represent the temperature in the middle point of the ring. At a further distance from the heater the measured temperature accurately represents the temperature in the middle of the measuring thermistor. The error between the real temperature and the measured

temperature is largest in the area where the temperature gradient is high. This does not, however, affect the measured temperature gradient significantly.

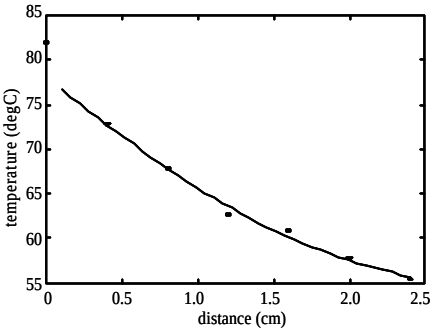

Figure 4.7. The measured bulk temperature distribution (circles) in the sample when the TO heating element was heated up to 82 °C. The solid curve shows the fit of the complementary error function to the measured data.

The experimental temperature distribution alone was too robust to interpolate the temperature close to the heating element. A good estimate of the temperature differences between the two poly-Si resistors and waveguide was obtained through a semi-empirical model approaching the real measurement conditions. Therefore, the temperature modeling of the TO-phase shifter was performed assuming a steady state condition. In the model, a cross-section of the waveguide structure was studied including the effect of the adjacent heating element and thermistor. The effect of the geometry was considered to have only a minor effect on the temperature distribution in the area with a close vicinity to the heating element including both the thermistor and the ring waveguide. The temperature distribution was solved from the static two-dimensional thermal conductivity equation using the PDE2D program based on the finite element method (FEM) [138]. The boundary conditions were set by specifying the heat flow through the surfaces of the structure. The heating and measuring elements were not explicitly included in the model but the heat flow through them was described choosing the heat transfer coefficient and the external temperature appropriately. This approximation simplified the calculation remarkably. Even if the elements were included explicitly, the exact determination of the heat flows through them would have been difficult.

The heat transfer was assumed to be larger from the substrate to the sample holder than from the sample to air. The fitted curve in figure 4.7 was used to fix the parameters of the thermal model to give a similar temperature profile as was measured at a further distance from the heating element. An approximate value of 15 W/Km^2 was used for the heat transfer coefficient between air and silicon dioxide interface. The heat transfer coefficient between the substrate and the sample holder was approximated to be 30 W/Km^2. The thermal conductivities of silicon and silicon dioxide were 1.5×10^2 W/m°C and 1.4 W/m°C, respectively [139]. The temperature distribution near the heating element was obtained from the model. The result is shown in figure 4.8, where the modeled temperature distribution is plotted together with the cross-section of the waveguide structure. The shown result corresponds to the situation where the poly-Si heater has been heated up to 82.1 °C whereas the surrounded media is at room temperature. The temperature model predicts that a single complementary error function does not hold near the heating element but the model is very consistent with the measurement further away (≥ 500 µm) from the heating element. Because of this the first measured data point in figure 4.7 was excluded from the calculated fit.

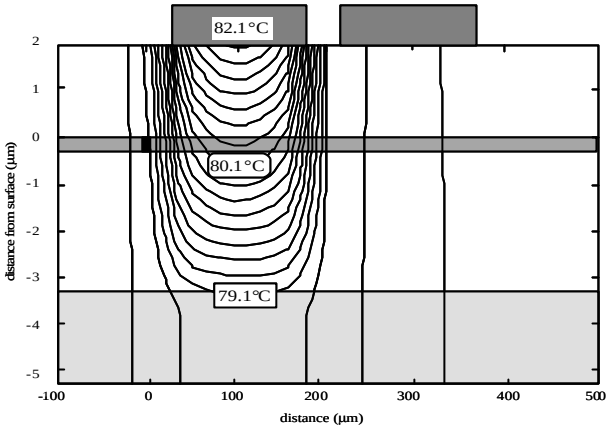

Figure 4.8. The modeled temperature distribution in the sample when the poly-Si heater has been heated up to 82.1 °C. The spacing of the temperature contours is 0.25 °C.

The temperatures in the distances of 100 µm and 175 µm from the center of the heating element corresponding to the center points of the waveguide and the measuring thermistor were 77.9 °C and 77.5 °C, respectively, as the temperature of the heating element was 82.1 °C. Thus the temperature difference between the waveguide and the thermistor was 0.4 °C. If the situation is changed so that the poly-Si element closer to the waveguide acts as a thermistor then the temperature difference between the waveguide and the thermistor becomes 0.3 °C. With lower temperatures the temperature gradient becomes smaller and the difference between the two measurement configurations decreases. In practice the two configurations gave similar results. The most ideal would have been to place thermistor on top of the waveguide but on the other hand this would have led to radiation and absorption of light in poly-Si.

4.4.6 Response speed and power consumption

The speed of the TO-phase shifter was evaluated. In a ring resonator the speed to tune the device between two consecutive resonances (one FSR) corresponds to a phase shift of 2π, in some applications such as in Mach-Zehnder interferometer based devices the response speed of the π phase shift is more relevant. The response times for the π or 2π phase shifts were evaluated from the measured time-temperature curves for several heating powers (figure 4.9 a) by fitting a sum of error functions [140] to the measured data points. In this way the response time obtained as a time needed to achieve a temperature change of ΔT= 7.6 °C varied from order of 10 s to 10 ms by increasing the heating power. The response time for a π phase shift obtained as a time needed to achieve a temperature change of $(1/2)\Delta T$ was only one tenth of the response time for 2π phase shift. The time to cool the temperature down was remarkably longer (in the order of seconds). The overall slow response of the device was considered to be mainly due to the poor thermal conductance to the surrounding media.

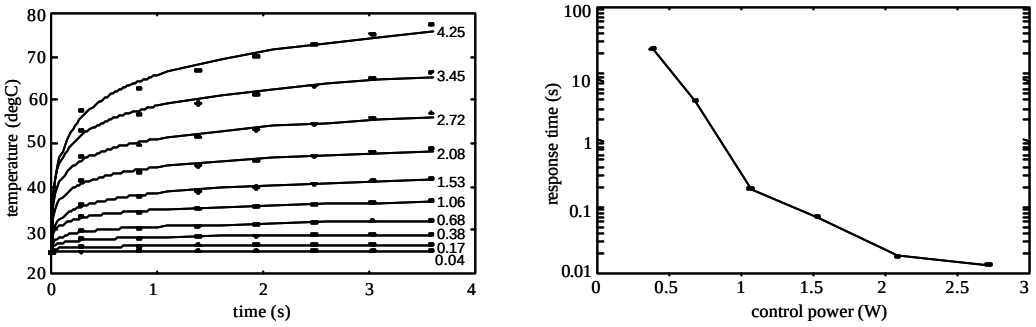

(a) (b)

Figure 4.9. a) Temperature response of the samples with different heating power levels (circles) and the fitting of sum of error functions (solid lines) and b) the corresponding response speed versus control power calculated from the fitting curves.

As the application of the error function fitting was not considered to be completely reliable, the temperature response was measured with higher time resolution. Thus a sample was characterized by: I) a chip without heat sink and II) a chip mounted on a copper heat sink with a thermally conductive adhesive (Epotek H70E). The calibration curve of the temperature coefficient of the poly-Si resistor was applied to accurately trace the sample surface temperature. A constant current was driven through the thermistor to measure voltage across it and thus indirectly measure the temperature with an oscilloscope (HP54501). The accuracy for the temperature measurement was ±0.05 °C. Measurement current was 30 mA, corresponding to a 250 mW heating power and to a temperature change of 2.5 °C from room temperature. This was considered as an offset and not to have any effect on the device operation. The width and the amplitude of the heating power pulse were programmed to find an appropriate power to control the device temperature (Keithley-220). The pulse width and the duty cycle were 500 ms and 1.5 s, respectively, with the pulse power of 0.25-4.8 W. The risetime and falltime for a 2π phase shift were defined as a temperature rise of 7.5 °C from room temperature and 90 % fall from this level, respectively. This definition can be justified as the optical phase was considered instead of the optical transmission. Furthermore the optical transmission was assumed to change linearly as a function of temperature. The surface temperature of both samples is shown in figure 4.10 when the heater element was driven with different power levels. The response speed with the risetime and falltime are shown in table 4.4 when maximum control power was used. Clearly the falltime of sample I limited the speed of the device. When the chip was mounted on a heat sink (sample II) the risetime was declined slightly but a drastic improvement was achieved in the falltime. In sample II an efficient vertical heat transfer occured and the chip temperature increased only slightly due to the lateral heat diffusion, thus the improvement in the falltime means higher power consumption. The risetimes obtained from curves in figure 4.10 are shown in figure 4.11 versus the control power. With both samples the power consumption was too high for practical applications. Furthermore the response speed was moderate compared with the power consumption of the TO-phase shifter. The device operation could be enhanced by proper thermal design and with an appropriate micromachined silicon structure.

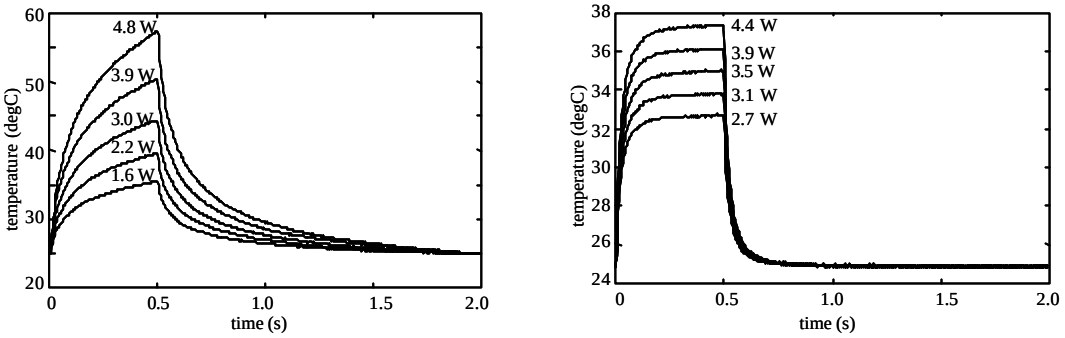

(a) (b)

Figure 4.10. Temperature response of the samples with different heating power levels (a) I without a heat sink, and (b) II with device mounted on a heat sink.

Table 4.4. Thermal response of the samples: I) without a heat sink and II) with a heat sink as the heating power was varied. The heating power difference between the two cases was due to a shift difference in the resistance values of the heater elements.

sample	power (W)	rise time (ms)	fall time (ms)
I	0.48	24	230
II	0.44	26	65

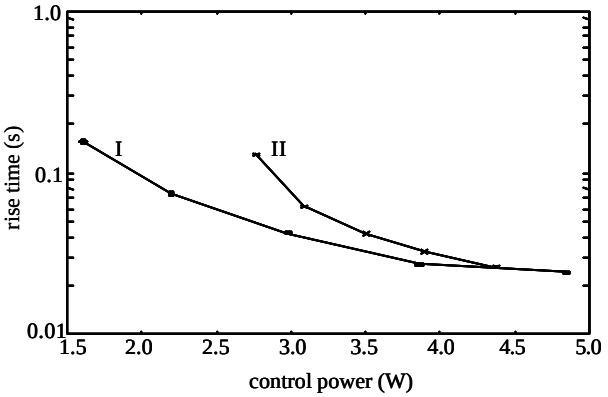

Figure 4.11. Rise time of the samples with different heating power levels, (a) I without a heat sink, and (b) II with device mounted on a heat sink.

4.5 Conclusions

The properties of the integrated optical ring resonator, TO-phase shifter and poly-Si thermistor as a single unit on the basis of the thermal model and the measurements have been studied. The monolithic integration of the thermistor close to the waveguide gives a means to in situ measurement of the temperature changes of the ring guide heated by a TO-phase shifter. The use of the TO-phase shifter in the ring resonator measurement eliminated the need for a wavelength tunable narrow spectral width source with the problem of frequency drift, e.g. see [134]. Also, a large number of resonance peaks can be detected by temperature tuning. In practical applications, e.g. a narrow tunable filter, or an optical sensor head, the TO-phase shifter together with a thermo-electric element provides the controllability of the resonator to reach the designed operation point.

In the case of wafer 1 the highest finesse was measured with a device with the highest theoretical coupling efficiency (chip 6.4). This contradicts theory, but can be explained by assuming that the coupling efficiency varied due to the large variation in linewidth and rib height. The measured finesse and calculated coupling efficiency changed monotonically in samples of wafer 2, as expected due to changing d_{DC}. The weaker coupling solution gave average propagation loss of 0.5 dB/cm (for the samples showing single mode operation). The stronger coupling solution gave 0.06 dB/cm, which is a very low value when considering this type of waveguide [35].

The response time to achieve the 2π phase shift using the TO-phase shifter can be shortened by using larger heating power but this is in many applications not favorable. The operation speed of the device can also be increased by using a thermal heat sink [3]. In the measurements the heat transfer from the sample to the sample holder was not optimized by any means. In fact, there was a small air gap between the silicon chip and the sample holder acting as a thermal insulation. It is due to this that the fall time for the 2π phase shift was long without appropriate heat sinking (order of seconds). When optimizing the operation of the poly-Si TO-phase shifter for switching purposes the thermal model has to be enhanced by including the transient modeling of the device so as to better understand the time related properties of the phase shifter. In some applications such as in Mach-Zehnder interferometer based devices the response speed of the π phase shift is more relevant.

Thermal crosstalk is a critical parameter in practical components and thus isolation of the TO-phase shifters using micromachined bridge structures may be needed. When the TO-phase shifter is isolated from the silicon substrate the electrical power consumption decreases [115]. There is a trade-off between the electrical power consumption and the response time [141]. In our case there was no need to optimize the components with respect to the thermal crosstalk because the components were designed to operate individually.

The silicon nitride structure is highly birefringent having a large form birefringence due to the high refractive index differences in the waveguide stack. The birefringence is also temperature dependent due to the stress-optical effect and this can lead to a polarization dependent operation [142]. Changes in stress due to the temperature change may shift the location of the resonance peaks in the temperature scale due to the elasto-optic effect [22,143]. The refractive index change due to isotropic stress in the structure is larger for TM mode. In our case the TE mode was only propagating and the thermal stress induced change in the measured ΔT was considered to be negligible. Accurate determination of thermal polarization sensitivity

would be possible with the demonstrated structure if transmission at both polarizations could be measured.

Stress releasing grooves have been suggested to reduce the temperature induced stresses and thus the polarization dependency in applications where both polarization modes are present [142]. Furthermore thermal control can be applied to waveguide birefringence through stress-optical effect as shown with optical gyro based on ring resonator [143].

The difference between the measured temperature coefficient of the optical path length and the temperature coefficient used in the design did not affect the operational characteristics of the device significantly. The most significant difference was that the measured spacing of the resonances (ΔT) was about half the spacing expected from the design. This can be explained by the fact that the poly-Si resistors and aluminum films increase the stress in the device thus increasing the temperature coefficient of the optical path length compared to the situation with processed waveguides only. This directly affects the finesse measured for the devices.

The temperature tuning and the control of the phase are applied in applications in all TO devices, e.g. tunable filters and TO-switch fabrics, for telecommunication and interferometric sensors. A ring resonator based chromatic dispersion compensator for optical communication purposes, utilizing thermo-optic control in tuning the group delay has been demonstrated [54,55]. In other applications such as interferometric sensors the TO-switch can provide a control mechanism for the optical phase. Depending on the waveguide materials and the basic functional devices under TO-switch, different results have been achieved for the response time and the power consumption of the TO-phase shifter [53,116]. For example, response time below 0.2 ms has been reported for a silica based Mach-Zehnder optical 2×2 switch with the power consumption of 110 mW [116]. With similar configuration a SOI based 2×2 switch has been reported to achieve rise time below 3.5 µs with power consumption of 50 mW [53].

The ring resonators have many applications fields. In optical telecommunications the ring resonator structures can be exploited in frequency selective filters [56], optical switching [57], and in devices for compensating the chromatic dispersion [54,55]. In sensing applications, a micro ring resonator on a micromachined cantilever as sensitive displacement sensor for scanning probe microscopies has been presented [41]. The WDM network has typical channel spacing of 50 to 200 GHz which necessitates very large FSR. Very small sized ring resonators based on high refractive index difference using silica-on-silicon technology have been recently demonstrated with FSR over 60 GHz [144].

The optical properties of the small size thermally controlled ring resonator made with silicon nitride technology on silicon have been studied. The optical and electrical characteristics of the device have been evaluated. The ring resonator was controlled with an integrated poly-Si TO-phase shifter and the surface temperature of the device was measured with an integrated poly-Si thermistor. The thermo-optical phase shifter with an integrated thermistor makes the device suitable especially for sensor applications. The thermal characteristics of the ring resonator structure on silicon with a TO-switch and a thermistor have been experimentally studied. The response speed of the optical 2π phase shift has been evaluated with the integrated heater and thermistor on top of the waveguide structure. An accurate temperature control has been achieved by introducing an integrated poly-Si thermistor. The thermal characteristics of the device were shown to be improved when the device was mounted on a heat sink that effectively cooled the chip due to an increased vertical heat flow. The feasibility of the

TO-effect with an integrated thermistor for an accurate control of the optical phase shift in a waveguide has been demonstrated, and the usage of this scheme is likely to be found advantageous in applications such as interferometric sensors.

5 INTEGRATED OPTICAL BEAM COMBINER

In this work an integrated optical beam combiner test components have been developed for demonstration purposes in an optical phased array antenna. Free space optical communication systems are under rapid development for inter-satellite and satellite-to-earth station links. Progress in small size Nd:YAG lasers and semiconductor lasers has pushed these systems forward. The short wavelength band at 1064 nm is especially interesting as compact solid state diode-pumped Nd:YAG lasers are available. Earlier optical space communications channels have been point-to-point links applying direct laser modulation [145]. Recently planar optical circuits have been applied in phase array antenna applications for the beam forming [59,60], steering in the microwave systems [61,62], and in astronomical interferometry for the beam combining [63,64]. Planar beam combiners based on indium phosphide waveguides for phased array antennas have been studied [59]. A beam combiner with active phase control on chip was recently developed based on similar InP technology [60]. The compound semiconductor technology enables integration of active functions such as phase control and detectors on the same substrate. The drawbacks of the presented solutions based on the InP technology have been high chip losses and low coupling efficiency with the optical fibers [59,60].

The need for reducing the system complexity and weight with integration necessitates the development of planar optical devices for space applications. Couplers and splitters made of polarization maintaining (PM) fiber are commercially available but integrated optical devices offer an attractive option to enhance reliability and performance. Applying integrated beam combiner circuits reduces the length and number of fiber loops in the system. The system handling and maintenance become easier as complexity can be reduced with integration.

The research and development work done in this project aimed at proving the feasibility of integrated optics based technology to implement a 16×16 port beam combiner for a system demonstrator built at the Technical University of Vienna (TUV) under the European Space Agency's technology program. The target system was a coherent optical link, in which the transmission wavelength is 1064 nm and the receiver has a phased array antenna. Figure 5.1 shows how the input signal is constructed from the sub-antenna signals by adding the signals coherently in the beam combiner. The development work was started by first considering less complex 4×4 port beam combiner. To have a constructive interference sub-aperture signals must be phase controlled before the summing 3-dB couplers. The phase control is done with the external phase actuators. In case silica-on-silicon device thermo-optical phase shifters are a possible technical solution to integrate also the phase actuators in the same chip. The phase control was implemented in our case with integrated actuators in the input fibers.

To ensure coherent operation, polarization is fixed by applying components that preserve polarization such as polarization maintaining fiber. The final beam combiner would have 32 ports arranged in 16 input ports and in 16 output ports. This beam combiner would consist of 15 3-dB couplers arranged in a binary tree fashion to sum the signals from the sub-apertures [146]. Tuning the basic fabrication schemes to shorter wavelengths is challenging as surface roughness and thus scattering effect become more intense and cause evidently higher losses. The alignment tolerances become smaller as the fiber and waveguide dimensions are reduced.

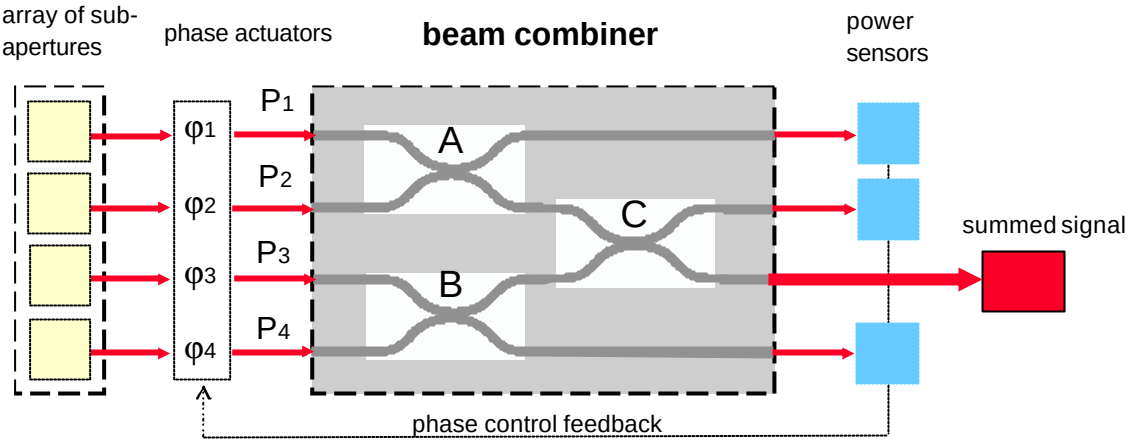

Figure 5.1. Schematics of the principle of using a beam combiner to combine coherently the signals with the couplers (A-C) from the sub-apertures of a phased array antenna.

5.1 Design considerations

The basic building blocks that are needed for the final 32-port device were designed and tested. These include straight waveguide structure, waveguide crossing, waveguide bend, and 3-dB coupler. Four test devices were used to evaluate the optical performance and maturity of the silica-on-silicon planar optical chips. The fabricated components are based on silicon oxynitride material on a silicon substrate. The test devices had one or three 3-dB couplers to evaluate the coupler properties in terms of the coupling ratio and insertion loss. At first different couplers were considered by evaluating their process sensitivity. Finally a multi mode interference (MMI) coupler was selected for the application. The waveguide propagation loss, waveguide crossing excess loss, bending loss, coupler imbalance and excess loss and polarization extinction ratio (PER) of the fabricated structures were measured. Furthermore fiber attachment and interfacing techniques of the waveguide components with PM-fibers were studied. Test pigtailing applying passive alignment and silicon V-grooves were carried out. The pigtailing method applying active alignment and silicon U-grooves was subsequently tested. All components were optically evaluated before and after the fiber attachment.

5.1.1 Layouts of test devices

The configuration of the four fabricated test devices is summarized in table 5.1. Figure 5.2 and 5.3 represent the 8-port schematic layouts and figure 5.4 represents the 12-port schematic layout [146]. The first 8-port device consists of three 3-dB couplers, two following 8-port devices have one 3-dB coupler and two straight waveguides and the 12-port device consists of three 3-dB couplers and of two crossing waveguides.

Table 5.1. Summary of the manufactured devices. Each device consisted of one or three couplers. Additionally, straight waveguides were tested with device #2 and #4 and waveguide crossings with device #3.

device	number of ports	Layout
1	8	3 cascaded couplers
2	8	1 coupler + 2 test waveguides
3	12	3 cascaded couplers + crossing waveguides
4	8	1 coupler + 2 test waveguides

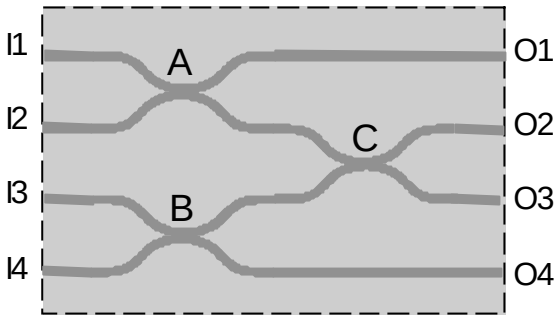

Figure 5.2. Schematic layout of the first 8-port (device #1) with three 3-dB couplers (A,B and C). The input ports are denoted I1-I4 and the output ports O1-O4.

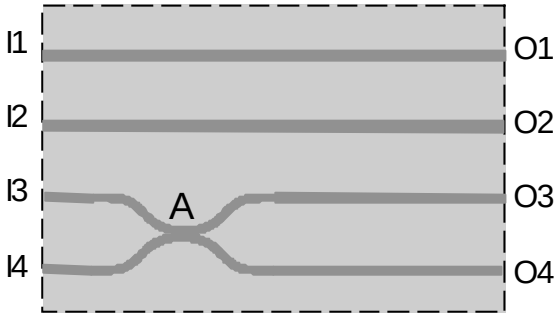

Figure 5.3. Schematic layout of the two 8-ports (device #2 and #4) with one 3-dB coupler (A) and two straight waveguides. The input ports are denoted I1-I4 and the output ports O1-O4.

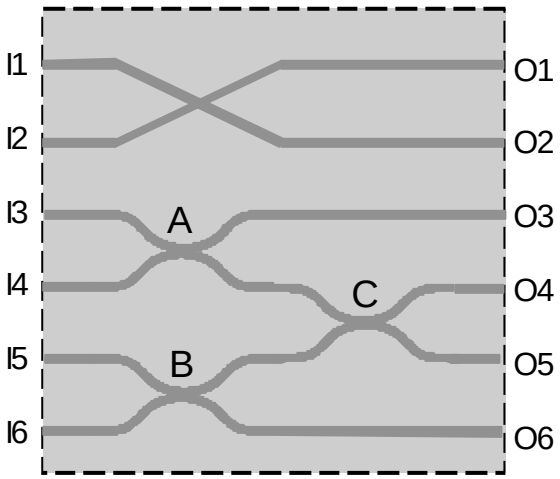

Figure 5.4. Schematic layout of the 12-port (device #3) with three 3-dB couplers (A,B and C) and one waveguide crossing. The input ports are denoted I1-I6 and the output ports O1-O6.

5.1.2 Specifications of test devices

The specifications for the test devices were derived from the specifications of the 32-port device (see table 5.2). Table 5.3 introduces the specifications of the test devices that are not common with the 32-port device. The specifications were considered as 'target' values which against the feasibility of the technology could be evaluated. In the following the specifications are reviewed and shortly discussed.

Table 5.2. Summary of the specifications for a 32-port beam combiner. The given value indicates the worst acceptable value. All specifications are given for a pigtailed device.

Wavelength of operation	1064 nm
Insertion Loss	3.5 dB
Polarization Extinction Ratio	10 dB
Return Loss	27 dB
Coupling ratio of 3-dB coupler (imbalance)	47:53
Optical power handling capability	1 mW
Maximum optical path length difference of signal path	100 µm
Operating temperature range	+15…+35 °C

Table 5.3. Target specifications for a 3-dB coupler used in devices #2 and #4 and in a binary tree formation in devices #1 and #3, and for a waveguide crossing. The specifications for the test devices were derived from the specifications of the 32-port devices. All specifications are given for a pigtailed device.

3-dB coupler	**Target value**	**Device #**
Insertion loss of single coupler	1.3 dB	#1 and #3
Insertion loss of three couplers in a binary tree configuration	2.5 dB	#2 and #4
Polarization Extinction Ratio	15 dB	all
Waveguide crossing		
Excess loss	1.2 dB	#3
Polarization Extinction Ratio (PER)	15 dB	#3
Crosstalk	-20 dB	#3

Wavelength of operation

The device was designed to operate at 1064 nm wavelength. Allowed deviation from this wavelength is limited by the coupler and the waveguide designs. The coupling ratio of the couplers is wavelength dependent. The input and output fibers could be used over a much wider bandwidth than the couplers, typically the cut-off wavelength of the fiber limits the wavelength span. The acceptable wavelength window for the couplers is later discussed. Material dispersion and absorption of the silicon oxynitride waveguide do not limit the wavelength in this application.

Insertion Loss

The 32-port beam combiner is specified to have an insertion loss 3.5 dB. The insertion loss target for the 8-port device with three couplers is 2.5 dB. This specification can be divided into fiber coupling losses and insertion loss of the integrated optical circuit.

Insertion loss is formed of the waveguide propagation loss, and radiation losses in the bent waveguide sections. Insertion loss includes the excess loss of the couplers and excess loss from the waveguide crossings, which should be taken into account because the final 16×16 port beam combiner would have at least 4 waveguide crossings on the signal path when considering conventional layout as shown e.g. in figure 5.1., in which the inputs and outputs are located on opposing sides. The waveguide crossings could be completely avoided by mixing the input and output ports, and applying 90 and 180 degree waveguide bends.

Input/Output fibers

The input fibers, and the signal output fiber are single-mode, polarization maintaining fiber. The PM-fibers are a class of highly birefringent waveguides, in which the two orthogonal polarizations states are considered to be perfectly decoupled. The fiber usually has stress members that create birefringence in order to degenerate the polarization states (see figure 5.5). The fiber slow axis is parallel to the stress field and it is normally preferred as a coupling axis as it has lower bending sensitivity and better cross-talk damping.

The PM-fiber was determined to be type HB1000 (Fibercore Inc., UK). The fiber specifications are summarized in table 5.4. All input pigtail lengths must be equal in length to within 10 mm to guarantee equal optical path length for each input beam. The optical path length difference between any input and the signal output on the beam combiner chip must be smaller than 100 µm. The signal output is specified to be a PM-fiber in the 32-port beam combiner. The output ports of the test devices were pigtailed also with a PM-fiber to gain experience with pigtailing.

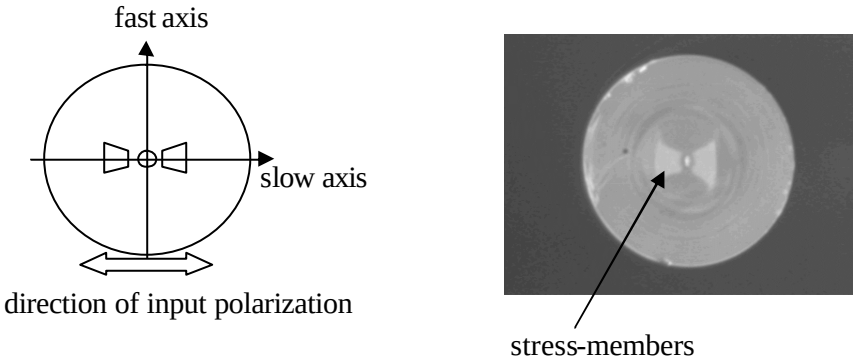

Figure 5.5. Schematic cross section of a polarization maintaining fiber and a photograph of the bowtie-type PM-fiber (HB1000, Fibercore) with the stress-members and core being visible. Light coupled to the input fibers (sub-aperture signal) is polarized parallel to the stress members.

Table 5.4. Specifications of the polarization maintaining fiber (HB1000, Fibercore).

Cut-off Wavelength	980 nm
Attenuation	1.6 dB/km @1060 nm
Numerical Aperture	0.15..0.2
Optimum launch spot-size	4.6 µm
Modefield diameter	5.62µm @1064nm
Modefield ellipticity	1.3 @1064nm
Cladding refractive index	1.457 @633nm
Core eccentricity	<1 µm
Fiber outer diameter	125µm
Coating outer diameter	245µm ± 2.5µm

Polarization Extinction Ratio

In the 32-port beam combiner the worst case output PER must be higher than 10 dB. The PER target specification of the test devices is 15 dB. The polarization extinction ratio describes the extent to which the energy of the light field is confined in one polarization. The input beams of the beam combiner are linearly polarized, parallel to the slow axis of the PM-fiber. The polarization axis defined by the stress members must be aligned parallel to the appropriate polarization axis of the waveguide so that either TE or TM polarization is excited in the waveguide. The PER can be degraded by the perturbations in the waveguide such as deformations in the core shape and irregularities between the core and the cladding layers. The waveguide was assumed to be ideal and highly birefringent i.e. the TE and TM modes were assumed to be perfectly decoupled so that the PER would not degrade due to the waveguide.

In the application the polarization crosstalk is considered to occur due to imperfect interfaces; at the input beam-to-PM-fiber and fiber-to-waveguide interfaces. In the waveguide chip the polarization is defined to be TM. If the fiber's slow axis is not perpendicularly aligned with the waveguide core the input field partially excites both TE and TM polarization states, i.e. E_x and E_y fields (see figure 5.6). The light coupled to the PM-fiber is assumed to be perfectly polarized and coupled perfectly along the polarization axis of the fiber. Then the maximum PER as function of the angular misalignment f is given as

$$\mathrm{PER} = -10 \times \log(\tan^2 j) . \qquad (5.1)$$

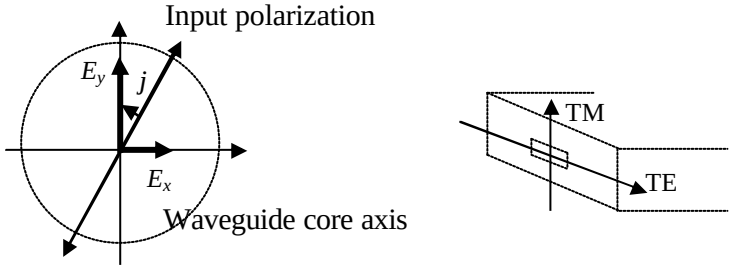

Figure 5.6. A misalignment between the fiber slow axis (input polarization) and the horizontal axis of the waveguide core causes partial coupling of the power to the TE mode of the waveguide thus increasing the polarization cross talk.

Coupling ratio of the 3-dB couplers

The couplers were specified to have a coupling ratio better than 47:53. This equals 0.5 dB deviation from the nominal 50:50 coupling ratio. Depending on the coupler type the imbalance can be due to a number of reasons. For directional couplers the critical process factors are linewidth accuracy and the refractive index control. For multimode interference couplers the critical process parameter is the refractive index control. These issues are further considered in the chapter devoted to design issues.

Return Loss (RL)

The return loss at the input ports must be higher than 27 dB. The return loss is the ratio of the total input power and the power reflected backwards from the device. Typically in silica-on-silicon based integrated optics the back reflections are caused from the fiber-to-waveguide interface. Back reflections can also occur between different sections in the waveguide device and due to the shape irregularities in the waveguide.

Other specifications

Additional specifications were set for the power handling and for the operating temperature range. The beam combiner was specified to handle 1 mW optical power at the signal output. When compared to typical 200 mW requirement for fiber optical telecommunications components, including integrated optical silica based devices, the required 1 mW power handling capability is low and was not considered critical.

The operation temperature range was specified to be between +15 to +35 °C. Again considering the requirement for fiber optical network components (-10 to +70 °C), this requirement was seen not critical. The fabricated devices were not tested against these specifications.

5.2 Design of test devices

The described application has particular requirements when comparing to conventional optical network components. The wavelength of operation is 1064 nm and the input fibers are polarization maintaining fibers. The packaging issues were challenging due to the special fiber selected for the device and due to the polarization maintaining nature of the application. The development process is described in a flow chart shown in figure 5.7. The available resources i.e. equipment and processes determined the manufacturing technology. In our case the VTT clean room facilities provided the possibility to manufacture silica-on-silicon waveguides. Both silicon oxynitride waveguides and phosphosilicate glass (PSG) materials were available in a plasma enhanced chemical vapor deposition (PECVD) reactor. Both SiO_xN_y and PSG offer the refractive index and the thickness range needed in the application. The refractive index control is more flexible when using silicon oxynitride as the material composition could be tuned continuously from pure silicon oxide (SiO_2) to silicon nitride offering control of refractive index from 1.46 to 2.0. While silicon oxynitride is stable as deposited, PSG material needs to be annealed to stabilize it. On the other hand phosphorus doped oxide performs glass flow process in a high temperature treatment. This phenomenon is an advantage in the cladding layer deposition to improve the step coverage and to avoid a void formation. Due to process issues (annealing and safety) SiO_xN_y was selected to be

the waveguide material. Test process runs were performed to calibrate the control of the layer thickness and refractive index. Subsequently the design of the waveguide structure was started. The target was to design a structure with a wide process window and large fiber-to-waveguide alignment tolerance. The device design focused on studying the effects due to moderate variation of the refractive index, linewidth, and film thickness. A coupler design least sensitive to these effects was selected for test devices.

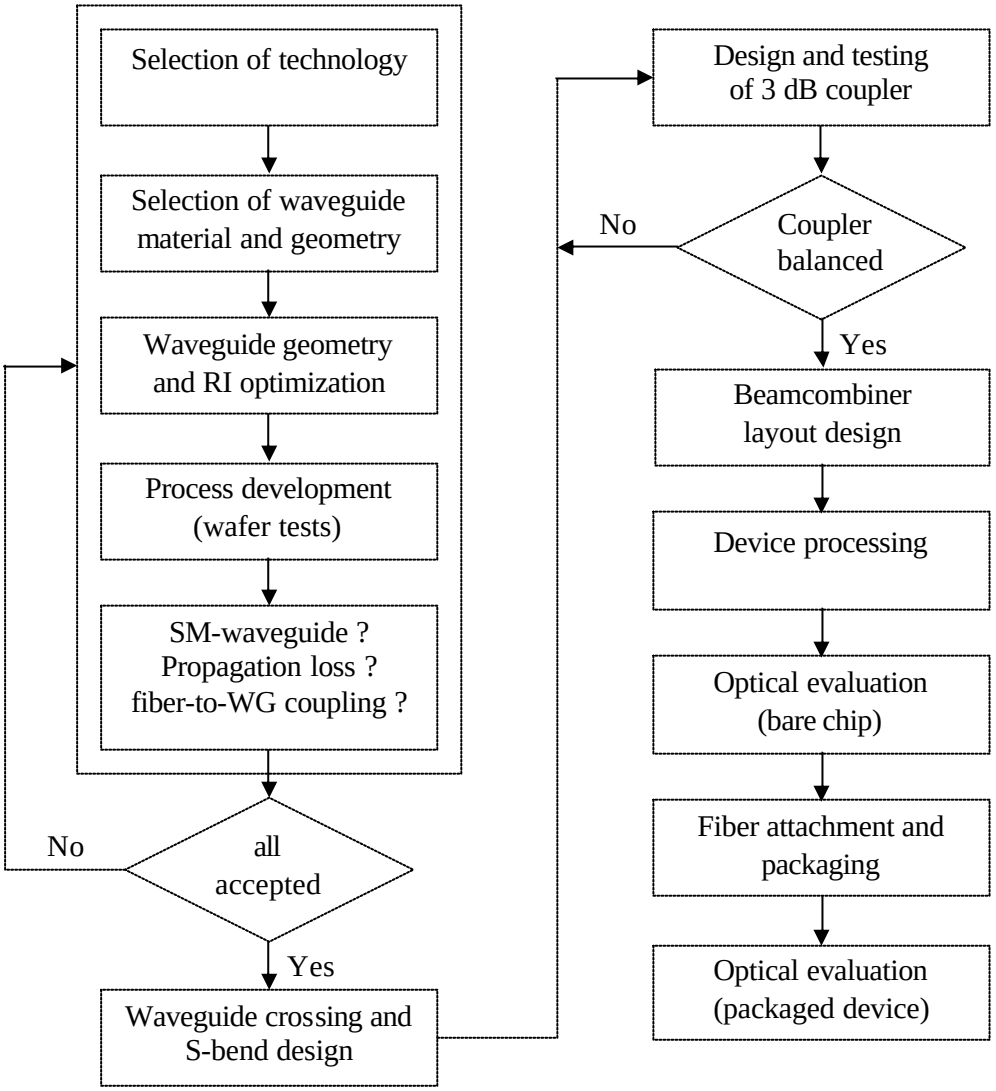

Figure 5.7. The development flow of the test devices. Application wavelength, fiber connectivity, and availability of fabrication tools determined the choice of the technology. This choice dictated structural and geometrical limitations on the waveguide parameters. The fiber interface-issues set the exact waveguide parameters. Test process runs and waveguide evaluation runs were needed to verify the feasibility of the chosen technology and the waveguide structure. The design of functional structures was completed after the technology and waveguide parameters were established.

Waveguide structure

Design of the waveguide structure was targeted to have a single-mode operation, loose alignment tolerance and high fiber-to-waveguide coupling efficiency. The waveguide

geometry was based on the consideration of the fiber parameters represented in table 5.4. The main design parameter is the mode field diameter. The fiber-to-waveguide coupling loss was minimized by fitting the waveguide mode to the fiber mode, and while ensuring a large tolerance for the fiber alignment. Other aspects to consider are the refractive index difference, waveguide geometry and dimensional control. High refractive index difference enables tighter waveguide bends (though in the test devices these were not needed). The waveguide geometry and dimensions are related to the etching step, sidewall quality and step coverage.

A buried strip waveguide with a rectangular cross section was chosen to be applied in the test devices. The free design parameters were the layer thickness and refractive indices of the layers. Restrictions on these parameters were set by the fabrication issues: Firstly a thin core layer was preferred to ease the core forming step i.e. the etching through the silicon oxynitride layer (SiON). Thin waveguide stack is beneficial as stress is lower and smaller wafer warping can be expected. Secondly the minimum channel width was considered to be 3.0 to 3.5 µm. To guarantee good repeatability and uniformity the refractive index difference was preferred to be higher than 4×10^{-3}.

The waveguide cross section and the refractive index profile is depicted in figure 5.8. Cladding layer refractive index was chosen so that $n_{cl}=n_b$. The refractive index structure was chosen so that it was possible to use optionally another waveguide material (PSG). The waveguide structure was designed on a silicon substrate with a SiO_2 buffer layer (n_b, thickness H_b), a SiO_xN_y core (n_c, width W, height H) and SiO_2 cladding layer (n_{cl}, thickness H_{cl}).

The cut-off condition, for the waveguide to be single moded, could be confirmed by applying 2D model and effective index method [140]. In our case the single mode condition (dimensions) was verified by applying the mode solver program Selene.

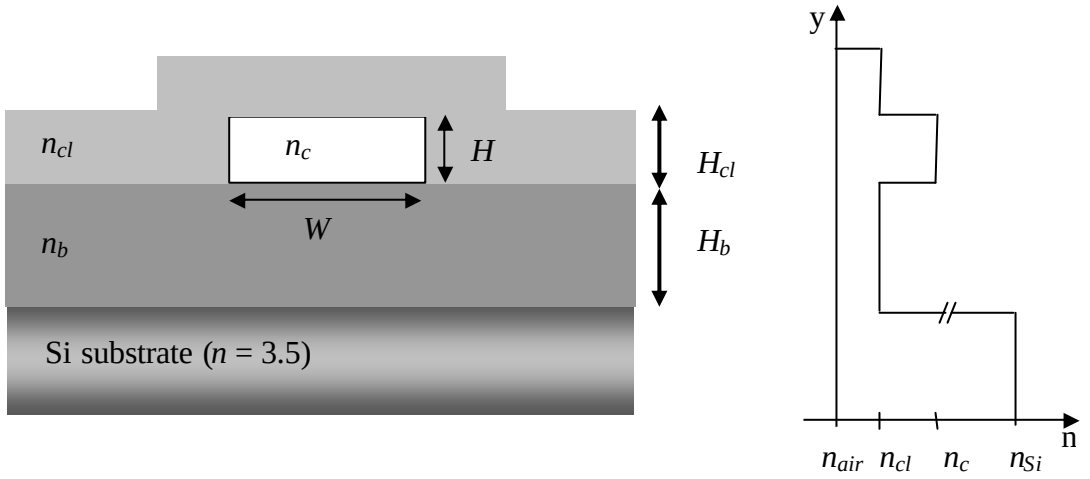

Figure 5.8. The schematic cross section of the waveguide structure and the corresponding refractive index profile of the vertical axis of the waveguide. W and H are the core width and height. n_c , n_{cl} and n_b are the refractive indices of the layers. H_b and H_{cl} are the buffer and cladding heights.

A compromise between above mentioned restrictions and the fiber coupling efficiency was seeked. Commercial CAD simulation tool (Olympios/Prometheus, C2V(BBV), NL) was used to optimize the coupling efficiency and to find the appropriate values for the refractive indices, waveguide width and height. The estimated

layer thickness and refractive index structure needed for the waveguide were calculated prior to process runs.

Figure 5.9 shows the calculated coupling efficiency and sensitivity to alignment as a function of the refractive index difference (Δn). The figure shows the allowed maximum thickness for the core layer (H_{max}). The optimum coupling loss between the PM-fiber and the design waveguide structure was calculated to be 0.1 dB. The modefield of the waveguide was slightly elliptical as width was set to be $1.1 \times H_{max}$. The alignment tolerance was considered more important than the coupling loss. The waveguide was optimized to have low sensitivity to lateral and vertical alignment offsets. Higher Δn (0.01) gives optimum coupling efficiency, but has also narrower fiber coupling window. If the fiber is offset 1 µm in lateral and vertical directions, the coupling loss is 0.7 dB. The alignment sensitivity was reduced by choosing slightly lower Δn. The refractive index difference (Dn) between the waveguide core and cladding layers was chosen to be 8×10^{-3}, while the refractive index of core was chosen to be 1.48. With these values the thickness limit for the core from single mode condition was 3.5 µm.

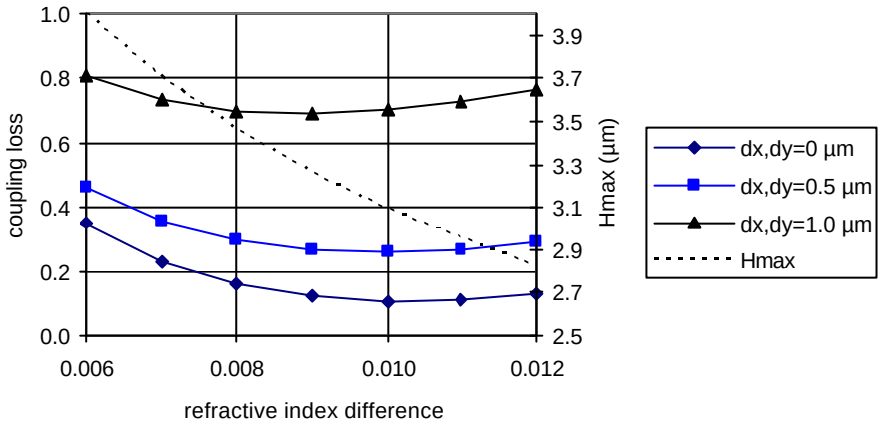

Figure 5.9. Fiber coupling tolerance as a function of refractive index difference (Δn). Three curves show the coupling loss in case lateral (dx) and vertical (dy) misalignment is 0, 0.5 and 1.0 µm. The dashed line (H_{max}) indicates the cut-off thickness for the core layer. The waveguide height and width changes as a function Δn. Furthermore the width was chosen to be $1.1 \times H_{max}$ to relax the coupling losses.

The waveguide core had to be isolated optically from the high index silicon substrate with a buffer layer. Radiation coupling between the core and the substrate was designed to be less than 0.1 dB/cm for the TM mode (see figure 5.10). The buffer layer thickness was calculated to be 6 µm, following the radiation loss model given by Stutius et al. [37].

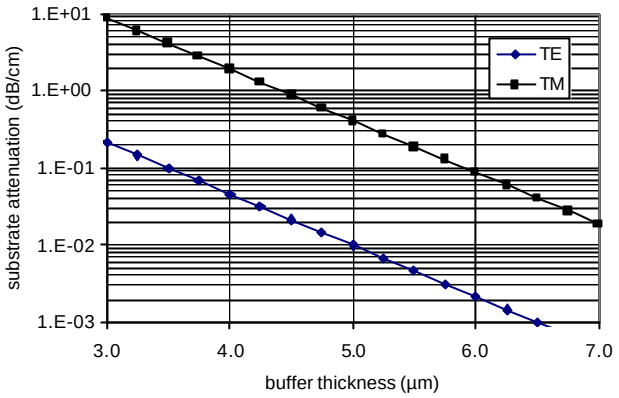

Figure 5.10. Substrate attenuation for TE and TM polarization was calculated to drop below 0.1 dB/cm with a 6.0 µm buffer layer. The waveguide parameters used for estimating the substrate coupling were (H=3.0 µm, n_c=1.479 and n_b, n_{cl} =1.471).

The parameters of the chosen waveguide structure are summarized in table 5.5. The deposition process was calibrated to these values. The waveguide width was varied on the mask between 3.5 and 7.0 µm.

Table 5.5. The selected waveguide parameters.

Layer	**thickness (µm)**	**refractive index**
Cladding	6.0	1.472
Core	3.5	1.480
Buffer	6.0	1.472

Coupler design

The beam combiner has several 3-dB couplers and the main task was to design a low-loss 3-dB-coupler which would meet the specifications under moderate process variation. Several different designs were considered for the 3-dB coupling function. Conventional directional coupler, two-mode interference (TMI) coupler, and MMI-coupler were studied and compared. In the following the main design considerations of the couplers are presented by showing the sensitivity of different coupler types to the process variations. Although the design of couplers was done with CAD tools, the basic structures and their fundamental properties are reviewed.

Directional coupler and two mode coupler

A symmetric directional coupler was studied as a first option. Figure 5.11 shows a schematic layout of a directional coupler. The optical power P_{in} launched into one input port of the directional coupler is split into two output ports. The power splitting ratio depends on the coupler dimensions. The effective coupling length can be defined as $L_{DC} = L_{ST} + L_{BENDS}$, where the L_{ST} is the length of the straight coupling region and the L_{BENDS} is the length of the bent waveguide sections where the fields are coupled. The power transfer equations are

$$P_{bar} = P_0 \cos^2(f/2)e^{-az} \qquad (5.2)$$
$$P_{cross} = P_0 \sin^2(f/2)e^{-az}$$

Where f is the accumulated phase difference between the two waveguides and a is loss factor. f is given by $f=\int \Delta b(z)dz$, integrating over the distance the waveguides are coupled (i.e. $L_{ST}+2L_{BENDS}$). Δb is the phase difference between the symmetric and antisymmetric modes of the waveguide pair.

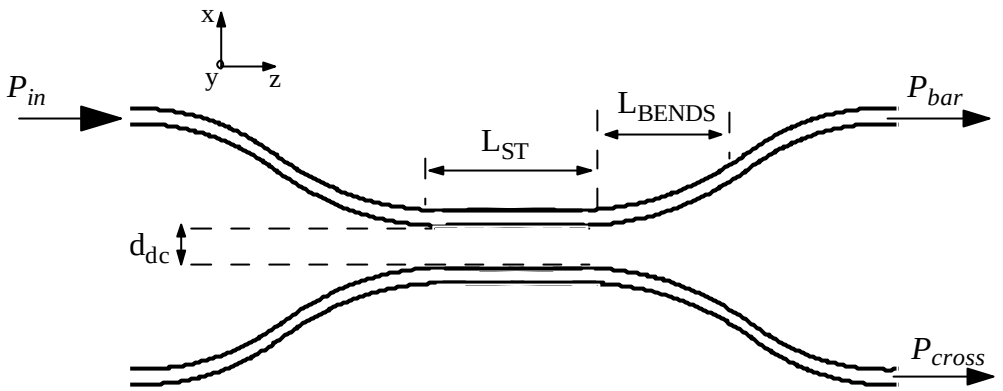

Figure 5.11. A symmetric directional coupler is formed of two coupled waveguides. The power splitting ratio depends exponentially on the gap d_{dc} between the waveguides.

Multi mode interference couplers are known to be less sensitive to process variations than directional couplers. A basic MMI coupler, a two-mode interference coupler with a continuous coupling region is formed from a directional coupler when the gap between the waveguides is filled or the gap is reduced to zero. A schematic layout of a TMI coupler is shown in figure 5.12. The TMI coupler's operation can be described with the equations (5.2).

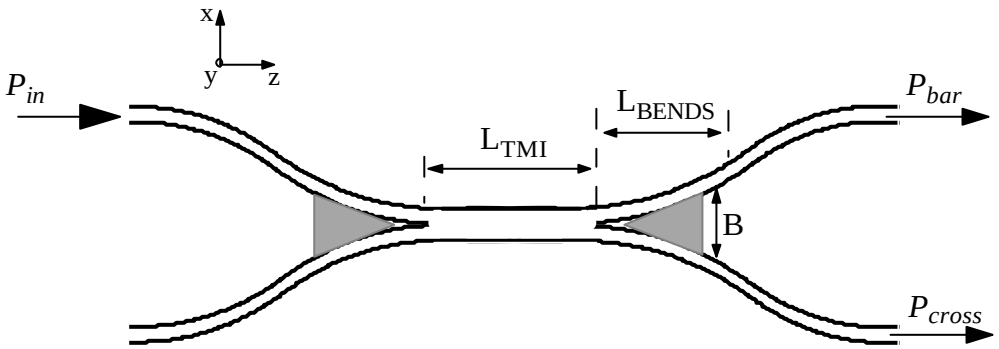

Figure 5.12. Two-mode interference coupler is a special type of multimode interference coupler. Compared to a directional coupler there is no gap between the waveguides and the sensitivity to small linewidth changes is improved. The shaded areas may not open in a lithographic process thereby creating a fabrication problem. The parameter B denotes the smallest Y-junction gap that opens in the lithographic and etching process.

MMI coupler

The MMI device is based on the so called self-imaging principle [146,147]. It is a property of a multimode waveguide by which an input field is reproduced in single or multiple images at periodic intervals along the direction of propagation. A schematic layout of a 2×2 MMI coupler is represented in figure 5.13.

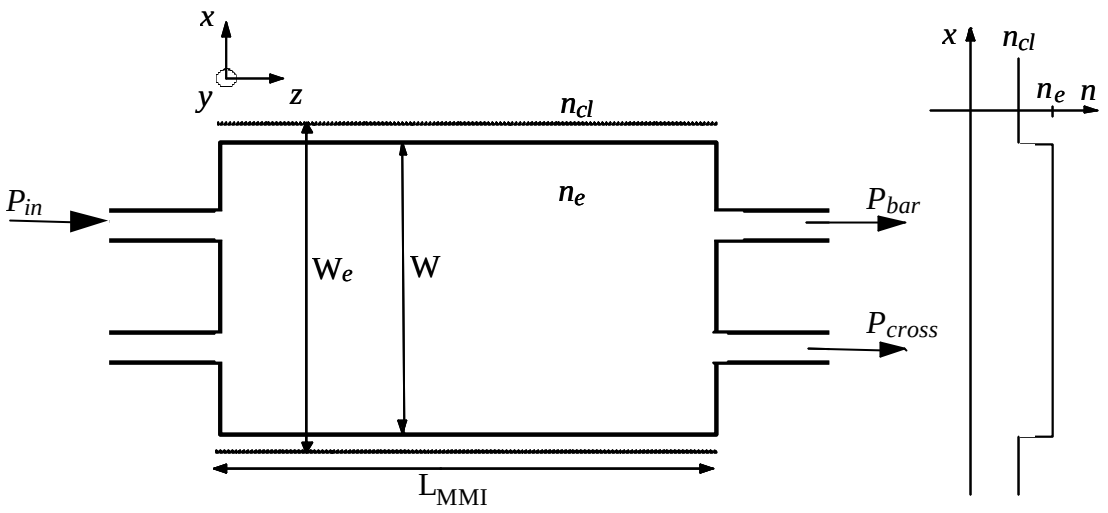

Figure 5.13. Schematic diagram of a 2×2 multi-mode interference coupler. The critical parameters are length (L_{MMI}) and width (W) of the multimode section and the positioning of the access waveguides. The effective width (W_e) defines the position of the access waveguides. On the right is the refractive index profile of the structure. The n_{cl} denotes the cladding index and inside the MMI area n_e denotes the effective index.

A multimode waveguide section supports several modes and these modes are excited by the fundamental mode introduced by the access waveguides. A complex interference pattern is produced in the MMI-section due to differences in the phase velocities of the different modes. At certain distances the so called self-imaging or multiple imaging takes place. As the lateral dimensions are much larger than the vertical dimensions the modes are assumed to have similar behaviour over the waveguide. Thus the analysis can be reduced to two dimensions by applying the effective index method (EIM) and beam propagation method (BPM). The first approximation for the MMI layout parameters can be obtained by using arithmetic formulas as given in [147]. The MMI device can be described by introducing effective width W_e and beat length parameter L_p. The effective width takes into account the lateral penetration of modes i.e. Goos-Hähnchen shift caused by the phase shift at the reflection boundaries. The effective width is given by

$$W_e = W + \left(\frac{l_0}{p}\right)\left(\frac{n_{cl}}{n_e}\right)^{2s}\left(n_e^2 - n_{cl}^2\right)^{-1/2} \quad , \tag{5.3}$$

Where the l_0 is wavelength in free space, W is the width of the MMI section, n_e is the effective index and n_{cl} is the cladding index, and parameter σ is determined by the polarization so that σ=0 for TE modes and σ=1 for TM modes. The propagation constants of the modes in the waveguide can be approximated by

$$b_n = k_0 n_e - \frac{(v+1)^2 p\, l_0}{4 n_e W_e^{\,2}} \quad , \tag{5.4}$$

where $k_0 = 2p/l_0$ and v is the mode number. The beat length is defined as

$$L_\pi = \frac{p}{b_0 - b_1} = \frac{4 n_e W_e^{\,2}}{3 l_0}, \tag{5.5}$$

Thus the beat length has quadratic dependence of the width of the multimode waveguide. The excitation of modes in the MMI section depends on the lateral positioning of the access waveguide. The mode excitation coefficient c_v can be estimated with an overlap integral between the access waveguide mode and the mode E_v in the MMI section

$$c_v = \frac{\int E(x) E_v(x) dx}{\sqrt{\int E_v^{\,2}(x) dx}} \tag{5.6}$$

The two parameters W and L_π can be used for synthesizing the MMI layout. The meaning of the L_π is explained in table 5.6. MMI devices can be divided into three categories depending on the mode excitation in the MMI section [147] (see table 5.6): N×N general interference, 2×N restricted paired interference and 1×N restricted symmetric interference. The image distance depends on the number of modes and the mode phase factor of the excited modes [147]. A 2×2 coupler can be best realized by applying the paired interference mechanism. In figure 5.14 the fields are represented by

$$E_v(x) = \sin\left[p\,(v+1)\frac{x}{W_e} \right] \tag{5.7}$$

as shown in figure 5.14 the modes v=2,5,8… can be avoided if the symmetric exciting field is positioned laterally in the position x = ± W_e/6.

Table 5.6. General characteristics of the MMI devices divided into three categories with general, paired and symmetric interference mechanisms [147].

	General	**Paired**	**Symmetric**
Inputs × Outputs	N × N	2 × N	1 × N
Single image distance	$3L_\pi$	L_p	(3/4) L_p
Excitation requirement	Free	$c_v = 0$ for v=2,5,8…	$c_v = 0$ for v=1,3,5…
Access waveguide positioning	Free	x = ± W_e/6	y = 0

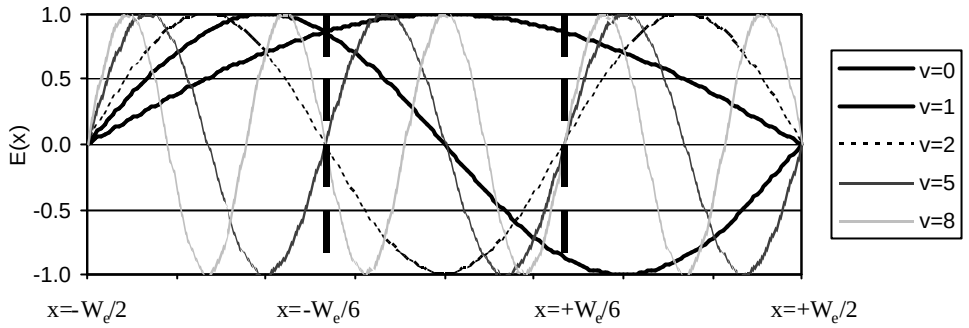

Figure 5.14. Mode excitation of paired interference of 2×N couplers. Only the lateral mode pairs v=0,1; 3,4; 6,7…become excited if the access waveguide is correctly positioned. The overlap between lateral modes v=2,5,8… and the access waveguide mode then becomes negligible.

Key figures of 3-dB coupler

The coupler is in a bar state when $P_{bar} \approx P_{in}$ and in a cross state when $P_{cross} \approx P_{in}$. The excess loss of a coupler is defined as the extent of the power not coupled to either of the two output states.

$$\text{Excess loss} = -10 \log \frac{P_{bar} + P_{cross}}{P_{in}}. \tag{5.8}$$

A 3-dB coupler should have $P_{bar} = P_{cross}$. Imbalance is defined as

$$\text{Imbalance} = -10 \log \frac{P_{bar}}{P_{cross}} \tag{5.9}$$

5.2.1 Comparison of couplers

Directional coupler

The performance of the DC was modeled by using the CAD simulation tool. Based on the lithographic resolution limits and on the width of the waveguide, the waveguide axial distance d_{DC} was designed to be at least 6.5 µm. The waveguide structure was based on the rectangular refractive index profile, Δn=8×10^{-3} and W=H=3.5 µm. Both input and output waveguides were designed to have constant curvature S-bends, with radius of curvature of 10 mm. The proper length for the straight coupling section (L_{ST}) was found to be 280 µm. Figure 5.15 shows the change of power coupling as a function of coupler length with the d_{DC} being the parameter. Characteristic sinusoidal operation of the DC is not shown due to a relatively large gap between the coupled waveguides. To adjust coupling length accurately, knowledge of the exact effective index and the waveguide gap are essential. Absolute value of effective index is a difficult magnitude to measure. Thus the optimization of DC is commonly done experimentally. In this case the reproducibility of the DC was studied by calculating allowed tolerances of axial

distance (d_{DC}), process linewidth accuracy (dp) (later referred to as linewidth), and refractive index difference (Dn). Tolerance window was defined by the imbalance specification of 0.5 dB.

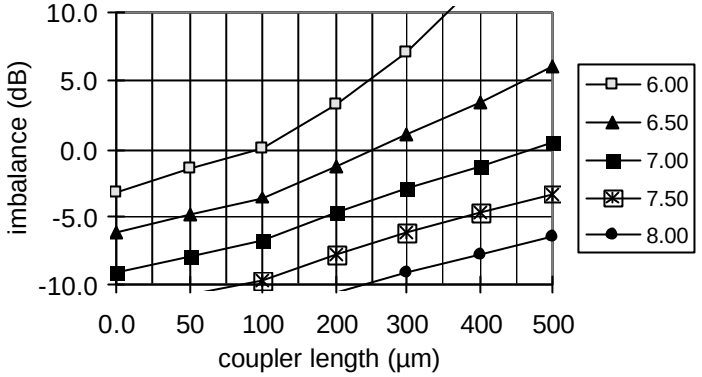

Figure 5.15. Imbalance of the directional coupler as the length of the coupling section changes. The curves are plotted for a waveguide axial distances (d_{DC}) of 6.0 µm to 8.0 µm in steps of 0.5 µm.

The effect of small variations in relative index difference and linewidth was modeled with 2D-BPM. Different values of d_{DC} (6.0, 6.5, 7.0, 7.5 and 8.0 µm) were studied. Figure 5.16 shows the sensitivity of the DC to small variation in the linewidth. The change of the linewidth can be considered to have two effects: Firstly the propagation constant changes and secondly the waveguide gap changes. The accuracy of the lithography and the etching process was known to be within 0.2 µm. Figure 5.16 shows that the coupler's performance can be maintained within the specified 3 dB ±0.5 dB with the estimated linewidth accuracy of the process. Figure 5.17 shows the sensitivity of the DC to small changes in refractive index. The operation is acceptable if the refractive index change is smaller than $\pm 2.5 \times 10^{-4}$. This value should be compared against the uniformity and repeatability values presented later in tables 5.12 and 5.13.

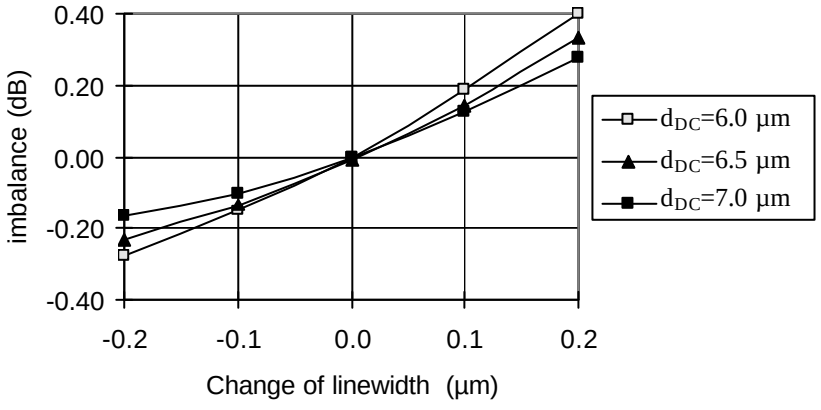

Figure 5.16. Imbalance of a directional coupler in cases where the linewidth changes from the nominal. The three cases are for waveguide axial distances (d_{DC}) of 6.0, 6.5 and 7.0 µm. As the waveguide gap increases, the device becomes less sensitive to the variation of linewidth. The directional coupler has a coupling length (L_{DC}) of 280 µm.

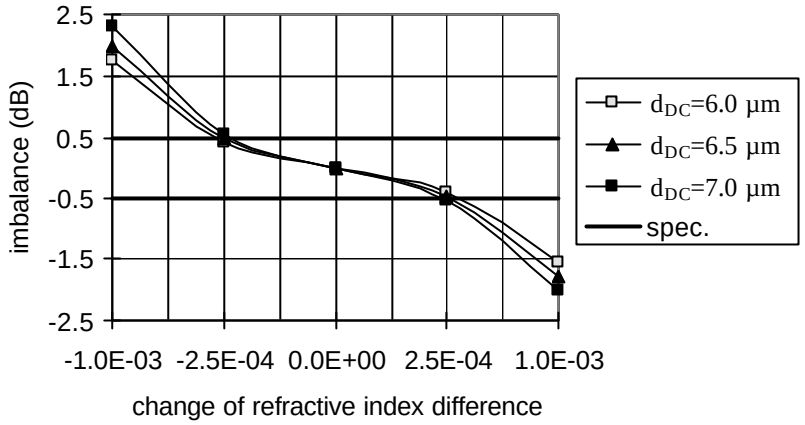

Figure 5.17. Imbalance of a directional coupler in cases where the refractive index difference changes from the nominal. The three cases are for waveguide axial distances (d_{DC}) of 6.0, 6.5 and 7.0 µm. As the waveguide gap increases the device becomes more sensitive to the refractive index changes. The directional coupler has a coupling length (L_{DC}) of 280 µm.

The worst case performance of a single coupler was estimated by taking into account both previously mentioned effects. These results are shown in table 5.7, which shows that if variation in Δn and in linewidth have the same sign the coupler performance is within acceptable limits, and only if variation in Δn and in linewidth have opposite signs is the coupler performance degraded beyond the design limits.

Table 5.7. Worst case performance of imbalance of the designed DC (d_{DC}=6.5 µm) when maximum process variation occurs.

maximum change of linewidth	**maximum change of refractive index difference (Dn)**	
	-2.5×10^{-4}	2.5×10^{-4}
dp = -0.20 µm	0.25 dB	-0.70 dB
dp = 0.20 µm	0.80 dB	-0.11 dB

TMI coupler

To improve the performance and manufacturability of the beam combiner the sensitivity to expected process fluctuations must be reduced to a minimum. One choice is to replace the symmetrical directional coupler with a TMI coupler. A TMI 3-dB coupler was designed together with the above described DC. A noticeable difference to the DC is that the TMI device has two input and output waveguides in close proximity, which makes it sensitive to finite lithographic resolution. If the opening of the Y-junction at the input and at the output sides can be guaranteed at the processing, the device performance is expected to be good. This opening tolerance or filling parameter for the lithographic process is denoted with B (see figure 5.12). Both input and output waveguides were designed to have constant curvature S-bends (ρ = 10 mm). The access waveguides are separated by 5 µm at the ends of the TMI section. Partial coupling due to this small separation has been taken into account so as to have correct 3-dB

performance. The TMI coupler was simulated by using a mode analysis (Selene) and 2D-BPM. Figure 5.18 shows the TMI operation as the length of the TMI section is varied. The optimum parameters for the coupling region were found to be 8.5 μm, the gap between the input/output waveguides is set to 1.5 μm and the length of the TMI section is 228 μm.

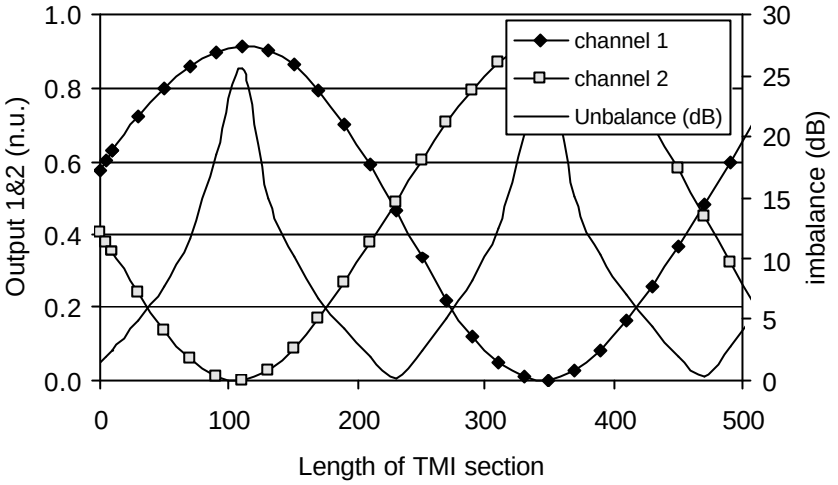

Figure 5.18. The power coupled to each output waveguide as a function of length of the TMI section.

The effect of a variation of linewidth together with the finite lithographic resolution (*B*) is shown in figure 5.19. The TMI coupler's performance degrades sharply after a certain point for each *B* value. In the simulation script the Y-junction becomes filled at these points. The value *B*=1.2 μm was chosen to be the acceptable minimum value for the lithographic resolution. From figure 5.19 an acceptable value for linewidth variation is ±0.25 μm. Imbalance and excess loss, versus the change in refractive index difference (*Dn*), are shown in figure 5.20. The simulation of the TMI coupler takes into account the excess loss unlike the simulation of the DC. This is due to the imaging nature of the TMI coupler: Poor imaging in the TMI section means that the field is not coupled to the output waveguide and power is lost in the surrounding area. The TMI coupler has acceptable performance (imbalance within ±0.5 dB) when variation in *Dn* is smaller than $\pm 2.5 \times 10^{-3}$. These three effects: *Dn*, *dp* and *B*, when reaching extreme values, give the worst case performance. These results are shown in table 5.8.

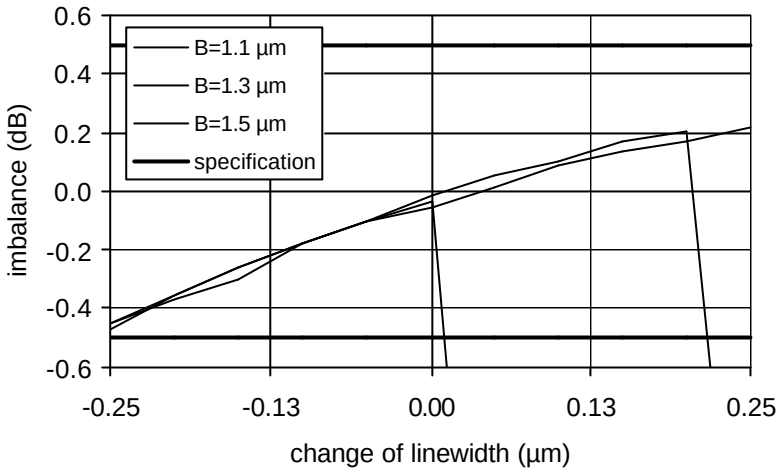

Figure 5.19. The imbalance of a TMI coupler in cases where the linewidth changes from the nominal. Three cases with different value of *B* are shown. Abrupt change in imbalance is due to the filling of the gap between the input and output waveguides. If the filling parameter *B*=1.1 µm the linewidth could change by 250 nm and the TMI coupler would still be within the given limits. The specification for imbalance is marked with red horizontal lines.

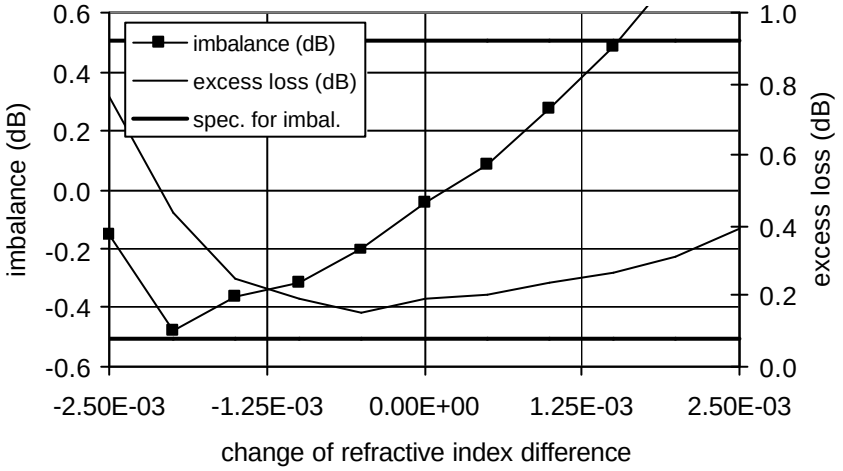

Figure 5.20. The imbalance and excess loss of a TMI coupler in cases where the refractive index difference changes from the nominal. The specification for the imbalance is marked with red horizontal lines.

Table 5.8. The worst case performance of the imbalance of the designed TMI coupler when maximum process variation is taken into account. The lithographic resolution (*B*) was assumed to be better than 1.2 µm.

maximum change of linewidth (dp)	**maximum change of refractive index difference (*Dn*)**	
	-2.5×10^{-4}	2.5×10^{-4}
dp = -0.20 µm	-0.44 dB	-0.31 dB
dp = 0.20 µm	0.14 dB	0.26 dB

MMI coupler

The MMI coupler is based on the paired restricted interference phenomenon (see table 5.6). This approach gives the shortest 2×2 MMI coupler. The width of the multi mode section (W) is initially chosen to be 40 µm with a total of 6 modes, applying the CAD tool. Smaller number of modes would yield more compact device (as in case of TMI), and on the other hand increasing the number of modes could yield improved self-imaging but longer device. As the mode dispersion properties of the real structure are not exactly known due to inaccuracy in the geometrical dimensions and in the refractive index structure. Increasing the MMI width would probably not improve the imaging properties as restricted mode excitation becomes more difficult.

The effective width W_e is chosen to be 43 µm as the difference of the effective indices of the 0^{th} and 1^{st} order modes is 0.0018. The approximate length for the MMI section L_{MMI} becomes 1700 µm using (5.5). The MMI coupler's performance was optimized with a CAD-tool. The simulation was run by varying the effective width and length to find the optimum geometry. To improve the imaging properties and enhance the transmission a tapering section was introduced on the access waveguides. The tapering length was long enough to maintain adiabatic operation. Figure 5.21 shows the calculated imbalance and excess loss versus these two parameters. The coupler outputs are balanced with L_{mmi} = 1754 µm and with W_e= 43 µm. The excess loss is even lower with a longer MMI section but then the coupler is in imbalance by 0.1 dB.

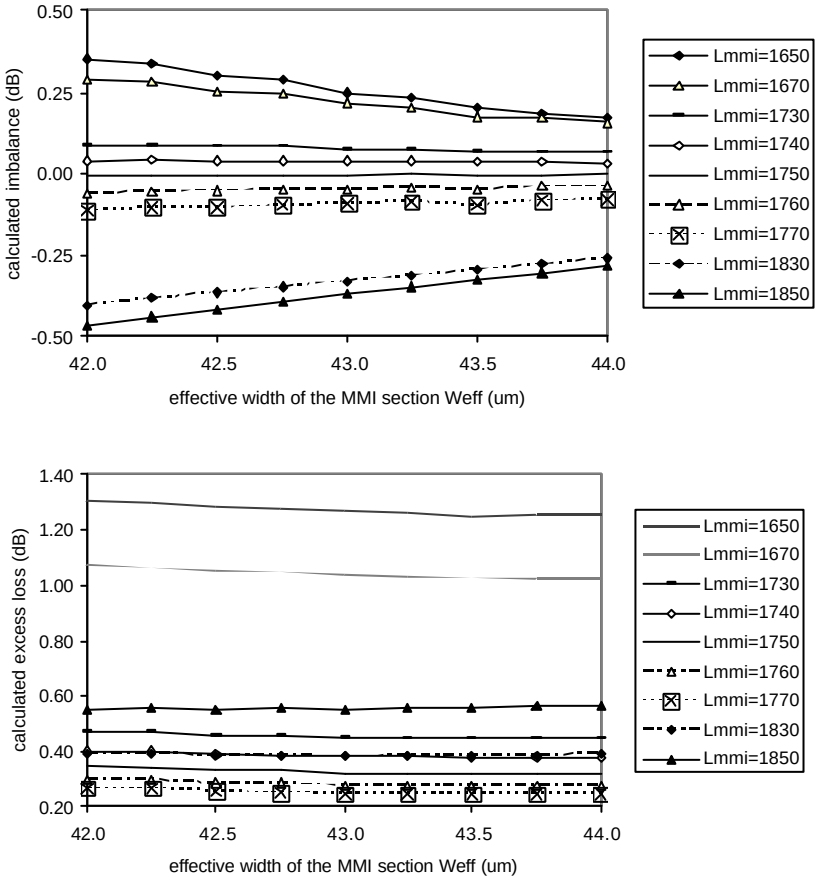

Figure 5.21. Calculated imbalance (top) and excess loss (bottom) of a MMI coupler when L_{mmi} and W_e are varied (changing W_e changes the position of the access waveguides). The coupler outputs are balanced when W_e=43 µm and L_{mmi}=1750 µm.

Figure 5.22 shows the imbalance of an MMI coupler versus a change of linewidth and refractive index difference. The refractive index difference was varied between low and high values that had been acquired in the process measurements i.e. between ±0.5 µm. The variation range of linewidth is based on process uniformity measurements. The extremums of Δn (0.007 and 0.009) are chosen based on process repeatability measurements (see table 12). Change of imbalance is below 0.2 dB. Figure 5.23 shows the excess loss of an MMI coupler versus a change of linewidth and refractive index difference. Simulation shows maximum excess loss of 0.25 dB. Maximum excess loss within process variations is 0.75 dB.

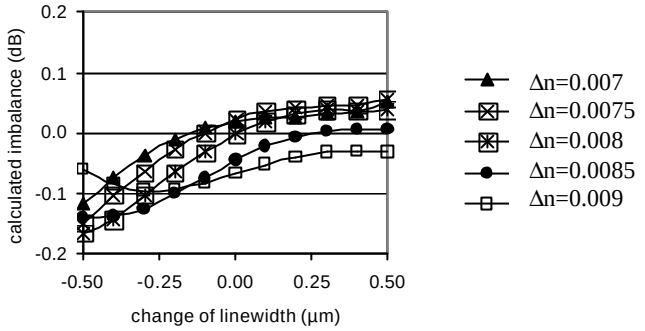

Figure 5.22. The imbalance of a MMI coupler versus a change of linewidth for different values of refractive index difference.

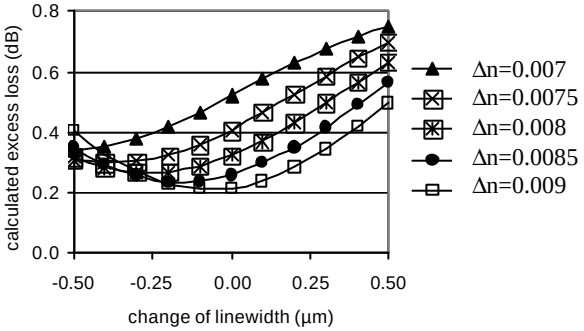

Figure 5.23. The excess loss of a MMI coupler versus a change of linewidth for different values of refractive index difference.

5.2.2 Design conclusions and summary

The comparison between the three 3-dB couplers is represented in table 5.9. Both DC and TMI couplers seem to be as sensitive to linewidth changes, with acceptable variation being 250 nm. The core thickness layer was also studied and it shows that 200 nm and 400 nm thickness variation is acceptable for DC and TMI couplers, respectively. The DC was found to be nearly 10 times more sensitive to changes in refractive index than TMI. Only the filling factor *B* was noticed to limit the TMI coupler with comparison to the DC. Overall the TMI coupler that was designed has lower sensitivity to the fabrication fluctuations than the DC. The refractive index must be controlled with an accuracy of $\pm 2.5 \times 10^{-4}$ to fabricate directional couplers with a good reproducibility.

With these limits the directional coupler was considered not to be a practical approach. Although the sensitivity of the directional coupler could be reduced by applying wider channels, this was not studied.

The problem with the TMI coupler is the narrow gap between the access waveguides. The TMI has a somewhat larger refractive index and thickness tolerance but the filling of the narrow Y-junction gap between the access waveguides can drastically change the coupling properties. A more advanced coupler design was adapted to improve the tolerance to variations in linewidth and refractive index changes. The MMI coupler's sensitivity to small process variations was found to be negligible. The MMI coupler was considered to offer the widest process window and was selected for the application. The imbalance specification of 0.5 dB is within fabrication tolerances with the MMI coupler. Table 5.10 summarizes the selected dimensions for the MMI coupler for the first process runs. The layout parameters were varied on a test mask to find experimentally the optimum dimensions. We chose to vary the length of the MMI section, and to keep width W constant. The nominal distance of the access waveguide was determined to be $\pm W_e/6$ from the center axis. To study the effect of the positioning of the access waveguides, the nominal value was varied ±1 µm in steps of 0.5 µm.

Table 5.9. Comparison of the sensitivity of the DC, TMI, and MMI couplers versus critical process parameters. For DC and TMI couplers imbalance is the critical parameter. Thickness variation of the core layer is limited by the single-mode condition for the TMI coupler. The lithographic resolution is the gap opening tolerance for the DC and MMI coupler, and for the TMI coupler it is the filling factor (B). The core height and gap opening are not considered critical parameters for MMI device.

Acceptable variation from nominal value:	**DC**	**TMI**	**MMI**
linewidth (µm)	± 0.25	± 0.25	± 0.5
core thickness H (µm)	± 0.2	± 0.4	not critical
refractive index difference Δn	$\pm 2.5\times10^{-4}$	$\pm 1.5\times10^{-3}$	$\pm 1.0\times10^{-3}$
lithographic resolution B (µm)	3.5	1.2	not critical

Table 5.10. The layout parameters for a 2×2 MMI coupler in mask I. The nominal values are the optimum values according to the simulation. The designed layouts on the mask were varied to find experimentally the optimum parameters. The length L was varied in steps of 2.5 % from the nominal value and the effective width was varied in steps of 0.5 µm.

	Nominal value	**Variation on mask**	**Step on mask**
W	41 µm	-	-
W_e	43 µm	± 1 µm	0.5 µm
L_{mmi}	1750 µm	± 350 µm	43.75 µm

The results presented are obtained from three masks, denoted as mask I, II and III. The manufacturing of the test structures was done applying mask I. The nominal dimensions were slightly adjusted in subsequent masks II and III. The beam combiner test devices were from mask II and mask III. Mask I contained MMI test structures, mask II had a layout for device #1. Mask III had a layout for device #2, #3 and #4.

Device size

In general it is advantageous to keep the device size small as homogeneity is better across the component. The footprint of a beam combiner with a binary tree configuration is determined by the minimum acceptable bending radius of a waveguide and the minimum pitch of the input/output fiber array (see table 5.11 and figure 5.24).

Table 5.11. The chip length (L_{tot}) and the corresponding optical path length (Δz) of an 8-port beam combiner with three couplers. The total chip length is given for different bending radius (R_{bend}) assuming a constant curvature bending. The fiber array pitch is assumed to be 0.25 mm. Each waveguide bend begins and ends with a 0.1 mm straight waveguide section to ensure a symmetric single mode field. The length and the width of a coupler are assumed to be 1.5 mm and 0.04 mm, respectively.

R_{bend} (mm)	**L_{tot} (mm)**	**Δz (mm)**
10	11.0	11.9
20	13.7	15.0
40	17.6	19.4

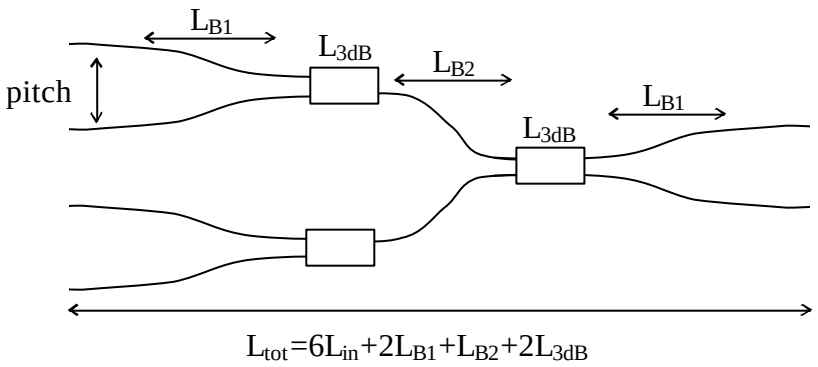

Figure 5.24. The chip length depends on the fiber array pitch and on the acceptable bending radius. A straight section of length L_{in} is added in the beginning and at the end of each bent waveguide section.

5.3 Manufacturing technology

The manufacturing of the test waveguide devices targeted at the optimisation of the waveguide losses and the 3-dB coupler. Low loss can be achieved by applying materials with low material absorption and by having smooth sidewalls. With silica-on-silicon structures a negligible substrate coupling must be guaranteed. This requires a thick under cladding layer to be deposited between the substrate and core layer. Low surface roughness and high birefringence were expected to provide decoupled polarization states to reach high PER [148]. The waveguide structure is based on silicon oxynitride layers deposited with a PECVD system (Surface Technology Systems plc, UK). The critical etching of the waveguide core was done with a plasma etcher (Lam Research, US). All processing took place at VTT Electronics clean room facilities (Espoo, Fi). The evolution of the manufacturing process during the project included a change from a thin substrate (525 µm) to a thick substrate (1.3 mm) [146]. The first waveguide processing was done on thin substrates and did not yield satisfactory results. The deposited films induced stress and caused large warping of the substrates. The selection of an appropriate masking material after many tests was another big step in the development of the fabrication process. A two layer masking process was selected for the core etching process. During the project several process schemes were studied to find a suitable fabrication process. The test devices and all test structures were fabricated according to the process flow shown in figure 5.25.

The process quality was controlled by running a test batch of 9 wafers through the buffer and core deposition steps. The formed slab waveguide structures were optically characterized by using a prism coupling set-up. In the measurement the thickness and refractive index of both the buffer and the core layers were evaluated. The used prism coupling equipment was known to have a resolution of 1×10^{-4} in refractive index and a resolution of 10 nm in thickness [149]. The used method was suitable for evaluating the process quality in terms of the repeatability (wafer-to-wafer) and the uniformity (on-wafer). Furthermore the process quality was studied with a SEM and optical microscope. With an optical microscope it was possible to check the guiding properties of the structure.

Refractive index and thickness calibration

The refractive index difference was calibrated by depositing test films and measuring the film characteristics with a prism coupling method. The calibration was done first for thin substrates before the wafer warping problem was detected. A new refractive index calibration was done for thick substrates. The difference between the thin and thick substrates is believed to be due to wafer doping as it was changed from N to P-type. Figure 5.26 shows the calibration curves to control the silicon oxynitride index with the silane flow. The refractive index changed linearly as a function of silane flow.

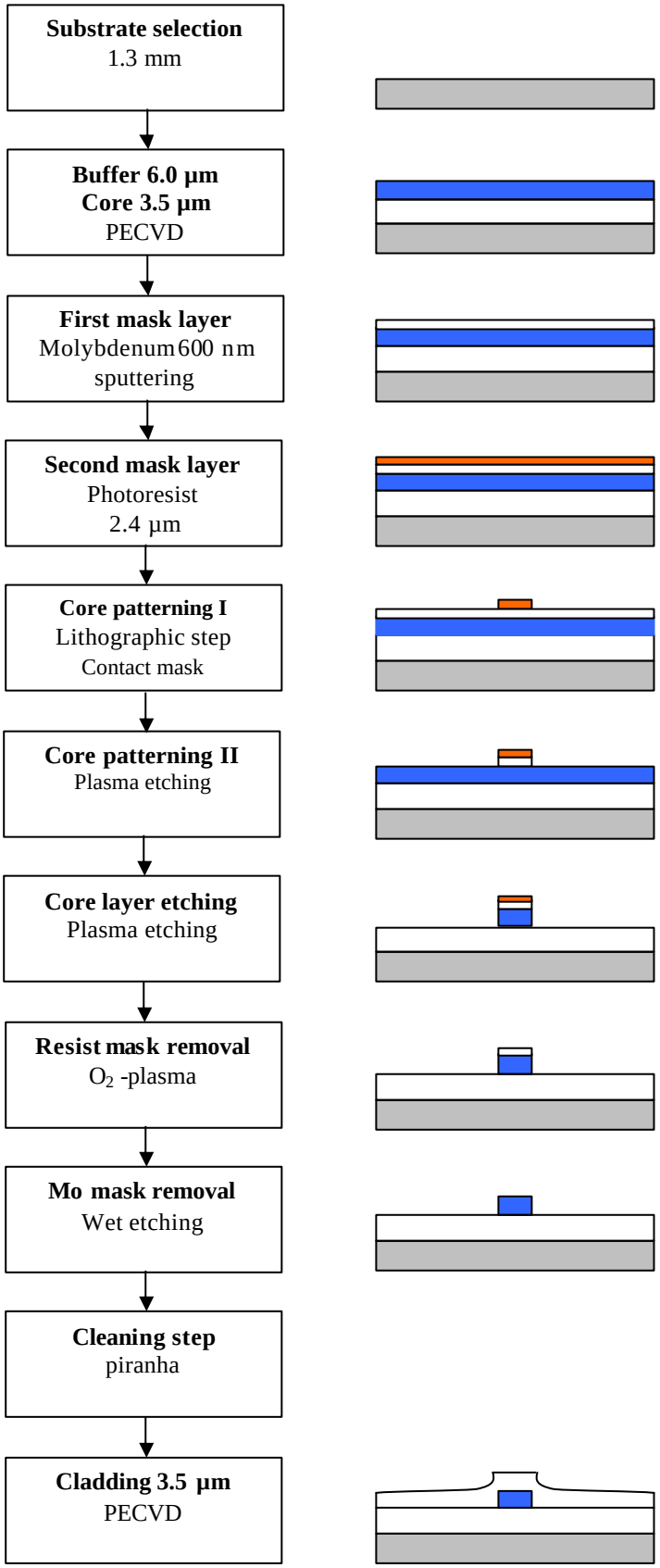

Figure 5.25. The process scheme used for fabricating the test devices, and illustration of forming of the waveguide structure. The main process steps are the deposition of the buffer and core layers with a PECVD, the mask layer deposition for etching the waveguide core, and the deposition of the cladding layer with the PECVD.

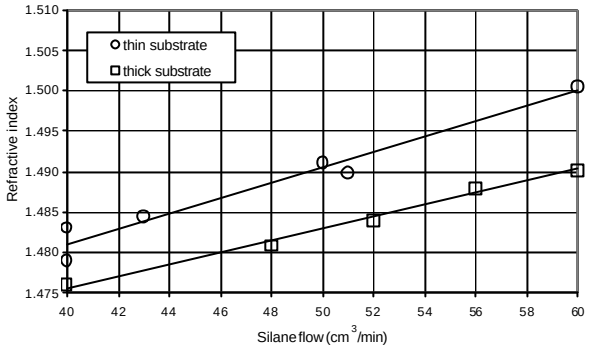

Figure 5.26. A calibration curve for SiO_xN_y. The refractive index is adjusted by controlling the silane flow. The calibration curve is shown for both thin and thick substrates.

Repeatability

Table 5.12 summarizes the results obtained from the nine (9) separately grown wafers. The test wafers had a double layer slab waveguide structure. The measurement point was in the center of the wafer. The refractive index variation of the buffer layer was measured to be 1.3×10^{-3}. The thickness variation of the buffer layer was 350 nm. The refractive index variation of the core layer was measured to be 2.2×10^{-3}. The thickness variation of the core layer was 400 nm. The refractive index difference (Δn) was measured to vary between 7.2×10^{-3} and 8.6×10^{-3}. The relative repeatability of the refractive index difference Δn was thus better than 10 %. The relative thickness repeatability was better than 6.3 % for the core, and better than 4.5 % for the buffer layer.

Table 5.12. The repeatability results from the test run of 9 wafers. The target was 6.0 µm for the buffer layer and 3.5 µm for the core layer with a refractive index difference of $\Delta n=8\times10^{-3}$. The values were measured from the center of each wafer. Average values and the standard deviation are shown for all parameters. The last column shows the variation in Δn.

Wafer	**Thickness (µm)**		**Refractive index***		
	core	**buffer**	**core**	**buffer**	Δn
#1	3.40	6.22	1.4897	1.4819	0.0079
#2	3.31	6.06	1.4902	1.4821	0.0081
#3	3.41	6.27	1.4897	1.4823	0.0074
#4	3.72	6.23	1.4901	1.4823	0.0078
#5	3.41	6.25	1.4918	1.4832	0.0086
#6	3.36	6.12	1.4896	1.4822	0.0074
#7	3.45	6.19	1.4897	1.4825	0.0072
#8	3.65	5.93	1.4896	1.4819	0.0077
#9	3.5	6.16	1.4906	1.4825	0.0081
Average	3.47	6.16	1.4901	1.4823	0.0078
std. dev.	0.13	0.11	0.0007	0.0004	0.0004
Max	3.72	6.27	1.4918	1.4832	0.0086
Min	3.31	5.93	1.4896	1.4819	0.0072

*) refractive index at the measurement wavelength of 633 nm.

Uniformity

One of the 9 wafers (#9) was further studied so as to observe the variation of refractive index and thickness of the deposited layers. The measured values are shown in figure 5.27. The refractive index variation of the buffer layer was measured to be 8×10^{-4}. The refractive index was seen to be lower on the edges of the wafer. The thickness variation of the buffer layer was measured to be <50 nm. The refractive index variation of the core layer was measured to be 1×10^{-3}. The refractive index of the core layer was also lower on the edges of the wafer. The thickness variation of the core layer was measured to be <40 nm. These values were considered to represent typical variations of the process (table 5.13). The refractive index difference thus typically changes by 2×10^{-4} across the wafer. This change was estimated to have a negligible effect on the optical performance.

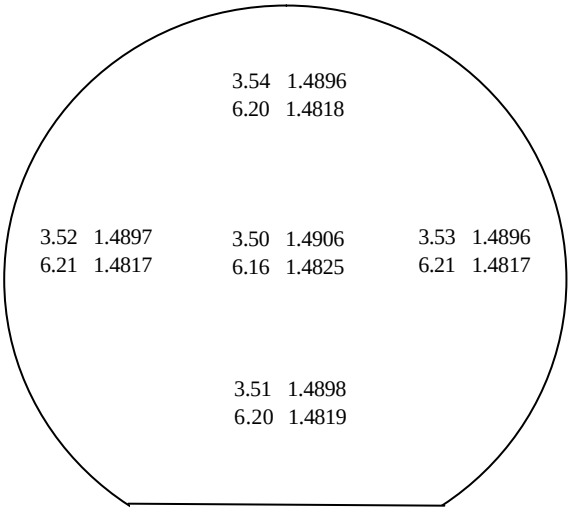

Figure 5.27. The on-wafer-uniformity of a double layer structure. The thickness and refractive index were measured with a prism coupling method from a 4" wafer. The target was 6.0 µm for the buffer layer and 3.4 µm for the core layer with a refractive index difference of 8×10^{-3}.

Table 5.13. Typical variation of the thickness and refractive index on a 4" wafer in absolute and relative units.

	Variation of thickness		**Variation of refractive index**	
	d*h* (nm)	d*h*/*h* (%)	d*n*	d*n*/*n* (%)
core layer	< 40	±1.2	1×10^{-3}	±0.07
buffer layer	< 50	±0.8	8×10^{-4}	±0.05

Fabricated waveguides

The waveguide structures were first studied with a scanning electron microscope (SEM) and optical microscope (see figure 5.28 and 5.29). The sidewall roughness was estimated to be <100 nm with the SEM (see figure 5.28). The change of linewidth was measured to be -1.0 µm compared to the linewidth on the mask (mask I), and later the linewidth change was -0.4 µm (applies to wafers manufactured with masks II and III). Variation in linewidth over the wafer was measured to be -250 nm. Figure 5.30 shows two samples from early process; one with good guiding properties (wafer #17) and

another sample (wafer #22) with abnormal optical performance. The non-guiding structure was considered to be due to a failure in the gas flow control during the core or top cladding deposition process.

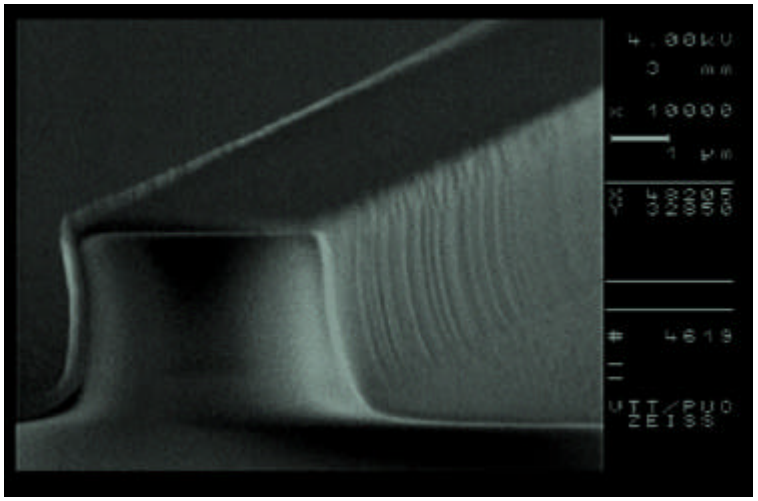

Figure 5.28. The etching quality of the fabricated waveguides. The vertical grooves were induced by the edge roughness of a molybdenum masking layer. Roughness was estimated to be smaller than 100 nm on the sidewalls. The sample was from wafer #20.

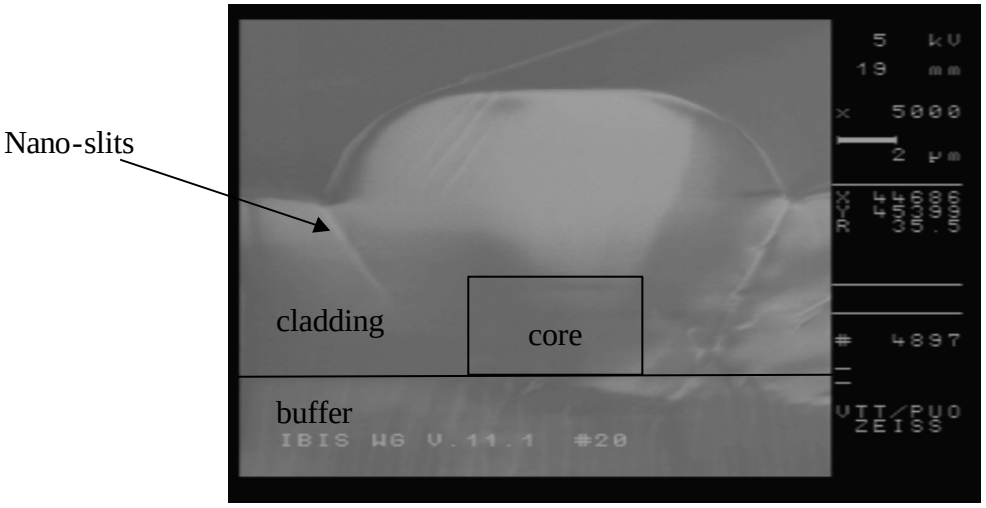

Figure 5.29. The facet of a waveguide revealed the step coverage quality and the nano-slit formation between the two growth planes next to the sidewall. The sample was from wafer #20.

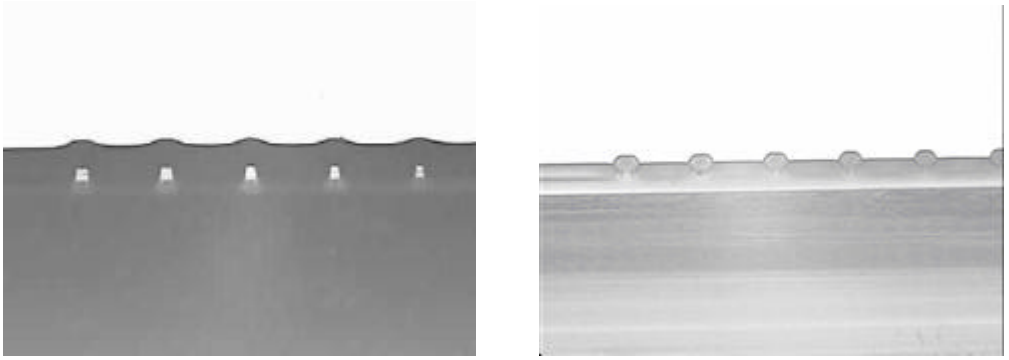

Figure 5.30. Photos taken with an optical microscope from the facet of cleaved samples when white light was coupled into the waveguide structure. Sample from wafer #17 (left) shows light coupled into the waveguides. The sample from wafer #22 (right) shows no guiding.

5.4 Results from chip measurements

Measurement set-up

The measurements at VTT were made using the set-up shown in figure 5.31. The light source was a 1064 nm diode pumped Nd:YAG laser (LCS-DTL-021, Power technology Inc., US). The degree of polarization of the laser output was higher than 1:100. The power was coupled to a PM-fiber pigtail with an objective lens, and a precision fiber rotator (MG 17 HFR 003, Melles-Griot, US) was used to align the fiber polarization axis with the polarization axis of the waveguide. An output polarizer (PL) was used to scan the minimum and maximum transmission to find the correct alignment of the PM-fiber. The output polarizer was used in estimation of PER. The measurement of the PER is not accurate with this set-up because the phase difference of the two fields (TE and TM) remains nearly constant. To evaluate the worst case PER, the temperature of the sample should be scanned [150]. The power measurement was made with a HP 8153A. For the spectral transmission measurements a spectrum analyzer was used (A6300, Ando, JP). In these measurements the laser source was replaced with a thermal source.

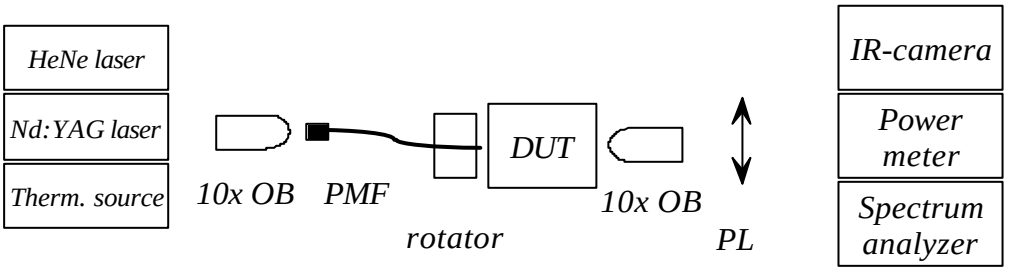

Figure 5.31. The measurement set-up used for the characterization of the samples. Three different light sources were used. A HeNe laser for alignment purposes, a Nd:YAG laser for measuring of device characteristics at 1064 nm wavelength, and a white light source to measure the spectral transmission characteristic of the MMI couplers. A precision rotator was used to align the polarization axis of the PM-fiber. The device under testing (DUT) was mounted on microcontrollers. The output from the DUT was coupled with a 10× lens through a polarizer to the power meter.

Straight waveguide properties

The waveguide propagation loss was measured using either a cut-back method or a two-phase method using a multi-mode fiber as a collecting fiber. In the cut-back method the propagation loss and the fiber coupling loss can be deduced by measuring the waveguide transmission for different lengths. In the two-phase method the waveguide transmission is measured both with a single mode and a multi mode output fiber. Then assuming that the multi mode fiber collects all the light from the waveguide end, the coupling loss between the waveguide and the single mode fiber and the propagation loss can be deduced.

The transmission measurement results are summarized in table 5.14 for different channel widths from 6 wafers. The samples were either ground and polished, or cleaved. The large variation in measurement results was due to the different quality of samples. The lowest propagation loss was 0.4 dB/cm. The best transmission were obtained with waveguide widths of 5.5 µm (wafer #17) and 6.0 µm (wafer #9 and #41). The fiber coupling loss was measured to be between 0.2 dB (wafer #41) and 0.5 dB (wafer #17). The polarization extinction ratio of a straight waveguide was measured to be above 23 dB. The PER measured for the input fiber and the set-up was 25±1 dB.

Table 5.14. The measured propagation loss values (in dB/cm) of six wafers. Results were obtained with a cut-back method. The results are average values of several samples. The propagation loss was measured with a two-phase method from wafers #17 and #41 before the cutback measurement.

	Channel width (µm)						
Wafer #	**3.0**	**3.5**	**4.0**	**4.5**	**5.0**	**5.5**	**6.0**
2	3.4	2.1	1.7	-	-	-	-
3	7.0	5.6	6.3	5.7	-	-	-
9	-	-	4.7	1.7	1.0	0.8	0.6
17[1]	-	-	-	0.6	0.6	0.4	-
17[2]	-	-	-	2.6	0.6	0.4	0.8
31[3]	5.3	2.5	1.2	0.8	0.8	0.7	1.0
41[1]	5.8	-	2.0	-	1.2	-	0.5
41[4]	6.3	-	3.0	-	1.6	-	0.8

1) 2-phase measurement
2) cut-back measurement
3) includes one fiber coupling loss.
4) cut-back measurement, average value from five samples

Waveguide crossing

Figure 5.32 shows a SEM picture of a waveguide crossing before the cladding layer deposition. The excess loss and degradation of PER were studied with test structures shown in figure 5.33. A large number of dummy crossings intersected a waveguide, whose transmission was measured as a function of intersecting crossings. The transmission measurement was taken by using a cut-back method. Three different lengths of the waveguide were measured and each intercepted waveguide transmission was subtracted from transmission of a reference waveguide. Each length contained a different number of crossings. Table 5.15 represents the measured results from one set of samples. The results from two other samples (Wafer #17) showed the same magnitude for excess loss (figure 5.34). The waveguide crossing had an average cross talk of -24 dB (TM polarization) and -22 dB (TE polarization).

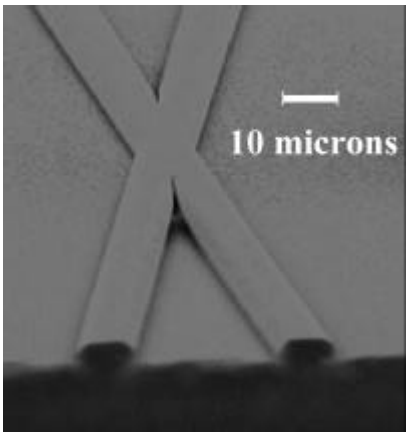

Figure 5.32. SEM picture of a waveguide crossing with a crossing angle of 20° prior to the cladding layer deposition. The core ridges are well defined and no gap filling can be seen in the Y-junction between the waveguides.

Figure 5.33. Schematic representation of the test layout for measuring the excess loss, and degradation of the PER due to a waveguide crossing at different angles. The test waveguide had 60 dummy crossings. Transmission of the intersected waveguide was referenced to a continuous waveguide along side it.

Table 5.15. Measured effect of waveguide crossings on loss and PER. Sample from wafer #02, waveguide width was 3.5 μm. The measured PER for the reference waveguide was 24 dB. PER of 25±1 dB was measured for the set-up without a waveguide sample.

Crossing angle (deg)	**20**	**40**	**60**	**80**
Excess loss (dB)	0.44	0.33	0.15	0.02
Change of PER (dB)	-0.18	-0.17	-0.02	-

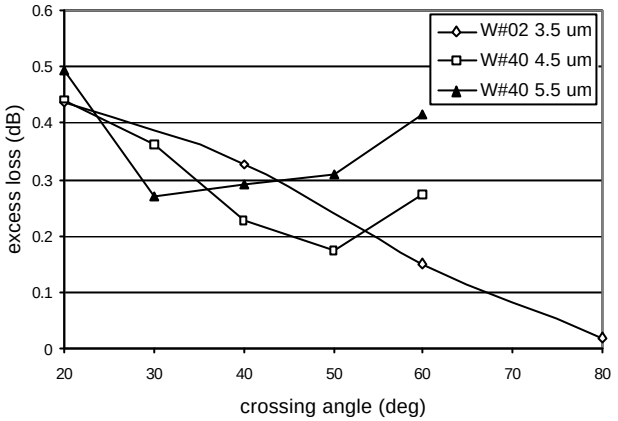

Figure 5.34. The measured excess loss as function of the crossing angle. The width of the sample waveguide was 3.5, 4.5, and 5.5 μm, samples were from wafers #2 and #40. The results from sample W#2 were obtained with a cutback method (this involved cutting the sample two times and taking three measurements). The result from sample W#40 is an average of three channels obtained with a 2-phase method.

S-bends

An S-bend with a radius of 10 mm incurred an excess loss of 7.7 dB/90° when compared to an S-bend with a radius of 20 mm (width 3.5 μm). Constant curvature S-bends with a radius of 20 mm were used in MMI structures on mask I and III. In mask II (device #1) the S-bend radius was 10 mm.

MMI couplers

The optimum length for the MMI coupler was determined experimentally. Figure 5.35 shows a typical measured imbalance versus the MMI length (L_{mmi}). The coupler was nearly balanced close to the center length (L_C) that was selected based on simulation. The bending radius of the access waveguides was 20 mm. Sample with a relative length of 0.9 (L_{mmi}=1579 μm) had imbalance below 0.3 dB and excess loss of 3.8 dB

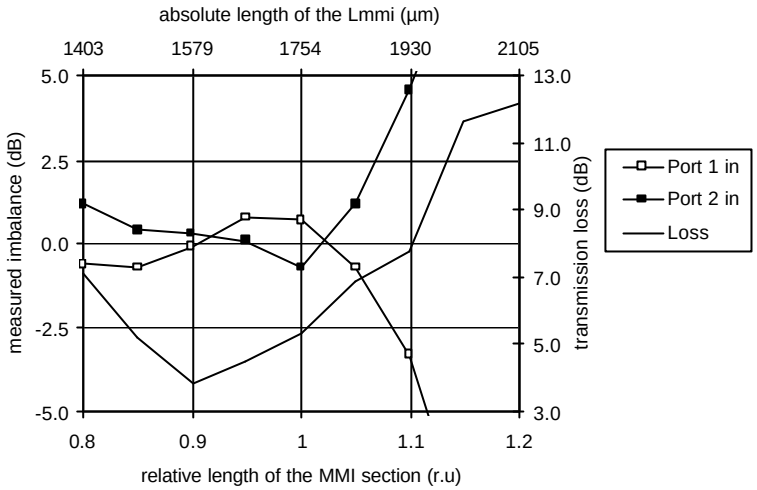

Figure 5.35. The measured imbalance (for both input ports) and average transmission loss of the 2×2 MMI coupler as a function of the MMI length (mask I). The relative length 1 is equal to 1754 µm. The width of the MMI (W_{mmi}) was 40 µm. The layout parameters dimensions of the coupler were W_e=42.5 µm, W_T=10 µm and R_B=20 mm. The length of the chip was 28 mm.

Mask II: Device #1

The length (L_{mmi}), effective width (W_e), and the tapering width of the MMI layout were varied on mask II for device #1. The length was varied ±20 % from the center length L_C=1714 µm. The effective width (W_e) was varied from 42 to 44 µm. The tapering width was either 0 (no taper) or 6 µm. The width of the access waveguide was 6.0 µm. The bending radius of the access waveguides was 10 mm. Figure 5.36 and 5.37 show the measured imbalance and transmission loss of the coupler versus the layout parameters. The measured imbalance and transmission loss of the sample P43 was 2.2 dB and 1.8 dB, respectively. The relative length of the coupler P43 was 0.9 (L_{mmi} =1714 µm). The effective width was 43 µm and the tapering width was 10 µm. The dimensions of the coupler P43 were chosen for device #1.

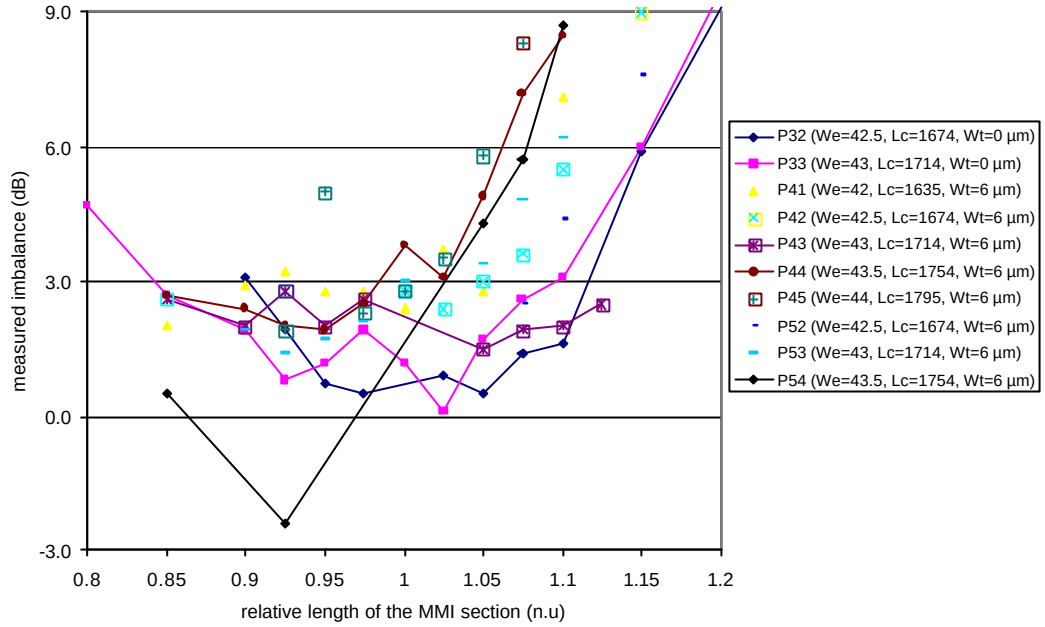

Figure 5.36. The measured imbalance of 2×2 MMI coupler as a function of the MMI length (Mask II). The relative length 1 is equal to L_C given in the legend. The effective width was varied from 42 µm to 44 µm. The chip length was 19 mm.

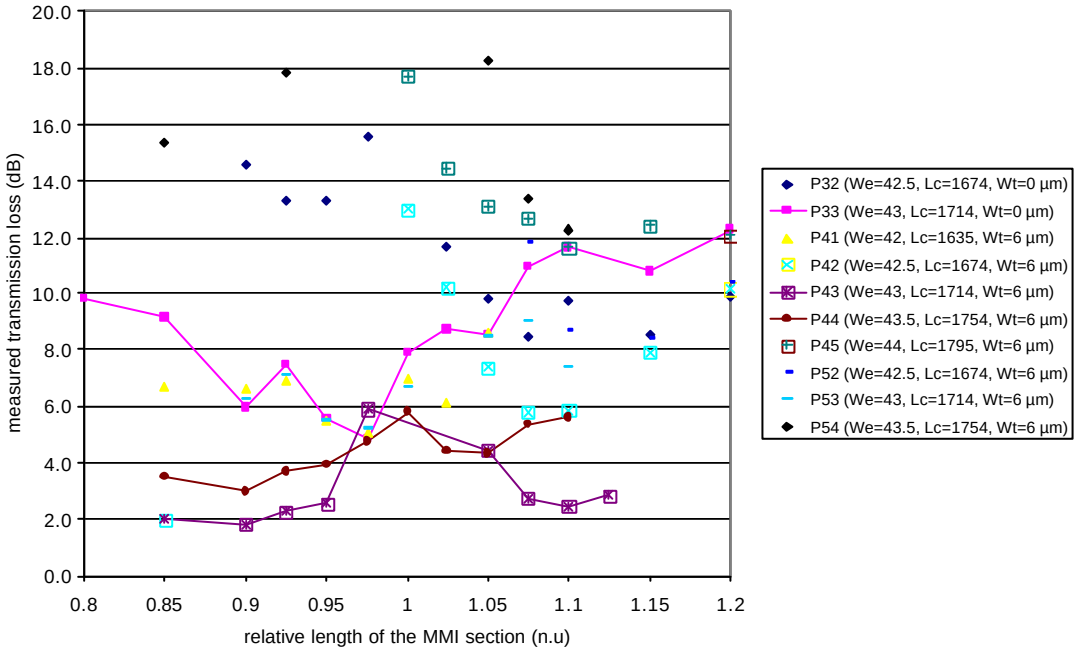

Figure 5.37. The measured transmission loss of a 2×2 MMI coupler as a function of the MMI length (Mask II). The inherent 3 dB loss of the coupler was subtracted from the transmission loss value. The relative length 1 is equal to L_C in the legend. The effective width was varied from 42 µm to 44 µm. The chip length was 19 mm.

Mask III: Device #2, #3 and #4

The layout parameters of the MMI coupler were varied on mask III to experimentally find optimum parameters. Minor changes were made from mask II. The bending radius of the access waveguides was changed back to 20 mm as in mask I. The length was varied ±10 % from the center length L_C=1714 µm. The effective width (W_e) was varied from 42 to 44 µm. The tapering width was either 0 (no taper) or 6 µm. The width of the access waveguide was 5.5 µm. Figure 5.38 and 5.39 show the measured imbalance and transmission loss of the best coupler series (P32) versus the layout parameters. A coupler with the effective width of 44 µm was chosen for devices #2, #3 and #4. The measured imbalance and transmission loss of the chosen coupler was 0.3 dB and 4.3 dB, respectively. The relative length of the chosen coupler was 0.9 (L_{mmi} =1543 µm).

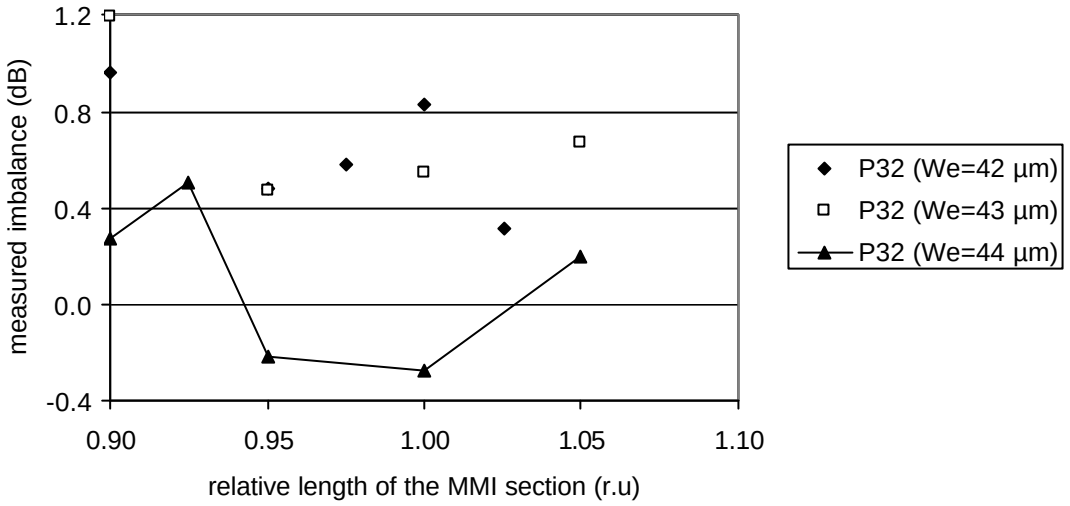

Figure 5.38. The measured imbalance of the 2×2 MMI coupler versus the MMI length and the effective width W_e (Mask III, sample P32). The relative length 1 is equal to 1714 µm.

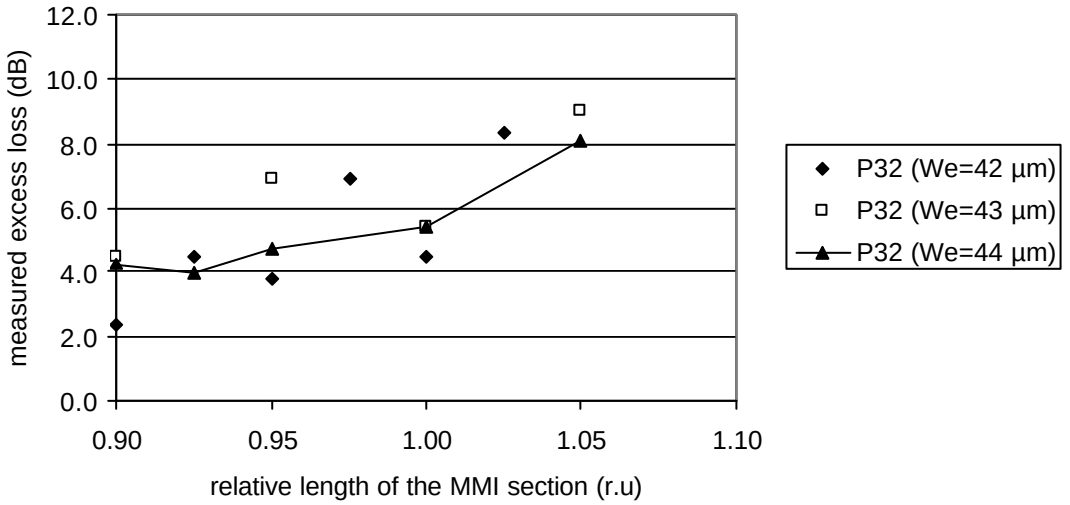

Figure 5.39. The measured transmission loss of the 2×2 MMI coupler versus the MMI length and the effective width W_e (Mask III, sample P32). The relative length 1 is equal to 1714 µm.

Spectral response of the MMI coupler

The MMI coupler's wavelength dependence was studied by measuring the spectral transmission with a spectrum analyzer. Polarized light was coupled to the input fiber of the device from a white light source. Figure 5.40 shows the spectral transmission through a 2×2 MMI coupler in device #4. The power transmission of the device was measured to vary from 19% to 31% depending on the input port. The MMI coupler was measured through the better port to improve the signal-to-noise ratio. Figure 5.41 shows the measured imbalance of device #4.

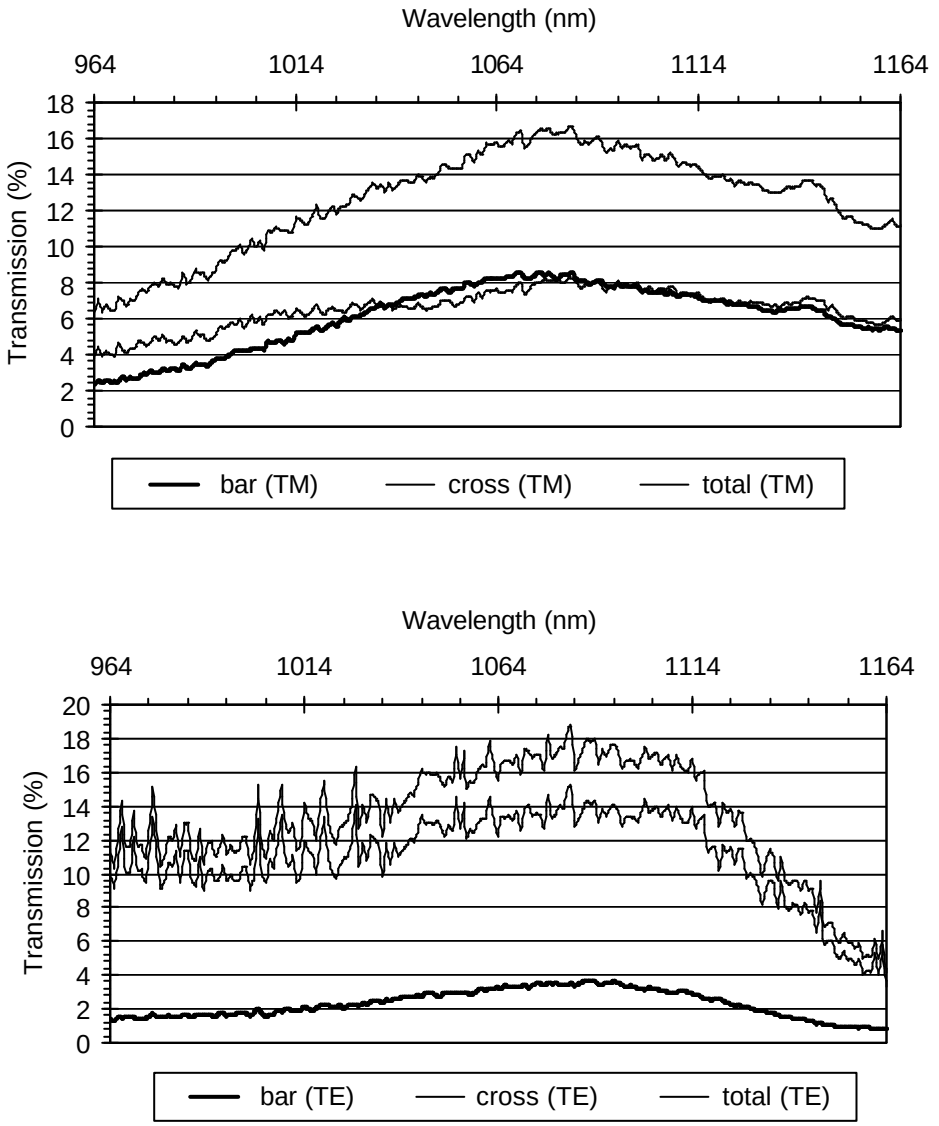

Figure 5.40. Measured transmission of the pigtailed 2×2 MMI coupler of device #4 on TM (upper graph) and TE (lower graph) polarizations. (The transmission curve with the highest power is the sum of the bar and cross port powers in both graphs).

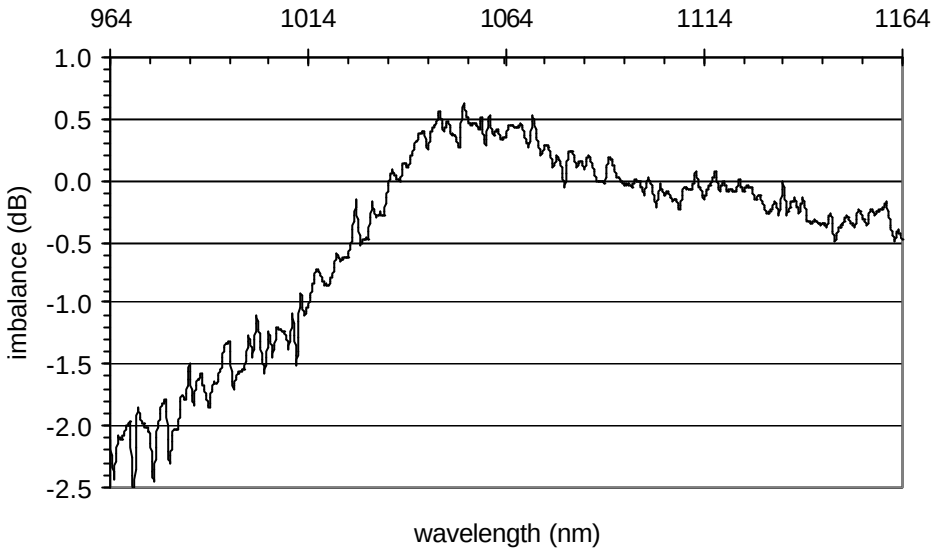

Figure 5.41. Measured imbalance as a function of wavelength (for TM polarization, device #4). Imbalance is the ratio of the bar and cross port transmissions shown in figure 5.40.

MMI couplers as power splitter

Device #4 was tested before the fiber attachment. The three cascaded 2×2 couplers form a 1×4 power splitter if the device is operated in the reverse direction (see figure 5.4). The device output was recorded with a IR-camera (see figure 5.42). The output transmissions were measured by coupling a multimode fiber to each output. The measured flatness was better than 1.6 dB. Measured excess loss was 9.1 dB.

Figure 5.42. The output of the 1×4 power splitter recorded with an IR camera.

5.5 Fiber attachment

Three devices were pigtailed by applying a passive alignment, and one device was pigtailed by actively aligning each fiber. Table 5.16 lists the different approaches.

Table 5.16. The pigtailing procedures used with the test devices.

Device #	number of ports	pigtailing procedure	pigtailing done at
1	8	passive V-groove	VTT/Optonex Oy
2	8	passive V-groove	Opto Speed SA (Ch)
3	12	passive V-groove	Opto Speed SA (Ch)
4	8	active U-groove	VTT

The first device was pigtailed at VTT Electronics by applying V-groove fiber blocks (Optonex Oy, Fi). The fiber array was based on separate silicon V-groove chips. The PM-fibers were aligned, mounted and attached to the V-groove chip with slowly curing glue. Figure 5.43 shows a microscope image of the fiber array. Fibers cores were illuminated with white light. The microscope image shows that the rightmost fiber had been displaced in a vertical direction. Figure 5.44 shows the same block with changed illumination revealing angular misalignment. Because fibers seem to be misaligned in the same direction it was reason to believe that the polarizer used in maximum-minimum search was slightly misaligned. The second and third device was pigtailed in a similar technique (Optospeed S.A., Ch). The fourth device was again pigtailed at VTT Electronics by applying silicon U-grooves and active alignment.

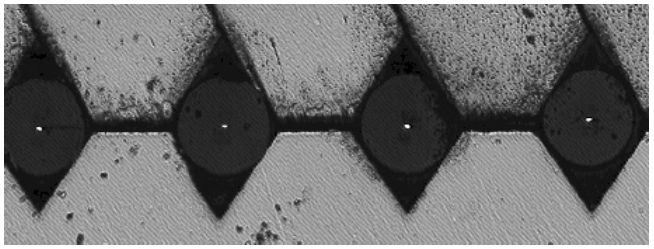

Figure 5.43. Microscope photograph of a fiber V-groove block used with device #1.

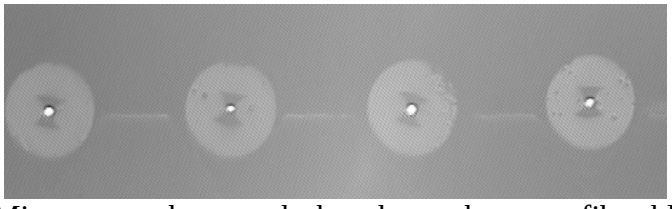

Figure 5.44. Microscope photograph that shows the same fiber block as in figure 5.43. The orientation error is clearly visible from the stress members.

PM-Fiber properties

After the first results from the passive fiber attachment with V-grooves, the fiber geometry was measured to understand better the limitations set by the fiber tolerances (measurement done at Nextrom Oy, Fi). The measurements were done with a high resolution camera system that could extract the cladding diameter, cladding non-circularity and core eccentricity. The results are shown in table 5.17. The cladding non-circularity and the core eccentricity were 0.9% and >1.1 µm, respectively. The cladding

diameter varied between ±0.5 µm. The measured values differ slightly from the fiber specifications, but not remarkably.

Table 5.17. The PM-fiber dimensions were measured to assess the specifications. (HB1000, Fibercore Inc. batch: YD 557-05A).

Geometrical parameter	**Average**	**Min**	**Max**
Cladding diameter (µm)	123.3	123.03	123.81
Cladding non-circularity (%)	0.92	0.90	0.93
Core eccentricity (µm)	1.14	1.10	1.19

U-groove technique

An active alignment procedure was introduced where each input fiber was separately aligned and attached to a waveguide chip. Figure 5.45 shows a schematic cross section of the pigtailed device and figure 5.46 schematically shows the fiber mounting on the U-groove block. A common glass substrate was used to align and attach the U-groove blocks to the waveguide chip. For this approach a silicon U-groove block was designed and processed for the last 8-port (device #4). The fabrication of the U-groove is depicted in figure 5.47. The deep silicon grooves were processed with reactive ion etching. The U-groove dimensions are: groove width 140 µm, pitch 250 µm and depth 150 µm. Before mounting the fibres, the U-groove block was attached to the waveguide chip. The alignment of the groove chip to the waveguide chip was done under a microscope (figure 5.48). The fiber attachment procedure is shown in figure 5.49. UV-curable glue was used for fixing the fiber to the U-groove block. A glue with low viscosity and low shrinkage (<1%) was selected for this (OG198-50, Epoxy Technology Inc., US). Fixing with UV glue offers good stability during curing. The degradation of transmission during the curing was measured to be < 0.5 dB.

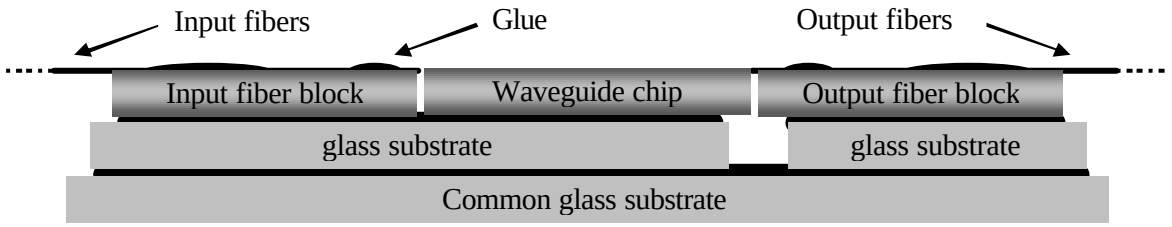

Figure 5.45. A schematic longitudinal cross-section of the hybridization of waveguide chip and U-groove chips on common glass substrate. The thin gaps between the two chips and the three substrates have been partly filled with glue. The thickness of the glass substrate thickness is 1.0 mm. The chip size is 10×15 mm^2 and the fiber blocks are 10×15 mm^2.

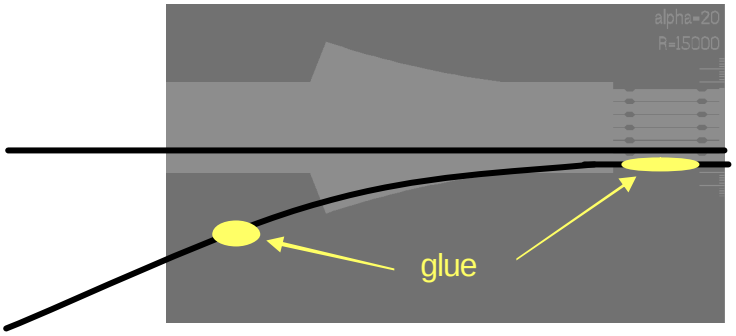

Figure 5.46. A schematic top view of a U-groove block used as a platform for the fiber mounting. The fiber was first attached close to a waveguide chip, next the fiber was turned apart and secured with glue to have space to align the next fiber. The waveguide chip (not shown) is on the right side of the fiber block.

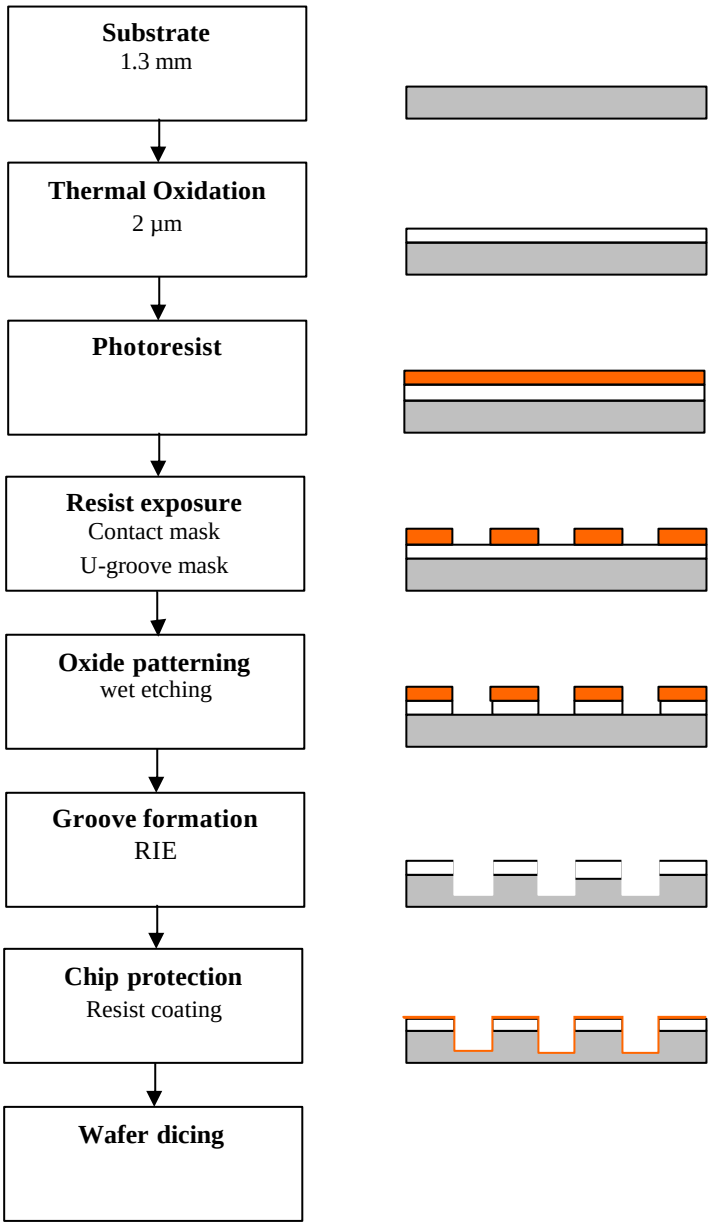

Figure 5.47. Steps to fabricate silicon support chips used in the active fiber attachment.

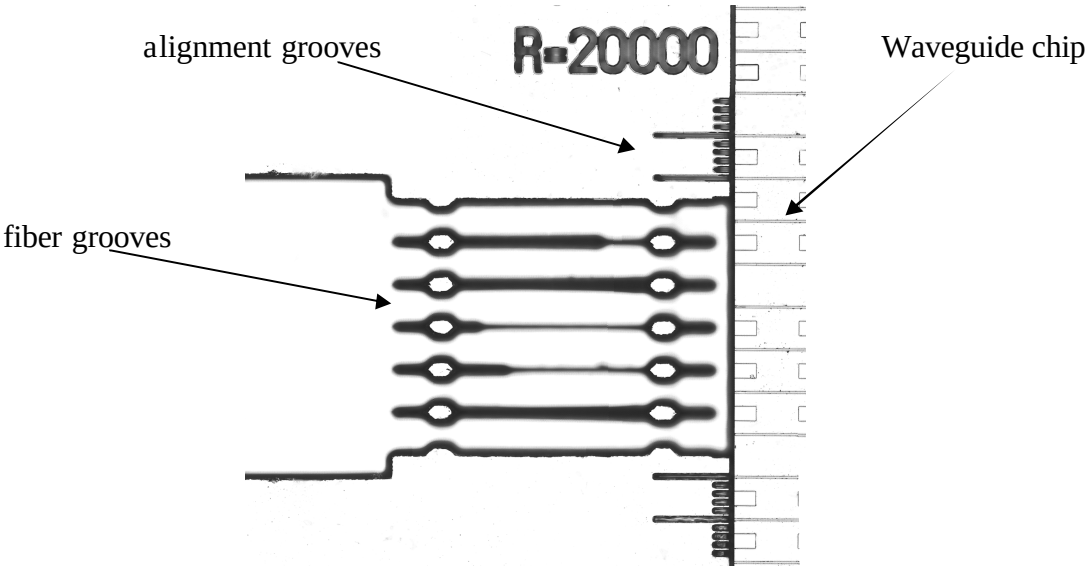

Figure 5.48. An optical microscope picture showing the U-groove block (left side) aligned and attached to the beam combiner chip (on the right). The separation of the waveguides was 250 µm. The depth of a fiber groove was 100 µm. The narrow grooves on the U-groove chip were used as alignment marks.

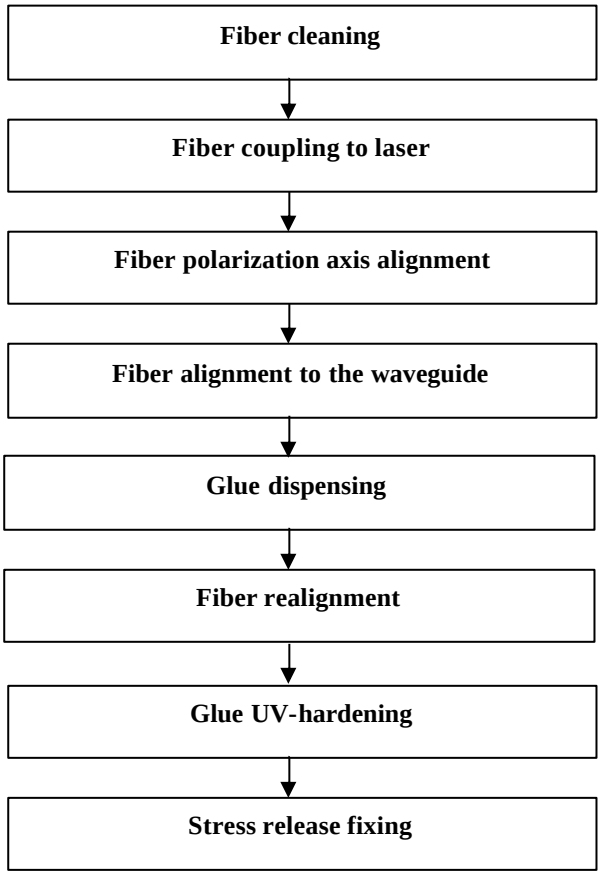

Figure 5.49. The fiber attachment procedure. Each fiber was attached separately. First the fiber polarization axis was aligned next the fiber was aligned to the waveguide. After dispensing glue a re-alignment was necessary, and after the re-alignment the fiber was fixed by hardening the glue with UV exposure.

5.6 Results from fiber attachment

Table 5.18 represents the pigtailing results from the four fabricated devices. The maximum excess loss per interface and average excess loss are compared. The results from the three first devices show that a passive method is not feasible unless waveguide-fiber coupling tolerance can be increased. Device #3 had an average excess loss of 2.6 dB for the best 7 ports, while two of the ports had an excess loss >20 dB. The average excess loss/interface for device #4 was 1.0 dB.

Table 5.18. Excess loss due to the fiber attachment. Maximum excess loss is the worst value measured, except for device #4, which had one broken fiber with excess loss of 68 dB.

device #	**number of ports**	**max excess loss / interface (dB)**	**average excess loss / interface (dB)**
1	8	37.6	8.5
2	8	12.2	2.3
3	12	24.8	4.7 (best 7 ports give 2.6)
4	8	3.2	1.0

5.7 Optical performance

In the following the main results are summed up and compared against the design goals. Tables 5.19-5.31 represent results of the internal coupling ratio of the 2×2 MMI coupler, coupling ratio after pigtailing, maximum excess loss and worst case polarization extinction ratio, and compare them with the design goals. The devices were characterized before and after the fiber attachment. The final characterization was done also at TUV and complementary results obtained at TUV are marked. The performance of the devices is divided into bare chip and pigtailed device characteristics. The following definitions are used to describe the device and coupler performance:

Internal coupling ratio, neglects the effects from the input/output waveguides and fiber pigtails connected to the coupler.

Coupling ratio pigtailed, includes the effects from the input/output waveguides and fiber pigtails connected to the coupler.

Device #1:

Table 5.19 shows the insertion loss before fiber pigtailing of the chip. Excess loss of the coupler was measured to be 2.2 dB.

Table 5.20 shows the insertion loss of device #1 (chip pigtailed). The results show that the fiber pigtailing causes an additional excess loss of 10 to 20 dB. Table 5.21 summarizes the main results. The PER varied between 1.6 dB and 31 dB, depending on the measurement port. The measured internal coupling ratio was 37:63 or 2.5 dB (see table 5.22). The measured return loss was higher than 29 dB at all input ports.

Table 5.19. The insertion loss before fiber pigtailing (chip measured in reversed direction).

	I1	**I2**	**I3**	**I4**
O1	6.4	4.2	-	-
O2	11.0	13.4	11.4	8.5
O3	7.6	10.1	12.4	9.7
O4	-	-	6.3	4.3

Table 5.20. The insertion loss and PER (in parenthesis) for fiber pigtailed device #1. The insertion loss between ports I2-O4 and I3-O1 should be infinite.

	I1	**I2**	**I3**	**I4**
O1	14.3 (11.0)	19.7 (17.3)	54.6	-
O2	37.9 (7.0)	24.9 (24.1)	15.8 (10.3)	31.5 (3.2)
O3	45.2 (5.6)	24.9 (7.2)	15.8 (24.3)	30.7 (31)
O4	-	56.3	18.5 (7.1)	24.8 (3.2)

Table 5.21. Summary of the results for device #1.

device #1	**target value**	**results : (best / worst)**
Coupling ratio pigtailed	within 47:53	25:75 / -
Max. excess loss (dB)	0.3	15.8 / >45
Worst case PER (dB)	20	31 / 1.6 +

+ result obtained from TUV after final characterization of the device.

Table 5.22. The measured coupler performance of device #1. The coupler imbalance was equal to 2.5 dB (see figure 5.2 for explanation of A,B and C). Results were obtained from the pigtailed device measurements.

Coupler	**Internal coupling ratio**
A	37:63
B	36:64
C	37:63

Device #2:

Device #2 (an 8-port, one 3-dB coupler and two straight waveguides) and device #3 (a 12-port, three cascaded 3-dB couplers forming a binary tree and two crossing waveguides), were subsequently manufactured. The insertion loss of the chip before fiber pigtailing is represented in table 5.23. The internal coupling ratio was measured to be 49:51. Excess loss of the coupler was 4.9 dB.

Table 5.24 shows the insertion loss of device #2 (chip pigtailed). Results for device #2 are summarized in table 5.25. The insertion loss of the pigtailed straight waveguides was 3.6 dB and 5.2 dB. The PER of the pigtailed straight waveguide was 12.4 dB and 18.7 dB. The excess loss of the pigtailed coupler was between 4.4 dB and 17.5 dB. The PER of the pigtailed coupler was between 0.7 and 11.2 dB, depending on the measurement port. The power splitting ratio of the pigtailed coupler in the nominal direction of operation was better than 44:56.

Table 5.23. The insertion loss before fiber pigtailing. The ports numbered 1-2 are of the straight waveguide and ports 3-4 are the ports of the 2×2 MMI coupler.

	I1	**I2**	**I3**	**I4**
O1	3.8	-	-	-
O2	-	2.5	-	-
O3	-	-	6.7	7.0
O4	-	-	6.9	7.5

Table 5.24. Insertion loss and PER (in parenthesis) for device #2. The ports numbered 1-2 are the ports of the straight waveguide, and ports 3-4 are the ports of the 2×2 MMI coupler.

	I1	**I2**	**I3**	**I4**
O1	3.6 (12.4)		-	-
O2	-	5.2 (18.7)	-	-
O3	-	-	7.4 (11.2)	16.8 (1.8)
O4	-	-	7.4 (7.9)	17.4 (0.7)

Table 5.25. Summary of the results for device #2.

device #2	**target value**	**results (best /worst)**
Coupling ratio pigtailed	within 47:53	50:50 / *
Max. excess loss (dB)	1.3	4.4 / 17.5
Worst case PER (dB)	15	18.7 / 0.7 +

* indicates balance worse than 10:90
+ result obtained from TUV after final characterization of the device.

Device #3:

The insertion loss of the chip before fiber pigtailing is represented in table 5.26. The insertion loss of the straight waveguide was 4.7 dB. The crosstalk attenuation of the crossing was higher than 28 dB. Average insertion loss through a single coupler was 9.1 dB and through two couplers average insertion loss was 14 dB. Maximum excess loss of the coupler tree was 7.2 dB (target value was 2.3 dB). Worst case PER was 17 dB (target value was 15 dB). The measured internal coupling ratio was 48:52.

The insertion loss of device #3 is represented in table 5.27. The insertion loss of the pigtailed waveguide crossing was 8.1 dB and 18.5 dB. The worst-case PER of the pigtailed crossing waveguides was 11.7 dB and 12.2 dB. The worst-case PER of the pigtailed coupler tree was between 10.1 and 14.5 dB. Results of the beam combiner device #3 are summarized in table 5.28.

Table 5.26. Insertion loss of the chip for device #3. The ports numbered 1-2 are the ports of the waveguide crossing and ports 3-6 are the ports of the 2×2 coupler tree.

	I1	**I2**	**I3**	**I4**	**I5**	**I6**
O1	28.5	4.7	-	-	-	-
O2	4.7	28.4	-	-	-	-
O3	-	-	9.1	9.1	-	-
O4	-	-	14.1	13.6	13.6	14.5
O5	-	-	14.2	13.9	13.4	14.5
O6	-	-	-	-	9.0	9.2

Table 5.27. Insertion loss and PER (in parenthesis) of device #3. The ports numbered 1-2 are the ports of the waveguide crossing and ports 3-6 are the ports of the 2×2 coupler tree.

	I1	**I2**	**I3**	**I4**	**I5**	**I6**
O1	42.5	18.5 (12.2)	-	-	-	-
O2	8.1 (11.7)	32.4	-	-	-	-
O3	-	-	13.3 (13.6)	12.6 (13.2)	-	-
O4	-	-	38.9 (11.8)	37.7 (13.4)	39.0 (10.1)	36.7 (10.8)
O5	-	-	15.8 (10.5)	14.6 (11.3)	15.6 (13.5)	14.0 (11.5)
O6	-	-	-	-	12.3 (14.5)	10.5 (14.5)

Table 5.28. Summary of the results for device #3.

device #3	**target value**	**results (best /worst)**
Coupling ratio pigtailed	within 47:53	47:53 / *
Max. excess loss (dB)	2.3	8.0 / 33.7
Worst case PER (dB)	15	14.5 / 10.1 +

* indicates balance worse than 10:90, + result obtained from TUV after final characterization of the device.

Device #4:

Device #4 was developed in order to improve the manufacturing process, especially the technique used to attach PM-fiber pigtails to the integrated optical chip. The fourth component was manufactured using an active fiber alignment procedure. The layout of this device was the same as that of device #2.

The insertion loss of the chip for device #4 is represented in table 5.29. The insertion loss of the straight waveguide was 2.0 dB. The internal coupling ratio was better than 0.4 dB. Maximum excess loss of the coupler was 4.5 dB. The measured worst case PER for the chip was above 20 dB.

Table 5.30 shows the insertion loss of device #4 (chip pigtailed). The insertion loss of the pigtailed straight waveguides was 68.0 dB and 4.2 dB. The PER of the pigtailed straight waveguide was 8.1 dB. The excess loss of the pigtailed coupler was between 5.1 dB and 7.3 dB. The PER of the pigtailed coupler was between 11 dB and 18 dB, depending on the measurement port. The power splitting ratio of the pigtailed coupler in the nominal direction of operation was better than 44:56. Results for device #4 are summarized in table 5.31.

Table 5.29. Insertion loss of the chip for device #4. The ports numbered 1-2 are the ports of the straight waveguide and ports 3-4 are the ports of the 2×2 coupler tree.

	I1	**I2**	**I3**	**I4**
O1	2.0	-	-	-
O2	-	1.9	-	-
O3	-	-	7.4	7.3
O4	-	-	7.6	7.2

Table 5.30. Insertion loss and PER (in parenthesis) of device #4. The ports numbered 1-2 are the ports of the straight waveguide and ports 3-4 are the ports of the 2×2 coupler tree. The fiber connected to port I1 was found to be broken explaining thus the high loss.

	I1	**I2**	**I3**	**I4**
O1	68.0	-	-	-
O2	-	4.2 (8.1)	-	-
O3	-	-	9.2 (16.7)	10.3 (9.3)
O4	-	-	8.1 (9.3)	8.6 (9.7)

Table 5.31. Results for device #4.

device #4	**target value**	**results : (best / worst)**
Coupling ratio pigtailed	Within 47:53	47:53 / 40:60
Max. excess loss (dB)	2.3 dB	5.1 / 7.3
Worst case PER (dB)	15 dB	18 / 11 +

+ result obtained from TUV after final characterization of the device.

5.8 Conclusions

Silicon oxynitride planar optical circuits have been designed and fabricated in this work. Optical beam combiner test devices and related test structures have been manufactured to show the feasibility of the technology in the novel application area of coherent communications. The four manufactured devices were milestones prior to the manufacturing of the complex 32-port beam combiner device. A 2×2 MMI device has been developed for 1064 nm wavelength to function as a 3-dB coupler. The 2×2 MMI 3-dB couplers have been shown to have good balance with the available manufacturing facilities. The waveguide propagation losses have been measured to be 0.4 - 0.6 dB/cm. This is not an acceptable level for more complex structures with higher port counts such as with the case of a 16×16 beam combiner. Waveguide bends with a bending radius of 10 and 20 mm were used in test devices. The excess loss of the test devices was assumed to have its origin in bent waveguide sections. A possible reason for this was the cladding quality. A porous cladding and voids formed on the sidewalls of the waveguides were considered to modify the guiding properties of the channel. Especially the bent waveguide sections were considered to be sensitive to these effects.

Transmission results of device #4 verified that the 3-dB coupler was balanced at wavelength of 1180 nm. More accurate optimization would be needed to adjust the slight deviation from the intended central wavelength of 1064 nm. With TM polarization the bar and cross state are in balance but TE shows imbalance of about 9 dB i.e. the coupler was nearly in a cross state. As explained the correct coupling length was chosen by measuring a series of couplers of varied length. Uncertainty of these measurements and the small variations in the fabrication process inevitably led to a small shift from the central wavelength. The MMI coupler maintains an acceptable 3-dB coupling window over 50 nm wavelength span. This result shows that the MMI coupler is suitable for systems applying multiple closely spaced wavelength bands.

The PECVD grown silicon oxynitride layers have been shown to have a stress induced birefringence due to a compressive stress [30]. The waveguide stack was shown to be compressively stressed indicating high birefringence [145]. Large stress could have shifted the propagation constants and their relative difference, which could have caused high excess loss of the MMI coupler.

As the fiber attachment technique determined the device performance, different approaches have been studied. Passive and active fiber pigtailing methods have been applied and compared. Even with good chip level performance the fiber attachment technique was crucial. The applied fiber attachment techniques suffered from high insertion loss. Especially in cases where the passive alignment was applied, device #1, #2 and #3 showed high insertion loss values. The passive method has shown to have too large a variation in port losses. For the best 4 ports pigtailed using the passive method, the variation was more than 9 dB. To improve uniformity an active method has been proposed and tried. The uniformity was clearly improved compared with the passive method. Only one device was manufactured with active alignment but the results were encouraging as the port uniformity of the manufactured 8-port (device #4) was better than 2.2 dB. The worst port had an insertion loss of 7.3 dB. Passive fiber attachment is not feasible if the objective is to manufacture a device with 32 ports. The PM-fiber must have tight geometrical tolerances if a purely passive method is chosen. The proposed active method is a possible solution for high port count devices. For any practical approach the active method needs modifications and further testing. A 32-port device sets new challenges and limitations to the pigtailing method. Thermal and mechanical shock testing should be carried out to validate the fiber attachment reliability.

The experience from device #1 (an 8-port with three cascaded 3-dB couplers forming a binary tree) showed that the quality of the fiber pigtailing as well as the 3-dB couplers' performance must be improved in order to meet the specifications of the 32-port device. The coupler imbalance of 36:64 was thought to due to last minute design changes, in which the bending radius of the access waveguides was changed from 20 mm to 10 mm. The excitation of the higher order modes in the multi mode section could have been influenced by this change. Additionally variation in fabrication process was considered to as likely reason. Although the coupler imbalance was large, the couplers were uniform. Three separate couplers in device #1 had only 0.2 dB variation in imbalance. This variation could also be due to uncertainty in the measurements. PER strongly depended on the fiber alignment quality. The PER was sufficient in most of the ports.

Device #2 shows improved coupler performance. The coupling ratio was better than 44:56. The input port I4 shows high insertion loss and low PER. The reason was thought to be because of the misaligned fiber. One reason that could have led to this was the large variation of the fiber dimensions. Three out of six connections showed acceptable PER (> 10 dB).

Device #3 had the same coupler as device #2 so the characteristics were expected to be the same. This was the case as concerns the reproducibility. The coupling ratio was better than 47:53 if the port with high losses (O4) is neglected. Six out of 12 possible paths of the coupler tree did not meet the excess loss specification of 10.3 dB. The most severe losses were probably caused by excessive coupling loss at the chip-fiber interface of O4. The power splitting ratio of the pigtailed coupler tree did not fulfill the maximum imbalance specification of 5 dB. The measured coupling ratio of each coupler was close to the target specification of 47:53.

The experience from the first three devices showed that the passive method using silicon V-grooves was not accurate enough to produce a low-loss fiber-waveguide interface. The MMI coupler was balanced, but had a rather high excess loss (1-3 dB).

With device #4 the active pigtailing improved results when a high variation of the fiber dimensions could be compensated by optimizing each fiber-waveguide coupling individually. Compared to the previously manufactured devices #2 and #3, the measurement results showed similar coupler imbalance. The biggest improvement with respect to earlier devices was that the fiber pigtailing resulted better uniformity. Silicon oxynitride technology with active alignment is considered a promising choice for manufacturing high port count devices. Table 5.32 represents a summary of the status of the fabrication technology.

Table 5.32. Main waveguide parameters defining the status of the technology.

Waveguide parameters	
Propagation loss	0.4 dB/cm
Coupling loss	0.2 dB
Excess loss of a waveguide crossing	< 0.1 dB
Minimum bending radius	20 mm
PER (straight)	> 20 dB
ΔPER due to a waveguide crossing (20 deg)	< -0.2 dB
Process uniformity	
Refractive index difference (%)	10
Core layer thickness (%)	6

6 MEMS VARIABLE OPTICAL ATTENUATOR

A MEMS based variable optical attenuator has been developed for power management purposes in optical networks. Modern fiber optical networks are based on dense wavelength division multiplexing (DWDM). The transmission is divided between several discreet wavelength channels, each carrying information with data rates exceeding Gbits/s speed. These channels are created and controlled with advanced optoelectronic circuits. The fundamental components of the optical network include semiconductor lasers, add/drop-devices, optical switches and optical amplifiers. Power management and control issues are induced by non-ideal components and the complex nature of the network. Firstly, the launch power level from the transmitters should be equalized to ease the control of the network. The equalization of the erbium doped fiber amplifier's (EDFA) non-flat spectral gain profile is the second application for VOAs. Because VOAs are normally non-wavelength dependent components, the amplified channels must be divided into separate fibers prior to the equalization by discrete VOAs. Thirdly, as the network is dynamically reconstructed through add-drop operations and re-routing via optical switches, the power levels in the optical fiber lines change continuously. This reflects the highly dynamic characteristic of the DWDM networks. This power fluctuation must be controlled and managed with VOAs. In general, the purpose is to balance and control the power level impinging the detector. Figure 6.1 shows applications of the VOAs in the optical networks.

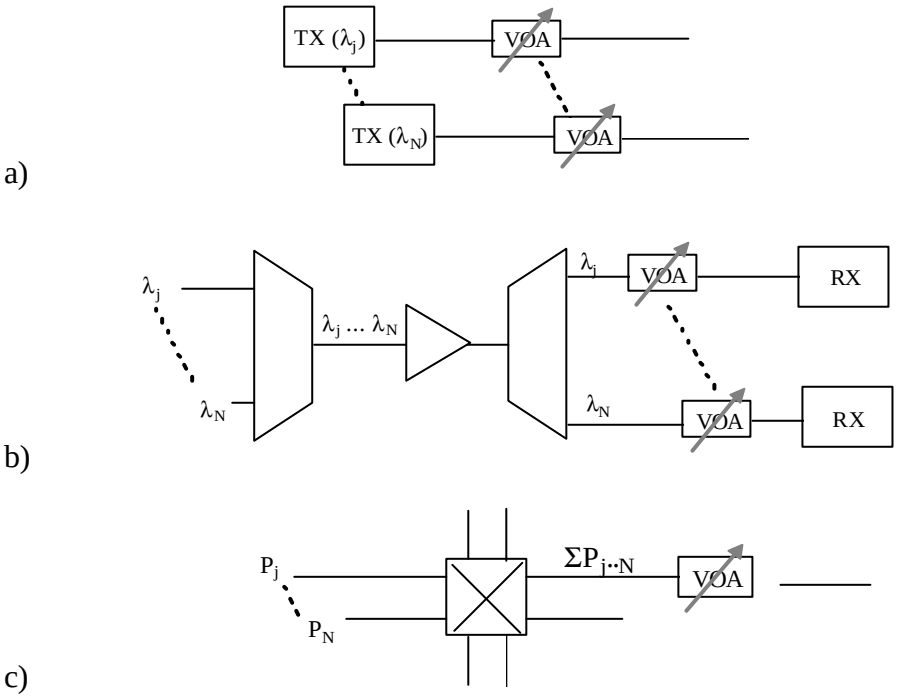

Figure 6.1. Applications of VOAs in optical network: a) Power equalization after transmitters, b) EDFA gain spectrum equalization, and c) power control after optical cross connects and add-drop operations.

6.1 Specifications for VOA

The lightwave based networks and subsystems place stringent performance requirements on VOAs. There are varying needs for different network architectures depending on the applied wavelength bands and power levels.

In general the specifications can be divided into optical, electrical and other parameters which relate to reliability, packaging, storage, and environmental issues. In the scope of this work the discussion is focused on the optical parameters. General specifications have been defined for optical attenuators in Telcordia's *General Requirements*, and in ITU's recommendation series [151,152,153]. Table 6.1 lists the main optical parameters and gives typical values for devices based on integrated optics or MEMS. These specifications were the target values for the developed MEMS VOAs.

Table 6.1. The main optical specifications for VOAs and typical values.

Parameter	**Symbol**	**Typical value**	
Wavelength range	-	1530 – 1625, C+L band	nm
Insertion Loss	IL	< 1.0	dB
Return Loss	RL	> 45	dB
Polarization Dependent Loss	PDL	< 0.5	dB
Wavelength Dependent Loss	WDL	< 0.5	dB
Temperature Dependent Loss[1]	TDL	< 2	dB
Dynamic Range	DR	> 20	dB
Isolation	BL	> 45	dB
Optical attenuation repeatability	R	< 0.05	dB
Dynamic Range	DR	> 20	dB
Optical resolution	-	continuous	dB
Power Handling	-	200	mW
Electrical power consumption	-	< 50	mW

[1]) in open-loop mode

Wavelength range

The wavelength range is defined for a 1.55 µm (or 1.3 µm) communication window. Typically the wavelength range is conventionally defined as 1530 to 1565 nm (C-band) or 1565 to 1625 nm (L-band) [154]. Applying a wider band means a compromise with other parameters such as wavelength dependent loss. Our target was to develop a wide band VOA that would meet specifications over C+L band (1530-1625 nm).

Insertion loss and return loss

The most important figure of merit for the VOA is the insertion loss it causes when inserted in the transmission channel. The return loss specifies the acceptable level of back reflections the device can cause. Due to the nature of developed MEMS VOAs the level of back reflections varies as the attenuation setting is changed.

Loss variation specifications

The attenuation of a VOA can show small variation due to a changing input polarization, signal wavelength, or the ambient conditions. The following three parameters define VOA sensitivity to these factors.

Polarization Dependent Loss defines maximum variation of attenuation due to a varying state of input polarization. Typically PDL is defined piecewise over the dynamic range so that PDL tolerance is larger at higher attenuation levels.

Wavelength Dependent Loss [1] defines maximum variation of attenuation for different input wavelengths. Typically this parameter can be defined for a certain wavelength range and attenuation setting. We define WDL piecewise over the dynamic range as later shown.

Temperature Dependent Loss [1] defines maximum variation of attenuation under varying ambient temperature conditions. Typically TDL is defined in an open-loop configuration and with an electronic driver. TDL is (commonly) defined as the maximum change from the set value at 25°C i.e. TDL = A_{T2} - A_{T1}; T2=-10°C, or +70°C, and T1=+25°C.

Dynamic Range

The dynamic range (DR) defines the difference between minimum and maximum attenuation settings. Typically this should be above 20 dB. Additionally isolation or a blocking value (BL) can be defined for transmission when device 'closes' the channel. Typically this transmission-off state is set above 45 dB.

Attenuation repeatability

This parameter defines the accuracy with which the attenuation value can be re-set after power off, or between different attenuation settings. The repeatability R is defined as the difference between two attenuation settings (A_1 and A_2) within the time interval of a few seconds i.e. $R = A_1 - A_2$.

Other specifications

Additional parameters define VOA response time which describes the VOAs speed when attenuation state is changed. The polarization mode dispersion (PMD) defines the group velocity difference of two transmitted polarization. Power handling capability defines the maximum power the VOA can withstand. Typically the demanded value is 23 dBm.

[1] The ITU recommendations include WDL and TDL under parameter *insertion loss tolerance*, and gives the acceptable window as ± 15% of the attenuation setting [154].

6.2 VOA concepts

Two different concepts were proposed to develop and produce a VOA. Figure 6.2 represents the configuration concept of direct transmission VOA (later TVOA), and reflection based VOA (later RVOA). In the TVOA a blocking vane is moved between the two parallel optical fibers to control the transmitted power. In the RVOA the optical fibers are perpendicularly aligned and the transmission takes place through a reflection from a movable mirror. The transmitted power is now controlled by adjusting the position of the mirror and by causing thus lateral and longitudinal shift between the fibers. The TVOA was designed to be normally closed (NC). This means that the optical beam is intercepted in the power off state. In contrary to this the RVOA is normally open (NO) in the power off state. The origin of both concepts lies in the availability of the MEMS process and appropriate lensed optical fibers. The special fiber allows the free space propagation through the MEMS, while the movable vane or mirror is used to control the optical beam transmission.

The blocking vane and the moving mirror were based on an electrostatic comb drive actuator. An electrostatic actuator was considered suitable to deliver the required displacement to control the transmission of an optical beam with a diameter of 15 to 20 µm on the control plane. A Comb drive architecture was chosen as a transducer for VOAs. A low power-consumption can be achieved with electro-static control, though the mechanism is a non-latching. A mechanical spring system returns the rotor (the blocking vane or mirror) to the initial position while the comb drive is non-biased. The benefits of electrostatic actuation were single mask fabrication process with SOI-technology and reliability. These type of silicon structures had been shown to have life time exceeding billions of displacement cycles [93]. Low power consumption and reliability were considered especially attractive for an optical network application. A known drawback with the comb drive was response speed. A design which compromises between the low control voltage and high resonance frequency had to be achieved.

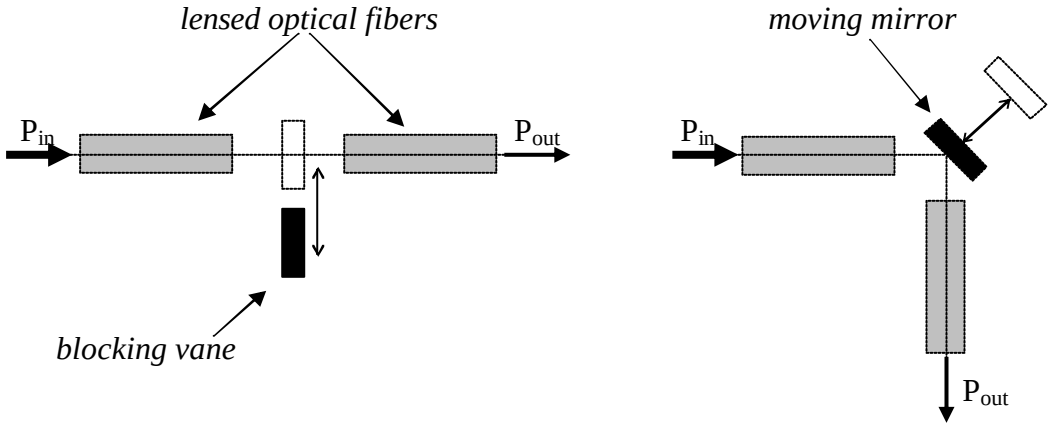

Figure 6.2. The proposed concepts of direct transmission type VOA (TVOA) on the left, and a reflection based VOA (RVOA) on the right. In both concepts the lensed optical fiber is the key enabling component. The control plane with a moving vane (or a mirror) is located at the beam waist.

Based on the same process technology different concepts and device configurations to the two aforementioned were also considered. A two shutter TVOA configuration was one option. The claimed benefits would have been enhanced resolution and lower WDL [94]. However, increasing the system complexity with an additional actuator might have reduced the component reliability. Another proposed and tested approach was an RVOA with a curved mirror, in which the fibers would have an angle less than 90 degrees [156]. Futhermore a configuration, in which the fibers are perpendicular to the die surface was considered. Unfortunately the latter two configurations did not meet the original objective of manufacturing the VOA with the existing front-end (FE) and back-end (BE) processes.

The development of the presented VOAs consisted of three main steps *concept review*, *proof of concept* with test structures, and *industrialization*. Figure 6.3 illustrates the associated topics that were considered in the development phase, in the MEMS design process, and in the layout synthesis. The starting point was the VOA application and the product design with set specifications. The performance objective was dictated by the typical specifications listed in table 6.1. The design of the actuator and die layout were based on the defined fabrication technology, taking into account the application dependent features, packaging features and electronic driver issues. The FE- and BE- processes defined the boundaries of manufacturing technology.

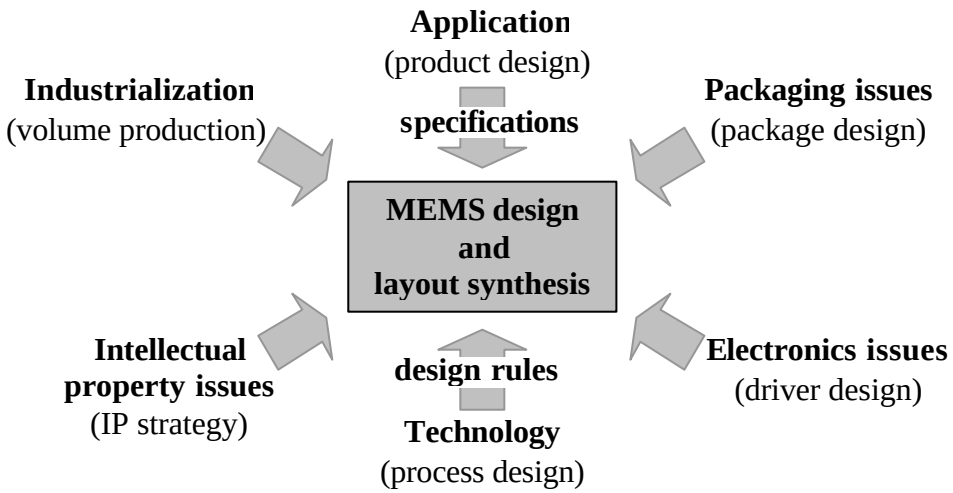

Figure 6.3. The design and layout synthesis of the MEMS VOA component was restricted and defined by the application, and selected fabrication technology. The application dictated the design objective in terms of specifications. Packaging issues and optical fiber attachment set constraints on the fiber-to-fiber configuration and on layout details such as fiber grooves and die size.

The process technology set the design rules such as minimum linewidth, and maximum etching areas, as will be discussed in the following chapters. The fabrication defined the MEMS design rules and limitations on layout details. Additional constraints were set by the electronics and the necessity of considering the industrialization aspects. Intellectual property issues were considered to avoid conflicts with protected architectures and products. Many useful configurations of electrostatic comb drive schemes were found to be protected [157,158]. The design processes were parallel and simultaneous, and the information flows as depicted in figure 6.3 are by nature two way, as the core design influences and serves the other processes. Although not depicted here the other design processes are also linked. This is later shown by

introducing some constraints to packaging, which rose directly from product specifications. The focus of the following study is the interaction of the FE process development and the electromechanical and optical design of the MEMS element. In the development process this phase consisted of combining the design issues to form a preliminary design, and carrying out a concept review so as to consider the feasibility of the proposed technical concepts.

6.3 Manufacturing technology

The manufacturing issues related to front-end processing are here discussed. The manufacturing process was the same for both VOA configurations. The manufactured VOAs were based on a SOI substrate. Well defined smooth and vertical surfaces were objectives of the process development. The vertical surface smoothness was important as it influences the backreflection properties in a TVOA and insertion loss of the RVOA. As the product was targeted at the optical telecommunication sector, a low cost process and high yield were natural objectives. Back-end fabrication issues such as die attachment to substrate, wire bonding, fiber attachment, and cover attachment are not discussed in detail. The fiber alignment process was identified to be a critical step. The alignment tolerances in case of TVOA are discussed based on analytical model and experimental results.

The component fabrication was divided into R&D process development and into industrial volume production. R&D process development was done with contact masks and 4" wafers. The volume production was done with a reticle mask and 8" wafer size. The advantage of starting the development work with contact masks was that several layout variations could be tested with one process run. The manufacturing was changed into applying a reticle mask after the layout was tried out, finalized and fixed. In our process the reticle mask offered better reproducibility and linewidth control over the wafer than the contact mask lithography.

The main steps of the fabrication process in the volume production are outlined in figure 6.4, also included are illustrations of the wafer cross-sections at each step. The device is formed on a 8" SOI substrate, with a 80 µm thick silicon device layer and a 2 µm thick silicon dioxide layer on a 625 µm thick substrate. The substrate was coated with a resist masking layer which was patterned in the lithography step using a reticle mask. A silicon etching step then followed. A 80 µm deep silicon etching was performed using a reactive ion etcher (Alcatel RIE 601). After the etching step the resist residuals were removed with oxygen plasma. A smoothing step was performed to lower the surface roughness on vertical surfaces. Subsequently freely standing structures were formed in a release step. The sacrificial oxide layer was etched in an HF vapour. The electromechanical characteristics were measured for the first time in wafer test I. Subsequently a gold metallization step was carried out to make the silicon vane opaque or reflecting. The second wafer test II was performed to re-measure the electromechanical characteristics before proceeding to die separation step. The wafer dicing and die separation step was done with automatic scribe-and-break equipment. The third test was carried out to make a final selection of the separated dies before proceeding with the packaging. Because the dies were exposed to particle contamination in the dicing and die separation step, this Known Good Dies (KGD) step was important to remove the bad dies from the packaging process. In the back-end manufacturing typical packaging steps were performed, including die to substrate mounting, wire bonding to enable the biasing of the actuator, attachment of the optical fibers, and cover attachment. The optical characteristics of the VOAs were largely

defined by the quality of the alignment and positioning of the optical fibers. Later experimental results verifying the importance of the fiber attachment procedure and its quality are presented.

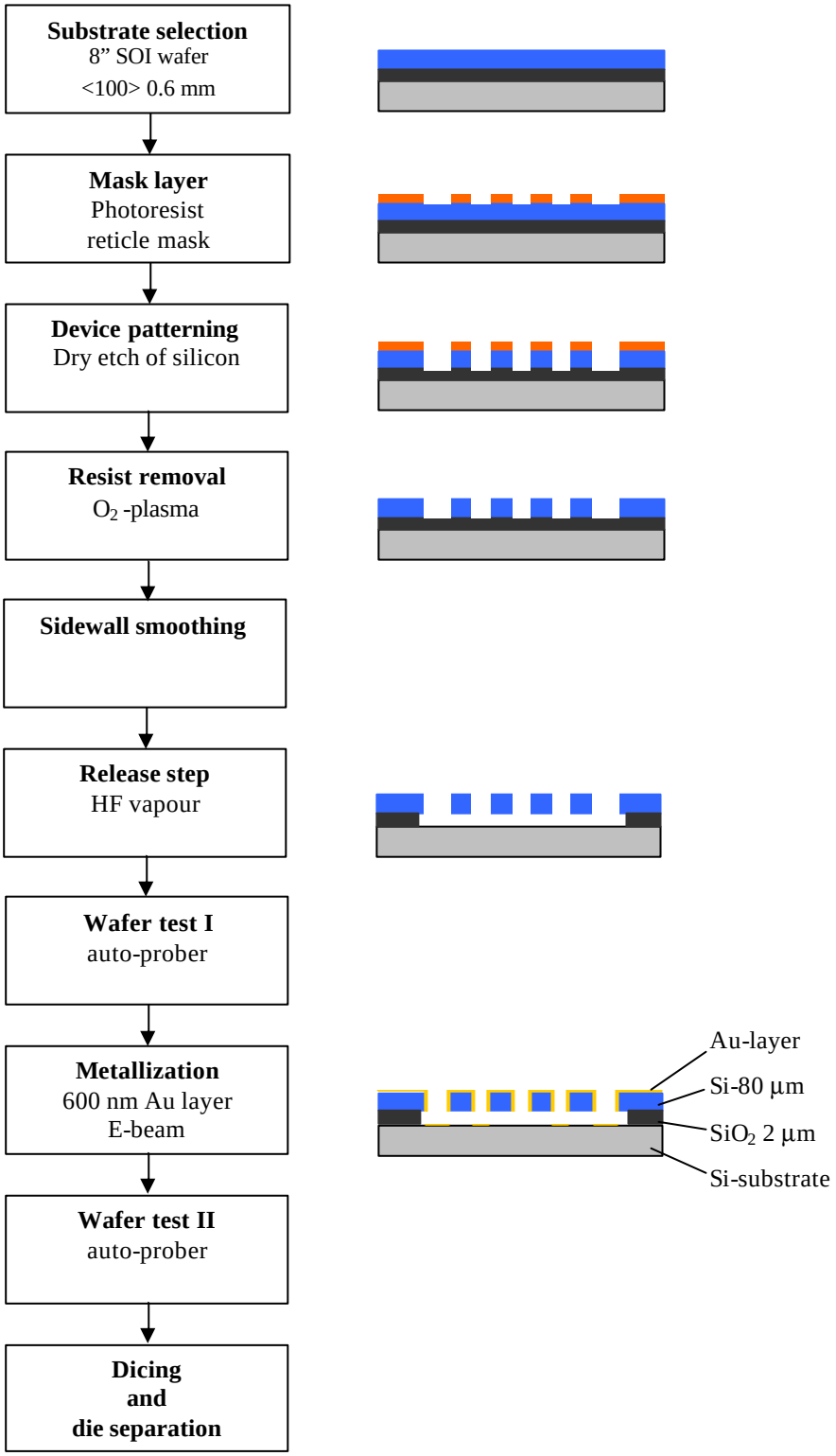

Figure 6.4. Front-end process scheme used for fabricating MEMS VOAs. Main process steps were the deep silicon etching step, the release step in which the sacrificial oxide was removed, and the metallization step. Two wafer tests were done

to study the electromechanical performance and yield before the metallization and dicing step.

6.3.1 Design rules

The defined manufacturing process set the design rules that had to be followed in the MEMS design. The quality and linewidth resolution of the process set certain limits on the layout design. Table 6.2 lists the absolute extremum values used in the MEMS design. The linewidth resolution was limited by the silicon etching step. The aspect ratio of released structures was defined to be 1:26. The minimum linewidth was 3 µm with the chosen substrate height of 80 µm. The groove aspect ratio was 1:26. The dry etching step set limitations on the closely designed released structures meaning that they had to be separated by a gap of at least 3 µm. The sacrificial oxide layer was removed from underneath the moving structures in the release step. An the same time the oxide was partly etched away underneath the fixed structures. A small under etching of fixed structures is necessary to achieve electrical isolation of the moving structures. The under etching was between 15 to 25 µm depending on the local conditions. This value set minimum dimensions for supporting structures. The maximum area to be removed (loaded area) in the dry etching was limited to 30 % of the total wafer area. The loaded area due to the MEMS was below 8 %. The loaded area was increased with the packaging and the fabrication features. The loaded area of the finalized VOA layout was close to 25 %.

Table 6.2. The design rules followed in the design of the VOAs.

Parameter	Value	Unit
Minimum linewidth	3	µm
Minimum groove width (finger gap)	3	µm
Under-etching (release step)	20	µm
Maximum linewidth for released feature	30	µm
Minimum square size to remain fixed	60	µm
Maximum total loaded area on wafer	30	%

6.4 Design of VOAs

The VOA design was divided into mechanical and optical design. In the following the principle of the optical design is explained and the main modeling results are presented. The TVOA and RVOA applied similar actuator structures and optical fibers. The differences were in the fiber orientation with respect to the actuator, and in the mirror structure. Figure 6.5 shows a schematic layout of the electrostatic actuator and its positioning with respect to the optical fibers in TVOA. The design was divided into two parts as highlighted in figure 6.5. The optical design (part A) included the modeling of the free space propagation, and calculation of optical attenuation response to shutter movement. The electro-mechanical design (part B) included the modeling of the electrostatic comb drive.

The design served as a starting point from which the front-end process could be developed and optimized with a preliminary layout. The design was a continuous and cyclic process. As process measurement data became available, the design was adjusted to improve uniformity and quality of the dies. The optical model gave

tolerances for the fiber alignment procedure in the back-end fabrication. The actuator design and the layout were fully parameterized. A parameterized design allowed revisioning of the layout automatically.

The design methods included theoretical modeling of the structure, and experimental studies to optimize the device layout. Numerical design was done by applying a commercial CAD tool ANSYS (Ansys Inc., US) for mechanical FEM simulations and in-house MATLAB (Mathworks Inc., US) routines in optical modeling. The layout generation was done with a MEMSPRO (Memscap S.A., Fr). The mechanical behaviour of the actuator was presented with analytical formulas. The FEM tool was applied to study critical aspects such as side-stability, finger rod rigidity, and stress levels on the beams. The VOA performance was calculated by embedding the analytical formulas describing the mechanical functioning of the actuator in the optical model. The optical propagation in free space and diffraction from the blocking vane was calculated by applying angular spectrum method [6,7]. The influence on the optical response could be re-evaluated if actuator's or fibers' parameters were subject to change. Only major changes in the actuator design required new finite element analysis (FEA).

The design objective was to produce a normally closed TVOA and a normally open RVOA with the specified optical performance as described earlier (see table 1). The NC configuration means that the actuator returns to a fully blocking position in power-off state. It was possible to identify four principle aspects as guidelines for the design: The device had to apply available lensed optical fiber, the transmission had to drop below -30 dB when VOA is in 'closed' state, the maximum driver voltage had to be below 100 V. Lastly the actuator's resonance frequency should be as high as possible to allow fast response. Commercially available VOAs have a typical response time of 0.1 ms to 20 ms. An additional requirement was a narrow structure to allow array configuration of actuators in multichannel TVOAs.

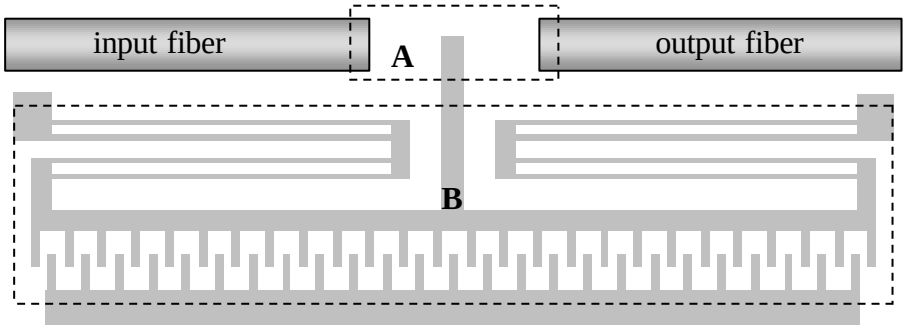

Figure 6.5. Schematic layout of TVOA with input and output fibers and the electrostatic actuator. The outlined areas highlight (A) the optical elements (shutter and optical fibers) and (B) the electrostatic drive with folded springs and the comb finger structure.

6.4.1 Optical fiber for TVOA and RVOA

The special lensed fiber used was Optifocus OF18 from (Corning Inc., US). The fiber is made of standard single mode fiber (SMF-28) with a diameter of 125 µm. It has a hemispherical lens at the tip that provides longer working distance (WD) and thus a larger gap between the fibers. The fiber lens has a wideband anti-reflection (AR) coating. Fiber-to-fiber return loss was specified to be >50 dB over C+L band. A

micrograph of a lensed fiber and a fiber-to-fiber coupling scheme is shown in figure 6.6. The nominal mode field diameter (MFD, $2w_0$) is 18 µm ± 2 µm and ½WD of 150 µm ± 30 µm. Due to the fiber fabrication method there is a small uncertainty in these parameters so that the beam waist distance (½WD) and MFD varied ±10% [159].

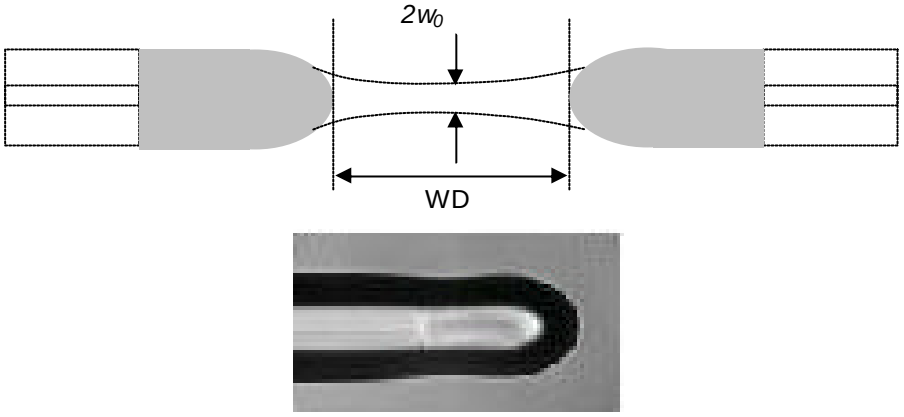

Figure 6.6. Schematic of a pair of Optifocus fibers and a microscope photo of an OF18 lens.

The free space propagation was determined by the fiber. The selected special optical fiber largely determined the optical performance of this type of VOA. The fiber characteristics determined the necessary silicon thickness so that the beam had to be guaranteed to remain below the top edge of the silicon as shown in figure 6.7. To choose the MFD correctly, the tolerances of the fiber and the substrate were considered. The fiber outer diameter accuracy was ± 1 µm and the pointing error was ± 12 mrad. The pointing error is the angle between the emerging beam and the plane of the die. Figure 6.7 shows a schematic cross section of the fibers mounted in a groove on the die.

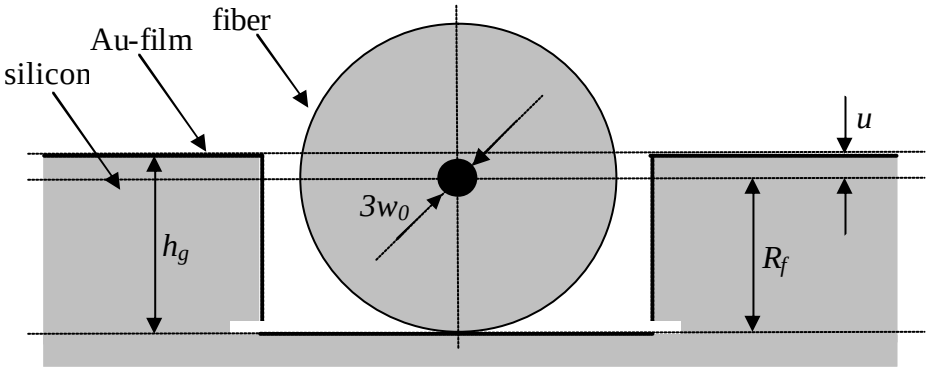

Figure 6.7. The beam waist on the shutter plane was limited by the silicon height. In figure 6.7 the full power circle ($3w_0$) is depicted. The groove depth is h_g. The parameter u defines the distance of the center of the beam to the top edge of the shutter. The fiber radius is R_f. Dimensions are not shown in scale.

A spot diameter of $3w_0$ was used to estimate a circle that maintains all energy in the gaussian beam. The beam waist must satisfy the condition

$$3w_0 < 2u \ , \qquad (6.1)$$

to guarantee that the beam is below the silicon edge. The nominal groove depth (82 μm) is the sum of the thicknesses of the silicon device layer and the removed oxide layer. The nominal value of R_f is 62.5 μm. The nominal value for u is thus 19.5 μm, setting the limit for the beam radius at the shutter plane. This allowed a beam waist radius of 13.0 μm.

In the worst case the diameter of the fiber could vary ±1 μm, thus maximum R_f is 63.0 μm. The minimum groove depth h_g is 81 μm, by adding the thickness of the removed silicon oxide layer (2 μm). The maximum 12 mrad pointing error effectively decreases the silicon height by 1.8 μm at a distance of 150 μm. In this case the minimum value for u is 16.2 μm, this would allow a 10.8 μm beam waist radius. Additional tolerance is needed when taking into account that the fiber may not touch the bottom of the groove. Due to availability of the fibers, a compromised selection with a beam waist of 9.0 μm ($1/e^2$ value) and a focus length of 150 μm was made. Thus the working distance was 300 μm.

6.4.2 Fiber-to-fiber alignment tolerance

The optical performance of the TVOA at zero attenuation state depends solely on the fiber characteristics and the alignment quality, while the mirror has an additional impact on the RVOA performance at zero attenuation state. The insertion loss specification set fiber-to-fiber alignment tolerance. The fiber-to-fiber coupling efficiency was calculated by assuming gaussian beams for the fiber modes, whose beam radius changes as per [160]

$$w(z) = w_0\left[1+\left(\frac{lz}{pw_0}\right)^2\right]^{1/2}. \tag{6.2}$$

The power coupling coefficient (h) between two gaussian beams with beam waists of w_0 and w_1 can be calculated by [161]

$$h = k\exp\left(-k\left\{\frac{x^2}{2}(1/w_1^{\,2}+1/w_0^{\,2})+p^2q^2\left[w_1^{\,2}(z)+w_0^{\,2}\right]/2l^2 - xq\Delta z/w_1^{\,2}\right\}\right), \tag{6.3}$$

where,

$$k = \frac{4w_1^{\,2}w_0^{\,2}}{(w_1^{\,2}+w_0^{\,2})+l^2\Delta z^2/p^2} \tag{6.4}$$

where x is lateral misalignment, q is angular misalignment, and Dz refers to longitudinal shift between beam waists and w_1(z) can be replaced in (6.3) with (6.2). Figure 6.8 shows the coupling loss between two fibers due to a longitudinal offset Δz when the fiber has a beam waist of 8, 9, or 10 μm. The coupling loss is less sensitive to the longitudinal misalignment with a larger beam waist. Considering the alignment procedure the longitudinal alignment was easiest to handle in fabrication and was considered to have negligible contribution to the coupling loss. The combined effect of the lateral and angular misalignment was calculated by (6.3). Figure 6.9 shows the sensitivity to angular and lateral misalignment occuring with longitudinal offset Dz=0 for a case with nominal beam waist of 9 μm.

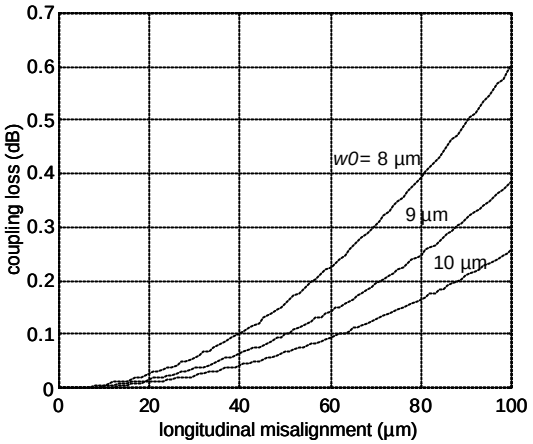

Figure 6.8. The coupling loss between two perfectly matched fibers due to the longitudinal misalignment (w_0=*8*, 9 and 10 µm).

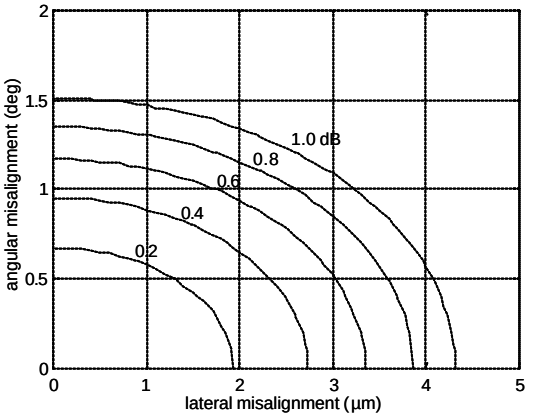

Figure 6.9. Contour lines of constant excess loss of 0.2, 0.4, 0.6, 0.8 and 1.0 dB due to the lateral and angular misalignment (Dz = 0 µm, w_0=9 µm).

6.4.3 Fiber-to-MEMS alignment tolerance and attenuation response

TVOA

The optical beam size varies in direction z as shown in figure 6.10. The longitudinal misalignment window is defined when in the worst case u=16.2 µm. At the fiber plane the spot size is nearly 40 µm and it reaches minimum $3w_0$ at the focal plane at the distance of ½WD. To avoid optical beam to pass over the shutter, the positioning of the fibers becomes critical. The allowed variation of the shutter position with respect to the beam waist is described by the parameter d_S (see figure 6.11). By taking into account the worst case dimensions the tolerance for longitudinal shutter positioning is ½WD ± 70 µm.

The tolerance for the lateral alignment of the fibers is set by the specified dynamic range, blocking value and actuator travel range. The initial position of the shutter relative to the optical axis will affect the behavior of the TVOA (see figure 6.12). The variation in the response curves for different values of L_0 is shown in figure 6.13, where L_0 is the distance between the shutter tip and the optical axis. The curves shown are for WD=300 µm and beam waist w_0=9 µm. The shutter was assumed to be located symmetrically in the center between the fibers i.e. in the beam waist. The

optical model shows that a shutter displacement of 20 to 30 µm is needed to reach 0 dB attenuation level, depending on the value of L_0.

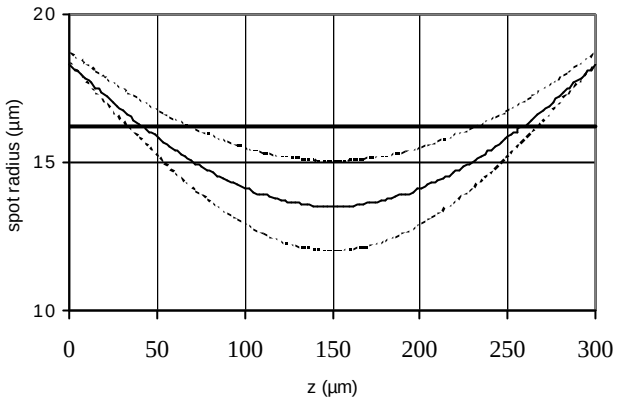

Figure 6.10. The evolution of the beam radius as a function of propagation distance *z*. Three cases with w_0=8, 9 and 10 µm. The plotted spot radius corresponds with the full power area 1.5w_0 and the thick horizontal line depict the acceptable range in the worst case (u=16.2 µm).

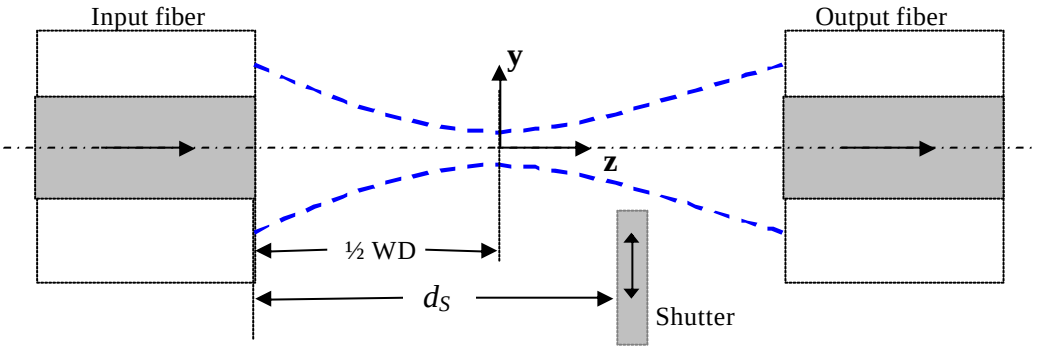

Figure 6.11. Longitudinal fiber alignment tolerance. The beam waist must be located at the shutter plane. The fiber alignment tolerance is d_S. The shutter is shown in a displaced position.

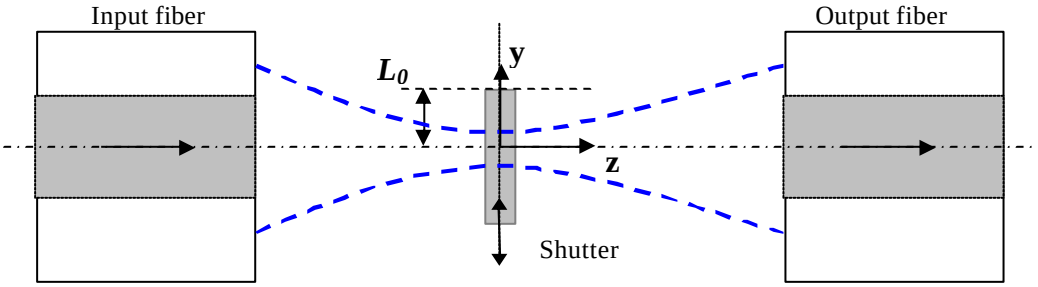

Figure 6.12. Lateral fiber alignment tolerance. The distance of the optical axis to the shutter tip (L_0) defines attenuation response curve. The shutter is shown in the initial position.

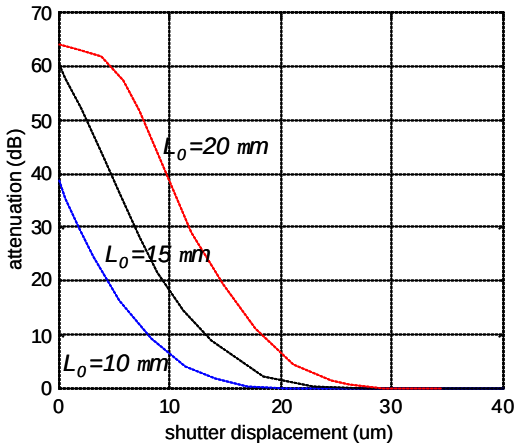

Figure 6.13. Calculated attenuation response for TVOA. The three different cases correspond to different initial positions of the optical fibers with respect to the optical axis (WD=300 µm and w_0=9 µm) [6].

RVOA

Figure 6.14 shows the change of attenuation versus the mirror displacement for RVOA. The optical response was calculated by applying (6.3). The angular spectrum method was also used to calculate the response, and the obtained results were consistent with those of equation (6.3) [7]. The needed displacement for a full attenuation (30 dB) with RVOA is 15 µm to 18 µm, with a beam waist of 8 µm or 10 µm, respectively. The attenuation response of the RVOA does not depend on the fiber-to-MEMS alignment assuming that the mirror is located close to the beam waist. The mirror's horizontal dimensions were assumed to be large enough so that reflected beam is negligibly diffracted from mirror edges. And, as the fiber grooves were 200 µm wide, the alignment accuracy of the optical axis with respect to the mirror symmetry axis necessitated a large mirror. The size of the mirror in lateral direction was chosen to be 10 times the beam waist.

In the RVOA the optical quality of the MEMS mirror influences the insertion loss and other optical parameters already at the 0 dB attenuation state. The IL is degraded due to a reflection from the mirror. The non-verticality, surface roughness and metallic coating properties determine the mirror performance. An additional issue arises in the RVOA packaging due to the fact that the RVOA can have a non-monotonous response function when there is a small misalignment of the fibers. A small shift in mirror position could compensate initial misalignment leading to a higher transmission i.e. non-monotonous response as depicted in figure 6.15.

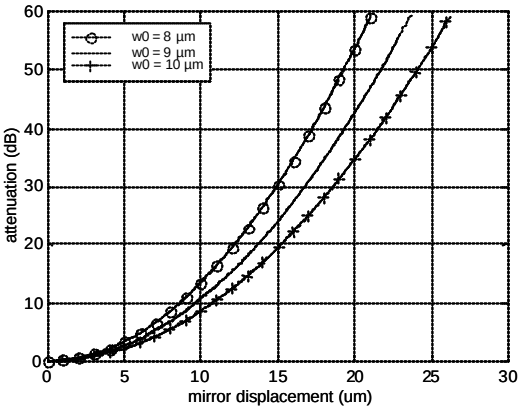

Figure 6.14. Calculated attenuation response versus mirror displacement for RVOA (WD=300 µm and w_0=8, 9 and 10 µm).

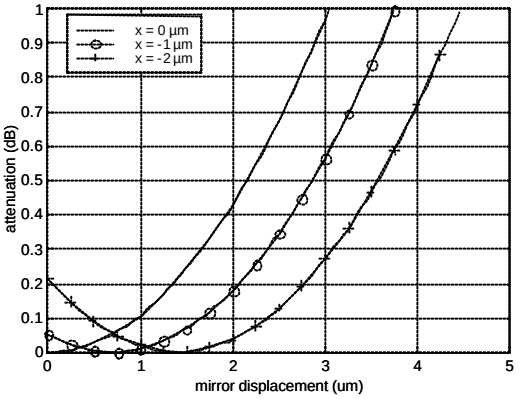

Figure 6.15. Calculated attenuation response versus mirror displacement for RVOA for initial lateral fiber-to-fiber misalignment of 0,-1, -2 µm (WD=300 µm and w_0=9 µm).

6.4.4 Actuator design

The actuator displacement versus control voltage was described with analytical formulas. Firstly, optical attenuation *A*, as a function of the shutter displacement *d*, was calculated for both TVOA and RVOA. The function *A(d)* was used to design the actuator geometry to deliver the needed travel range. Next the mechanical model was applied and embedded in the optical simulation so as to produce the attenuation *A* as a function of the control voltage *U*. Conventional folded spring structure was adapted for the comb drive (as depicted in figure 6.5). This type of structure provides mechanical rigidity and side stability needed for relatively large displacement [162]. Parameters describing the process quality were measured from test structures so as to take process non-idealities into account (see table 6.8). Detailed information of the process was needed to define accurately the analytical model for the folded springs. Four process parameters were introduced to describe the real geometry of the processed structure: these were linewidth change (Δl), verticality for spring beams (a_1), verticality for finger beams (a_2), and substrate height variation (Δh). The parameters were considered to be constant over the wafer. It is possible to apply non-constant process parameters that describe the geometrical structure more accurately over the wafer. The target was to minimize the variation in control voltage over the wafer and between fabricated batches. The largest change from ideal structure was induced by non-vertical sidewalls.

The under-etching of finger plates, occuring due to the notching effect in dry etching step, proved to be a problem in the first process runs. The stiffness of the spring beams is modeled by using a trapezoidal cross-section. The folded beams became narrower at the bottom due to the RIE lag (see figure 6.16). The comb fingers also had a non-vertical sidewall, but due to the narrow trench the fingers became wider at the bottom i.e. the sidewall had a positive angle.

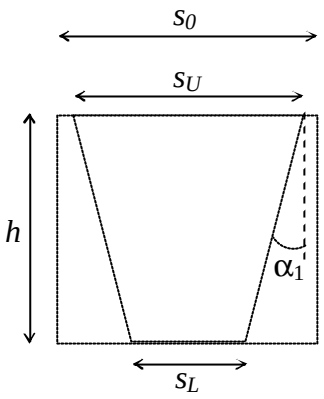

Figure 6.16. Cross section of dry etched beam. The sidewall non-verticality is modeled by introducing the parameter α_1. The nominal width of the beam is s_0. The difference s_U - s_0 represents the change of linewidth Dl.

The control voltage is

$$U = \sqrt{\frac{k_y y g_{ave}}{e_0 n(h+\Delta h)}}, \tag{6.5}$$

where e_0 is the vacuum permittivity, k_y is the forward spring constant, y is the displacement of the comb drive, h is the height of the fingers, Δh is the height variation due to change in substrate thickness, g_{ave} is the average gap between two finger plates and n is the number of the fingers in the comb drive. Average gap is

$$g_{ave} = \frac{g_U + g_L}{2}, \tag{6.6}$$

where the gap at the top of the finger is $g_U=g_0-Dl$, and the gap at the bottom is $g_L=g_U-2htan\alpha_2$, where g_0 is the nominal gap between the finger plates, α_2 is the sidewall verticality of the fingers, and $\Delta\lambda$ is the change of linewidth. The forward spring constant k_y of the double folded beam depends on the Young's modulus E, the moment of inertia of the beam I, and the beamlength B_L

$$k_y = \frac{24EI}{B_L^{\,3}}, \tag{6.7}$$

where the moment of inertia of the trapezoidal beam is given by [163]

$$I = h\frac{(s_U + s_L)(s_U^{\,2} + s_L^{\,2})}{48}, \tag{6.8}$$

where the beamwidths at the top surface (s_U) and at the bottom (s_L) are

$$s_U = s_0 + \Delta l \quad \text{and} \tag{6.9}$$

$$s_L = s_0 - 2h\tan a_1 + \Delta l\,, \tag{6.10}$$

where s_0 is the nominal beamwidth and a_1 is the sidewall verticality of the beams. Figure 6.17 shows the actuator's response curve i.e. displacement versus control voltage. The response curve was calculated with the measured process parameters using (6.5). The sidewall verticality of spring beams and finger plates was 0.5 and -0.5 degrees, respectively and the linewidth reduction was 1.3 µm. The in-plane Young's modulus for <100> silicon is 130 GPa.

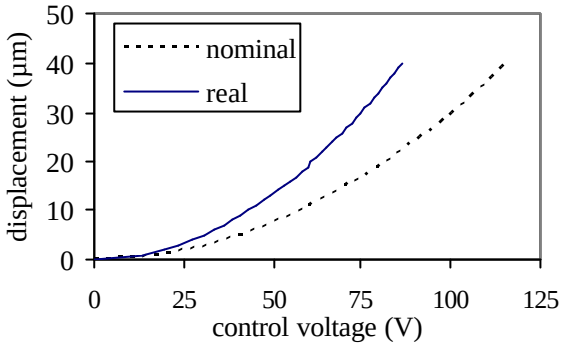

Figure 6.17. Displacement versus control voltage of the designed actuator, nominal response curve (dashed) and expected response with corrections, taking into account the process parameters (solid line). The parameters used with the actuator are summarized in table 6.9.

Resonance frequency

The undamped resonance frequency depends on moving mass m and the spring constant k_y as [164]

$$f_{res} = \frac{1}{2p}\sqrt{\frac{k_y}{m}} \tag{6.11}$$

where m is the moving mass of the comb drive. The resonance frequency of the structure was limited by the maximum control voltage, which was set by the external electronic driver circuitry. The finger rod contributed 40 % of the moving mass, the folded spring system 24 % and the finger plates 17 %. With the designed spring constant of 10.9 N/m and moving mass 3.2×10^{-8} kg, the resonance frequency of the structure was 2.9 kHz (TVOA actuator). This value was calculated by (6.11) before the metallization. The metallization adds the mass of the moving structure and increases the spring constant. The finger gap reduction was estimated to cancel the change of control voltage due to the increased spring constant. Because gold density is much larger than silicon density the increase in moving mass was estimated to change the resonance frequency as is shown in figure 6.18.

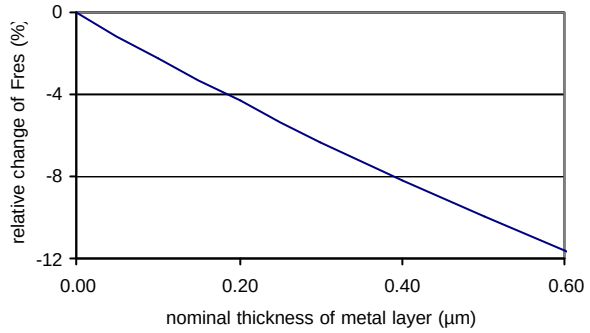

Figure 6.18. Relative change of the resonance frequency due to the Au metallization of the silicon structure and change of the moving mass. Au bulk density is 19000 kg/m^3, sidewall thickness was assumed to be 30% of the nominal thickness on the surface. It was assumed that the k_y remains constant. Actuator parameters are shown in table 6.8.

6.4.5 Numerical modeling

A finite element model was implemented through the use of the ANSYS tool so as to numerically study the side stability of the spring system, mechanical rigidity of the finger rod, and stress levels in the structure. Figure 6.19 shows a layout model of the spring system. The H-walls were used in early process runs to protect the spring beams and to achieve rectangular beams.

A 2-dimensional *plane82*-element was applied in the finite element analysis. This element allowed rotational freedom to study side stability of the structure. The loads were introduced to the mechanical structure as point loads. The load (electrostatic force) consisted of two perpendicular force vectors $F_{ES,Y}$ and $F_{ES,X}$ in our model. The magnitude of the forces was dependent on the applied control voltage. Figure 6.20 shows the displaced spring system.

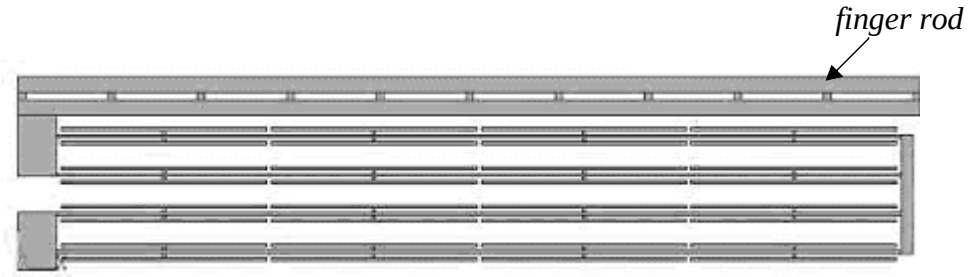

Figure 6.19. Half of the spring system of the model. The structure is symmetric with respect to the Y-axis. The spring beams have protection walls to avoid excessive etching.

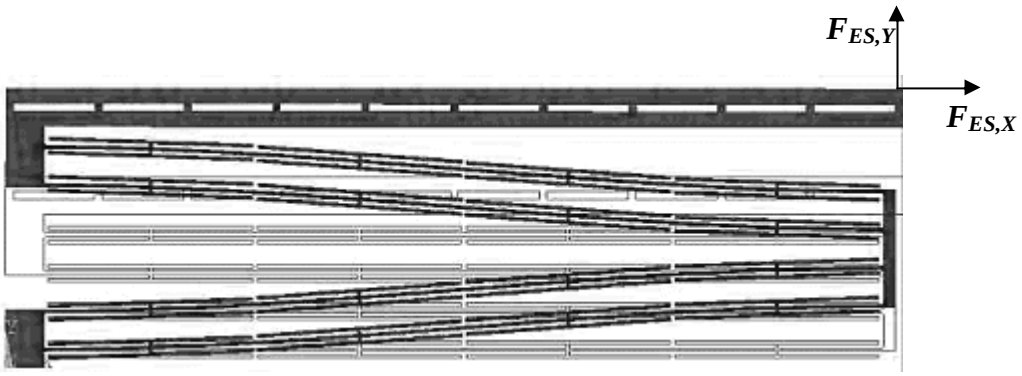

Figure 6.20. The modeled displacement of the spring system.

The beams of the folded springs became strained while displaced as shown in figure 6.21. The maximum strain occurred close to the attachment point. For the designed spring system the maximum calculated strain was 0.39×10^{-3}, with maximum displacement of 40 µm (see table 6.3). Silicon has linear elastic properties, thus stress linearly follows strain [165]. Maximum stress had a calculated value of 61 MPa. The lowest material strength value reported in literature is 0.6 - 1.3 GPa which was experimentally measured for RIE processed silicon beams [166]. We assumed that our beams have similar surface roughness as those reported. As the stress on the beams was considerably lower than the reported strength, we considered that the stress will not limit the life time of the springs. Furthermore it is not likely that the maximum displacement is repeatedly used.

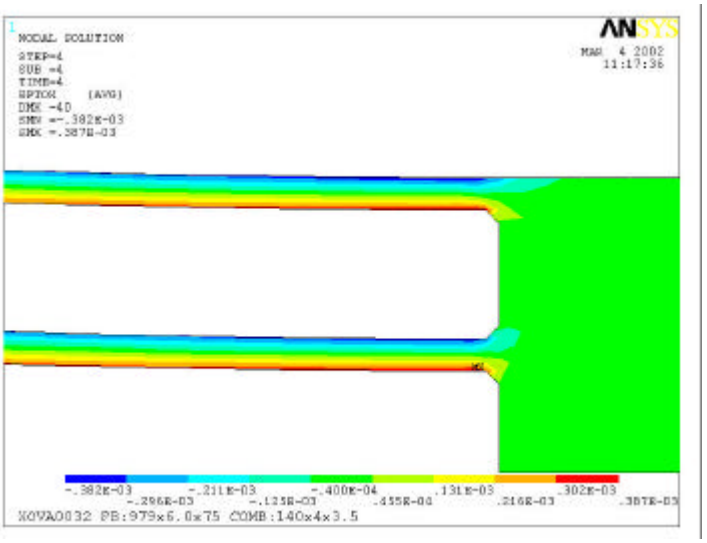

Figure 6.21. The modeled strain of the spring beams using the ANSYS FEM tool. The above figure shows the maximum strain (0.39×10^{-3}) on the beams at the displacement of 40 µm. The maximum strain is in the direction of the beam axis.

Table 6.3. Calculated maximum strain (two components $\varepsilon_{X,MAX}$ and $\varepsilon_{Y,MAX}$) versus displacement, and the maximum stress in a typical structure. The maximum stress point was in the pivot of the spring beams. The beam length and width were 980 µm and 6.0 µm.

U (V)	*y* (µm)	$e_{X,MAX}$	$e_{Y,MAX}$	s_{MAX} (MPa)
43	10	0.97E-4	0.37E-4	15
63	20	0.19E-3	0.73E-4	29
81	30	0.29E-3	0.11E-3	45
94	40	0.39E-3	0.15E-3	61

Finger rod rigidity

To choose optimum thickness for the finger rod, its rigidity was studied applying FEA. The finger rod structure is shown in figure 6.19. The finger rod bending at full displacement of 40 µm is shown in figure 6.22. Two cases are illustrated with beamwidths of 3 µm and 6 µm, when the finger rod length is 2200 µm. For 3 µm beams the bending is below 0.1 µm when the finger rod thickness is >25 µm, and for 6 µm spring beams the bending is below 0.1 µm when the finger rod thickness is >35 µm.

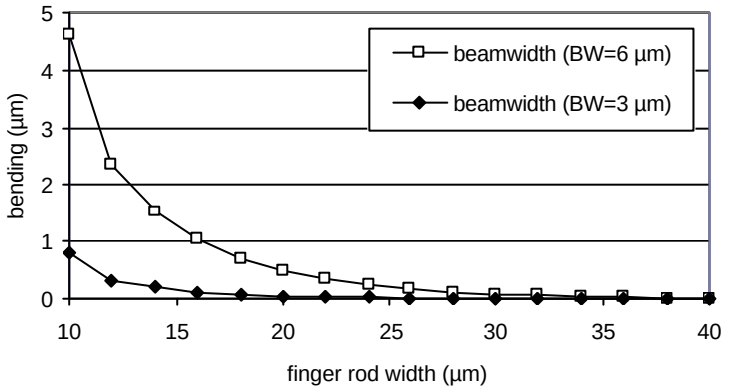

Figure 6.22. Typical finger rod bending at the full displacement of 40 µm. The finger rod shows negligible bending when the rod width is larger than 35 µm (beamwidth 6 µm, and spring constant of 5.8 N/m). The finger rod length was 2200 µm in both cases.

Side stability

The side stability (*S*) tends to decrease rapidly when the initially straight spring beams become bent. It is necessary to consider side stability of the spring system under large displacements. Various methods have been proposed in literature to improve the side stability of comb drives. The comb drive can be positioned between the folded springs, or the spring beams can be made pre-bent [158]. Actuator operation remains stable while $S > 1$. Jermann et al. stated a rule that *S* should be >10 [157]. The side stability *S* has been defined as the ratio of side stiffness to the derivative of the side electrostatic force [162]

$$S = \frac{k_x}{\left\{\frac{dF_{ES,X}}{dg}\right\}}, \tag{6.12}$$

where the transversal spring constant k_x represents the side stiffness, and $F_{ES,X}$ is the perpendicular electrostatic force pulling the finger plates together. As the displacement y increases, the retrimental electrostatic force $F_{ES,X}$ grows. At a given displacement the $F_{ES,X}$ was estimated to be [162]

$$F_{ES,X} = \frac{1}{2}\frac{ne_0 h(y + y_0)}{g^2}U^2, \tag{6.13}$$

where y_0 is the initial overlap of the fingers. The derivative of the $F_{ES,X}$ represents the speed at which the retrimental side force increases.

$$\left\{\frac{dF_{ES,X}}{dg}\right\} = \left[\frac{2ne_0 h(y + y_0)}{g^3}\right]U^2, \tag{6.14}$$

Thus the side stiffness should change more rapidly to keep the actuator stable. The side stability (S) was studied numerically using the FEM tool. The displacement y versus control voltage U was estimated by an analytical formula (6.5). The side stiffness was solved by introducing the $F_{ES,X}$ in direction -x on the comb bar (middle of the frame) and calculating the displacement in x-direction (dx), thus the transversal spring constant is

$$k_x(y) = \frac{F_{ES,X}}{dx}. \tag{6.14}$$

The side stability was calculated for different displacements and different geometrical layouts. Figure 6.23 shows the side stability of the designed folded spring. Side stability is nearly constant with only a small variation of comb parameters and side stability remains over 10 up to displacements of 30 µm.

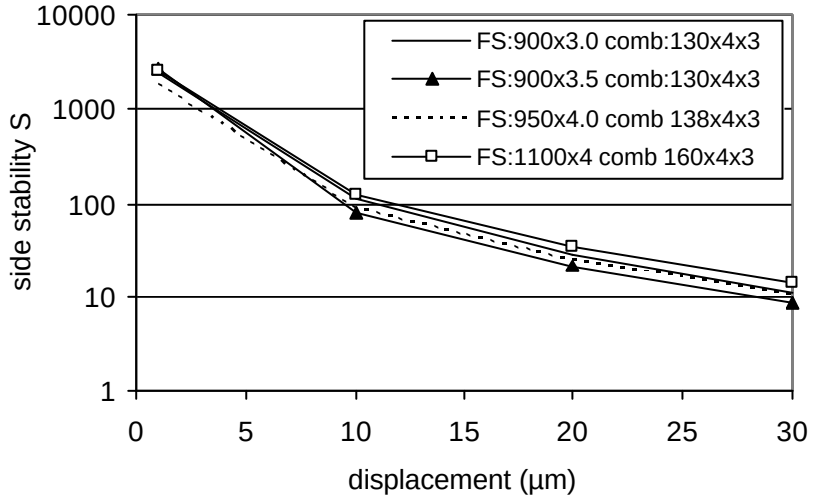

Figure 6.23. Typical side stability S of different designs as a function of displacement. Four different folded spring configurations were studied with beamlengths of 900, 950, and 1100 µm, and beamwidths of 3.0, 3.5, and 4.0 µm, as shown in the legend. The number of fingers was increased for longer beams as finger rod length increased.

6.5 TVOA shutter

The influence of the shutter geometry on PDL was studied experimentally. Dummy shutters on a standard silicon wafer were fabricated using a process similar to the real VOA process. We studied arrow and rectangular geometries as shown in the SEM pictures in figure 6.24. The main parameter was the width of the shutter tip. Arrow type shutters had incidence angles of 45, 20, 15 and 10 degrees. The arrow was designed with a sharp tip in the layout, or with a flat tip. The width of the flat tip was 3 µm. The nominal width of the rectangular shutter was 5 or 10 µm. The linewidth reduction of all test structures was 1.3-1.8 µm. The test shutters were fixed and the optical evaluation was done by moving the shutter die between the two fibers. Fibers with two different working distances of 150 µm and 310 µm were tested, and had a spot diameter of 17 and 19 µm, respectively. Figure 6.25 shows the set-up used for acquiring the PDL versus attenuation. A stabilized light source at a 1.55 µm, a polarization scrambler (Agilent 11896A), and a power meter module (Agilent 816x) were used in the set-up. The polarization scan time was 10 s, with an averaging time of 20 ms. Polarization states were scanned in a random fashion. All measurement points were acquired at least three times. The PDL was the measured worst case value.

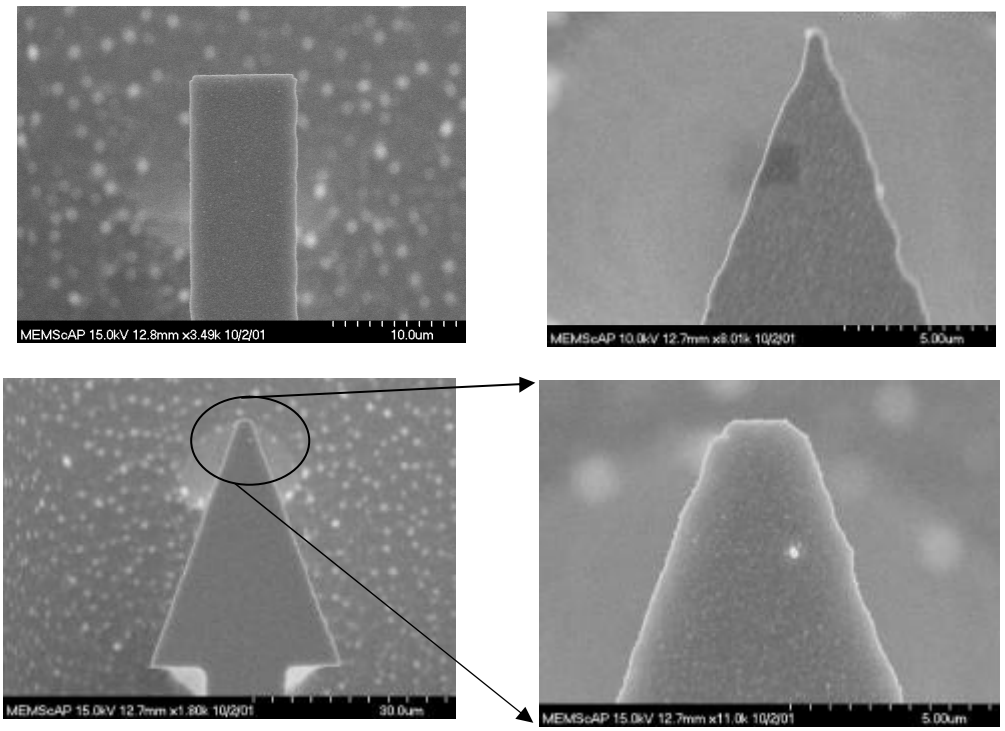

Figure 6.24. SEM pictures (viewed from above) the type of the tested shutter structures. A rectangular shutter with a width of 10 µm and an arrow shutter with an angle of 20 degree and a flat tip of 3 µm. The linewidth reduction from the nominal value was 1.3-1.8 µm.

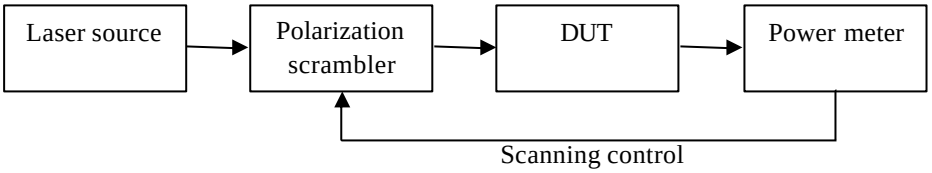

Figure 6.25. The measurement scheme used for the optical evaluation of the dummy shutter test structures. For each measurement a polarization scanning was triggered by the power meter module which recorded the minimum and maximum transmission levels during the scan. The measured transmission difference represented the polarization sensitivity i.e. PDL. Attenuation was adjusted by manually shifting the shutter (DUT) between the two fibers.

Figures 6.26 and 6.27 represent the results obtained with different shutter geometries, thickness and fibers. Figure 6.26 (a) compares arrow type shutters with a sharp tip, to rectangular shutters. The PDL was lower with an arrow shaped shutter compared to rectangular shaped shutters. PDL for a rectangular shutter with nominal width of 5 µm was over 1.5 dB at an attenuation level of 10 dB. All arrow shutters gave PDL below 0.8 dB up to the attenuation level of 30 dB. Figure 6.26 (b) shows the PDL characteristics of arrow type shutters with a sharp tip from three different samples. The lowest PDL was measured to occur with small incidence angles.

Figure 6.27 (a) compares arrow type shutters with a sharp tip (samples A), and a flat tip (samples D). The sharp tip shutters showed lower PDL than flat tip structures. The PDL correlated with the tip width, or arrow shutter angle, PDL was lower for sharper arrow structures.

Figure 6.27 (b) shows the PDL measured with two different sets of fiber with a WD of 150 and 310 µm, for arrow type shutters with a sharp tip. Different working distance did not change significantly the polarization sensitivity.

A clear difference was found to be between the different types of shutter geometries. The lowest PDL was achieved with arrow type shutters with a sharp tip. The arrow shutter with an incidence angle of 10 degrees was chosen for the TVOA.

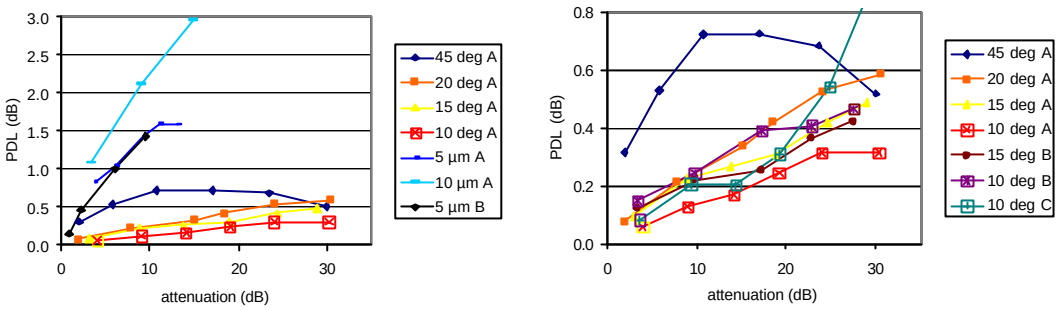

(a) (b)

Figure 6.26. PDL versus attenuation. a) Four arrow shaped shutters (angles 45, 20, 15 and 10 degrees) and two rectangular shutters (widths 5 and 10 µm). Measured PDL curves are from two dies A and B. b) Four arrow shaped shutters (angles 45, 20, 15 and 10 degrees) with a sharp tip from samples A, B and C. Fiber's WD is 310 µm.

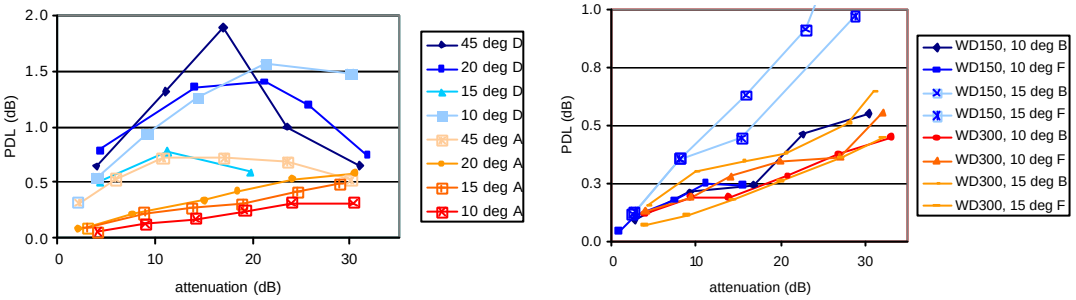

(a) (b)

Figure 6.27. PDL versus attenuation. a) Four arrow shaped shutters with flat tips of 3 µm (sample D) and four arrow shaped shutters with sharp tips (sample A). Fiber's WD is 310 µm. b) measured with two different fibers with a working distance of 150 and 310 µm. Arrow type shutter, samples B and F.

6.6 WDL and PDL sensitivity to fiber alignment

The PDL and WDL sensitivity with the chosen fiber was studied by making packaged samples with two fibers mounted, aligned and attached to the silicon dies. The WDL and PDL were studied for fibers, fiber alignment, and MEMS mirror. Direct and reflection coupling corresponding to the TVOA and RVOA configurations were studied (see figure 6.2). The purpose of these tests was to study the optical quality and reproducibility of the alignment. The samples were fully packaged MEMS dies and the results directly revealed the manufacturing quality of the back-end process. Furthermore the tests showed the feasibility of the selected fiber in the application. Final approval of the fiber for the application was based on these results. The fiber pairs were chosen randomly from the fiber batch. The MFD in the batch varied between 15.5 µm and 19.2 µm. The nominal WD was 300 µm. The variation in the WD was not measured. The fiber pairs were manually aligned in silicon grooves (see figures 6.2 and 6.7).

The average insertion loss for a direct and reflection coupling was 0.80 dB and 1.03 dB, respectively. Standard deviation of the insertion loss was 0.3 dB in both cases. Total number of sample dies with fiber pairs mounted, aligned, and packaged in

TVOA and in RVOA configuration was 200, of which only these with insertion loss below 2 dB were included in the study. Figure 6.28 shows the measured PDL for the two studied cases. Average PDL for TVOA configuration was 0.020 dB with a standard deviation of 0.009 dB (number of samples was 194). Average PDL for RVOA configuration was 0.078 dB with a standard deviation of 0.016 dB (number of samples was 178).

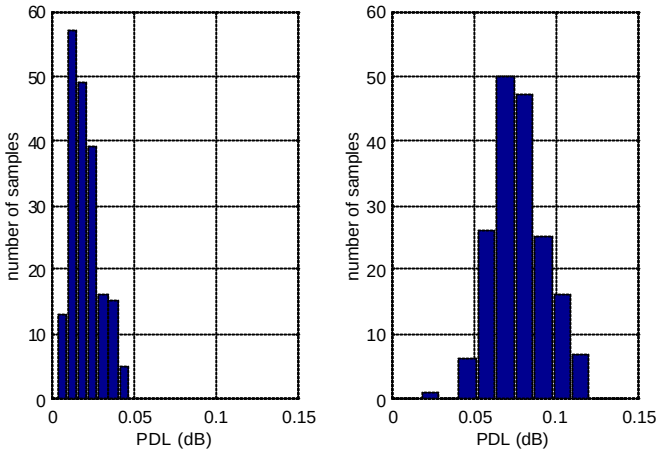

Figure 6.28. Measured PDL dispersion of aligned fibers for TVOA (left) and RVOA configuration (right).

Figure 6.29 shows the measured WDL for the two studied cases. Average WDL for TVOA configuration was 0.12 dB with a standard deviation of 0.11 dB (number of samples was 194). Average WDL for RVOA configuration was 0.13 dB with a standard deviation of 0.12 dB (number of samples was 178).

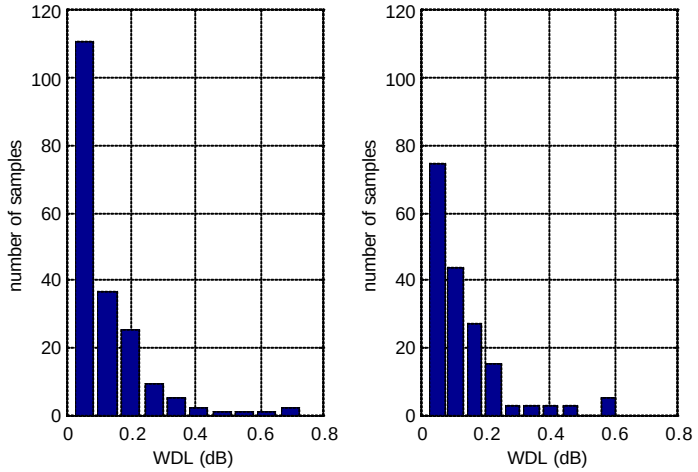

Figure 6.29. The measured WDL at zero attenuation state for TVOA (left) and RVOA (right).

The PDL sensitivity of the TVOA was studied by shifting the shutter's relative position to the beam waist (d_S). These measurements were taken with TVOA dies and with two different MFDs, as shown in figure 6.30. The PDL was measured later with the same die fully packaged using fibers with a MFD of 19 μm. Figure 6.31 shows the evolution of PDL versus attenuation as the shutter was shifted from the beam waist closer to the input fiber. Similar results were obtained when the shutter was shifted towards output fiber. The shutter was arrow type with tip angle of 10 degrees.

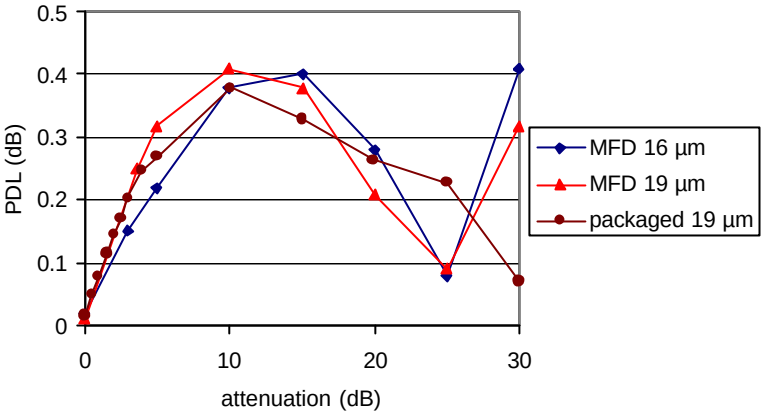

Figure 6.30. Comparison of PDL of TVOA using fibers with a MFD of 16 µm and 19 µm, and the result after doing the final packaging using a fiber pair with a MFD of 19 µm.

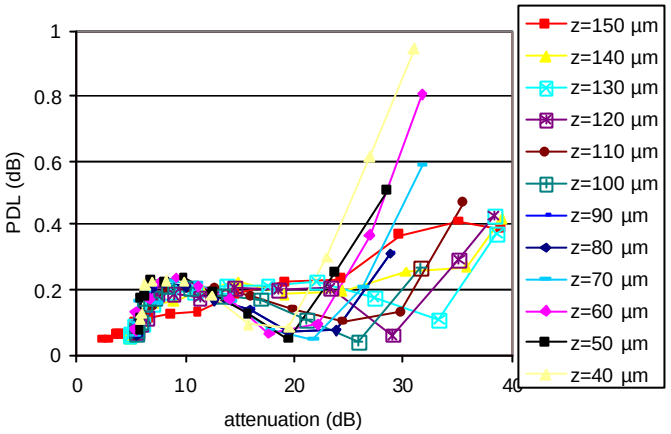

Figure 6.31. Typical evolution of PDL as the shutter position was changed from the beam waist (*z*=150 µm). The shutter was moved gradually closer to the input fiber. The MFD of the fibers was 16.3 and 18.4 µm.

6.7 Process non-idealities

The mask layout cannot be perfectly transferred to silicon and geometrical dimensions are slightly changed in the lithography and etching processes. This applies especially when considering vertically thick structures such as 80 µm SOI layer. Variation in geometrical dimensions due to the process was studied to identify necessary design corrections. The critical dimensions (CD) on the mask were measured by the reticle mask manufacturer. The critical dimensions were the beamwidth of the spring (CD_1) and the comb finger width (CD_2). The accuracy of the reticle mask was found to be better than 0.1 µm. It was necessary to take into account the variation in the sidewall verticality with thick SOI layer, as shown in the actuator design. The sidewall verticality was divided into two separate parameters to take into account the different local conditions, or feature dependency on the wafer. This effect can be reduced by an appropriate layout design. The variation in substrate thickness and in the process was taken into account using parameters listed in table 6.8.

The on-wafer linewidth variation ΔCD_1 and ΔCD_2 was initially too large to include in the device model with a constant parameter over the wafer. Optimization of the mask layout would have been possible by increasing the linewidth linearly from nominal at the center of the wafer, to the maximum value indicated by the parameters CD_1 and CD_2. This would have necessitated a contact mask. In the volume production with a reticle mask this change could be compensated by adjusting the exposure parameters in the lithography step or by using discreet layouts on the reticle for different wafer sections.

Figure 6.32 shows a SEM picture of test structure processed using a contact mask on 4" wafer. These test structures resemble the comb finger array of an electrostatic actuator. The linewidth measurements were taken using a SEM and calibrated image processing software. Several width measurements were taken to acquire the average width due to high surface roughness. The sideline of the beams and the fingers appear quite coarse at the surface level. The peak-to-peak roughness was 150 to 200 nm (figure 6.32). Table 6.4 shows the linewidth measurement results from one of the test wafers (W#2361). The results from two different sets structures are presented. Set I was designed to resemble the spring beams and set II the comb fingers of the electrostatic actuator. The linewidth was reduced from nominal value by 1.2 µm while the standard deviation is 0.1 µm. The peak-to-peak variation for set I and set II was 0.54 µm and 0.42 µm, respectively. Figure 6.33 shows the linewidth change dependency against distance from the center of the wafer for each wafer in the batch. The linewidth dispersion was larger towards the edge of the wafer. All four wafers showed similar behaviour with an average linewidth reduction of 1.1 µm to 1.3 µm with standard variation of 0.1 µm as summarized in table 6.5. The two sets (I and II) showed the same average change.

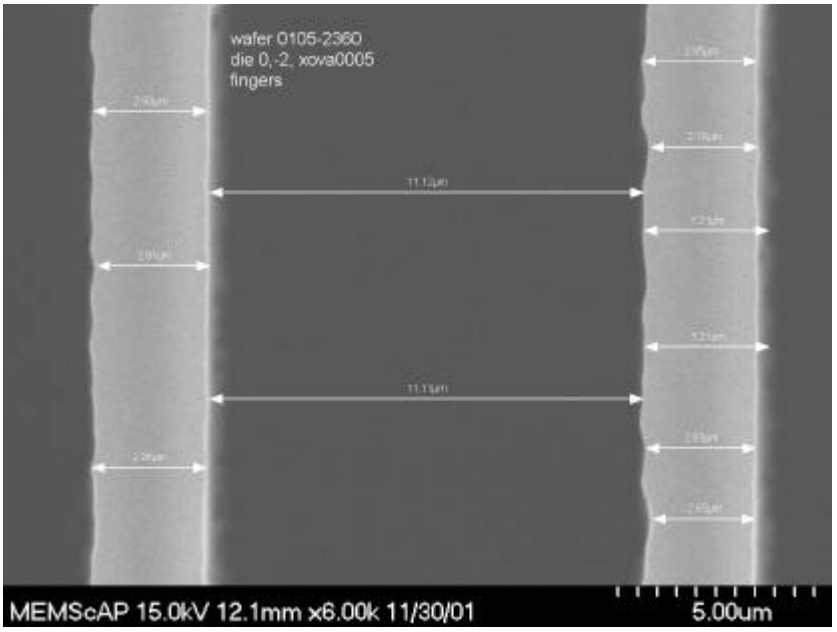

Figure 6.32. The CD measurements were taken with a SEM tool combined with calibrated image processing software. Shorter arrows indicate minimum and maximum beam width, longer arrows indicate the gap between the beams. Due to the surface roughness several width measurements were taken to acquire the average width. On the right side two short arrows indicate the estimated width of the beam at the bottom level from the non-focused image. Sample was wafer W#2360.

Table 6.4. Measured absolute ΔCD_1 and ΔCD_2 of test structures from 20 points for one typical wafer (W#2361). Set 1 was a long narrow beam resembling folded beams without close by structures (distance >50 µm) and set 2 had short narrow beams located close to each other so as to resemble comb finger plate structure (distance <14 µm). The average ΔCD_1 and ΔCD_2 was 1.2 µm with standard deviation of 0.1 µm.

	Set 1				Set 2			
die	**min**	**max**	**nom.**	**average ΔCD_1**	**min**	**max**	**nom.**	**average ΔCD_2**
-5,1	2.70	2.99	4.0	1.16	2.80	2.96	4.0	1.12
-4,1	2.68	2.88	4.0	1.22	2.78	2.93	4.0	1.15
-3,1	2.71	2.91	4.0	1.19	2.80	3.00	4.0	1.10
-2,1	2.56	2.85	4.0	1.30	2.73	2.89	4.0	1.19
-1,1	2.78	2.96	4.0	1.13	2.68	2.91	4.0	1.21
0,1	2.58	2.81	4.0	1.31	2.74	2.90	4.0	1.18
1,1	2.62	2.84	4.0	1.27	2.86	2.92	4.0	1.11
2,1	2.65	2.78	4.0	1.29	2.62	2.91	4.0	1.24
3,1	2.71	2.84	4.0	1.23	2.67	2.91	4.0	1.21
4,1	2.71	2.84	4.0	1.23	2.80	3.02	4.0	1.09
5,1	2.58	2.70	4.0	1.36	2.86	2.95	4.0	1.10
1,5	2.64	2.84	4.0	1.26	2.67	2.91	4.0	1.21
0,4	1.80	1.96	3.0	1.12	2.74	2.96	4.0	1.15
0,3	2.76	2.82	4.0	1.21	2.80	2.88	4.0	1.16
0,2	1.67	1.89	3.0	1.22	2.77	2.91	4.0	1.16
0,-1	1.74	1.85	3.0	1.21	2.68	2.83	4.0	1.25
0,-2	2.74	2.84	4.0	1.21	2.66	2.88	4.0	1.23
0,-3	2.74	2.92	4.0	1.17	2.78	2.89	4.0	1.17
0,-4	2.78	2.88	4.0	1.17	2.75	2.98	4.0	1.14
-1,-5	2.84	3.10	4.0	1.03	2.86	3.04	4.0	1.05
Min. measured ΔCD (µm)				**0.90**				**0.96**
Max. measured ΔCD (µm)				**1.44**				**1.38**
Average ΔCD (µm)				**1.21**				**1.16**
Standard deviation, σ (µm)				**0.12**				**0.11**

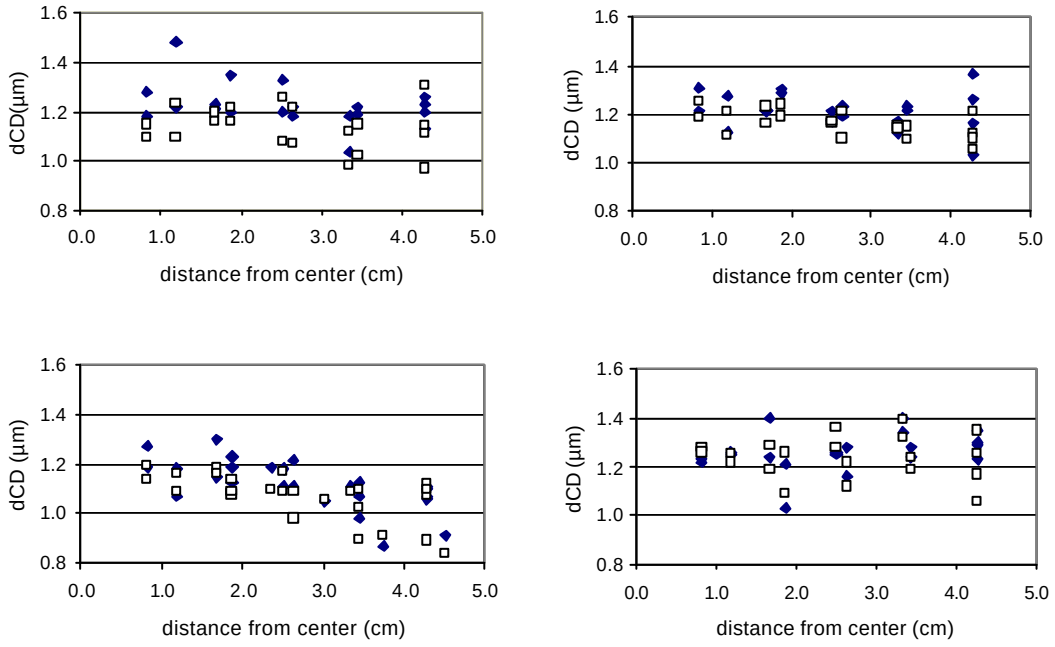

Figure 6.33. The measured absolute value of ΔCD of the two test structure sets (see previous table) on batch 1 of four wafers (W#2350,#2360,#2361,#2413). The rectangles (ð) and diamonds (♦) represent set 1 and set 2, respectively. The linewidth was reduced by ΔCD on the wafer compared to the nominal value.

Table 6.5. Summary of the CD measurements from the four wafers in batch 1. The values indicate change from the nominal linewidth on the mask.

set	parameter	W#2350	W#2360	W#2361	W#2413
I	ave. (µm)	-1.1	-1.2	-1.2	-1.3
	std.dev. σ (µm)	0.1	0.1	0.1	0.1
II	ave. (µm)	-1.1	-1.1	-1.2	-1.3
	std.dev. σ (µm)	0.1	0.1	0.1	0.1

The process quality was improved later as shown in figure 6.34. The linewidth measurement was simplified with less individual measurements along the beam as the peak-to-peak width variation was reduced below 100 nm. Batch-to-batch variation was studied by characterizing another set of wafers as shown in figure 6.35, and summarized in table 6.6.

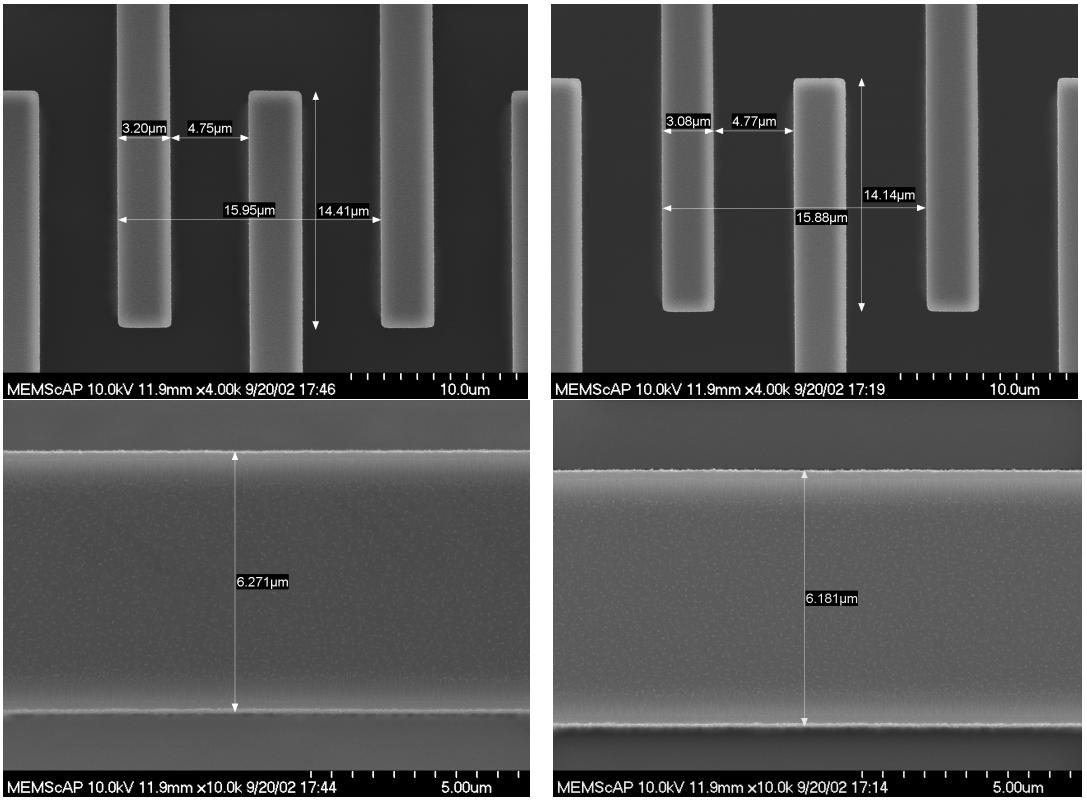

Figure 6.34. Typical CD measurement was simplified after the process was stabilized and the beams had smooth sidewalls. The upper pictures show the finger structure, and the lower the spring beams. The samples were from wafers W#0057 and W#0059.

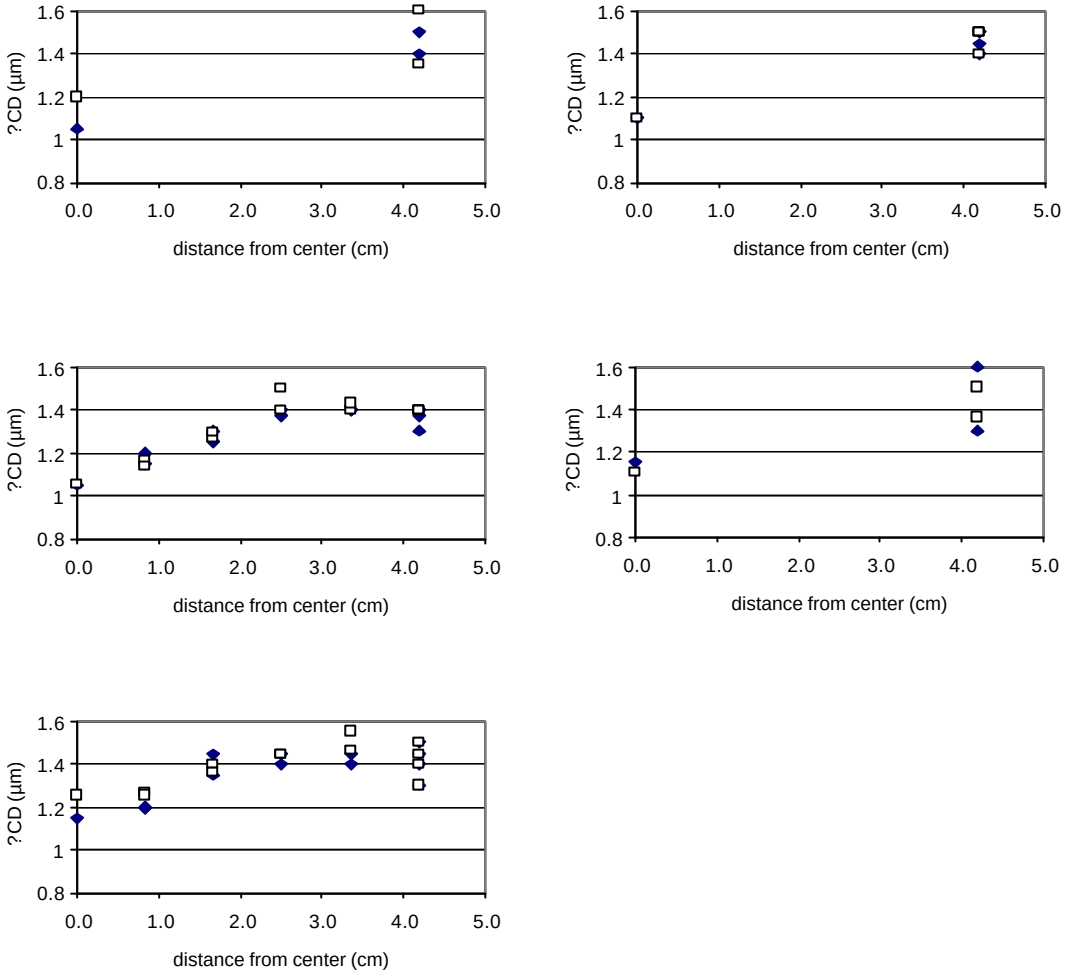

Figure 6.35. The measured absolute value of ΔCD of the spring beams ( ) and comb fingers (♦) of a batch of five wafers. The batch 2 (wafers W#2290, #2242, #2243, #2303, #2305) was fabricated using the same process. The linewidth was narrower by ΔCD on the wafer than on the mask.

Table 6.6. Summary of the CD measurements from the five wafers in batch 2. The values indicate change from the nominal linewidth on the mask.

area	parameter	W#2290	W#2242	W#2243	W#2303	W#2305
spring beams	ave. (µm)	-1.3	-1.4	-1.3	-1.4	-1.4
	std.dev. σ (µm)	0.2	0.2	0.1	0.2	0.1
comb fingers	ave. (µm)	-1.4	-1.4	-1.3	-1.3	-1.4
	std.dev. σ (µm)	0.2	0.2	0.1	0.2	0.2

The control voltage dispersion was measured from batch 2 as shown in figure 6.36, and summarized in table 6.7. A displacement of 40 µm was achieved using average (on wafer) control voltage between 76 and 81 V, before and after the metallization, respectively. The actuator parameters were as summarized in table 6.9 for TVOA.

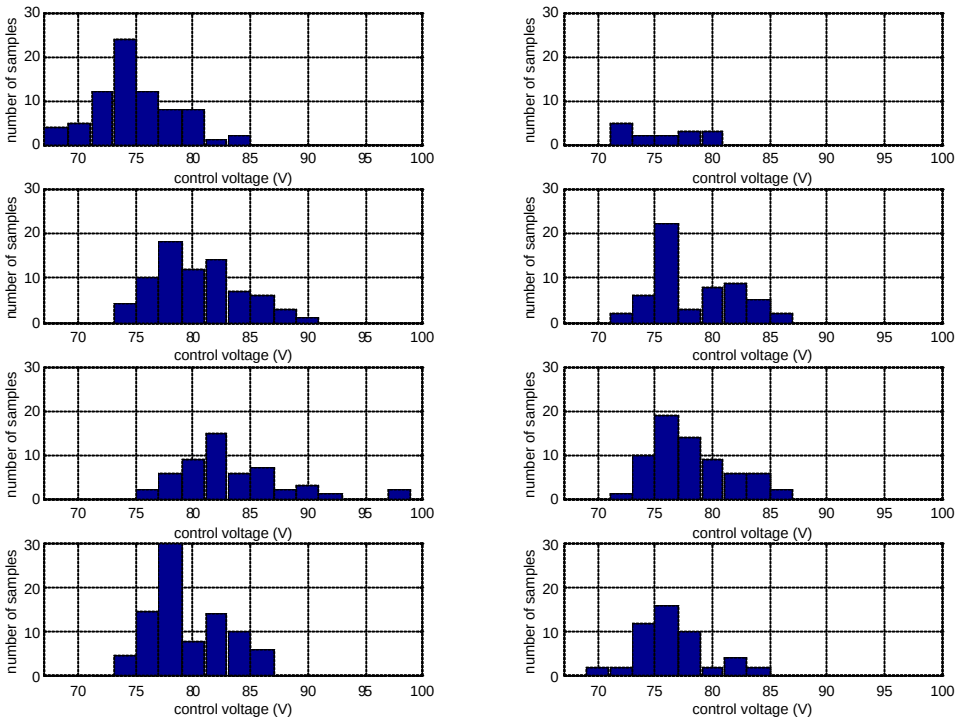

(a) (b)

Figure 6.36. Measured control voltage dispersion in batch 2 a) before the metallization, and b) after the metallization (wafers W#2290, #2242, #2303, #2305).

Table 6.7. Average measured control voltage before and after metallization corresponding with 40 µm displacement. Nominal control voltage was 81 V.

	W#2290	**W#2242**	**W#2243**	**W#2303**	**W#2305**
before metallization (V)	75	82	*	84	79
after metallization (V)	76	80	81	78	78

* data not available

Figure 6.37 (a) shows positive sidewall angles of parallel closely spaced finger plates of the electrostatic comb drive. The nominal gap between the parallel plates in the overlap area was 4 µm and in the wider area 12 µm. Figure 6.37 (b) shows the same effect in a non-symmetric structure with a positive side angle in a narrow trench. The gap between the parallel plates was 6 µm. The average sidewall verticality was found to be 0.5 degrees for closely spaced beams and -0.5 degrees for beams with large opening next to them.

Table 6.8 summarizes the measured process parameters for linewidth change (DCD_1 and DCD_2), verticality for spring beams (a_1), verticality for finger beams (a_2) and SOI layer thickness Dh variation (SOI wafer manufacturer's specification).

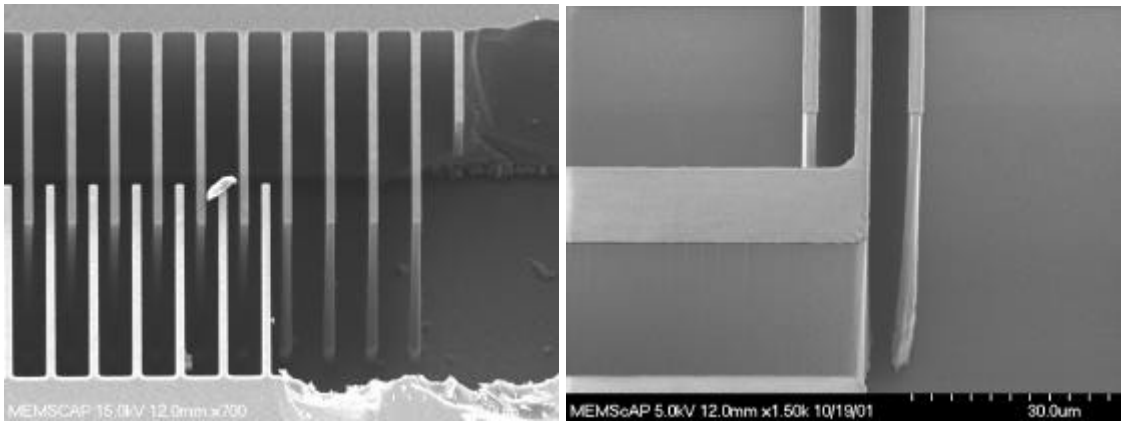

(a) (b)

Figure 6.37. a) A SEM picture of the comb fingers with a positive sidewall angle in a narrow trench, and b) a vertical plate with non-symmetric sidewalls. The right hand vertical sidewall has a positive sidewall angle due to a narrow gap while the left hand has a negative sidewall angle (W#2361).

Table 6.8. Summary of process parameters adapted for the layout design. The values have been obtained from processed structures on 4" wafers.

Parameter	Symbol	Value	s	Unit
On-wafer linewidth variation, center-to-edge (large open areas : spring beams)	ΔCD_1	-1.1 to -1.3	0.1	µm
On-wafer linewidth variation, center-to-edge (narrow trench areas : comb fingers)	ΔCD_2	-1.1 to -1.3	0.1	µm
Sidewall verticality (negative in large open areas: spring beams)	α_1	-0.5	0.05	deg
Sidewall verticality (positive in narrow trenches: fingers)	α_2	0.5	0.05	deg
SOI layer thickness variation	Δh	± 1	-	µm

6.8 Design conclusions and summary

The main design parameters are summarized in table 6.9 for TVOA and RVOA. The actuator design was slightly changed for the RVOA. The beam width was reduced from 7 µm to 5 µm. Thus the control voltage was reduced nearly by half and the resonance frequency was reduced from 2.9 kHz to 1.8 kHz. The beam width was reduced to lower the expected drive voltage below 50 V to ease the driver design. The SOI thickness variation ± 1 µm changed the maximum control voltage U_{max} ± 0.15 % and ± 0.2 % for TVOA and RVOA, respectively. Dispersion of the attenuation versus control voltage due to dispersion in linewidth and sidewall verticality parameters, was calculated by taking into account the measured standard deviation (see table 6.8).

Figure 6.38 shows the attenuation response for TVOA with actuator parameters summarized in table 6.9. The fiber-to-MEMS alignment parameter L_0 is shown to determine the attenuation characteristics versus control voltage.

Figure 6.39 (a) shows the expected dispersion of the control voltage for RVOA. The expected dispersion of attenuation response for RVOA is shown in figure 6.39 (b). The control voltage varied between 26 and 36 V to reach a 30 dB attenuation level.

Table 6.9. Summary of the main parameters of the two designs.

Parameter	Symbol	TVOA	RVOA
Maximum actuation voltage	U_{max}	133 V [1]	80 V [2]
Optical blocking displacement (30 dB)	Y_{OBD}	30 µm / 86 V	17 µm / 30 V
Full travel range	y_{max}	40 µm @133V	40 µm @80V
Spring beams (length × width)	$BL \times BW$	950 × 7.0 µm	950 × 5.0 µm
Spring constant	k_Y	10.8 N/m	3.9 N/m
Comb (fingers, width × gap)	-	140, 4.0 × 4.0 µm	140, 4.0 × 4.0 µm
Moving mass	m	3.2×10^{-8} kg	3.2×10^{-8} kg
Nominal resonance frequency	$Fres$	2.9 kHz	1.8 kHz
Shutter incidence angle	b	10 deg	45 deg
Fiber groove width	W_F	145 µm	200 µm

[1]) nominal from layout, expected to give 100 V after process.
[2]) nominal from layout, expected to give 47 V after process.

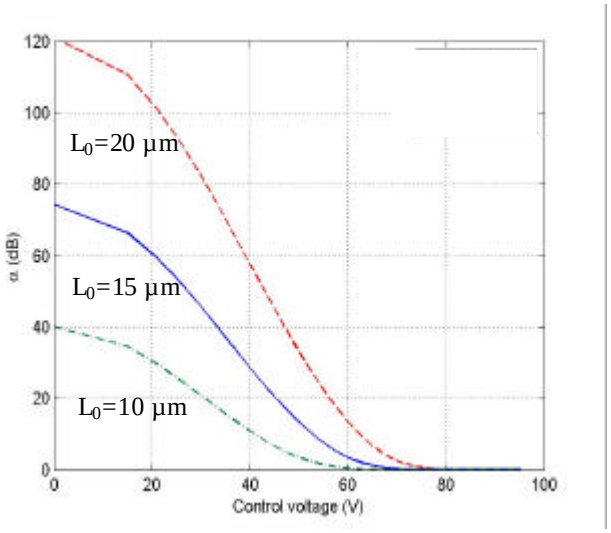

Figure 6.38. Attenuation versus control voltage for TVOA. The parameter L_0 has been varied to study the effect of fiber-to-MEMS alignment accuracy.

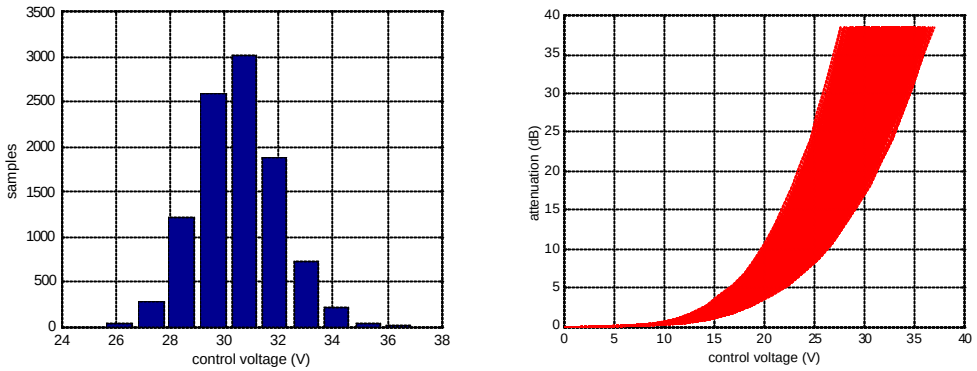

(a) (b)

Figure 6.39. Calculated control voltage dispersion for RVOA. a) Simulated distribution of control voltage based on the measured process parameters. The parameters were assumed to be gaussian distributed with mean and standard deviation as indicated in table 6.8. b) Dispersion on attenuation versus control voltage performance. In the calculation a nominal fiber beam waist was used (w_0=9 µm).

6.9 Pictures of fabricated structures

Figure 6.40 a TVOA structure from an early process run is shown. The spring beams had a H-wall protection in the first structures. In final structures the beams were without these H-walls as shown in figure 6.41. Mechanical stoppers were included in the layout to prevent the pull-in of the comb fingers. Figure 6.42 shows the TVOA shutter. In figure 6.43 is the RVOA mirror structure. Figure 6.44 shows the packaged TVOA and RVOA devices. The package sizes were for TVOA and RVOA were 13×40×8 mm^3 and 30×25×8 mm^3, respectively.

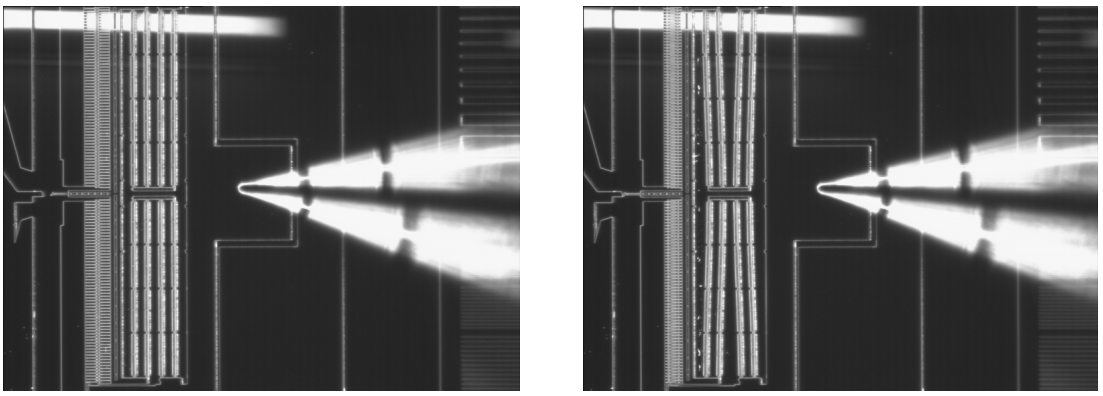

Figure 6.40. The electrostatic actuators were tested with automatic probe station. The measurement revealed the travel range and control voltage (here 40 µm was achieved with a control voltage of 79 V). The displacement is limited by mechanical stoppers. Residuals were visible under the finger rod.

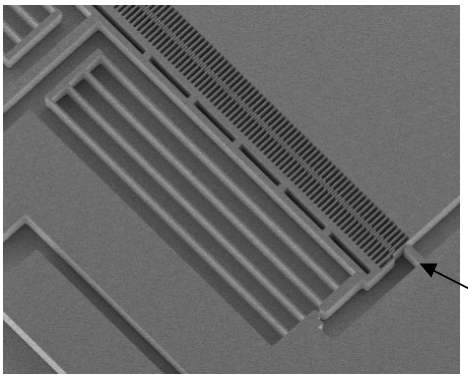

Figure 6.41. A fabricated TVOA chip. Length of the spring beams is 1 mm and nominal beamwidth is 6 µm. The width of the comb fingers is 4 µm, and gap between fingers is 4 µm. The number of fingers is 140. The mechanical stopper to prevent pull-in is indicated with an arrow.

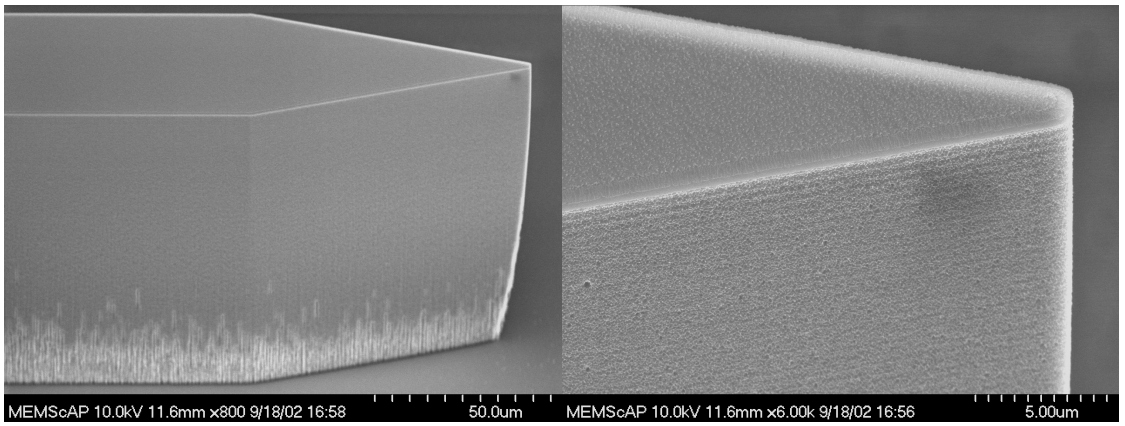

Figure 6.42. The shutter structure used in TVOA [167]. Shutter tip was designed to have a nominal width of 2 µm in the layout. After the process the width was typically between 0.5 µm to 0.7 µm. The cone of the shutter has an angle of 20 degrees i.e. optical incidence angle is 10 degrees.

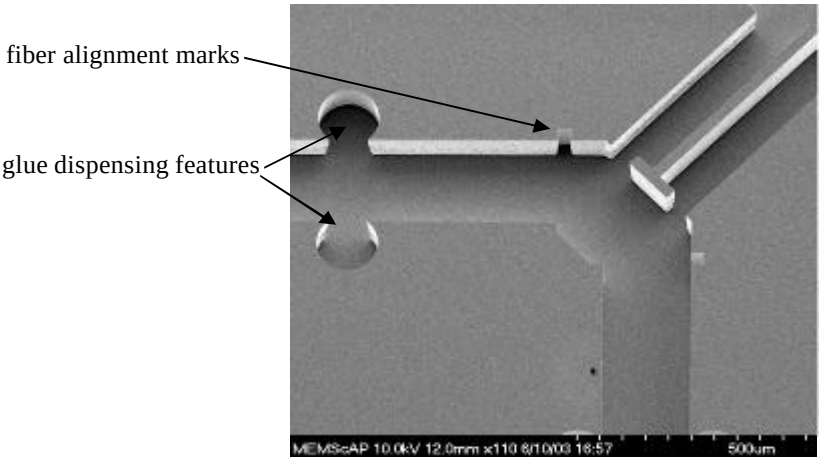

Figure 6.43. The mirror structure used in RVOA. The width of the mirror is 100 µm. The fiber grooves have alignment marks to ease the fiber positioning and features for glue dispensing. Fiber grooves are perpendicular to each other i.e. optical incidence angle is 45 degrees.

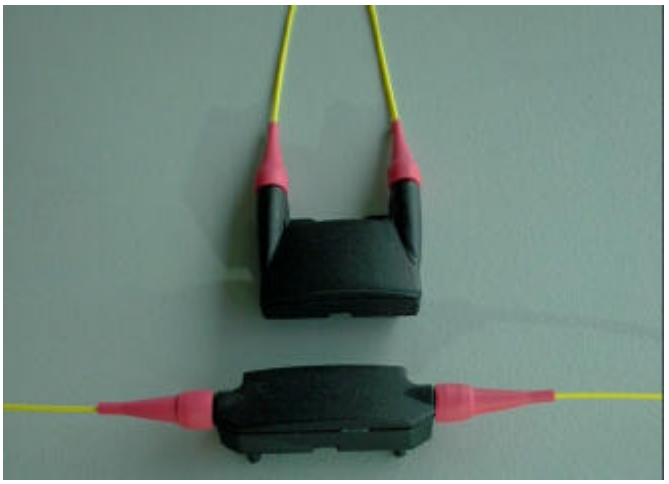

Figure 6.44. The packaged devices TVOA (bottom) and RVOA (on top). The package sizes for TVOA and RVOA were 13×40×8 mm^3 and 30×25×8 mm^3, respectively.

6.10 Optical performance

As several process cycles were carried out, dozens of test components were fabricated in total. Typical results acquired from one fabricated batch of TVOA and RVOA is next presented. The given results present the typical characteristics of the TVOAs and RVOAs.

The optical performance was evaluated by measuring IL, PDL, WDL, RL, TDL, and optical repeatability. The results are presented separately for TVOA and RVOA devices. The insertion loss was measured by applying the cut-back method. PDL and WDL were measured as earlier explained. The values for the PDL were measured at two distinct wavelengths of 1525 and 1630 nm. It is possible that there is some wavelength dependent polarization dependency. To confirm this some samples were scanned over short wavelength span with 0.1 nm wavelength steps. Some ripples occuring that exceeded the PDL measured with 1530 and 1620 nm were found, especially with TVOAs. With RVOA these ripples were substantially lower and did not exceed the values measured at 1530 and 1620 nm.

The return loss measurements were taken by applying a high resolution reflectometer (AQ7413B, Ando Inc., JP). The return loss measurements were verified by applying a standard return loss measurement technique with a return loss module (81612A, Agilent Inc., US).

TDL was studied by tracking the device performance during a temperature scan with an environmental test chamber. The temperature scan was varied in tests a total of 5 or 10 times, from -10 °C to +70 °C. The humidity was un-controlled during the test. The sample was controlled with external electronics therefore the electronic circuitry's temperature dependency was not included in the measured TDL values.

Additionally to following results, the maximum power durability test according to Telcordia requirements was done. The micro mirror and vane showed no degradation after long exposure of several weeks to high power level (400 mW).

6.10.1 TVOA

Figure 6.45 shows typical attenuation characteristics for a batch of 19 TVOAs. The measured attenuation is shown versus the MEMS control voltage. The average MEMS control voltage was 65 V for a fully open VOA. The control voltage that corresponded to 30 dB attenuation varied between 30 and 52 V. All devices delivered the designed 30 dB dynamic attenuation range. The blocking varied between 54 and 72 dB, average measured blocking was 65 dB. The large dispersion on the MEMS control voltage can be considered to be due to several reasons: Variation in the electrostatic actuator control voltage, MFD, and in the fiber-to-shutter initial distance. The non-monotonic response above 50 dB attenuation range was considered to be due to multiple reflections from the shutter cavity walls. Also optical, electrical, and mechanical noise could have caused the ripple in the high attenuation levels. Average insertion loss for the batch was 0.61 dB.

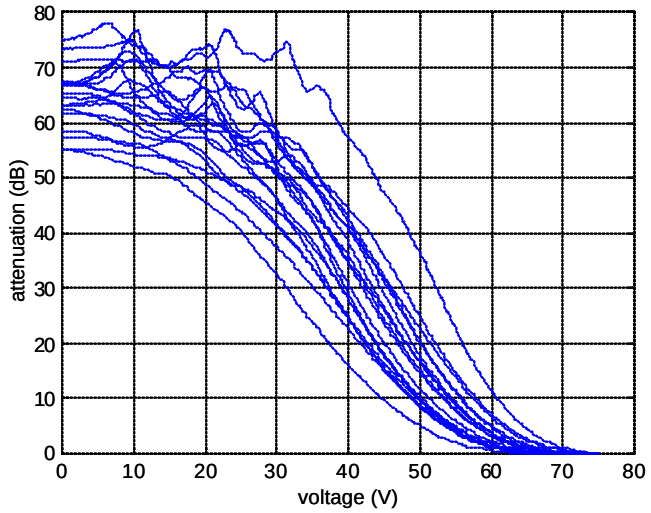

Figure 6.45. Measured attenuation characteristics of 19 packaged TVOA samples. Attenuation is given versus MEMS control voltage. Non-monotonic response at high attenuation level was considered to be mainly due multiple reflections in the shutter cavity.

Figure 6.46 shows typical PDL performance for TVOAs. The samples presented had dies from the same wafer. The sample with the best PDL performance was P246, with insertion loss of 0.6 dB. The worst case (sample P238, insertion loss of 0.62 dB) was identified to have a die from the wafer edge. The PDL dependency on the location can be explained by the linewidth variation over the wafer. The shutter width changed according to the linewidth measurements. Figure 6.47 shows PDL results of one fabricated batch of 18 devices out of the same wafer. The PDL is plotted versus the distance from the center of the wafer. The PDL shows a trend to increase towards the wafer edges.

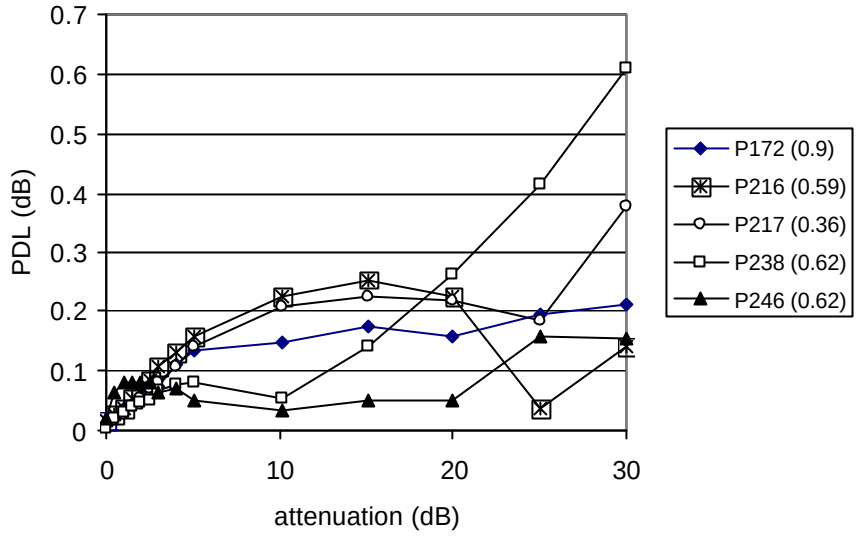

Figure 6.46. Typical PDL versus attenuation curves, measured from five different TVOAs, with dies from the same wafer (W#0049).

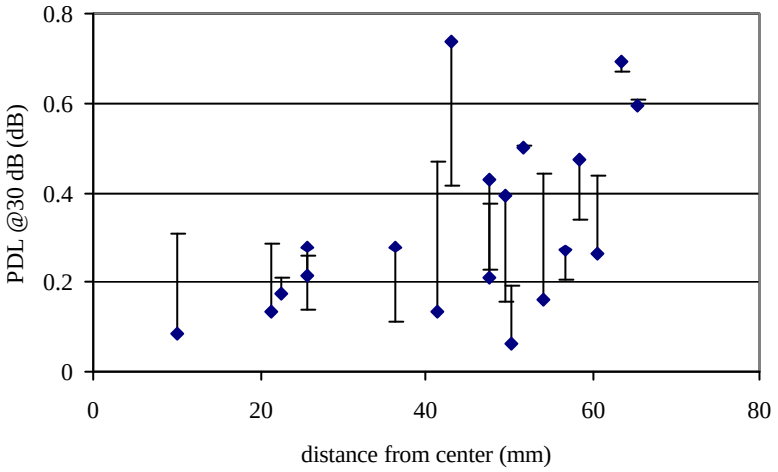

Figure 6.47. The measured maximum PDL and the distance of the die from the center of the wafer. The PDL measurement has been repeated at two wavelengths, 1525 nm (♦) and 1620 nm (-), for each sample.

Figure 6.48 shows the WDL performance for the same samples as in figure 6.46. Average WDL was below 1 dB. The reason for high WDL in sample P216 was later shown to be due to a problem in the fiber attachment.

Figure 6.49 shows typical back reflection spectra for TVOA. At 0 dB attenuation state the back reflections were from the optical fiber, and the return loss level was over 60 dB. When the shutter intercepted the optical beam the back reflection increased but remained below 45 dB. Average return loss was measured to be 51 dB at 30 dB attenuation level. Insertion loss of the sample (P092) was 0.27 dB.

The temperature dependent loss of the fabricated devices was measured without an electronic driver. Figure 6.50 shows a typical measured temperature dependency versus the nominal attenuation setting (sample P092). The insertion loss change was in order of 0.1 dB and maximum TDL was 1.8 dB. At the end of the test

insertion loss was 0.27 dB. The voltage needed to set the same constant attenuation level 30 dB changed –0.5 V when temperature changed from 25°C to –10°C, and –0.9 V when temperature changed from 25°C to 70°C. The measured absolute temperature dependent coefficient for attenuation was 0.040 dB/°C at 30 dB attenuation level.

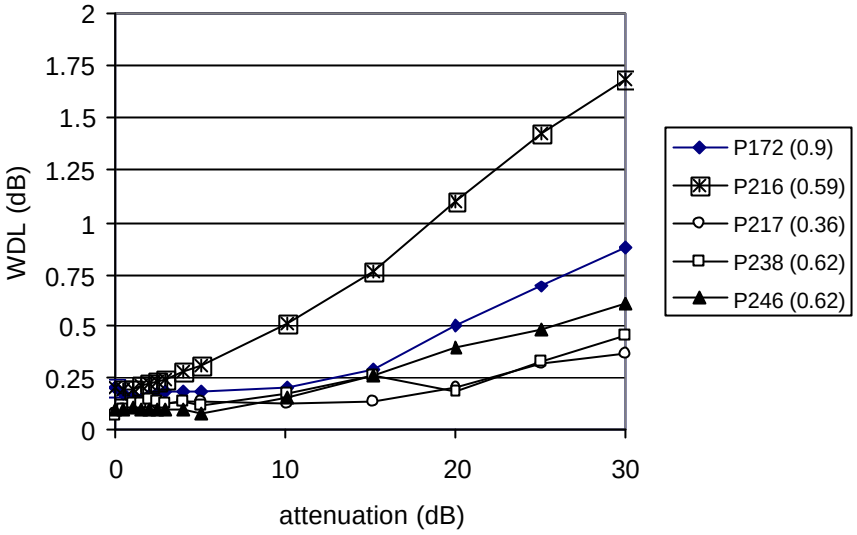

Figure 6.48. Typical WDL performance versus attenuation of TVOA. The peak WDL was typically below 1 dB.

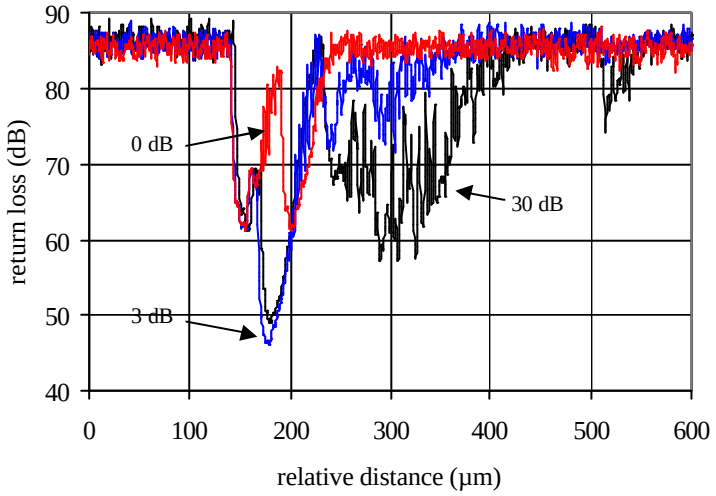

Figure 6.49. Typical TVOA backreflection spectrum versus relative distance for attenuation settings of 0, 3, and 30 dB. The first double peak belongs to the input fiber and can be clearly distinguished from the 0 dB spectra (highest return loss). The intervening shutter caused a back reflection peak at a distance of approximately 150 µm from the fiber. Sample was P092, W#0059.

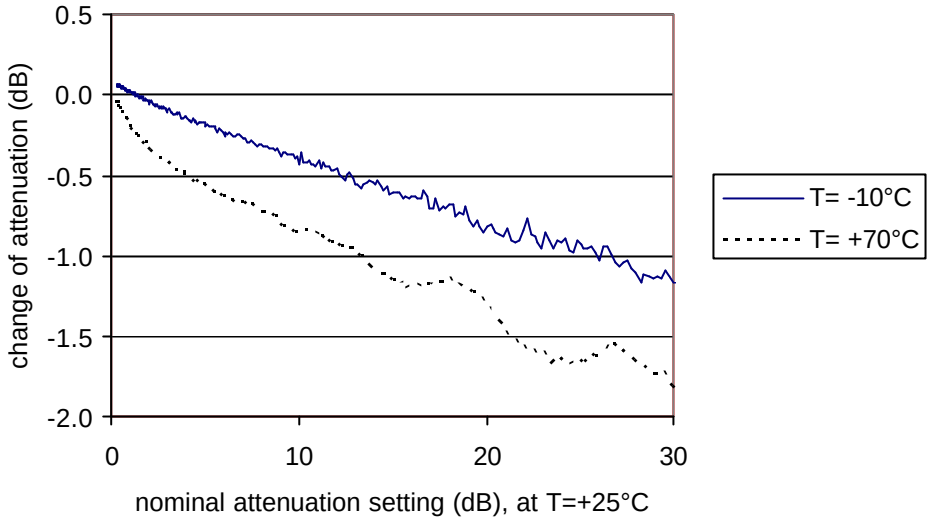

Figure 6.50. Typical TVOA temperature dependency versus attenuation. The two curves represent the change of attenuation measured at temperatures of -10 °C and +70°C. Sample was P092, W#0059.

6.10.2 RVOA

Figure 6.51 shows typical attenuation characteristics for a batch of 12 RVOAs. The measured attenuation is shown versus the MEMS control voltage. The average MEMS voltage was 32 V to reach a 30 dB attenuation level. The control voltage to reach a 30 dB attenuation level varied between 30 and 35 V. All devices delivered the designed 30 dB dynamic attenuation range. All devices reached blocking attenuation over 60 dB. In addition, the RVOA attenuation curves show similar dispersion to TVOA. Average insertion loss was 0.8 dB for packaged devices.

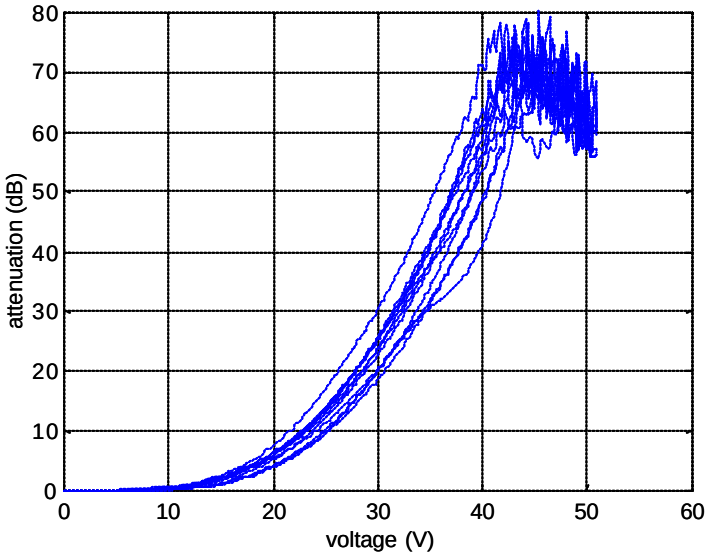

Figure 6.51. Measured attenuation characteristics of 12 packaged RVOA samples. Attenuation is given versus MEMS control voltage.

Figure 6.52 shows typical PDL performance for RVOAs. The samples presented had dies from the same wafer. The lowest PDL was for sample P243 with insertion loss of 0.51 dB. All measured PDL values were at 0.1 dB level or below. The PDL curves are plotted for a wider attenuation range to show the PDL at higher than 30 dB attenuation levels. The worst case performance of the batch reached 0.35 dB at 40 dB attenuation level (sample P248, insertion loss of 1.23 dB). No correlation between the measured PDL and the die location on the wafer was identified. However, it was assumed that the smoothing process was slightly non-uniform over the wafer.

Figure 6.53 shows the WDL performance for same samples as in figure 6.52. Average WDL was below 1 dB.

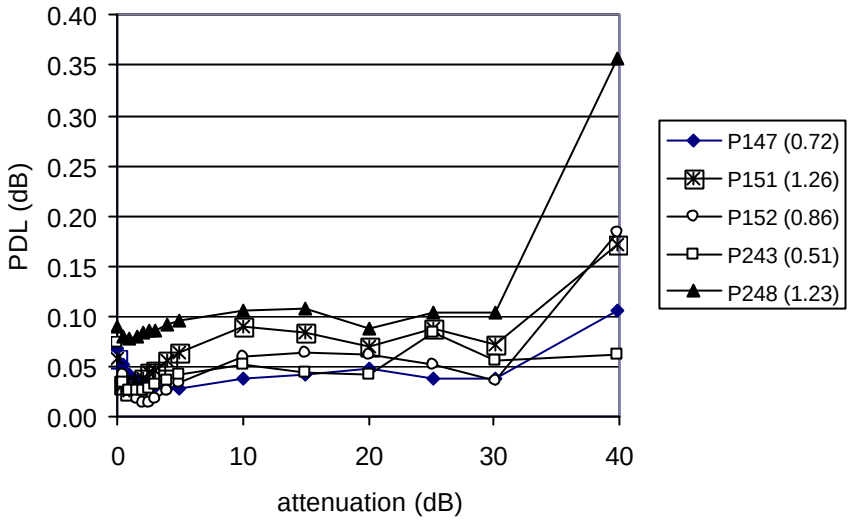

Figure 6.52. Typical PDL versus attenuation curves measured for five different RVOAs with dies from the same wafer (W#0043).

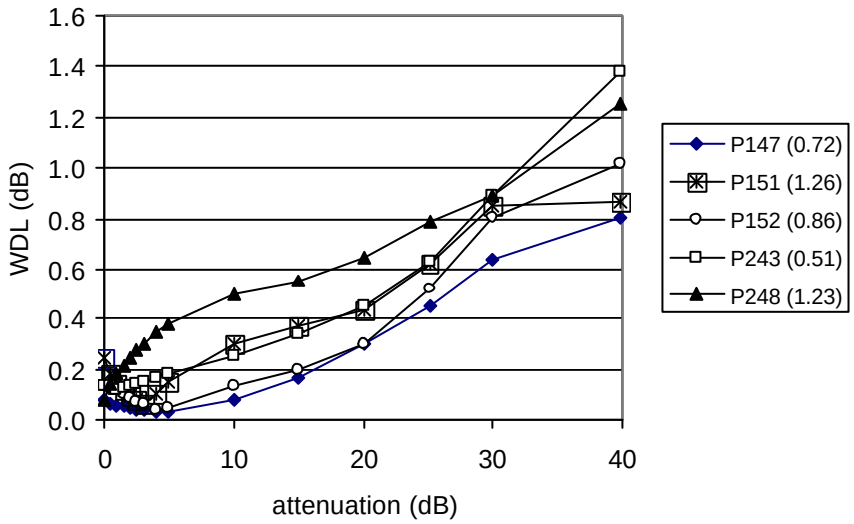

Figure 6.53. Typical WDL performance versus attenuation for RVOA. Peak WDL was below 1.0 dB for nearly all measured devices.

All measured RVOAs had return loss higher than 57 dB. The measured return loss values varied between 57 and 66 dB. The attenuation setting had negligible effect on back reflections.

Figure 6.54 shows a typical temperature dependent behaviour for RVOA. The initial change during the first ramp was substantially larger, and was considered to be due to relaxing the fiber fixation. Subsequent ramps show stabilized operation. The insertion loss change was in order of 0.1 dB and TDL was 1.1 dB. The absolute temperature dependent coefficient of attenuation was 0.025 dB/°C at 30 dB attenuation level.

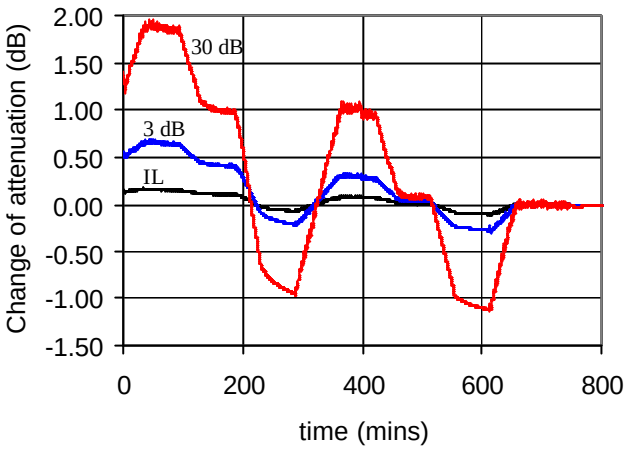

Figure 6.54. Typical measured TDL performance versus attenuation for RVOA. The attenuation was recorded during the temperature ramping at three setting levels. The temperature was ramped in cycles from +25 °C to -10 °C, and returning to +25 °C, and to +70 °C. Two cycles are shown. Sample is P249, W#0043.

6.10.3 Optical repeatability

The optical repeatability (R) for TVOA and RVOA is shown in figure 6.55. The figure shows the average measured repeatability and the worst case performance of all samples measured. The optical repeatability at 30 dB attenuation level was better than 0.02 dB and 0.03 dB for TVOA and RVOA, respectively.

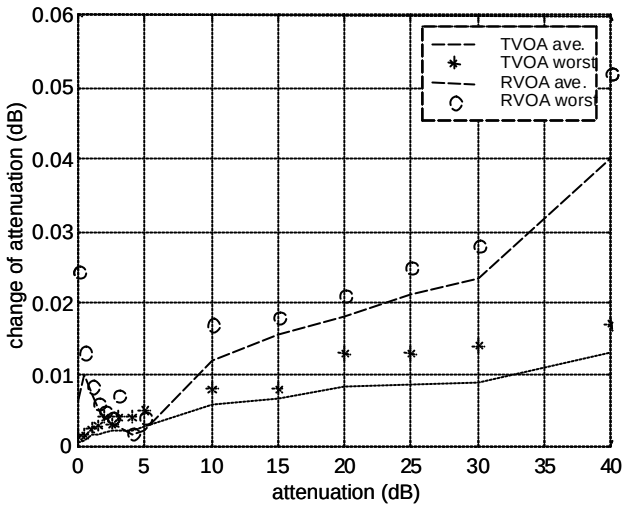

Figure 6.55. The optical repeatability for TVOA and RVOA over the dynamic range. The average repeatability and the maximum change of attenuation setting (the worst case performance) for ten samples is given (W#0049, W#0043).

6.11 Conclusions

Two different configurations for MEMS VOA were introduced in this project. In the manufacturing of the devices, common front-end and back-end processes were applied. The two VOAs had similar MEMS design with the same common building blocks such as lensed fiber, and similar electrostatic actuators. A transmission type VOA based on a blocking vane (TVOA) and a reflection type VOA (RVOA) based on a moving mirror were developed. Distinctive optical performances were identified in both cases to be due to the difference in the optical path.

Table 6.10 summarizes the measured optical performance of the two configurations. In table the average value for each parameter are listed, and in the parenthesis the standard deviation is given. Realistic specification value can be estimated by adding one sigma or two sigmas to the average value, giving a probability of 84% or 97.5% of the manufactured device to fall within the specification, respectively.

The performance of the two devices should be compared against the original target values and state-of-the art devices presented in chapter 2 (see tables 6.1 and 2.1). The insertion loss for TVOA and RVOA was measured to be 0.6 dB and 0.8 dB, respectively. The TVOA clearly meets the specification while the RVOA's IL is considered too high. Less than 84% of the fabricated devices fall within the specification. While the reflection losses are one reason for the difference between the

two, another reason is the fact that in the RVOA a narrower fiber groove (145 µm) was applied compared to the 200 µm grooves in the TVOA. There was less space for fiber manipulation and for adjusting the fiber in the optimum position to reach lower insertion loss. Thus it is assumed that the insertion loss could be improved to meet the specification by applying wider fiber grooves.

The measured average PDL values for the TVOA configuration are below the specification target (0.5 dB). In the TVOA the PDL was shown to be heavily dependent on the shutter tip geometry and thickness. The sensitivity of the PDL to small fluctuations in the manufacturing process seems problematic if considering volume production. Small linewidth variation on-the-wafer can induce significant changes to PDL. The dispersion of the manufactured TVOA components showed that the PDL was dependent on the longitudinal alignment of the fibers. The RVOA has PDL in the order of 0.1 dB over 30 dB dynamic range. The measured standard deviation was 0.03 dB. The RVOA could satisfy the PDL requirement even over larger dynamic range than 30 dB. Meeting the original 0.5 dB PDL specification seems achievable with both configurations.

The average WDL of the TVOA was measured to be below 1 dB. In the RVOA the WDL was higher, partly perhaps because of the worse fiber-to-fiber alignment. The test structures showed that the WDL was due to the fiber alignment quality. The same conclusion was made for the packaged devices. Having an objective of 0.5 dB wavelength dependent loss is difficult to achieve with the chosen optical fiber. The fiber performance could be enhanced by improving the achromatic performance by re-designing the AR coating on the fiber lens. Commonly the WDL is defined only for C or L band. We however defined the WDL over C+L bands, from 1525 to 1620 nm. A reduction of the total wavelength span relaxes the WDL specification. The measured average WDL over C band is then 0.4 dB for both TVOA and RVOA. Also customization of AR coating for narrower wavelength band would further aid to reach lower WDL.

Overall, the RVOA sensitivity to variations in front-end and back-end processes was lower. While typical linewidth changes were recorded to be as small as 0.5 µm from center-to-edge, the TVOA's PDL performance was noticed to deteriorate with dies coming from the edges of the wafers.

The attenuation versus voltage response changes in a similar fashion in both cases but this could be on the other hand compensated by properly calibrating the electronics driver. To produce TVOA dies with low linewidth dispersion over the wafer is very strict, and perhaps unrealistic requirement. The production of RVOA dies with the already established front-end process was successful. Certain modifications are required in the die design to allow improved fiber alignment to achieve lower WDL over C+L bands, and lower insertion loss.

The main objective of the project was to develop a MEMS VOA meeting Telcordia general requirements and optical specifications. These can be considered only as minimum criterias and additional requirements were introduced in the course of the project. For example tighter PDL and WDL specifications were a common request from customers. One of the major specifications was identified to be the package size. Packaged TVOA and RVOA devices have a footprint of 5 and 7 cm^2, respectively. To reduce the package size was identified the biggest challenge to improve the product. When comparing the two devices the TVOA benefits are: low IL, slightly smaller package size, and the possibility of implementing the device in an array configuration. RVOA has very low PDL but higher IL than TVOA. It is possible that the RVOA PDL could be reduced further by choosing an optimum angle between

the fibers so that the incidence angle would be closer to 90 degrees. Additionally the optical repeatability was measured to be worse with RVOA. From a fabrication point of view the TVOA is very sensitive to fiber alignment accuracy when compared to RVOA.

Table 6.10. Performance summary of fabricated MEMS VOAs. In the table average measured IL, PDL, WDL and the standard deviation (in parenthesis) are listed. The results represent typical device performance. For RL the given value is the worst measured and for TDL is given as a typical value.

		TVOA	**RVOA**
IL (dB)		0.6 (0.3)	0.8 (0.3)
PDL (dB)	**0-10 dB**	0.14 (0.07)	0.07 (0.02)
	10-20 dB	0.17 (0.09)	0.06 (0.03)
	20-30 dB	0.32 (0.20)	0.08 (0.03)
WDL (dB)	**0-10 dB**	0.18 (0.05)	0.35 (0.15)
	10-20 dB	0.45 (0.18)	0.55 (0.24)
	20-30 dB	0.74 (0.28)	0.95 (0.30)
RL (dB)		45	57
TDL[1] (dB/°C)		0.040	0.025
Attenuation repeatability, R (dB)		0.02	0.03

[1]Open loop, at maximum attenuation level without temperature dependency on the electronic driver.

7 DISCUSSION

Various silicon based optical microsystems have been studied in this work. Integrated optical structures and optical micromechanical structures have been designed, manufactured and evaluated. The four studied components were a surface plasmon resonance sensor, thermally tunable integrated optical ring resonator, integrated optical beam combiner, and MEMS variable optical attenuator. These components were all based on silicon technology, and were fabricated on silicon substrate. Again the components represent different fields of sensing and optical communications. The SPR sensor and optical ring resonator devices both have applications in chemical and biochemical sensing [1]. Optical ring resonators have applications in optical communications [54,55,56,57,58,143] and as a sensor structure for instance in optical gyros [142]. The integrated optical beam combiner was meant for a coherent free space communication receiver. Other possible applications are in microwave communications and in astronomy [61,63]. The MEMS VOA is applied in fiber optical communications in modern WDM networks for power management purposes.

The SPR device was based on silicon nitride slab waveguides and on totally reflecting silicon nitride-air mirrors. A three layer slab waveguide was formed on thermally oxidized silicon substrate by growing a silicon nitride core layer with LPCVD and forming a top cladding of low temperature oxide. Mirror elements were formed by etching through the three layer oxide-nitride-oxide structure with a reactive ion etching method. The dies were separated by manually cleaving the wafer. Subsequently, the active 50 nm thick Au-layer was formed by evaporation on the edge of the dies. Source and detector elements were external in this laboratory demonstration that was aimed to show a proof-of-concept: An SPR sensor with integrated optical slab waveguides. The demonstration was successful as the device was measured to be sensitive to humidity. Resonance shift of 3.5 – 4° was measured when humidity was introduced on the active surface. A large discrepancy with theory, that predicts a shift of 17°, was explained through the following reasons: Firstly a large difference could be due to different optical parameters. Error in effective index and metal layer refractive index could change the angular range. Contamination of the active layer before the measurement also could have changed the sensor properties. It is also possible that temperature variation could have changed the resonance properties in an unpredictable way [113].

The demonstrated functionality was achieved using a relatively simple configuration. The device fabrication included manual phases when the dies were separated and mounted on a evaporation jig. It is clear that this fabrication scheme is not feasible in industrial manufacturing. The process steps involved in the die separation and metal layer deposition should be automated. Additionally we recognized possible problems with metal film contamination and stability. The chip has deep mirror grooves that should remain clean to ensure proper functioning of the device. Metallized reflectors could be applied to avoid the possibility of contamination of the mirror grooves. The presented configuration needs more research, and perhaps completely different configurations based on for example silicon waveguide structures could be exploited [110].

The thermally tunable integrated optical ring resonator was based on silicon nitride rib waveguides and poly-silicon heater elements [2]. The introduced integrated thermal control of ring resonator provided an accurate way of controlling the device. Thermal tuning allowed a relatively simple way of tuning through the resonance spectrum of the ring cavity and thus enabled the evaluation of resonator characteristics. The introduced thermal control was based on the temperature dependency of the refractive index of the silicon nitride rib waveguides i.e. on the thermo-optical effect. The waveguide devices were fabricated based on thermally oxidized silicon substrate by growing silicon nitride core with LPCVD. The rib waveguides were wet etched in phosphoric acid and a top cladding oxide layer was formed with a PECVD. Finally resistive poly-silicon elements and an aluminium layer for a waveguide polarizer were formed. The ring cavity length was 6.76 mm with a free spectral range of 26 GHz. Typical finesse values varied between 37 and 111 with contrast values between 0.65 and 0.52, respectively. The deduced propagation loss was between 0.24 and 0.5 dB/cm, depending on the sample. The measured optical performance varied slightly from sample to sample. This was considered to be mainly due to variation in the process that caused changes in linewidth and rib height, and secondly due to varied layout parameters such as the axial distance of the waveguides of the directional coupler. The thermal tuning was demonstrated to be repeatable and to have good accuracy although small hysteresis was measured in the results depending on whether the device was under heating or cooling. Average temperature difference (ΔT) between resonances equaling to FSR was measured to be 7.5 °C. The response time of thermo-optical control was measured. Rise and fall times were measured to be 26 ms and 65 ms, respectively [3]. The response time could be faster with proper thermal design. The applications of ring resonator with thermo-optical control are in optical communications. Thermal control could be applied in sensor structures to tune the device to appropriate operation point i.e. for example to adjust sensor to function in the maximum slope of the resonance peak to enhance sensitivity. Naturally design and the waveguide structure need modifications depending on the application.

Four test devices for integrated beam combiner circuits have been designed, fabricated, packaged, and optically evaluated [146]. The target was to study the feasibility of integrated optical technology to replace bulky and cumbersome PM-fiber couplers in a phased array antenna demonstrator at the Technical University of Vienna [60,146]. The devices were based on silicon oxynitride waveguide technology. The waveguide structure was fabricated with PECVD on silicon substrate. The waveguide propagation loss was measured to be 0.4 dB/cm at the application wavelength of 1.064 µm. To combine the sub-aperture signals we applied multi mode interference devices as 3 dB couplers. These 3 dB couplers exhibited an imbalance of less than 0.5 dB. The excess loss of the coupler was measured to be between 2.2 and 7 dB. Insertion loss of the test devices varied depending on the actual configuration. The best measured insertion loss for three cascaded 3 dB couplers was measured to be between 14.0 and 15.8 dB. Single coupler insertion loss was between 10.5 and 12.6 dB. Large variation was considered to be due to non-uniform fiber pigtailing.

To meet the requirements of a 32-port needed in the phased array demonstrator several improvements are needed. The propagation loss was close to acceptable, but lower propagation loss would ease the task of meeting the 32-port insertion loss

specification. The excess loss of the MMI couplers should be reduced below 1 dB /coupler. The fiber pigtailing was considered to lack the repeatability and uniformity needed to accomplish a more complex 32-port device. The interfacing and alignment of the pigtails is critical as the signal channel inputs should have equal losses. New architectures for 32-port devices were considered during the work. Applying layouts to avoid waveguide crossings would be attractive to avoid excess loss and crosstalk from crossings. In the interfacing and device evaluation new techniques as presented for example in [150] could be applied.

Two different types of free-space micromechanical optical variable attenuators were designed, fabricated (and packaged) and optically evaluated. The two designs were both based on the same process on a SOI substrate. The first design (TVOA) was a transmission type device with a blocking vane between two lensed fibers controlling the attenuation level. In the second design (RVOA) a moving mirror was used that reflected the beam from one fiber on to another, and the attenuation was controlled by the mirror position [6,7]. The TVOA optical design was based on the angular spectrum method and modal overlap integral. In the case of RVOA, analytical model was applied to rapidly calculate the attenuation response due to lateral and longitudinal misalignment between the input and output fibers. The mechanical model was represented with analytical formulas while the device mechanical stability and functioning was verified with numerical simulation based on FEA. Recently analytical formulas in closed form for modeling free space VOAs were presented [168]. Applying analytical models in a closed form as presented in the case of RVOA is an attractive choice to speed up the modeling and design work.

In the fabrication deep silicon etching (80 µm) was done by applying reactive ion etching. Structures with aspect ratios of 1:26 were used. After deep silicon etching a smoothing step was done to achieve good optical quality on the blocking vane and on the mirror. A gold metallization was done to make the vane and the mirror opaque. A nominal thickness of 600 nm was deposited on the wafers. The same metallization layer also served as a wire bonding layer. An automatic scribe and break tool was used to separate the dies. Several sample devices were produced by aligning and fixing optical fibers in the dies.

Packaged devices were optically tested in a semi-automatic test bench. The measurements yielded insertion loss, polarization sensitivity, wavelength dependency, return loss, optical repeatability and temperature dependency. Main results for TVOA included IL of 0.6 dB, PDL below 0.32 dB over dynamic range of 30 dB, and WDL below 0.8 dB. Return loss was measured to be typically higher than 45 dB. Main results for RVOA included IL of 0.8 dB, PDL below 0.1 dB over dynamic range of 30 dB, and WDL below 1.0 dB. Return loss was typically higher than 57 dB. The optical performance of RVOA was considered better as very low PDL was achieved (even below 0.1 dB over 40 dB dynamic range). While the demonstrated IL and WDL could be reduced to acceptable level by improving the fiber fixing procedure and by proper customization of the AR-coating of the fibers. However, the demonstrated WDL is given for C+L band, and is comparable with WDL of state-of-the-art devices. The attenuation setting was measured to have moderate dependency on the temperature. TDL was measured to be 0.04 and 0.025 dB/°C for TVOA and RVOA, respectively (at maximum attenuation setting). These values should be projected against the performance of MZI

type PLC VOAs [169]. Resistive thin films, often Titanium, suffer from the resistivity changes when environment temperature changes. Integrated optical VOAs tested were shown to have as high as 0.05 dB/°C temperature dependency already at 10 dB attenuation level due to resistivity changes of heater elements [169].

The bottleneck of our devices proved to be their size and not their optical performance. The package size of the TVOA and RVOA takes footprints of 12.7×40 mm^2 and 25×30 mm^2. Design modifications are needed to reduce the package size when single channel VOAs with footprints below 6×30 mm^2 are already available and 20 channel VOAs with footprints of 70×28 mm^2 [170,171].

REFERENCES

[1] J.Lekkala, J.Sadowski, J.Kimmel, P.Katila, and J.Aarnio, Integrated optics in biosensor design, *Proc. of SPIE*, vol.**2631,** pp.2-13 (1995)

[2] P.Heimala, P.Katila, J.Aarnio, and A.Heinämäki, Thermally tunable integrated optical ring resonator with poly-Si thermistor, *J. of Lightwave Technology*, **14**(10), pp.2260-2267 (1996)

[3] P.Katila, P.Heimala, and J.Aarnio, Thermal response characteristics of thermo-optically controlled ring resonator on silicon, *Electronics Letters*, **32**(11), pp.1005-1006 (1996)

[4] P.Katila, T.Aalto, P.Heimala, and M.Leppihalme, Optical waveguides for 1064 nm and chip pigtailing with PM fibers, *International Conference on Space Optics (ICSO)*, pp.635–640 (2000)

[5] T.Aalto, P.Heimala, and P.Katila, Integrated optical circuits: An overview and an optical beam combiner circuit, *15th European Conference on Circuit Theory and Design (ECCTD)*, vol.III, pp.157-160 (2001)

[6] A.Bashir, B.Saadany, P.Katila, A.H.Morshed, and D.Khalil, PDL modeling in a transmission type MEMS based VOA, *4th Workshop on MEMS for Millimeterwave Communications (MEMSWAVE)* (2003)

[7] A.Bashir, P.Katila, N.Ogier, B.Saadany, and D.A.Khalil, A MEMS based VOA with very low PDL, *IEEE Photonics Technology Letters*, **16**(4), pp.1047-1049 (2004)

[8] J.Aarnio, S.Honkanen, Pintaplasmoniresonanssiin perustuva integroidun optiikan anturi nesteiden ja kaasujen mittaamista varten sekä menetelmä anturin valmistamiseksi, *Finnish patent* No. 91806 (1994)

[9] G.K.Ananthasuresh, Position paper in applications area: Manufacturing issues in integrated systems of small size, *NSF Workshop on Manufacturing of Micro-electro-mechanical systems*, pp.65-67 (2000)

[10] M.Leppihalme, P.Katila, P.Heimala, T.Aalto, M.Blomberg, and S.Tammela, Si-based integrated optical and photonic microstructures, *Proc. of SPIE*, vol.**3936**, pp.2-15 (2000)

[11] M.K.Smit, New focusing and dispersive planar component based on an optical phased array**,** *Electronics Letters*, **24**(7), pp.385-386 (1988)

[12] A.Liu, R.Jones, L.Liao, D.Samara-Rubio, D.Rubin, O.Cohen, R.Nicolaescu, and M.Paniccia, A high-speed silicon optical modulator based on a metal-oxide-semiconductor capacitor, *Nature*, **427**(6974), pp.615-618 (2004)

[13] M.Popovic, K.Wada, S.Akiyama, H.A.Haus, and J.Michel, Air trenches for sharp silica waveguide bends, *J. of Lightwave Technology*, **20**(9), pp.1762-1771 (2002)

[14] J.W.Judy, Microelectromechanical Systems (MEMS) - Their design, fabrication, and broad range of application, *J. of Smart Materials*, **10**(6), pp.1115-1134 (2001)

[15] M.Kawachi, Silica waveguides on silicon and their application to integrated-optic components, *Optical and Quantum Electronics*, **22**, pp.391-416 (1990)

[16] K.Okamoto, Integrated optics in planar lightwave circuits, *IEEE Lasers and Electro-Optics Society Meeting, lecture* (1997)

[17] J.A.Walker, The future of MEMS in telecommunications networks, *J. of Micromechanics and Microengineering*, **10**(3), pp.R1-R7 (2000)

[18] R.R.A.Syms, and D.F.Moore, Optical MEMS for telecoms, *Materials Today*, **5**(7), pp.26-35 (2002)

[19] Zh.Alferov, The history and future of semiconductor heterostructures, *Semiconductors*, **32**(1), pp.1-14 (1998)

[20] F.P.Kapron, D.Keck, and R.D.Maurer, Radiation losses in glass optical waveguides, *Applied Physics Letters*, **17**(10), pp.423-425 (1970)

[21] N.Takato, M.Kawachi, M.Nakahara, and T.Miyashita, Silica-based single-mode guided-wave devices, *Proc. of SPIE*, vol.**1177**, pp.92-100 (1989)

[22] G.N.Brabander, J.Boyd, and G.Beheim, Integrated optical ring resonator with micromechanical diaphragms for pressure sensing, *IEEE Photonics Technology Letters*, **6**(5), pp.671-673 (1994)

[23] F.Prieto, B.Sepulveda, A.Calle, A.Llobera, C.Dominguez, A.Abad, A.Montoya, and L.M.Lechuga, An integrated optical interferometric nanodevice based on silicon technology for biosensor applications, *Nanotechnology*, **14**(8), pp.907-912 (2003)

[24] S.Valette, State of the art of integrated optics technology at LETI for achieving passive optical components, *J. of Modern Optics*, **35**(6), pp.993-1005 (1988)

[25] O.Manzardo, H.P.Herzig, C.Marxer, and N.F.de Rooij, Miniaturized time-scanning Fourier transform spectrometer based on silicon technology, *Optics Letters*, **24**(23), pp.1705-1707 (1999)

[26] T.Bestwick, ASOC – A silicon based integrated optical manufacturing technology, *48th IEEE Electronic Components and Technology Conference*, pp.566-571 (1998)

[27] U.Fischer, T.Zinke, B.Schuppert, and K.Petermann, Concepts for optical waveguide switches in silicon, *Proc. of SPIE*, vol.**2449**, pp.332-339 (1995)

[28] M.Naydenkov, and B.Jalali, Advances in silicon-on-insulator photonic integrated circuit (SOIPIC) Technology, *IEEE International SOI Conference*, pp.56-66 (1999)

[29] T.Aalto, P.Heimala, and P.Katila, Integrated optical switch based on SOI-technology, *Physica Scripta*, **T79**, pp.123-126 (1999)

[30] K.Wörhoff, P.V.Lambeck, and A.Driessen, Design, tolerance analysis, and fabrication of silicon oxynitride based planar optical waveguides for communication devices, *J. of Lightwave Technology*, **17**(8), pp.1401-1407 (1999)

[31] M.Hoffmann, and E.Voges, Low temperature nitrogen doped waveguides on silicon with small core dimensions fabricated by PECVD/RIE, 7th *European Conference on Integrated Optics (ECIO)*, pp.299-302 (1995)

[32] B.J.Offrein, R.Germann, G.L.Bona, F.Horst, and H.W.M.Salemink, Tunable optical add/drop components in silicon-oxynitride waveguide structures, *10th European Conference on Optical Communications (ECOC)*, pp.325-326 (1998)

[33] B.Schauwecker, M.Arnold, G.Przyrembel, B.Kuhlow, and C.Radehaus, Optical waveguide components with high refractive index difference in silicon-oxynitride for application in integrated optoelectronics, *Optical Engineering*, **41**(1), pp.237-243 (2002)

[34] H.Bezzaoui, and E.Voges, Integrated optics combined with micromechanics on silicon, *Sensors and Actuators A*, **29**, pp.219-223 (1991)

[35] C.H.Henry, R.F.Kazarinov, H.J.Lee, K.J.Orlovsky, and L.E.Katz, Low-loss Si_3N_4-SiO_2 optical waveguides on Si, *Applied Optics*, **26**(13), pp.2621-2624 (1987)

[36] H.J.Lee, C.H.Henry, K.J.Orlovsky, R.F.Kazarinov, and T.Y.Kometani, Refractive-index dispersion of phosphosilicate glass, thermal oxide, and silicon nitride films on silicon, *Applied Optics*, **27**(19), pp.4104-4109 (1988)

[37] W.Stutius, and W.Steifer, Silicon nitride films on silicon for optical waveguides, *Applied Optics*, **16**(12), pp.3218-3222 (1977)

[38] P.Äyräs, S.Honkanen, K.M.Grace, K.Shrouf, P.Katila, M.Leppihalme, A.Tervonen, X.Yang, B.Swanson, and N.Peyghambarian, Thin-film chemical sensors with waveguide Zeeman interferometry, *Pure and Applied Optics*, **7**(6), pp.1261-1271 (1998)

[39] H.Sohlström, and M.Öberg, Refractive index measurement using integrated ring resonators, *8th European Conference on Integrated Optics (ECIO)*, pp.322-325 (1997)

[40] A.Ksendzov, M.L.Homer, and A.M.Manfreda, Integrated optics ring-resonator chemical sensor with polymer transduction layer, *Electronics Letters*, **40**(1), pp.63-65 (2004)

[41] I.Kiyat, C.Kocabas, and A.Aydinli, Integrated micro ring resonator displacement sensor for scanning probe microscopes, *J. of Micromechanics and Microengineering*, **14**(3), pp.374-381 (2004)

[42] D.A.Cohen, J.A.Nolde, A.T.Pedretti, C.S.Wang, E.J.Skogen, and L.A.Coldren, Sensitivity and scattering in a monolithic heterodyned laser biochemical sensor, *IEEE J. of Selected Topics in Quantum Electronics*, **9**(5), pp.1-8 (2003)

[43] J.Homola, S.S.Yee, and G.Gauglitz, Surface plasmon resonance sensors, *Sensors and Actuators B*, **54**(1-2), pp.3-15 (1999)

[44] Biacore AB, Surface plasmon resonance, *Technology Note 1*, BR-9001-15 (2001)

[45] M.Suzuki, F.Ozawa, W.Sugimoto, and S.Aso, Miniaturization of SPR immunosensors, *Analytical Sciences*, **17**, pp.265-267 (2001)

[46] R.D.Harris, B.J.Luff, J.S.Wilkinson, R.Wilson, D.J.Schiffrin, J.Piehler, A.Brecht, R.A.Abuknesha, and C.Mouvet, Integrated optical surface plasmon resonance biosensor for pesticide analysis, *IEE Colloquium on Optical Technology for Environmental Monitoring*, pp.1-6/6 (1995)

[47] R.D.Harris, B.J.Luff, J.S.Wilkinson, J.Piehler, A.Brecht, G.Gauglitz, and R.A.Abuknesha, Integrated optical surface plasmon resonance immunoprobe for simazine detection, *Biosensors & Bioelectronics*, **14**(4), pp.377-386 (1999)

[48] J.C.Abanulo, R.D.Harris, P.H.Bartlett, and J.S.Wilkinson, Waveguide surface plasmon resonance sensor for electrochemically controlled surface reactions, *Applied Optics*, **40**(34), pp.6242-6245 (2001)

[49] M.N.Weiss, R.Srivastava, and H.Groger, Experimental investigation of a surface plasmon-based integrated-optic humidity sensor, *Electronics Letters*, **32**(9), pp.842-843 (1996)

[50] M.Okuno, K.Kato, Y.Ohmori, M.Kawachi, and T.Matsunaga, Improved 8×8 integrated optical matrix switch using silica-based planar lightwave circuits, *J. of Lightwave Technology*, **12**(9), pp.1597–1605 (1994)

[51] R.Kasahara, M.Yanagisawa, T.Goh, A.Sugita, A.Himeno, M.Yasu, and S.Matsui, New structure of silica-based planar lightwave circuits for low-power thermo-optic switch and its application to 8×8 optical matrix switch, *J. of Lightwave Technology*, **20**(6), pp.993-1000 (2002)

[52] L.Guiziou, P.Ferm, J.M.Jouanno, and L.Shacklette, Low-loss and high extinction ratio 4×4 polymer thermo-optical switch, *13th European Conference on Optical Communications (ECOC)*, pp.138-139 (2001)

[53] R.L.Espinola, M.C.Tsai, J,T,Yardley, and R.M.Osgood, Fast and low-power thermo-optic switch on thin silicon-on-insulator, *IEEE Photonics Technology Letters*, **15**(10), pp.1366-1368 (2003)

[54] H.Takahashi, K.Nishimura, and M.Usami, Tunable chromatic dispersion compensator utilizing silica waveguide ring resonator having Mach-Zehnder interferometric variable coupler eliminating crossing point of waveguides, *Lasers and Electro-Optics Society, 15th Annual Meeting of the IEEE (LEOS)*, vol.2, pp.665-666 (2002)

[55] C.K.Madsen, E.J.Laskowski, J.Bailey, M.A.Cappuzzo, S.Chandrasekhar, L.T.Gomez, A.Griffin, P.Oswald, and L.W.Stulz, The application of integrated ring resonators to dynamic dispersion compensation, *All-Optical Networking: Existing and Emerging Architecture and Applications IEEE/LEOS*, pp.TuJ2-29-TuJ2-30 (2002)

[56] K.Sasayama, F.Fruh, T.Kominato, and K.Habara, Photonic frequency-division-multiplexing highway switch using integrated-optic multiple ring resonators, *IEICE Transactions on Communications*, **E78-B**(5), pp.674-678 (1995)

[57] A.Melloni, and M.Martinelli, The ring-based resonant router, *International Conference on Transparent Optical Networks (ICTON)*, vol.1, pp.37-40 (2003)

[58] J.M.Choi, R.K.Lee, and A.Yariv, Control of critical coupling in a ring resonator-fiber configuration: application to wavelength-selective switching, modulation, amplification, and oscillation, *Optics Letters*, **26**(16), pp.1236-1238 (2001)

[59] J.Stulemeijer, F.E.van Vliet, K.W.Benoist, D.H.P.Maat, and M.K.Smit, Compact photonic integrated phase and amplitude controller for phased-array antennas, *IEEE Photonics Technology Letters*, **11**(1), pp.122-124 (1999)

[60] G.Flamand, K.De Mesel, I.Moerman, B.Dhoedt, W.Hunziker, A.Kalmar, R.Baets, P.Van Daele, and W.Leeb, InP-based PIC for an optical phased-array antenna at 1.06 µm, *IEEE Photonics Technology Letters*, **12**(7), pp.876-878 (2000)

[61] M.M.Murphy, and C.R.Pescod, A silica-on-silicon integrated optic interface for microwave sub-systems, *IEEE Workshop on High Performance Electron Devices for Microwave and Optoelectronic Applications*, pp.167-172 (1995)

[62] K.Horikawa, I.Ogawa, T.Kitoh, and H.Ogawa, Photonic integrated beam forming and steering network using switched true-time-delay silica-based waveguide circuits, *IEICE Transactions on Electronics*, **E79-C**(1), pp.74-79 (1996)

[63] F.Malbet, P.Kern, I.Schanen-Duport, J.P.Berger, K.Rousselet-Perraut, and P. Benech, Integrated optics for astronomical interferometry. I. Concept and astronomical applications, *Astronomy and Astrophysics Supplement series*, **138**, pp.135-145 (1999)

[64] P.Haguenauer, J.P.Berger, K.Rousselet-Perraut, P.Kern, F.Malbet, I.Schanen-Duport, and P. Benech, Integrated optics for astronomical interferometry. III optical validation of a planar optics two-telescope beam combiner, *Applied Optics*, **39**(13), pp.1-10 (2000)

[65] K.E.Petersen, Silicon as a mechanical material, *Proc. of IEEE*, **70**(5), pp.420-457 (1982)

[66] http://www.dlpp.com (digital lightwave technology) and http://www.ti.com (Texas Instruments Inc.)

[67] C.Marxer, C.Thio, M-A.Gretillat, N.F.de Rooij, R.Bättig, O.Anthamatten, B.Valk, and P.Vogel, Vertical mirrors fabricated by deep reactive ion etching for fiber-optic switching applications, *J. of Microelectromechanical Systems*, **6**(3), pp.277-285 (1997)

[68] W.-H.Juan, and S.W.Pang, High-aspect-ratio Si vertical micromirror arrays for optical switching, *J. of Microelectromechanical Systems*, **7**(2), pp.207-213 (1998)

[69] D.T.Fuchs, C.R.Doerr, V.A.Aksyuk, M.E.Simon, L.W.Stulz, S.Chandrasekhar, L.L.Buhl, M.Cappuzzo, L.Gomez, A.Wong-Foy, E.Laskowski, E.Chen, and R.Pafchek, A hybrid MEMS-waveguide wavelength selective cross connect, *IEEE Photonics Technology Letters*, **16**(1), pp.99-101 (2004)

[70] P.Katila, D.Khalil, B.Saadany, and A.Bashir, Attenuateur optique variable et matrice de tels attenuateurs, *French patent ref.* 2 837 578 (2003)

[71] E.Ollier, C.Chabrol, T.Enot, P.Brune-Manquat, J.Margail, and P.Mottier, 1×8 micromechanical switches based on moving waveguides for optical fiber network switching, *IEEE/LEOS International Conference on Optical MEMS (MOEMS)*, pp.39-40 (2000)

[72] T.Miura, F.Koyama, and A.Matsutani, Novel variable optical attenuator using hollow waveguides, *IEEE/LEOS International Conference on Optical MEMS (MOEMS)*, pp.189-190 (2002)

[73] S.Kim and S.Nam, Novel MEMS variable optical attenuator with expanded core waveguides, *IEEE/LEOS International Conference on Optical MEMS (MOEMS)*, pp.65-66 (2002)

[74] J.D.Berger, Y.Zhang, J.D.Grade, H.Lee, S.Hrinya, H.Jerman, A.Fennema, A.Tselikov, and D.Anthon, Widely tunable external cavity diode laser based on a MEMS electrostatic rotary actuator, *Optical Fiber Communications (OFC)*, paper Tuj2 (2001)

[75] L.Dellmann, W.Noell, C.Marxer, K.Weible, M.Hofmann, and N.F.de Rooij, 4×4 matrix switch based on MEMS switches and integrated waveguides, *TRANSDUCERS '01, EUROSENSORS XV*, *Dig. of Technical Papers., Conference on Solid-State Sensors and Actuators*, vol.2, pp.1332-1335 (2001)

[76] G.J.Veldhuis, F.N.Krommendijk, and P.V.Lambeck, Integrated optic intensity modulator based on a bent channel waveguide, *Optics Communications*, **168**(5-6)**,** pp.481-491 (1999)

[77] I.E.Day, S.W.Roberts, R.O'Carrol, A.Knights, P.Sharp, G.F.Hopper, B.J.Luff, and M.Asghari, Single-chip variable optical attenuator and multiplexer subsystem integration, *Optical Fiber Communications (OFC)*, pp.72-73 (2002)

[78] O.Solgaard, F.S.A.Sandejas, and D.M.Bloom, Deformable grating optical modulator, *Optics Letters*, **17**(9), pp.688-690 (1992)

[79] J.J.Pan, H.Wu, P.Huang, X.Qiu, and F.Q.Zhou, High-reliability, miniature liquid crystal variable optical attenuator, *National Fiber Optic Engineering Conference (NFOEC)*, pp.1197-1203 (2002)

[80] K.Hirabayashi, and C.Amano, Liquid-crystal level equalizer arrays on fiber arrays, *IEEE Photonics Technology Letters*, **16**(2), pp.527-529 (2004)

[81] K.Hirabayashi, M.Wada, and C.Amano, Liquid-crystal variable optical attenuators integrated on planar lightwave circuits, *IEEE Photonics Technology Letters*, **13**(6), pp.609-611 (2001)

[82] M.J.Mughal, and N.A.Riza, 65 dB dynamic range 2.8 microseconds switching speed variable fiber-optic attenuator, *13th European Conference on Optical Communications (ECOC)*, vol.6, pp.56-57 (2001)

[83] F.Chollet, M.de Labachelerie, and H.Fujita, Compact evanescent optical switch and attenuator with electromechanical actuation, *IEEE J. of Selected Topics in Quantum Electronics*, **5**(1), pp.52-59 (1999)

[84] S.T.Kawai, M.Koga, M.Okuno, and T.Kitoh, PLC type compact variable optical attenuator for photonic transport network, *Electronics Letters*, **34**(3), pp.264-265 (1998)

[85] M.Svalgaard, K.Faerch, and L.U.Andersen, Variable optical attenuator fabricated by direct UV writing, *J. of Lightwave Technology*, **21**(9), pp.2097-2102 (2003)

[86] S.M.Garner, and S.Carazzi, Variable optical attenuator for large scale integration, *IEEE Photonics Technology Letters*, **14**(11), pp.1560-1562 (2002)

[87] N.S.Lagali, J.F.P.Nunen, D.Pant, and L.Eldada, Ultra-low power and high dynamic range variable optical attenuator array, *13th European Conference on Optical Communications (ECOC)*, pp.430-431 (2001)

[88] I.E.Day, I.Evans, A.Knights, F.Hopper, S.Roberts, J.Johnston, S.Day, J.Luff, H.Tsang, and M.Asghari, Tapered silicon waveguides for low insertion loss highly-efficient high speed electronic variable optical attenuators, *Optical Fiber Communications (OFC)*, pp.249-251 (2003)

[89] B.Barber, C.R.Giles, V.Aksyuk, R.Ruel, and D.Bishop, A fiber connectorized MEMS variable optical attenuator, *IEEE Photonics Technology Letters*, **10**(9), pp.1262-1264 (1998)

[90] C.R.Giles, V.Aksyuk, B.Barber, R.Ruel, and D.Bishop, A silicon MEMS optical switch attenuator and its use in lightwave subsystems, *IEEE J. of Selected Topics in Quantum Electronics*, **5**(1), pp.18-25 (1999)

[91] X.M.Zhang, A.Q.Liu, C.Lu, and D.Y.Tang, MEMS variable optical attenuator using low driving voltage for DWDM systems, *Electronics Letters*, **38**(8), pp. 382-383 (2002)

[92] C.Marxer, P.Griss, and N.F.de Rooij, A variable optical attenuator based on silicon micromechanics, *IEEE Photonics Technology Letters*, **11**(2), pp.233-235 (1999)

[93] C.Marxer, B.de Jong, and N.de Rooij, Comparison of MEMS variable optical attenuator designs, *IEEE/LEOS International Conference on Optical MEMS (MOEMS)*, pp.189-190 (2002)

[94] M.Morimoto, K.Morimoto, K.Sato, and S.Lizuka, Development of a variable optical attenuator (VOA) using MEMS technology, *Furukawa Review*, No.23, pp.26-31 (2003)

[95] X.Dai, X.Zhao, and B.Cai, Development and characterization of electromagnetic microshutter in MEMS variable optical attenuator, *IEEE/LEOS International Conference on Optical MEMS (MOEMS)*, pp.63-64 (2002)

[96] X.Dai, X.Zhao, W.Li, and B.Cai, MEMS based variable optical attenuator, *Proc. of SPIE*, vol.**4601**, pp.97-103 (2001)

[97] W.Li, X.Zhao, B.Cai, G.Zhou, and M.Zhang, Magnetically actuated MEMS variable optical attenuator, *Proc. of SPIE* vol.**4601**, pp.89-96 (2001)

[98] C.Ji, Y.Yee, J.Choi, and J.Bu, Electromagnetic variable optical attenuator, *IEEE/LEOS International Conference on Optical MEMS (MOEMS*), pp.49-50 (2002)

[99] R.Wood, V.Dhuler, and E.Hill, A MEMS variable optical attenuator, *IEEE/LEOS International Conference on Optical MEMS (MOEMS)*, pp.19-20 (2000)

[100] B.M.Andersen, S.Fairchild, N.Thorsten, and V.Aksyuk, MEMS variable optical attenuator for DWDM optical amplifiers, *Optical Fiber Communications (OFC)*, vol.2, pp.260-262 (2000)

[101] C.H.Kim, N.Park, and Y.K.Kim, MEMS reflective type variable optical attenuator using off-axis misalignment, *IEEE/LEOS International Conference on Optical MEMS (MOEMS)*, pp.55-56 (2002)

[102] S.S.Yun, H.N.Kwon, W.H.Kim, Y.Y.Kim, M.K.Lee, W.I.Jang, and J.H.Lee, An integrated tunable optical filter with variable attenuation using micromachined Si multiple reflectors, *IEEE/LEOS International Conference on Optical MEMS (MOEMS)* (2002)

[103] Y.Y.Kim, S.S.Yun, C.S.Park, J-H.Lee, Y.G.Lee, H.K.Lee, S.K.Yoon, and J.S. Kang, Refractive variable optical attenuator fabricated by silicon deep reactive ion etching, *IEEE Photonics Technology Letters*, **16**(2), pp.485-487 (2004)

[104] R.R.A.Syms, H.Zou, J.Stagg, and D.F.More, Multistate latching MEMS variable optical attenuator, *IEEE Photonics Technology Letters*, **16**(1), pp.191-193 (2004)

[105] E.Fontana, R.H.Pantell, and S.Strober, Surface plasmon immunoassay, *Applied Optics*, **29**(31), pp.4694-4704 (1990)

[106] M.T.Flanagan, and R.H.Pantell, Surface plasmon resonance and immunosensors, *Electronics Letters*, **20**(23), pp.968-970 (1984)

[107] L.M.Zhang, and D.Uttamchandani, Optical chemical sensing employing surface plasmon resonance, *Electronics Letters*, **24**(23), pp.1469-1470 (1988)

[108] H.Kano, and S.Kawata, Surface-plasmon sensor for absorption-sensitivity enhancement, *Applied Optics*, **33**(22), pp.5166-5170 (1994)

[109] H.P.Ho, W.W.Lam, S.Y.Wu, and M.Yang, A chemical sensor based on the measurement of differential phase related to surface plasmon resonance, *IEEE Electron Devices Meeting*, pp.56-59 (2001)

[110] S.Patskovsky, A.V.Kabashin, and M.Meunier, Properties and sensing characteristics of surface plasmon resonance in infrared light, *J. Optical Society of America A*, **20**(8), pp.1644-1650 (2003)

[111] R.G.Hunsperger, *Integrated Optics: Theory and Technology*, Springer-Verlag, 3rd Ed., New York (1992)

[112] H.Raethler, *Surface plasmons on smooth and rough surfaces and on gratings*, Springer-Verlag, Berlin (1988)

[113] M.Yamamoto, Surface plasmon resonance (SPR) theory : Tutorial, *Review of Polarography (JPN)*, **48**(3), pp.209-237 (2002)

[114] S.K.Özdemir, and G.Turhan-Sayan, Temperature effects on surface plasmon resonance: Design considerations for an optical temperature sensor, *J. of Lightwave Technology*, **21**(3), pp.805-814 (2003)

[115] Q.Lai, W.Hunziker, and H.Melchior, Low-power compact 2×2 thermo-optic silica-on-silicon waveguide switch with fast response, *IEEE Photonics Technology Letters*, **10**(5), pp.681–683 (1998)

[116] S.Sohma, T.Goh, H.Okazaki, M.Okuno, and A.Sugita, Low switching power silica-based super high delta thermo-optic switch with heat insulating grooves, *Electronics Letters*, **38**(3), pp.127-128 (2002)

[117] L.Eldada, Polymer integrated optics: promise vs. practicality, *Integrated Optoelectronic Devices, Proc. of SPIE*, vol.**4642** (2002)

[118] M.P.Earnshaw, M.Cappuzzo, E.Chen, L.Gomez, A.Griffin, E.Laskowski, and A.Wong-Foy, Highly-integrated planar lightwave circuit wavelength selective switch, *Electronics Letters*, **39**(19), pp.1397-1398 (2003)

[119] K.Okamoto, T.Kominato, H.Yamada, and T.Goh, Fabrication of frequency spectrum synthesiser consisting of arrayed-waveguide grating pair and thermo-optic amplitude and phase controllers, *Electronics Letters*, **35**(9), pp.733-734 (1999)

[120] K.Oda, N.Takato, H.Toba, and K.Nosu, A wide-band guided-wave periodic multi/demultiplexer with a ring resonator for optical FDM transmission systems, *J. of Lightwave Technology*, **6**(6), pp.1016-1022 (1988)

[121] M.Okuno, K.Kato, Y.Ohmori, M.Kawachi, and T.Matsunaga, Improved 8×8 integrated optical matrix switch using silica-based planar lightwave circuits, *J. of Lightwave Technology*, **12**(9), pp.1597–1605 (1994)

[122] K.Kato, M.Ishii, and Y.Inoue, Packaging of large-scale planar lightwave circuits, *47th IEEE Electronics Component and Technology Conference*, pp.37-45 (1997)

[123] http://www.photonics.dupont.com, 8×8 switch with integrated VOA's and power taps, specification sheet

[124] G.Ulbers, An integrated optics sensor on silicon for the measurement of displacement, force and refractive index, *Proc. of SPIE*, vol.**1506**, pp.99-110 (1991)

[125] L.Eldada, J.Fujita, A.Radojevic, R.Gerhardt, O.Zhuromskyy, D.Pant, F.Wang, and C.Xu, Self-balancing optical add/drop switching subsystem on a chip, *National Fiber Optic Engineering Conference (NFOEC)*, F9, pp.1-8 (2003)

[126] K.Sakuma, D.Fujita, S.Ishikawa, T.Sekiguchi, and H.Hosoya, Low insertion-loss and high isolation polymeric Y-branching thermo-optic switch with partitioned heater, *Optical Fiber Communications (OFC)*, vol.3, paper WR3 (2001)

[127] J.Bismuth, P.Gidon, F.Revol, and S.Valette, Low-loss ring resonators fabricated from silicon based integrated optics technologies, *Electronics Letters*, **27**(9), pp.722-724 (1991)

[128] T.Kominato, Y.Ohmori, H.Okazaki, and M.Yasu, Very low-loss GeO_2-doped silica waveguides fabricated by flame hydrolysis deposition method, *Electronics Letters*, **26**(5), pp.327-329 (1990)

[129] R.Adar, M.R.Serbin, and V.Mizraki, Less than 1 dB per meter propagation loss of silica waveguides measured using a ring resonator, *J. of Lightwave Technology*, **12**(8), pp.1369-1371 (1994)

[130] R.G.Walker, and C.D.W.Wilkinson, Integrated optical ring resonators made by silver ion-exchange in glass, *Applied Optics*, **22**, pp.1029-1035 (1982)

[131] J.Haavisto, and G.A.Pajer, Resonance effects in low-loss ring waveguides, *Optics Letters*, **5**(12), pp.510-512 (1980)

[132] P.Heimala, P.Katila, and J.Aarnio, Integrated optical ring resonator on silicon with thermal tuning and in situ temperature measurement, *SPIE International Symposium on Lasers and Integrated Optoelectronics, Proc. of SPIE*, vol.**2695A-07**, pp.71-77 (1996)

[133] G.Economou, R.C.Youngquist, and D.E.N.Davies, Limitations and noise in interferometric systems using frequency ramped single-mode diode lasers, *J. of Lightwave Technology*, **LT-4**(11), pp.1601-1608 (1986)

[134] Y.Inoue, T.Kominato, Y.Tachikawa, and O.Ishida, Finesse evaluation of integrated-optic ring resonators with heterodyne detection technique, *Electronics Letters*, **28**(7), pp.684-686 (1992)

[135] J.Aarnio, Optical integrated structures and circuits on silicon, *VTT Publications* 106, dissertation, VTT Technical Research Centre of Finland (1992)

[136] P.K.Tien, Light waves in thin films and integrated optics, *Applied Optics*, **10**(11), pp.2395-2413 (1971)

[137] G.Grand, and S.Valette, Optical polarizers of high extinction ratio integrated on oxidized silicon, *Electronics Letters*, **20**, pp.730-731 (1984)

[138] A.Heinämäki, *personal correspondence*

[139] A.S.Grove, *Physics and technology of semiconductor devices*, John Wiley & Sons Inc., pp.102-103, New York, (1967)

[140] H.Nishihara, M.Haruna, and T.Suhara, *Optical Integrated Circuits*, McGraw-Hill, New York (1985)

[141] R.Kasahara, M.Yanagisawa, A.Sugita, T.Goh, M.Yasu, A.Himeno, and S.Matsui, Low-power consumption silica-based 2×2 thermo-optic switch using trenched silicon substrate, *IEEE Photonics Technology Letters*, **12**(9) pp.1132-1134 (1999)

[142] Y.Inoue, K.Katoh, and M.Kawachi, Polarization sensitivity of a silica waveguide thermo-optic phase shifter for planar lightwave circuits, *IEEE Photonics Technology Letters*, **4**(1), pp.36-38 (1992)

[143] K.Suzuki, K.Takiguchi, and K.Hotate, Monolithically integrated resonator micro-optic gyro on silica planar lightwave circuit, *J. of Lightwave Technology*, **18**(1), pp.66–72 (2000)

[144] G.Bourdon, G.Alibert, A.Beguin, B.Bellman, and E.Guiot, Ultra low loss ring resonator using 3.5% index-contrast Ge-doped silica waveguides, *IEEE Photonics Technology Letters*, **15**(5), pp.709-711 (2003)

[145] H.P.Lutz, Review on ESA free-Optical Communications in Space - Twenty Years of ESA Effort, *ESA Bulletin* Nr. 91 (1997)

[146] W.Leeb, A.Kalmar, M.Leppihalme, P.Katila, and T.Aalto, Integrated-optics beam combiner in silicon technology (ibis), *Appraisal and Evaluation report, prepared for the European Space Agency*, No. 9673/91/NL/PB, Work Order No.3 (2000)

[147] L.B.Soldano, and E.C.M.Pennings, Optical multi-mode interference devices based on self-imaging and applications, *J. of Lightwave Technology*, **13**(4), pp.615-627 (1995)

[148] K.Takada, and S.Mitachi, Measurement of depolarization ratio and ultimate limit of polarization crosstalk in silica-based waveguides by using a POLCR, *J. of Lightwave Technology*, **4**(16), pp.639-645 (1998)

[149] P.Heimala, J.Aarnio, and S.Tammela, Precision prism coupling setup applied to measure planar silica films on silicon, *Report Series in Physics HU-P-258*, University of Helsinki, p.28 (1992)

[150] T.Aalto, M.Harjanne, and M.Kapulainen, Method for the rotational alignment of polarization-maintaining optical fibers and waveguides, *Optical Engineering*, **42**(10), pp.2861-2867 (2003)

[151] *Generic Requirements for Passive Optical Components*, GR-1209, Telcordia Technologies Inc. (2001)

[152] *Generic Requirements for Fiber Optic Attenuators*, GR-910, Telcordia Technologies Inc. (1998)

[153] Transmission systems and media, digital systems and networks, Transmission media characteristics – characteristics of optical components and subsystems, *Recommendation Series ITU-T G.671*, International Telecommunications Union (ITU) (2002)

[154] Transmission systems and media, digital systems and networks, Optical system design and engineering considerations *Recommendation Series G Supp.39*, International Telecommunications Union (ITU) (2003)

[155] K.Sato, T.Aoki, Y.Watanabe, Y.Oguri, N. Shibata, T.Nishiwaki, M.Oike, and T.Ota, Development of a variable optical attenuator, *Furukawa Review*, No. 20, pp.15-20 (2001)

[156] P.Katila, Attenuateur optique variable, *French patent ref*. 2 835 929 (2003)

[157] J.H.Jerman, J.D.Drake, and J.D.Grade, Electrostatic microactuator and method for use thereof, *US Patent* 5998906 (1999)

[158] J.D.Grade, H.Jerman, and T.W.Kenny, A large deflection electrostatic actuator for optical switching applications, *Sensor and Actuator Workshop*, pp.97-100 (2000)

[159] A.R.Mirza, G.Wu, S.K.Gamage, L.Ukrainczyk, and N.Shashidhar, Integration of fiber optic lenses with small form factor MEMS components, *Technical paper*, Corning Inc., US (2002)

[160] H.Kogelnik, *Topics in applied physics. Vol. 7, chap. 2*, ed. T.Tamir, Springer-Verlag, New York (1975)

[161] M.Saruwatari, and K.Nawata, Semiconductor laser to single-mode fiber coupler, *Applied Optics*, **18**(11), pp.1847-1856 (1979)

[162] R.Legtenberg, A.W.Groeneveld, and M.Elwenspoek, Comb-drive actuators for large displacements, *J. of Micromechanics and Microengineering*, **6**(3), pp.320-329 (1996)

[163] R.G.Budynas, and W.C.Young, *Roark's formulas for stress and strain*, 7th ed., McGraw-Hill, New York (1989)

[164] S.D.Senturia, *Microsystem design*, p.155, Kluwer Academic Publishers, Norwell, MA (2001)

[165] J.A.Gere, and S.P.Timoshenko, Mechanics of Materials, 4th ed., pp.507-514, PWS Publishing Company, Boston, MA (1997)

[166] K.S.Chen, A.A.Ayon, X,Zhang, and S.M.Spearing, Effect of process parameters on the surface morphology and mechanical performance of silicon structures after deep reactive ion etching (DRIE), *J. of Microelectromechanical systems*, **11**(3), pp.264-275 (2002)

[167] P.Katila, Attenuateur optique variable, *French patent ref*. 2 839 060 (2003)

[168] X.M.Zhang, A.Q.Liu, and C.Lu, New near-field and far-field attenuation models for free space variable optical attenuators, *J. of Lightwave Technology*, **21**(12), pp.3417-3426 (2003)

[169] G.Z.Xiao, Z.Zhang, F.G.Sun, and C.P.Grover, Effects of environment temperature induced heater resistance change on the attenuation of MZI type variable optical attenuators, *IEEE Photonics Technology Letters*, **16**(2), pp.482-484 (2004)

[170] http://www.photonics.dupont.com, Dupont, (online datasheet of iVOA2000D)

[171] http://www.diconfiberoptics.com, Dicon FO Inc., (online datasheet MEMS-VOA)